Organic Optoelectronic Devices Employing Small Molecules

by

Tyler Blain Fleetham

A Dissertation Presented in Partial Fulfilment
of the Requirements for the Degree
Doctor of Philosophy

Approved April 15, 2014 by the
Graduate Supervisory Committee:

Jian Li, Chair
Terry Alford
James Adams

ARIZONA STATE UNIVERSITY

May 2014

ABSTRACT

Organic optoelectronic devices have remained a research topic of great interest over the past two decades, particularly in the development of efficient organic photovoltaics (OPV) and organic light emitting diodes (OLED). In order to improve the efficiency, stability, and materials variety for organic optoelectronic devices a number of emitting materials, absorbing materials, and charge transport materials were developed and employed in a device setting. Optical, electrical, and photophysical studies of the organic materials and their corresponding devices were thoroughly carried out.

Two major approaches were taken to enhance the efficiency of small molecule based OPVs: developing material with higher open circuit voltages or improved device structures which increased short circuit current. To explore the factors affecting the open circuit voltage (V_{OC}) in OPVs, molecular structures were modified to bring V_{OC} closer to the effective bandgap, ΔE_{DA}, which allowed the achievement of 1V V_{OC} for a heterojunction of a select Ir complex with estimated exciton energy of only 1.55eV. Furthermore, the development of anode interfacial layer for exciton blocking and molecular templating provide a general approach for enhancing the short circuit current. Ultimately, a 5.8% PCE was achieved in a single heterojunction of C_{60} and a ZnPc material prepared in a simple, one step, solvent free, synthesis.

OLEDs employing newly developed deep blue emitters based on cyclometalated complexes were demonstrated. Ultimately, a peak EQE of 24.8% and nearly perfect blue emission of (0.148,0.079) was achieved from PtON7dtb, which approaches the maximum attainable performance from a blue OLED. Furthermore, utilizing the excimer formation properties of square-planar Pt complexes, highly efficient and stable white devices employing a single emissive material were demonstrated. A peak EQE of over 20% for pure white color (0.33,0.33) and 80 CRI was achieved with the tridentate Pt complex, Pt-16. Furthermore, the development of a series of tetradentate Pt complexes yielded highly efficient and stable single doped white devices due to their halogen free tetradentate design. In addition to these benchmark achievements, the systematic molecular modification of both emissive and absorbing materials provides valuable structure-property relationship information that should help guide further developments in the field.

ACKNOWLEDGEMENT

I would like to thank my advisor, Dr. Jian Li for his guidance and the opportunity to work on such exciting projects and my committee members Dr. James Adams and Dr. Terry Alford. I would also like to thank the wonderful chemists with whom I have worked over the past 5 years: Liang Huang, Eric Turner, Dr. Xiao-Chun Hang, Dr. Zixing Wang, Dr. Guijie Li, Dr. Lele Wen, and Dr. Zhi-Qiang Zhu. Without their insight and expertise my research would not have been be possible. I also want to thank my fellow device engineers: Nathan Bakken, Jeremy Ecton, Timo Park, Gregory Norby, Kody Klimes, Barry O'Brien, and my brothers Trever and Trenten for their help in device testing and characterization and the many helpful and constructive conversations. I would also like to acknowledge Professor Jiangeng Xue's group at University of Florida for their collaboration and support on much of this work. This work would not have been possible without the financial support provided by the National Science Foundation, Universal Display Corporation, the Advanced Photovoltaics Center, and the Department of Energy which is gratefully acknowledged. Finally, I would like to thank my friends and family for their love and support and in particular my wife for her unlimited patience and words of encouragement.

TABLE OF CONTENTS

LIST OF TABLES

Table Page

Table Page

LIST OF FIGURES

Figure Page

Figure Page

Figure Page

Figure Page

Figure Page

1. INTRODUCTION

Current worldwide consumption rate of energy is estimated to be over 13.5 terawatts.[1] Conservative estimates project that this rate will increase to as large as 27.6TW as a result of growing worldwide population and growing energy demand in an increasingly industrialized world. Furthermore, as the public becomes progressively more aware of the environmental, social, and economic costs of fossil fuels worldwide, it is apparent that a departure from the current worldwide dependence on these traditional energy sources is necessary.[2] Two major strategies taken by governmental entities, environmentalists, and academic researchers alike are the adoption of energy saving strategies including the development of energy efficient electronic devices, and the development and adoption of renewable sources of energy. The former strategy is the main drive behind the energy efficient lighting while the latter strategy requires the development and deployment alternative energy sources, in particular, solar energy to fulfill the urgent need for a replacement to traditional fossil fuel sources.

One potential route for the development of economically viable, efficient, and environmentally benign photovoltaic and lighting technologies is organic optoelectronic devices. Many current solutions to the white lighting or solar energy problems employ crystalline inorganic semiconductors as either light absorbing or light emitting devices. These technologies have been under constant development for over half a century and a number of promising and commercially available products have already been produced. Unfortunately, the crystalline nature of these devices often require complicated fabrication procedures in expensive clean rooms, high cost substrates, and often times expensive balance of system costs to support the rigid and heavy devices, as is the case for current solar cell products.[3] In contrast to these devices, organic materials are currently produced in large scale chemical reactions, are usually amorphous in nature, and have very strong optical properties. Organic materials, however, are typically considered insulators and historically have very unfavorable properties for use in electronic devices. With the discovery of conductive polymers by Alan Heeger, Alan MacDiarmid, and Hideki Shirakawa, this would be changed forever and the field of organic electronics was born, a feat that earned them the 2000 Nobel Prize in Chemistry.[4] Today, organic electronic devices, and in particular organic photovoltaics (OPV) and organic light emitting diodes (OLED), are one of the celebrated fields bringing together chemists, electrical engineers, physicists, material scientists, and a variety of other disciplines.

Organic electronic materials have a number of unique advantages over traditional inorganic materials. One of the most evident advantages of organic semiconductors is the ability to easily tunable structural, optical, and electrical properties through small molecular modification in synthetic methods that are compatible with commercial scale production.[5] The ability to synthesize and screen large classes of materials has allowed the field to progress very rapidly. Furthermore, improvements in computational chemistry are rapidly improving in the accuracy of predicting structural, energetic, and optical properties of molecular materials.[6] It could soon be realized that entire classes of organic materials can be screened for desirable properties for even more rapid progress. Secondly, due to the amorphous nature of organic materials constraints of lattice matching to substrates are greatly loosened and organic electronic devices can be compatible with a wide array of cheap substrates such as glass, plastic, or metal foils.[7] Furthermore, there are a wide variety of deposition methods of the active layers ranging from solution processing methods like spin coating and screen printing to simple thermal deposition methods.[7] Through these benefits, a plausible future in which organic electronic devices are fabricated through roll-to-roll processing on cheap flexible substrates employing easily synthesize organic materials using only environmentally friendly and earth abundant materials is clearly within sight.

Despite these numerous benefits to organic electronic devices, challenges remain. Organic materials have strong covalent pi bonds within individual molecules but only weak van der waals interactions between molecules.[8] As a result, there is strong orbital delocalization within molecules or polymer chains but minimal orbital overlap between molecules. Consequently, the processes of light absorption, light emission, charge transport, and exciton diffusion of organic films are related to highly localized interactions of individual orbitals rather than delocalized bands. In molecular light absorption a photon excites electrons between the discrete highest occupied molecular orbital (HOMO) and the lowest unoccupied molecular orbital (LUMO).[9] Similarly, molecular light emission occurs as a radiative relaxation of an excited state on a single molecule to the ground state configuration. Thus, the discrete nature of the molecular energy levels results in relatively narrow absorption and emission bands which can be a disadvantage, particularly in the case of OPVs. Furthermore, the picture of freely moving charge carriers characteristic of inorganic semiconductors is not appropriate so new entities must be described. Negative and positive charges in organic electronic materials are achieved through the removal or addition of an electron from the molecular orbitals, which is analogous to oxidation or reduction of the molecule, respectively. In this picture, the motion of an electron (hole) requires intermolecular hopping from the LUMO (HOMO) of a molecule to the LUMO (HOMO) of another. This endothermic hopping process has the effect of reducing the mobility of organic materials, typically on the order of 10^{-2} to 10^{-5} cm^2/Vs.[7] Similarly, excited states in organic materials are localized on a single or small number of molecules in a coulombically bound pair called a Frenkel Exciton, in contrast to excitons in inorganic crystals that exist over lengths of 10s to 100s of nanometers.[7] Excitons have a limited lifetime before recombining or can move through the film by exciton diffusion until it can be separated by an energetic asymmetry like a defect or an interface. As a result of these challenges much work is needed to design both materials with improved optical and electrical properties as well as design devices that alleviate such constraints where the advantages of organic materials can largely outweigh their prescribed disadvantages.

In this dissertation, I will discuss work on the development of efficient OPVs and stable and efficient blue and white OLEDs. In Chapter 2, I will discuss the background and operation of organic solar cells, followed by a discussion on new materials for enhancing open circuit voltage in Chapter 3 and enhanced short circuit current through the inclusion of anode buffer layers in Chapter 4. In Chapter 5, I will introduce the operation and materials for organic light emitting devices followed by progress on deep blue OLEDs in Chapter 6 and single doped white OLEDs in Chapter 7. In chapter 8 I will give a summary of conclusions and future outlook.

2. ORGANIC PHOTOVOLTAICS

Since the development of the first efficient solar cells by Chapin, Fuller, and Pearson at Bell Labs in 1954 employing silicon based p-n junctions gradual improvements in device efficiencies have been achieved.[10] Solar power in these p-n junctions is produced through a two-step process of absorption of photons followed by the charge separation of the resulting excited electrons and holes due to an electric field resulting from the p-n junction. An incident photon of energy greater than the band gap (Silicon Eg=1.1eV) is absorbed by either the p-type layer, n-type layer, or the depletion region where the efficiency of the absorption process is determined by the material bandgap, absorption strengths, and thicknesses.[11] If the thickness is sufficient, all photons with an energy greater than the bandgap will be absorbed and can be separated by the p-n junction to create an electrical current. Thus, if the bandgap of the semiconductor is large, photons with energy less than the bandgap will not be absorbed and the current will be significantly reduced. On the other hand, the energy a photon has greater than the band gap is lost as phonons (heat), so, if the bandgap of the semiconductor is very small then a large portion of the solar spectrum has the possibility of being absorbed (high current) but all the excess energy is lost which is manifest in low voltage outputs. This describes the essential tradeoff in solar cells which leads to a theoretical maximum power conversion efficiency, known as the Shockley-Quiser limit, determined to be a maximum power conversion efficiency (PCE) of about 31% efficient for a single pn-junction.[12] PCE is defined as the ratio of watts electrical power produced to watts sunlight incident, which is typically assumed to be on average about 100mw/cm^2 for terrestrial AM1.5G sunlight. Single crystalline Si based solar cells have reached efficiencies as high as 27.6% in a laboratory setting and GaAs based devices have reached even higher, 29.1%, which are approaching their respective theoretical maxima.[13] Thus, future improvements in single p-n junction photovoltaics are expected to be minimal.

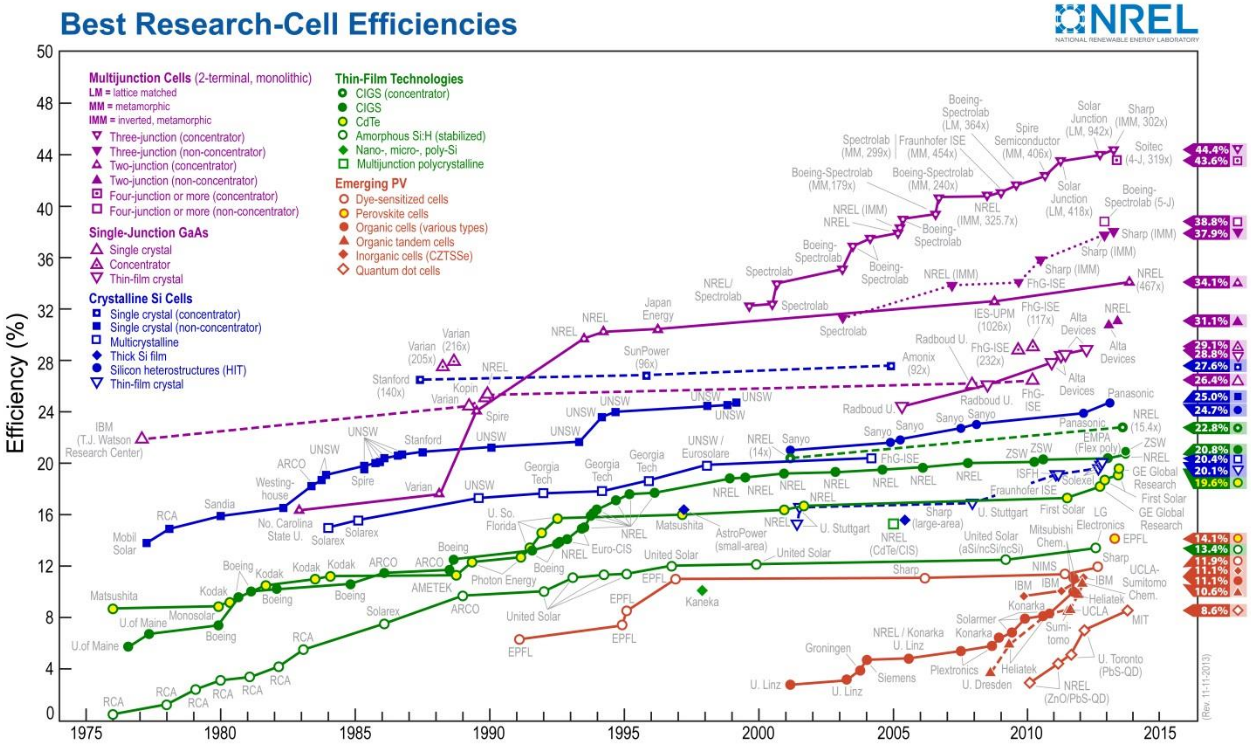

Figure 1. Solar cell efficiency tables[13]

Despite the intense research in crystalline silicon solar cells, the near theoretical maximum efficiencies, and dramatic reduction in costs over the past few decades, the technology has not been adopted as a major energy source. Silicon based solar cells, as well as other bulk crystalline materials require costly processing techniques, high purity control, and large amounts of material keeping costs these technologies rather high. Furthermore, the costs to consumers is still too high for large scale adoption due to module assembly costs, structural and electrical costs, installation costs among others which are considered the “balance of systems” costs. In some instances the balance of systems costs can make up 90% of the total cost of the photovoltaic system.[3] Thus, even if marginal reductions in the costs of the active materials are made, the costs of the total systems will remain high. Ultimately, the crystalline nature of these solar cells makes them necessarily thick and rigid which keeps module costs high as they are unable to be integrated into other systems such as building materials that would reduce the balance of systems costs. Another factor that remains to be shown is the ability to scale up the production of the current crystalline technologies to offset the 13.5 TW of electricity that primarily uses fossil fuels within a timely manner.

2.1 Organic photovoltaic development

Two potential options to reduce the costs of solar energy systems are to increase the efficiency of crystalline solar cells to get more power out of the same system, or use cheap and flexible organic materials that reduce the costs of both the cells and the overall system. The former option is currently a major focus of much research employing multiple junctions, concentrators, or trackers. Nevertheless, these technologies still suffer from problems of labor intensive processing or even larger structural costs.

Figure 2. Potential Applications of Organic Photovoltaics

Organic photovoltaics (OPVs) on the other hand use pigments that are currently produced cheaply in high volumes and only require total device thicknesses of about 100nm in amorphous nanocrystalline films.[14] The organic materials have the ability to be deposited in a wide variety of techniques including various solution processes[15-18] and without the concern for epitaxial growth or lattice mismatch, the materials can be deposited on a various low cost and flexible substrates including plastics, metals, or glass.[19,20] Furthermore, the potential for flexible solar cells affords a number of highly sought benefits such as compatibility with high throughput roll to roll processing which will significantly reduce fabrication costs or integration with a large number of products ranging from roofing shingles to window tinting which, unlike inorganic solar cells, will eliminate the need for bulky structural support and installation that are responsible for the bulk of the balance of systems costs.[21] Thus, organic photovoltaics have great potential as a highly scalable and low cost electricity source and the development of this technology is highly sought by both academic research and corporations alike.[22-24]

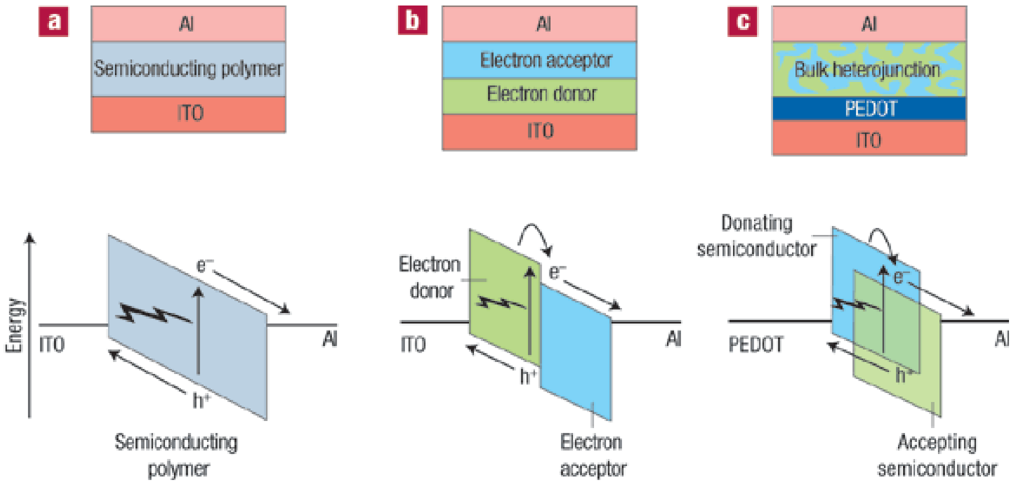

Figure 3. Various Device Structures

Initial attempts at organic photovoltaics consisted of sandwiching a semiconducting polymer between two electrodes and applying a bias, shown in Figure 3a.[25] These proved to have extremely poor performance because the strongly bound localized excitons were challenging to separate with just an applied field. Tang et. al. developed the first efficient organic solar cell using a donor-acceptor bilayer interface, as shown in Figure 3b.[26] The energy level asymmetry at the donor acceptor interface assists in the dissociation of bound excitons, into free electrons and holes. The archetypal device of this architecture is successively thermally evaporated layers of metal phthalocyanine (MPc) and C60 chosen for their high mobilities and strong absorption reaching power conversion efficiencies of around 3%.[27] Further improvement in this device architecture has proven challenging due to the low exciton diffusion length of the MPcs of around 5nm.[28] As a result of the low exciton diffusion length in organic materials, researchers developed the idea of a blended interpenetrating networks of donors and acceptors as shown in Figure 3c (15,16).[29-31] Here the donor and acceptor materials are mixed by either co-evaporation or by spin coating a mixture of the two materials. This structure allows there to be intimate contact of the two layers such that the distance to the interface is within the exciton diffusion length, yet the total absorption thickness is may be kept large. However, precise morphology control requires simultaneously optimizing a number of parameters. Thus, a large amount of research has been conducted in engineering molecules for improved self-organization of interpenetrating networks in addition to modifying the device architecture.[32] These developments, as well as development of new semiconducting organic materials, have resulted in increasing the efficiencies to over 10%.[13] For thermally evaporated devices, the development of planar mixed heterojunction with thin pure donor and acceptor layers with thicknesses on the order of the exciton diffusion lengths with a mixed layer between them allows for efficient exciton diffusion in addition to well controlled morphologies.[33] Other advanced device architectures include anode interfacial layers,[34] exciton blocking layers,[35] nanostructured electrodes,[36] or tandem cells.[37,38]

2.2 OPV operation

The current voltage characteristics of a typical organic solar cell is given in Figure 4 where J_{SC} is the short-circuit current density, V_{OC} the open-circuit voltage and $\mathrm{P}_{\mathrm{max}}$ is the maximum product of current and voltage. Another commonly measured parameter is the fill factor (*FF*) which is the ratio of $\mathrm{P}_{\mathrm{max}}$ to the product $J_{SC}*V_{OC}$ and is roughly a measure of the ideality of the photodiode. The power conversion efficiency (PCE, η_P) of a photovoltaic (PV) cell is given by equation 1 where P_O is the incident light intensity (optical power density)[11]:

$$\eta_P = \frac{J_{SC}V_{OC}}{P_O}\cdot FF \tag{1}$$

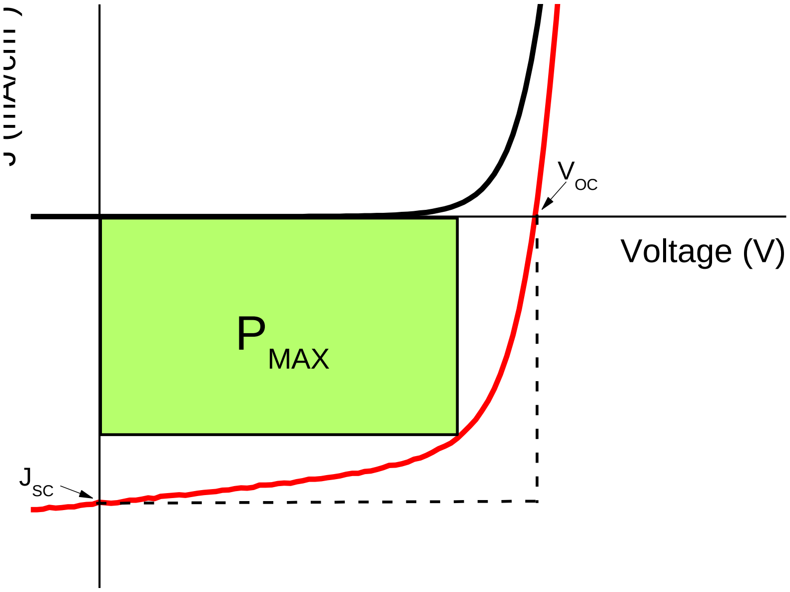

Figure 4. Current-Voltage characteristics of an organic solar cell in the dark (black) and under white light illumination (red)

From equation 1 it can be seen that the efficiency of an OPV can be enhanced by increasing FF, J_{SC}, or V_{OC} relative to the incident light intensity. Fill factor depends on a complex variety of parameters ranging from contact metal choice, to film morphology, to energy level alignment throughout the device all of which are important to the other performance parameters. Thus, the fill factor is typically controlled through logical materials choice and precise fabrication procedures and will not be the major focus of this research. Instead, the following research will focus on two main tasks: (1) increasing the J_{SC} through the development of strongly absorbing materials and through optimizing the efficiency of light to charge conversion and (2) increasing the V_{OC} through interface engineering and materials design.

2.2.1 Short Circuit Current

In contrast to crystalline inorganic materials, organic thin films have inherently different optical and electrical properties. Organic materials have strong covalent pi bonds within individual molecules but only weak van der waals interactions between molecules. As a result, there is strong orbital delocalization within molecules or polymer chains but minimal orbital overlap between molecules. Consequently, the processes of light absorption, exciton diffusion, and charge transport of organic films are related to highly localized interactions of individual orbitals rather than delocalized bands.[24] The production of photocurrent in OPVs is shown in Figure 5 to be the product of the processes of (1) light absorption to form a localized exciton, (2) exciton diffusion to the donor-acceptor heterojunction interface, (3) charge dissociation into radical anions (electrons) and cations (holes), (4) charge transport to the opposing contacts, and (5) charge collection by the anode and cathode contacts.

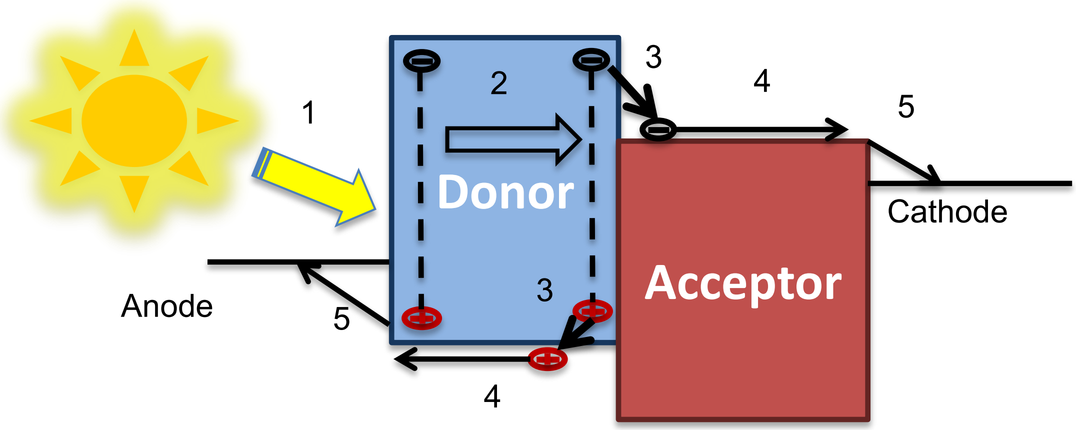

Figure 5. Diagram of current production in organic photovoltaics

In molecular light absorption (1) a photon excites electrons between the discrete highest occupied molecular orbital (HOMO) and the lowest unoccupied molecular orbital (LUMO). The discrete nature of the molecular energy levels results in relatively narrow absorption bands. Nevertheless, the organic materials typically exhibit very strong absorption coefficients near 10^{-5} cm^{-1} allowing the material to be relatively thin for complete absorption.[19-20] However, the excited electron is still localized on the molecule in a coulombically bound pair called a Frenkel Exciton, in contrast to excitons in inorganic crystals that exist over lengths of 10s to 100s of nanometers. Excitons have a limited lifetime before recombining and can move through the film by exciton diffusion (2) until it can be separated by an energetic asymmetry like a defect or an interface where the exciton diffusion length is typically in the range of 3-40nm.[39] The efficiency and rate of dissociation (3) of the exciton into radical cation and anions depends on a number of factors including: intermolecular overlap, exciton binding energies, and the HOMO and LUMO levels of the neighboring donor and acceptor molecules.[40] Finally, the conduction of the separated electrons and holes (4-5) occurs by a hopping mechanism where the electrons move from the orbital of one molecule to a neighboring molecule overcoming an energy barrier in a thermally activated process.[39] The efficiency of this process at a given wavelength is described by the external quantum efficiency (Equation 2).

$$\eta_{EQE}(\lambda) = \eta_{ABS}\eta_{ED}\eta_{CT}\eta_{CC} \qquad (2)$$

The external quantum efficiency is crucial in understanding the efficiency of the various photocurrent generation processes. From the EQE response integrated over the solar spectrum, the short circuit current can be derived following equation 3. Thus, to enhance the J_{SC}, much work will be done to optimize the efficiency of each process and broaden the spectral range in which these processes are efficient.

$$\mathrm{Jsc} = \int \frac{q\lambda}{hc}\mathrm{S}(\lambda)n\mathrm{EQE}(\lambda)d\lambda \qquad (3)$$

2.2.2 *Open Circuit Voltage*

To improve the PCE of OPV cells, the voltage output from these devices, i.e. the value of V_{OC}, also needs to be significantly improved beyond their typical values of around 0.5-0.6 V for many common devices, such as in those using phthalocyanines or poly(3-hexylthiophene) (P3HT) to form donor-acceptor heterojunctions with fullerenes.[19, 27,16] This means that the absorption of a photon with energy of 2-3 eV only creates an electrical energy of 0.5-0.6 eV for the collected electron-hole pair, corresponding to an energy loss of approximately 70-80%. Instead of being primarily related to the work functions of the electrodes as in inorganic solar cells, numerous studies have suggested that the V_{OC} is related to the energy gap between the donor material's highest occupied molecular orbital (HOMO) and the acceptor's lowest unoccupied molecular orbital (LUMO) energy levels at the DA heterojunction, ΔE_{DA}.[41-44] Significant efforts have been made in designing donor and acceptor materials with energy levels that increase ΔE_{DA} in order to achieve higher V_{OC}.[41, 44] However, the nature of the relationship between V_{OC} and ΔE_{DA} is still not well resolved as V_{OC} can be less than half of ΔE_{DA} for some material systems. As a result, the dependence of V_{OC} on the magnitude of ΔE_{DA} depends on the materials used.[45] Additionally, for a given donor-acceptor material system, V_{OC} has been shown to depend on a number of parameters including incident light intensity,[27, 46] the device architecture,[33,46,47] temperature,[45] and material purity.[48]

From a circuitry point of view, ultimately the physical origin of V_{OC} is based on the photocurrent generation and the diode current (dark current), specifically the voltage at which they offset each other. The electrical characteristics of organic photovoltaic cells under illumination have been shown to be accurately described by the modified Shockley equation for diodes (neglecting the effect of high shunt resistance)[27,49]:

$$J(V) = J_s\left[\exp\left(\frac{q(V - JR_{SA})}{nkT}\right) - 1\right] + J_{ph}(V), \tag{4}$$

where J_{ph} is the photocurrent density (which is negative at $V = 0$), J_s is the dark reverse-bias saturation current density, n is the ideality factor, R_{SA} is the specific series resistance, k is the Boltzmann constant, and T is the device temperature. Hence, at the open-circuit condition ($J = 0$) we have:

$$V_{OC} = \frac{nkT}{q}\ln\left[\frac{|J_{ph}(V_{OC})|}{J_s}\right] \approx \frac{nkT}{q}\ln\left(\frac{J_{SC}}{J_s}\right), \tag{5}$$

where the approximation assumes the photocurrent does not change significantly from 0 V (at short-circuit) to V_{OC}.

This equation is instrumental in explaining the observed increase in V_{OC} under higher light intensities, where J_{SC} is higher, and at lower temperatures, where J_s is minimized. Experiments show that the V_{OC} approaches a maximum attainable value for architecturally optimized devices at low temperatures and maximum light intensities.[27,45] Accordingly, the V_{OC} for devices under typical operating conditions of 1 sun and room temperature could be significantly lower than the maximum attainable value for an optimized architecture. Operating at high light intensities and low temperatures is not desired due to the increased structural and operational cost of maintaining light concentration and cooling mechanisms accompanied by the potential for increased degradation of organic materials at high light intensities. In order to maximize the power conversion efficiencies at the desired operating conditions for a given material system, the V_{OC} should be forced closer to the maximum obtainable value through the reduction of dark current.

3. METAL COMPLEXES FOR ENHANCED OPEN CIRCUIT VOLTAGE

3.1 Partially Chlorinated Zinc Phthalocyanine Based Devices

Zinc phthalocyanine (ZnPc) is a widely studied donor material due to its high hole mobility and strong absorption.[50] However, high efficiencies for these devices have been elusive due to the low V_{OC} reported at around 0.4 to 0.5 V under normal operating conditions of 1 sun and room temperature. Here it is shown that home-synthesized ZnPc containing chlorinated derivatives results in significantly increased V_{OC} in ZnPc/C_{60} donor-acceptor heterojunction OPV devices, compared to commercially obtained ZnPc. The V_{OC} dependencies on light intensity, temperature, and donor layer thickness for these two materials in identical device architectures are significantly different reflected by their differences in the dark current parameters. Furthermore the current-voltage behavior is primarily dependent on the material present at the donor acceptor interface.

3.1.1 Experimental

Two different sources of ZnPc materials were used for fabricating OPV cells in this study: a commercial source (CS) and a home synthesized source (HS), which are denoted as $ZnPc^{CS}$ and $ZnPc^{HS}$, respectively, to facilitate the discussions. The commercial ZnPc source is from Sigma Aldrich (99% purity), and the as-received material was further purified one to two times using the thermal gradient sublimation method prior to use for thin film deposition and device fabrication.[51] ZnPc was also synthesized in our own laboratories following the reaction scheme shown in Fig. 1.[52] Zinc chloride was mixed thoroughly with an excess of 1,2-dicyanobenzene in a 1:10 ratio in a round bottom flask. The reactants were quickly heated to 200°C and refluxed for 6 hours to yield a dark blue-violet solid product. The crude product was cooled to room temperature, washed with dichloromethane, and filtered to wash out the soluble impurities and remaining starting materials. The solid filtrate product was dried thoroughly then sublimed [36] in a four-zone thermal gradient furnace for 12 hours with the first two zones at 420°C, a middle zone of 380°C, and the cool zone at 340°C under a pressure of 10^{-6} Torr. After cooling to room temperature the violet purified crystals were collected from the middle temperature zone.

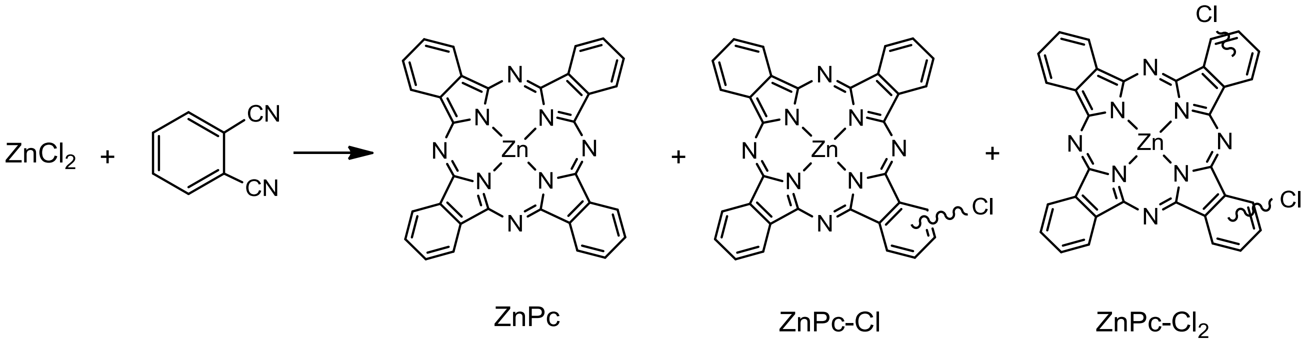

Figure 6. Synthetic route for the home-synthesized zinc phthalocyanine (ZnPc^{HS}) and the further chlorination to form mono- and di-chlorinated ZnPc (ZnPc-Cl and ZnPc-Cl_2, respectively).

For bulk composition analysis, ATR-FTIR measurements of the two different ZnPc powders were performed in air at ambient temperature and pressure using a Nicolet Nexus FTIR spectrometer equipped with a DTGS detector, a MVP-Pro ATR accessory from Herrick Scientific, and a silicon ATR crystal. The spectra were measured at 8 cm^{-1} resolution and six scans for a wavenumber range of 400–4000 cm^{-1}. The oxidation and reduction potentials of ZnPc^{CS} and ZnPc^{HS} were determined using cyclic voltammetry and differential pulse voltammetry in a solution of anhydrous dimethylformamide (DMF). Mass spectra of the two ZnPc sources were also obtained using matrix-assisted laser desorption/ionization (MALDI) technique, with matrix of terthiophene (658.95 g/mol) and 5,10,15,20-tetra(p-tolyl)porphine (670.31 g/mol) used as internal standard for molar mass calibration.

Composition of the two ZnPc materials was also compared using x-ray photoemission spectroscopy (XPS), although thin films deposited in high vacuum were used instead of bulk samples (see below on thin film deposition). The XPS measurement was performed in a Surface Science SSX-100 spectrometer with Al K_α x-ray source. The background pressure in the measurement chamber was about 4×10^{-9} Torr.

Thin films of ZnPc and other small molecule materials were deposited by vacuum thermal evaporation in custom-made high vacuum chambers (base pressure ~ 1×10^{-7} Torr). The film thickness was monitored by quartz crystal microbalances, and typical deposition rates of the organic thin films are in the range of 0.5 to 1.5 Å/s.

OPV devices were fabricated on glass substrates pre-coated with a patterned transparent indium tin oxide (ITO) anode. Prior to organic depositions the ITO substrates were successively cleaned by sonication in water, acetone, and isopropanol followed by UV-ozone treatment for 15 minutes. A ZnPc donor layer and a C_{60} acceptor layer were successively deposited, which constitutes the active region of the OPV cell. A bathocuproine (BCP) exciton-blocking layer was also deposited followed by the deposition of an Al cathode to complete the device.[19] The ITO and Al electrodes were patterned to form device areas of 4 mm^2 in cross-bar geometry. BCP was purchased from Sigma Aldrich and C_{60} was purchased from MER Corporation, both of which were purified using the thermal gradient sublimation method prior to use.

Current-voltage (I-V) characteristics in the dark and under illumination of a 150W Xe-arc solar simulator (Newport) with an AM 1.5G filter were measured using a Keithley

2400 source meter in a nitrogen filled glove box. Unless otherwise noted all tests were carried out at room temperature and 100 mW/cm^2 (or 1 sun AM1.5G) illumination determined using a Hamamatsu Si reference cell (Model C24 S1787-04) calibrated by NREL. The spectral mismatch is estimated to be less than 10%. For tests of variable light intensities, neutral density filters were used. For variable temperature testing, a Janis VNF100 series liquid nitrogen cooled cryostat was used to control the temperature from 100 to 300 K. To measure the external quantum efficiency (EQE, η_{EQE}) as a function of wavelength, a monochromatic beam of light was generated by using a Xe lamp (Optronic Laboratories) in conjunction with an Optronic Lab OL750 series monochromator, which was then chopped at 400 Hz prior to incident on the device. The photocurrent output was then measured using a lock-in amplifier (Stanford Research SR830), from which η_{EQE} was determined by comparing to the monochromatic beam intensity measured using a calibrated Si photodetector. Unless otherwise noted, the test cell was under short circuit while the wavelength of the incident monochromatic light was varied.

For measurement of electrical defect concentrations, 200 nm thick ZnPc thin films were sandwiched between the ITO electrode and a thermally evaporated Al electrode. The low work function Al electrode forms a Schottky contact with ZnPc. Capacitance-voltage (C-V) measurements were conducted in the dark using an Agilent 4155C semiconductor parameter analyzer.

3.1.2 Results and Discussion

Figure 7 shows a comparison of the FTIR spectra of ZnPc^{CS} and ZnPc^{HS} in the chemical fingerprint region from 400 to 1800 cm^{-1} (the spectra are vertically offset for clarity). Comparison of the spectra in the full scan range (400–4000 cm^{-1}) is also shown in the inset. There are no noticeable differences in the FTIR fingerprints between the two ZnPc samples. UV-vis measurement was also performed on the vacuum deposited ZnPc^{HS} and ZnPc^{CS} films with the same thickness, and have not found any noticeable difference in their absorption spectra.

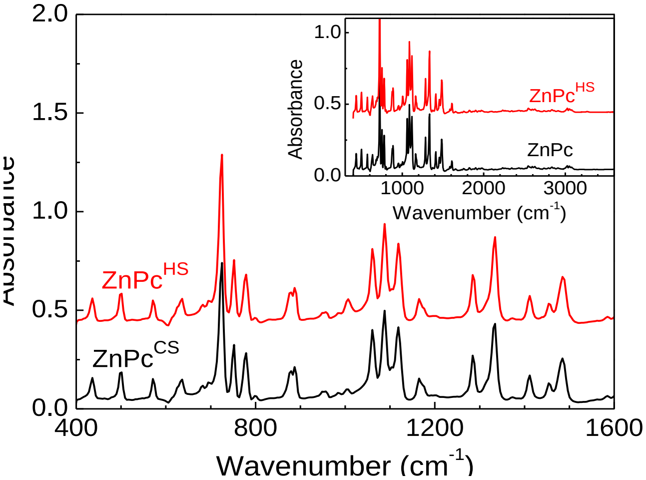

Figure 7. Comparison of the FT-IR absorption spectra of home-synthesized and commercial ZnPc sources, ZnPc^{HS} and ZnPc^{CS}, respectively

The oxidation and reduction potentials of ZnPc were determined using cyclic voltammetry and differential pulse voltammetry in a solution of anhydrous DMF. The oxidation potentials for ZnPc^{CS} and ZnPc^{HS} are determined to be 0.25 V and 0.27 V, respectively, versus Fc/Fc^{+}, showing only minor differences between the two ZnPc sources, which are similar to that reported in literature.[50]

The MALDI mass spectra of the two ZnPc sources do suggest some difference in their bulk composition. As shown in Fig. 3(a), the spectrum for ZnPc^{CS} show peaks in agreement with the actual molecular weight of ZnPc ($C_{32}H_{16}N_8Zn$), which is 577.91 g/mol. The higher molecular weight peaks in the spectrum correspond to the internal standards used; however, two lower molecular weight peaks at approximately 522 and 550 g/mol can also be identified, although it is not clear what molecular species they correspond to. On the other hand, as shown in Fig. 3(b), the ZnPc^{HS} source contains a significant amount of species with molecular weights of 610-615 and around 646, which are in agreement with mono and di-chlorinated ZnPc (ZnPc-Cl and ZnPc-Cl$_2$), respectively. The lower molecular weight species that are present in ZnPc^{CS} almost completely vanish in ZnPc^{HS}. Although it is believed that ZnPc is the main reaction product following the synthesis routine, it can be further oxidized by the chlorine or the chloride cations formed during the synthetic process of ZnPc. Thus, a small portion of mono- and di-chlorinated ZnPc, i.e. ZnPc-Cl and ZnPc-Cl$_2$, may also be formed (see Fig. 1). Mono-chlorinated copper phthalocyanine can also be synthesized in a similar reaction condition.[53] The separation of the chlorinated ZnPc from non-chlorinated ZnPc is challenging due to the relatively small molecular weight difference between them.

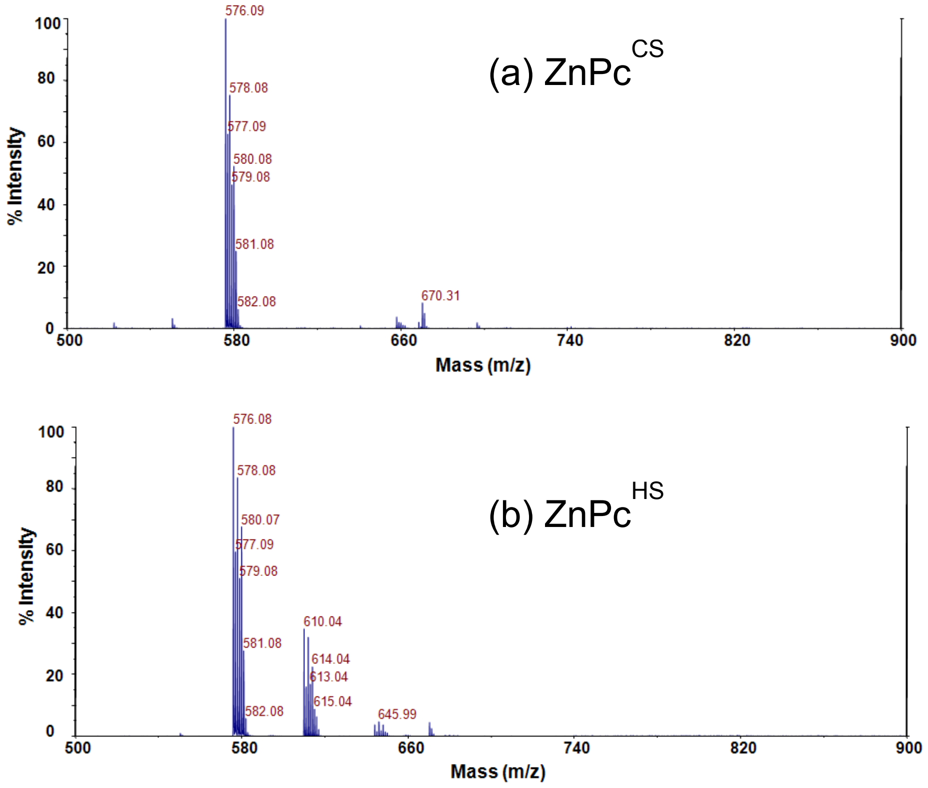

Figure 8. MALDI mass spectra of (a) ZnPc^{CS} and (b) ZnPc^{HS}. Matrix of terthiophene (658.95 g/mol) and 5,10,15,20-tetra(p-tolyl)porphine (670.31 g/mol) were used as internal standard for molar mass calibration.

The two ZnPc samples also possess a difference in electrical defect density as revealed by the C-V measurement on the thin films. Plotted in Fig. 5 are the $1/C^2$ vs. V curves for 200 nm thick ZnPc^{CS} and ZnPc^{HS} films sandwiched between ITO and Al, where C is the capacitance of the Schottky-type Al/ZnPc metal-semiconductor contact. The defect concentration is then determined via[49]:

$$N_D = \frac{2}{q\varepsilon_0\varepsilon_r A^2}\left[-\frac{1}{d\left(1/C^2\right)/dV}\right], \qquad (6)$$

where ε_0 is the vacuum permittivity, $\varepsilon_r \approx 9$ is the static relative dielectric constant obtained by measuring the capacitance when the semiconductor layer was fully depleted, and A = 4 mm^2 is the device area. By taking linear fits of $1/C^2$ vs. V as shown in Fig. 5,

$N_D = (8.1 \pm 0.5) \times 10^{16}$ cm^{-3} for ZnPc^{CS}, and $(4.3 \pm 0.6) \times 10^{16}$ cm^{-3} for ZnPc^{HS}, approximately a factor of two difference between the two ZnPc films. The nature of these defects and the reason for the difference in defect concentration are however unknown here. Since ZnPc^{HS} has a lower electrical defect density than ZnPc^{CS}, it is unlikely those defects are directly associated with the chlorinated ZnPc derivatives present in ZnPc^{HS}.

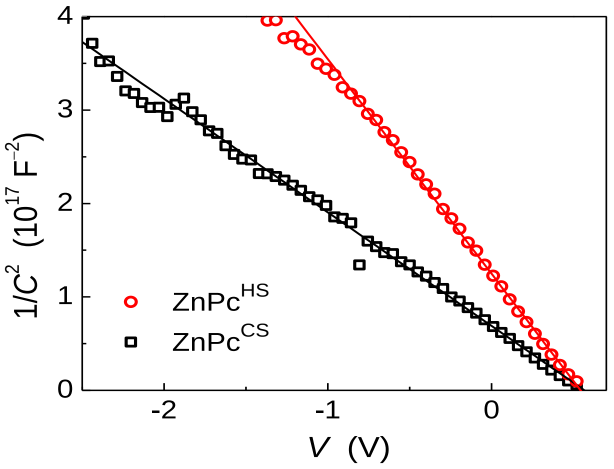

Figure 9. Comparison of the capacitance-voltage (C-V) characteristics of ITO/ZnPc/Al Schottky junctions using either ZnPc^{HS} and ZnPc^{CS}. The symbols are experimental data and the solid lines are linear fits of 1/C^2 vs. V.

Figure 10(a) shows the current density-voltage (*J*-*V*) characteristics of bilayer ZnPc/C$_{60}$ devices with structure of ITO/ ZnPc^{CS} or ZnPc^{HS} (20 nm)/C$_{60}$ (30 nm)/BCP (14 nm)/Al, both in the dark and under 1 sun AM1.5G (= 100 mW/cm^2) simulated solar illumination. The PV performance parameters of these two devices (J_{SC}, V_{OC}, FF, η_P) have been summarized in Table 2. The two devices have nearly identical $J_{SC} \approx 5.4$ mA/cm^2. The nearly identical EQE spectra of the two devices shown in Fig. 6(b) further suggest that the two different ZnPc source materials do not present any noticeable difference to the light absorption, exciton diffusion, and charge extraction when the OPV cell is under short-circuit ($V = 0$). However, there are significant differences in V_{OC} and FF between the two devices, $V_{OC} = 0.43$ V and $FF = 0.52$ for the ZnPc$^{\mathrm{CS}}$ device, whereas $V_{OC} = 0.63$ V and $FF = 0.65$ for the ZnPc$^{\mathrm{HS}}$ device. This leads to a near doubling in the PCE from $\eta_P = 1.2\%$ to 2.2% when the commercial ZnPc source is replaced by the home-synthesized ZnPc material in the OPV cell. The large difference in V_{OC} is strongly related to the drastic difference in the dark current of the two devices. For example, at $V = 0.5$ V, the dark current density is $J_d = 9.2$ mA/cm^2 and 0.13 mA/cm^2, for the ZnPc$^{\mathrm{CS}}$ and ZnPc$^{\mathrm{HS}}$ devices, respectively. Figure 10c shows fitting results of the dark J-V characteristics under forward bias according to the modified Shockley diode equation (Eq. 2 with $J_{ph} = 0$) [34], and the fitting parameters have been listed in Table 2. A nearly three orders of magnitude difference is obtained in the reverse-bias saturation current density J_s as well as a different diode ideality factor n. The difference in n also contributes to the different dependencies of V_{OC} on P_O as shown in Fig. 6(d). V_{OC} shows a linear dependence on the logarithm of P_O with the slope proportional to n as predicted by the diode theory (see Eq. 3),[27,49] except for the ZnPc$^{\mathrm{HS}}$ device at $P_O > 1$ sun where it tends to saturate.

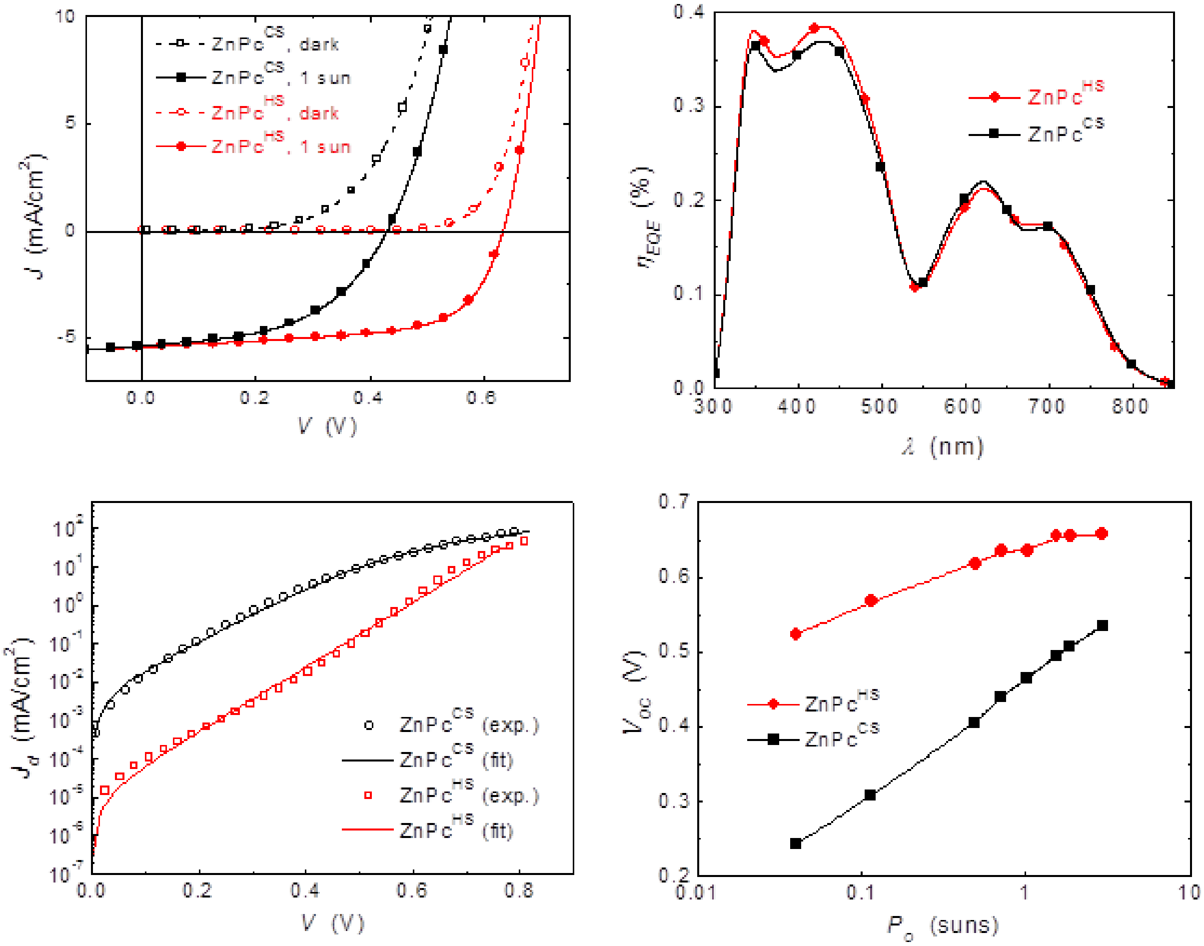

Figure 10. Comparisons of the performance of ITO/ZnPc(20 nm)/C_{60}(30 nm)/BCP(14 nm)/Al OPV devices using ZnPc^{HS} and ZnPc^{CS}: (a) current density-voltage (J-V) characteristics in the dark and under 1 sun (= 100 mW/cm^2) AM1.5G illumination; (b) external quantum efficiency η_{EQE} as a function of the wavelength λ; (c) forward-bias dark J-V characteristics with fits according to the modified Shockley diode equation; and (d) the dependence of the open-circuit voltage V_{OC} on the incident light intensity P_O.

To further explore the effect of the two different ZnPc sources on the OPV cell performance, devices were fabricated with both ZnPc sources in the same device. In one set of devices, the 20 nm ZnPc layer was split into two 10 nm thick layers from two different sources. The *J-V* characteristics of these two dual-ZnPc-layer devices in the dark and under 1 sun illumination are shown in Fig. 7(a) together with those for the two single-ZnPc-layer devices discussed previously. Among the four devices shown in Fig. 7(a), the dark current and PV response of the devices remain approximately the same as long as the same source of ZnPc material is used adjacent to the C_{60} acceptor layer, regardless which source was used for the part of ZnPc layer(s) near the ITO anode. This is a very important piece of evidence showing that the differences in device performance observed here for the two ZnPc sources are mostly related to the interfacial behavior at the ZnPc/C_{60} heterojunction, rather than the bulk properties of the ZnPc layer.

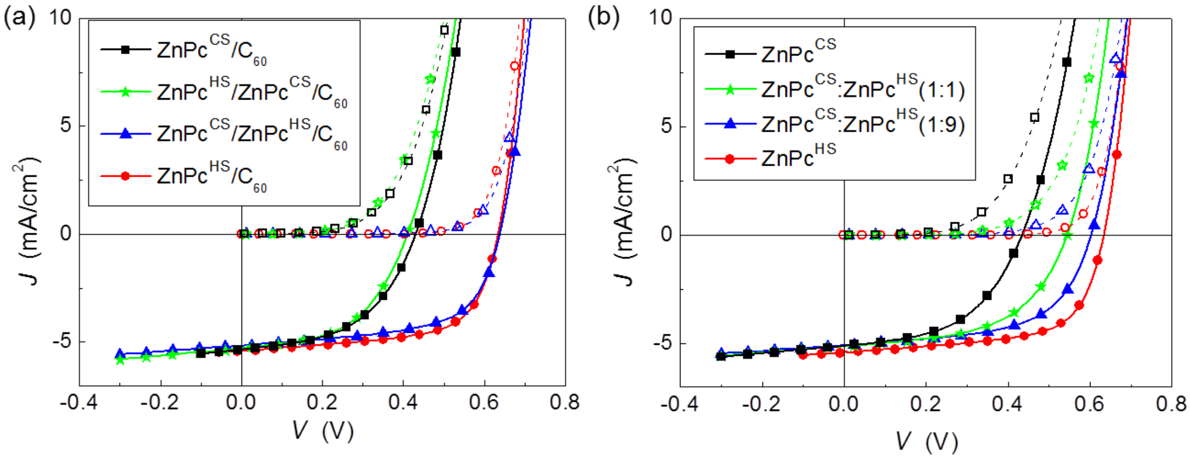

Figure 11. Comparison of the current density-voltage (J-V) characteristics in the dark and under 1 sun AM1.5G illumination for ZnPc(20 nm)/C_{60}(30 nm) planar heterojunction OPV cells: (a) devices with either a 20 nm thick ZnPc^{HS} or ZnPc^{CS} layer or two 10 nm thick ZnPc layers from different sources, and (b) devices with different ratio of ZnPc^{CS} to ZnPc^{HS} in the ZnPc layer.

In the other set of devices, the two ZnPc sources were co-evaporated at a specified ratio during the deposition of the 20 nm thick ZnPc layer. Figure 11b shows the *J-V* characteristics in the dark and under 1 sun illumination for devices with varying ZnPc^{CS} to ZnPc^{HS} ratio in the ZnPc layer. As the ZnPc^{HS} concentration increases in the ZnPc layer from 0% (pure ZnPc^{CS}) to 50% (1:1 mixed), 90% (1:9 mixed) and eventually

100% (pure ZnPc^{HS}), the dark current of the device consistently decreases and V_{OC} increases accordingly from 0.43 V to 0.54 V, 0.60 V, and 0.63 V.

The dark J-V characteristics of a ZnPc^{HS}-based device with the structure of ITO/ZnPc(20nm)/C_{60}(30nm)/BCP(14nm)/Al at temperatures ranging from 100 to 300 K are shown in Fig. 8(a). Also shown are the fits according to the modified Shockley diode equation. The temperature dependence of the fitting results for J_s has been shown in Fig. 8(b), along with that for a similar device based on ZnPc^{CS}. For both devices, J_s decreases drastically with decreasing temperature at $T \geq 175$ K, while remaining mostly unchanged at $T \leq 150$ K. Applying Arrhenius fits to the temperature dependence of J_s at $T \geq 175$ K, i.e., $J_s \sim \exp\left(-\Delta E / kT\right)$, yields an activation energy of $\Delta E = (0.5 \pm 0.1)$ eV for both devices. On the other hand, over the entire temperature range, J_s for the ZnPc^{CS} device is approximately three orders of magnitude higher than that for the ZnPc^{HS} device. Also shown in Fig. 8(b) are V_{OC} at various operating temperatures for these two devices under 2.5 suns of simulated solar illumination. The ZnPc^{HS} device exhibits a higher V_{OC} than the ZnPc^{CS} device over the entire temperature range; and for both devices, V_{OC} increases with decreasing the operating temperature from $T = 300$ K to 175 K, and then tends to saturate at $T \leq 150$ K. These trends agree well with the trends for J_s of these two devices as described above, considering the relationship between V_{OC} and J_s as depicted in Eq. (3). It is also relevant to note that the saturated value of V_{OC} at low temperatures for the ZnPc^{CS} device is within 0.03 V of that for the ZnPc^{HS} device, even though their difference is nearly 0.2 V at room temperature. If the saturated value of V_{OC} at low temperature (under 2.5 suns illumination), which is 0.80 V, is regarded as the maximum attainable V_{OC} for the ZnPc/C_{60} donor-acceptor material system, this means that, ZnPc^{HS}

achieved 79% of the maximum V_{OC} at room temperature and under 1 sun illumination, whereas the percentage is reduced to only 54% when ZnPc^{CS} was used.

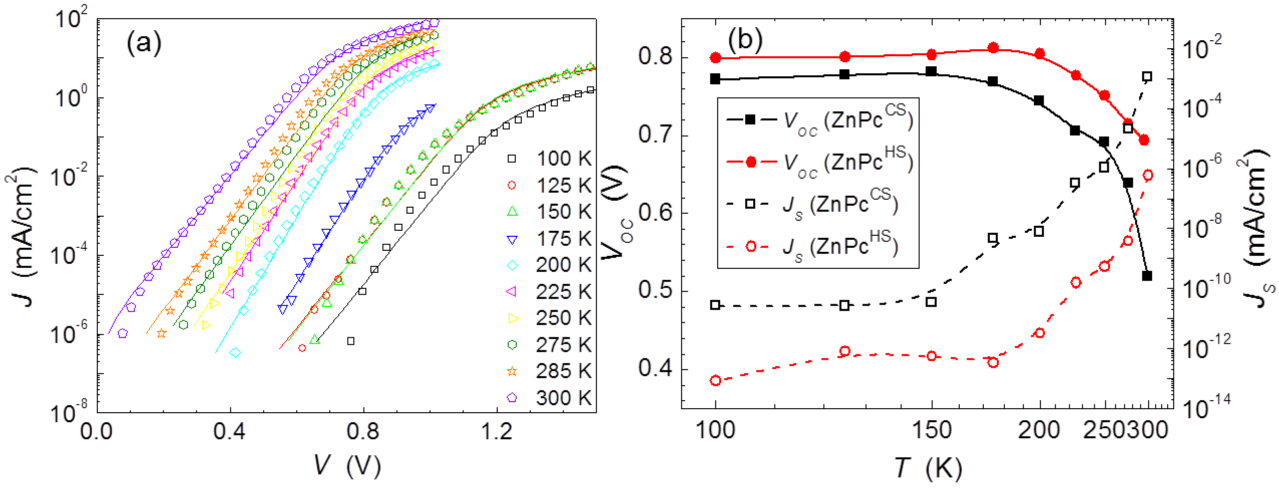

Figure 12. (a) Temperature-dependent J-V characteristics of a ZnPc^{HS}/C$_{60}$ planar heterojunction OPV cell in the dark; (b) comparisons of the temperature dependence of the open-circuit voltage V_{OC} and the reverse-bias dark saturation current density J_s for ZnPc/C$_{60}$ devices with either ZnPc^{CS} or ZnPc^{HS}.

The effect of the ZnPc source material on V_{OC} was further explored by fabricating devices with a varying ZnPc layer thickness in bilayer ZnPc/C$_{60}$ OPV cells (the C$_{60}$ layer thickness remained at 30 nm). Figure 13 shows that for devices with either ZnPc^{CS} or ZnPc^{HS}, V_{OC} (with the device under 1 sun AM1.5G illumination) increases with the ZnPc layer thickness. However, only a small increase of 0.03 V in V_{OC} was obtained as the ZnPc^{HS} layer thickness was increased from 10 to 60 nm, whereas a much larger increase of 0.15 V in V_{OC}, from 0.40 V to 0.55 V, was achieved as the ZnPc^{CS} layer thickness was increased from 10 to 60 nm.

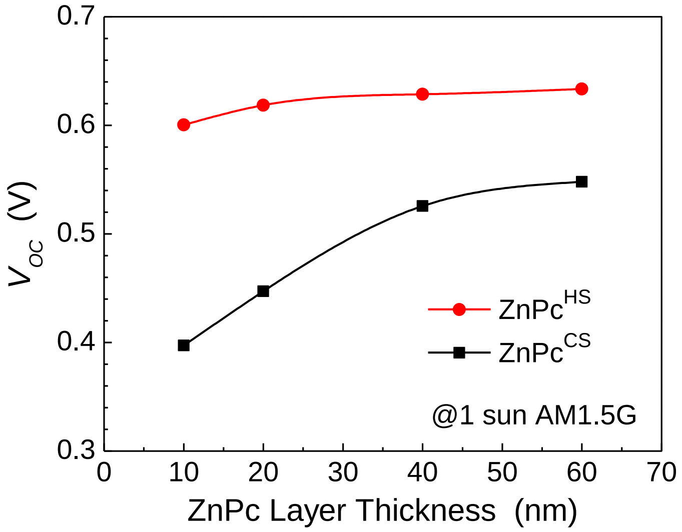

Figure 13. Comparison of the dependence of V_{OC} on the ZnPc layer thickness for devices with ZnPc^{CS} or ZnPc^{HS}.

The results presented above have clearly linked the higher V_{OC} obtained in ZnPc^{HS} based devices than in ZnPc^{CS} based devices to the lower dark current in the former devices. However, the different characteristics for devices from these two ZnPc sources are not limited to the dark current. Shown in Fig. 10 is a comparison of the photocurrent density, J_{ph}, for bilayer ZnPc/C_{60} devices with the different ZnPc sources, as a function of the voltage bias V. In this case, a white light beam with an intensity of 38 mW/cm^2 was chopped at 400 Hz using a mechanical chopper prior to incidence on the devices, and the photocurrent response from the device at different voltages was directly measured using a lock-in amplifier. This synchronous detection method provides accurate determination of J_{ph} with increasing forward biases as it removes the exponentially increasing dark current in the measurement. These two devices have similar values of J_{ph} at short-circuit, similar to the results shown in Fig. 5(a). However, as shown in Fig. 10, the magnitude of J_{ph} for the ZnPc^{CS} device is lower than that for the ZnPc^{HS} device under forward bias, especially in the range of 0.4 V < V < 0.8 V. The corresponding forward bias for a given J_{ph} is approximately 0.1 V higher for the ZnPc^{HS} device than for the ZnPc^{CS} device. This means that even if the ZnPc^{HS} and ZnPc^{CS} based devices have the same dark current levels, the ZnPc^{HS} based devices would have a higher V_{OC}, simply due to its higher photocurrent under forward bias.

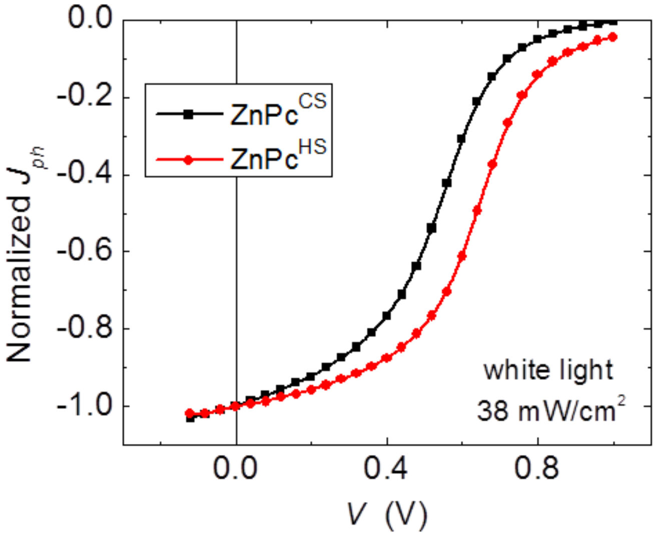

Figure 14. Comparison of the voltage dependence of the normalized photocurrent density J_{ph} for devices with ZnPc^{CS} or ZnPc^{HS}, under 38 mW/cm^2 of white light illumination.

The following statements briefly summarize the main results:

- The two ZnPc source materials, ZnPc^{CS} and ZnPc^{HS}, have nearly identical chemical composition other than the presence of Cl in ZnPc^{HS}; however ZnPc^{CS} has a nearly twice higher electrical defect concentration than ZnPc^{HS} although the nature of these defects is unknown.

- The bilayer ZnPc/C_{60} OPV cells have higher V_{OC}, higher magnitude for the photocurrent, and lower dark current when $ZnPc^{HS}$ is used instead of $ZnPc^{CS}$.
- The differences in performance of devices using the two different ZnPc sources are mostly related to the interfacial behavior at the ZnPc/C_{60} heterojunction, rather than the bulk properties of the ZnPc layer.
- The difference in V_{OC} between the $ZnPc^{HS}$ and $ZnPc^{CS}$ based devices (with the same overall device structure) decreases with decreasing the device operating temperature, or increasing incident optical power intensity, or increasing the ZnPc layer thickness.

The results presented here unequivocally demonstrated the different device characteristics using the two different ZnPc source materials. Salzman et al. previously reported the positive relationship between the purity of the copper phthalocyanine (CuPc) source material and the performance of the corresponding CuPc/C_{60} OPV cells.[48] The situation is somewhat different here as both ZnPc source materials have been purified using the same vacuum thermal gradient sublimation method for one to two cycles, and there is no observation of appreciable changes in device performance with additional cycles of purifying the ZnPc source materials using the same method. Hence the different concentration of electrically active defects in the two ZnPc source materials has to be associated with impurities that cannot be removed using this purification method for small molecules.

The partial chlorination of ZnPc in the home-synthesized source could impact the OPV cell performance to some extent. Chlorination is expected to lower the HOMO level of ZnPc, although the HOMO level lowering is small for mono-chlorinated ZnPc, and only 0.02 eV increase in oxidation potential for ZnPc^{HS} as compared to ZnPc^{CS} was observed in voltammetry measurement. This small energy difference is consistent with the 0.03 V difference of the low-temperature limit of V_{OC} for the bilayer cells, as the latter is directly correlated with the offset between the ZnPc HOMO and C_{60} LUMO levels, ΔE_{DA}. For recombination of electrons in the C_{60} LUMO and holes in the ZnPc HOMO, it has been shown that the reverse-bias saturation dark current follows:

$$J_s = J_{s0} \exp\left(-\frac{\Delta E_{DA}}{2nkT} \right), \tag{5}$$

where the constant J_{s0} may depend on a number of materials properties but is independent of the energy barrier ΔE_{DA} [29]. Hence a 0.02-0.03 eV higher ΔE_{DA} would lead to a factor of 2-3 reduction in J_s at room temperature, insufficient to fully account for the three orders of magnitude difference from experimental measurements.

A greater impact on the dark current could come from the unidentified electrical defects present in the two ZnPc sources. For phthalocyanine/C_{60} planar heterojunction cells, it has been shown that the dark current is dominated by nonradiative recombination of electrons and holes at the DA interface.[27,33,45,54] The HOMO and LUMO offsets at the DA interface lead to significant build-up of charge carriers near the interface, holes in the donor and electrons in the acceptor. Hence, recombination at the DA interface, as illustrated in Fig. 11, serves as a leakage path for these carriers, which tends to reduce the carrier concentrations near the DA interface. Myers et al. have shown previously that the diffusion current, driven by gradients of carrier concentrations, plays an important role in such planar heterojunction cells due to the high concentration of charges built up at the DA interface.[55] This report also explains that the photocurrent is always negative, i.e. flowing from the cathode to the anode (see Fig. 10.), even when the device is under sufficiently high forward bias where the net electric field points from the anode to the cathode (i.e. positive). In this case, as shown in Fig. 11, the drift motion moves charge carriers towards the interface, which contributes to an even higher concentration gradient for a higher (negative) diffusion current.[55]

Hence, higher V_{OC}, higher $|J_{ph}|$, and lower dark current in devices with ZnPc^{HS}, as compared to those in similar devices with ZnPc^{CS}, are attributed to the lower recombination current in the ZnPc^{HS} based devices. It is reasonable to expect that the recombination dominated dark current is lower in the ZnPc^{HS} based devices due to the lower defect concentration in the ZnPc source material. As recombination occurs mostly at the DA interface, this also explains that it is the ZnPc material in contact with C_{60} that determines the V_{OC} of the device. Furthermore, the lower recombination current in the ZnPc^{HS} based devices results in a higher carrier concentration near the DA interface, which in turn leads to a higher negative diffusion current and a higher $|J_{ph}|$.

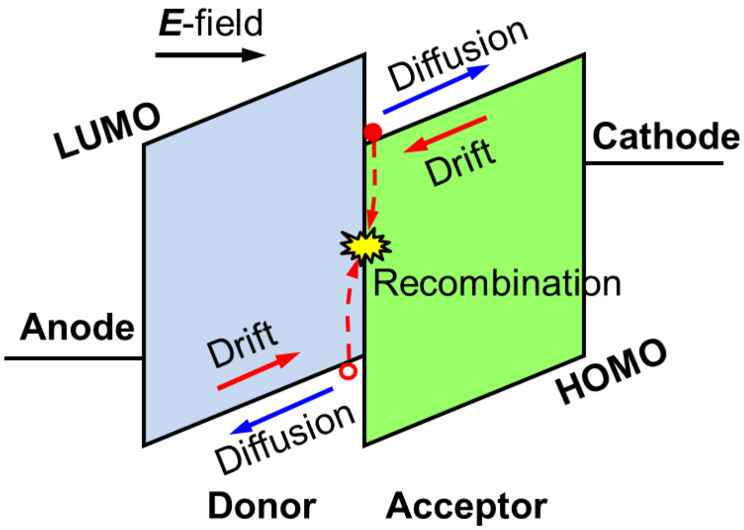

Figure 15. Schematic energy level diagram of a donor-acceptor planar heterojunction photovoltaic cell under a sufficiently high forward bias such that the electric field points from the anode to the cathode. The drift and diffusion of holes (in the donor) and

electrons (in the acceptor) are illustrated along with the recombination of charges at the donor-acceptor interface.

On the other hand, since the diffusion current is proportional to the carrier concentration gradient, the influence of diffusion current becomes less important when the ZnPc layer thickness increases. This suggests that the impact of lower recombination current in ZnPc^{HS} based devices becomes less significant when the ZnPc layer thickness increases, again in agreement with experimental observations.

Additionally, the impact of interface recombination also becomes less important when there exists a strong electric field in the active layer to sweep photogenerated charges away from the DA interface, such as in the short-circuit condition. As the short-circuit current densities from similar devices with the two ZnPc sources are approximately the same, this also suggests that the interface recombination is most likely nongeminate in nature, i.e. not due to recombination of the pair of electron and hole from the same exciton.

It is also recognized that further characterization is needed to identify the nature of the defects in ZnPc that contribute to charge recombination at the ZnPc/C_{60} interface. Depending on their electronic and chemical natures, different defects may have different impact on charge recombination, which may explain why a factor of two lower defect concentration in ZnPc^{HS} than in ZnPc^{CS} leads to orders of magnitude lower dark current. Device modelling may also be required to further explain this nonlinear dependence.

In summary, for bilayer, planar heterojunction OPV devices, it is desirable to improve the V_{OC} at normal operating conditions (1 sun illumination at room temperature) to its maximum attainable value, which is typically obtained at low temperature and under high intensity illumination. It is shown that by changing the material preparation,

$ZnPc/C_{60}$ OPV devices fabricated from the home-synthesized source material, $ZnPc^{HS}$, achieved 0.2 V higher V_{OC} at normal operating conditions, compared with a commercially obtained ZnPc source, although the maximum attainable V_{OC} (at T = ~150 K and under 2.5 suns illumination) for devices with different ZnPc sources only differ by 0.03 V or less. The use of $ZnPc^{HS}$ reduced the dark current in the device by approximately three orders of magnitude and a higher magnitude in the photocurrent while maintaining the same bulk composition and oxidation potentials. The observed differences in device performance is attributed to a combination of partial chlorination of ZnPc and the concomitant lower defect concentrations in for $ZnPc^{HS}$. While the nature of these defects is unknown, the results here show that a significantly higher percentage of the maximum attainable V_{OC} in $ZnPc/C_{60}$ OPV cells can be obtained at room temperature under 1 sun illumination by specific material synthesis and processing. The generalization of this finding to other material systems is the focus of ongoing research.

3.2 Cyclometalated Iridium complexes

Although cyclometalated Ir and Pt complexes are under heavy investigation as phosphorescent emitters for OLEDs (see chapters 5-7), the success of these metal complexes in OPVs has been limited.[56,57] This can be attributed to the fact that currently available metal complexes do not absorb strongly in the red and near infra-red (NIR) region since they were designed for full color displays with maximum emission wavelengths in the range of 450-650 nm. Moreover, metal complexes with ligands absorbing strongly and broadly in the visible and NIR ranges tend to have more complex molecular structures, making the process of materials synthesis and purification more difficult. However, the past studies focusing on the cyclometalated metal complexes for

OLED applications indicated that this class of materials can have favorable photophysical and electrochemical stability,[58] versatility in the modification of molecular properties, tunable highest occupied molecular orbital (HOMO) and lowest unoccupied molecular orbital (LUMO), long exciton lifetime[59] and potentially long exciton diffusion length. These properties make a compelling case that the cyclometalated metal complexes can be an excellent material candidate for PV applications with a judicious material design.

In order to develop Ir complexes as absorbers for organic PVs, ligands with strong absorption are needed. Thus, azaperylene[60] (AP) was chosen as a cyclometalating ligand to Ir complexes due to its structural similarity to commonly used organic dyes such as PTCDA and other perylene based OPV materials.[26, 61] The ligand of di-fluoro-phenyl-pyridine (dfppy) was chosen to increase oxidation potential (i.e. lower the HOMO energy level) and improve the volatility (i.e. lower the sublimation temperature) of the proposed metal complex.[62] The synthetic process of mer-bis(4',6'-difluorophenylpyridinato-N, C_2') iridium(III) azaperylene (denoted APIr) is shown in Scheme 1. The reaction between the chloride-bridged Ir(III) dimer, $[(\mathrm{dfppy})_2\mathrm{Ir}(\mu\text{-Cl})]_2$, and the ligand readily yields the product with the assistance of silver triflate and excess base in a refluxed solution of dichloroethane.

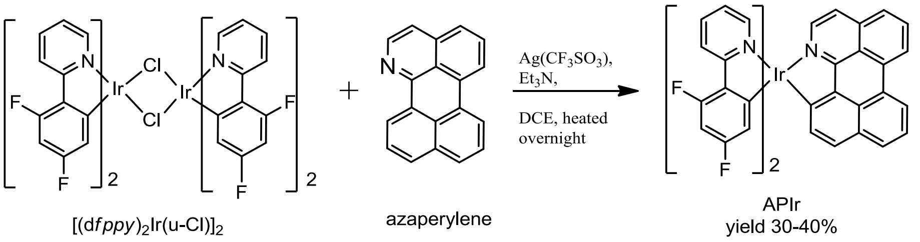

Figure 16. The synthetic condition for APIr.

The absorption spectra of APIr and the corresponding AP ligand in solution are shown in Figure 17. Both AP and APIr are observed to have high energy and intense absorption bands (380-460 nm, $\varepsilon > 10^4$ $cm^{-1}M^{-1}$) similar to those of perylene. Moreover, the cyclometalation results in lower energy and intense absorption bands (460-560 nm, $\varepsilon=$ 6000-8000 $cm^{-1}M^{-1}$) due to the newly formed Ir→AP transitions. The weak, lowest energy absorption band (782 nm, $\varepsilon= 30$ $cm^{-1}M^{-1}$) can be identified as a triplet absorption on the basis of the small Stokes shift between absorption (Figure 17 inset) and emission (Figure 18) at the room temperature. It is noteworthy that the intensities of both ligand-centered (LC) and metal-to-ligand-charge-transfer (MLCT) transitions of APIr are higher than the rest of reported $(dfppy)_2$Ir-based complexes,[58,62] indicating that the incorporation of a ligand like AP makes Ir complexes better suited as absorber materials. The thin film absorption spectrum of APIr in Figure 17 shows that there is a minimal change in the absorption features upon depositing in a thin film, suggesting minimal stacking or intermolecular interaction for APIr molecules in the amorphous film.

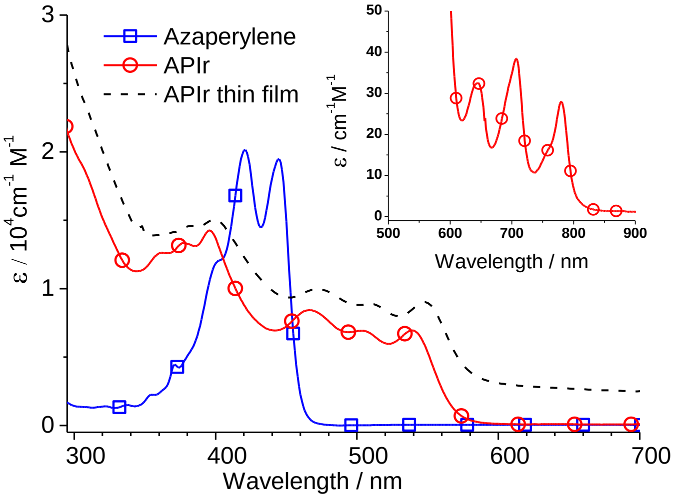

Figure 17. The absorption spectra of azaperylene (squares) and APIr (circles) in a solution of dichloromethane. The thin film absorption spectrum of APIr (dotted lines) is

scaled for comparison to solution spectrum. Triplet absorption of APIr in dichloromethane is shown in the inset.

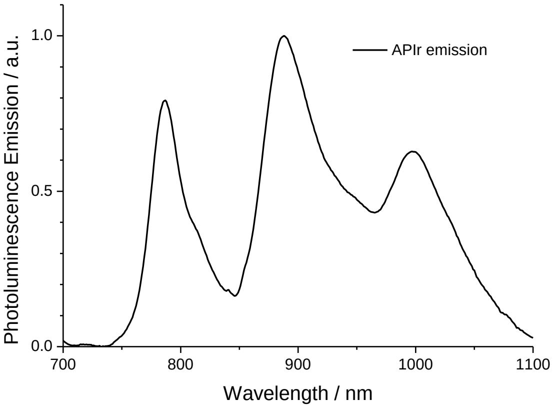

Figure 18. The emission spectrum of APIr in a solution of dichloromethane.

The electrochemical properties of APIr and AP were examined using cyclic voltammetry and the values of redox potentials were determined using differential pulsed voltammetry. All of the electrochemical data reported here were measured relative to an internal ferrocenium/ferrocene reference (Fc^+/Fc). The oxidation and reduction values for APIr are 0.56 V and -1.87 V while those for AP are 0.46 V and -1.90 V. The similarity in the oxidation values between APIr and other commonly used donor-type absorbers like ZnPc makes APIr suitable as donor materials for PV applications.[63] Moreover, it is also worth noting that APIr has a higher oxidation potential than the corresponding cyclometalating ligand (AP), which is not very common for such class of materials. This can be attributed to the use of the dfppy ligand which lowers the electron density of metal ions and makes the complex more difficult to oxidize.[62]

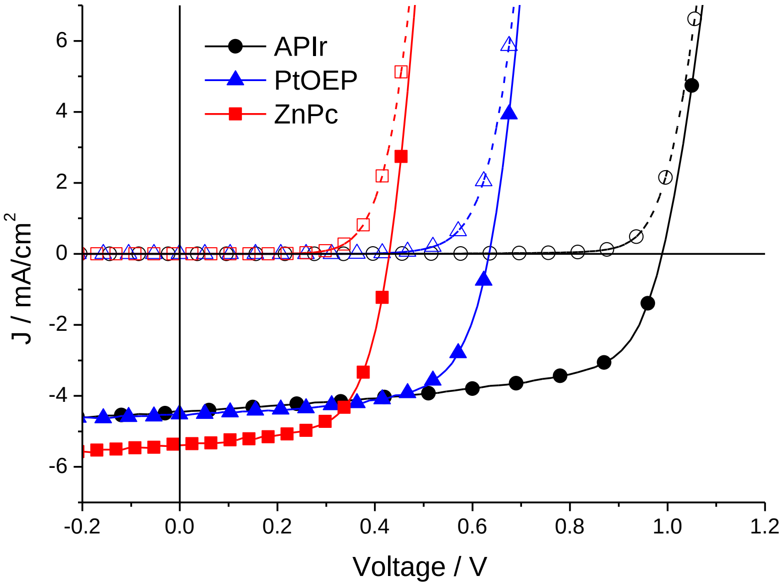

Figure 19. Current-voltage characteristics of APIr (circles), PtOEP (triangles) and ZnPc (squares) based bilayer solar cells under dark (open) and 1sun AM 1.5G simulated illumination (solid) in the device architecture ITO/donor(5 nm)/ C_{60} (30 nm)/PTCDI(10 nm)/BCP(14 nm)/Al.

APIr and azaperylene were first evaluated in a bi-layer solar cell device with a general structure of ITO/donor (5 nm)/ C_{60} (30 nm)/PTCDI (10 nm)/BCP (14 nm)/Al. N,N'-Dihexyl-perylene-3,4,9,10-bis(dicarboximide) (PTCDI) was added as an interfacial layer between the C_{60} acceptor layer and the bathocuproine (BCP) exciton blocking layer to improve the electron injection.[63] For comparison, control devices were fabricated simultaneously with zinc phthalocyanine (ZnPc) or Pt(II) octaethylporphine (PtOEP) as donor materials. The current density versus voltage (J-V) characteristics measured under both dark and 1 sun AM1.5G simulated illumination are shown in Figure 19.

The reasonable photocurrent and diode behavior demonstrate that select cyclometalated Ir complexes like APIr can function as donor-type materials in a bilayer device with C_{60} as an acceptor-type material. On the other hand, azaperylene cannot form a stable amorphous film, resulting in a device failure in a similar device structure. Moreover, the APIr device has a J_{SC} of 4.5 mA/cm^2, a FF of 0.62 and a V_{OC} of 0.99 V, leading to a high η_p of nearly 2.8% which is noteworthy for a simple bilayer device employing only a 5 nm donor layer. In comparison, PtOEP and ZnPc based devices had J_{SC} of 4.6 mA/cm^2 and 5.4 mA/cm^2, FF of 0.64 and 0.63, V_{OC} of 0.62 V and 0.43 V, and η_P of 1.8% and 1.5%, which are comparable to the literature reports on the same materials.[64] Compared with APIr and PtOEP based devices, ZnPc device generates more photocurrent, which can be attributed to its enhanced response (stronger absorption) in the range of 600-800 nm.

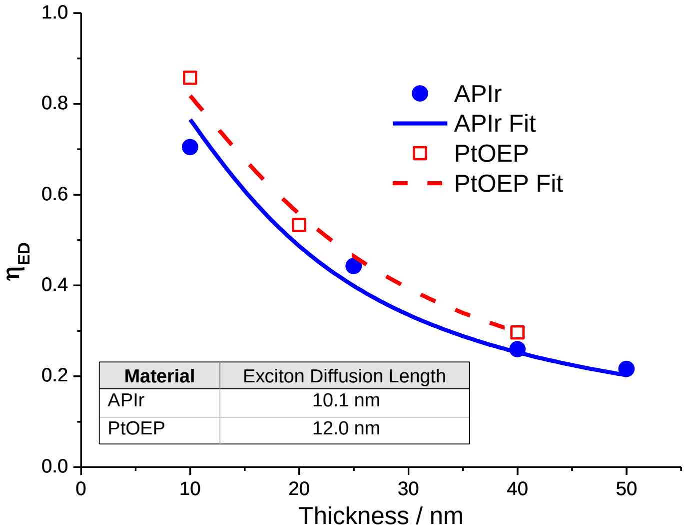

Figure 20. The plots of exciton diffusion efficiency (η_{ED}) vs. the film thickness for APIr (circles) and PtOEP (squares) materials. The derived exciton diffusion length (L_D) of APIr and PtOEP are shown in the inset of the figure

In order to fully utilize the benefits of APIr, enhancing J_{SC} is necessary to achieve. To realize improvement in J_{SC} through increasing active layer thicknesses long exciton diffusion lengths are necessary. Previous reports suggest that phosphorescent materials such as APIr may have longer exciton diffusion length due to their strong triplet character.[59] Thus, the exciton diffusion lengths for both APIr and PtOEP were determined using photoluminescent (PL) quenching calculations. The exciton diffusion length for ZnPc, however, could not be determined using this method due to significant self-absorption but has been previously estimated at 5 nm.[28] Thin films of PtOEP and APIr with various donor layer thicknesses with and without a C_{60} quenching layer were deposited. The exciton diffusion efficiency, η_{ED} is plotted against donor layer thickness in Figure 20, from which the exciton diffusion length is determined (Inset). The estimated exciton diffusion length for both APIr and PtOEP are greater than 10nm which is much higher than that of phthalocyanine materials such as ZnPc. Therefore, it would be expected that creating thicker films of these phosphorescent donor materials would yield higher current densities.

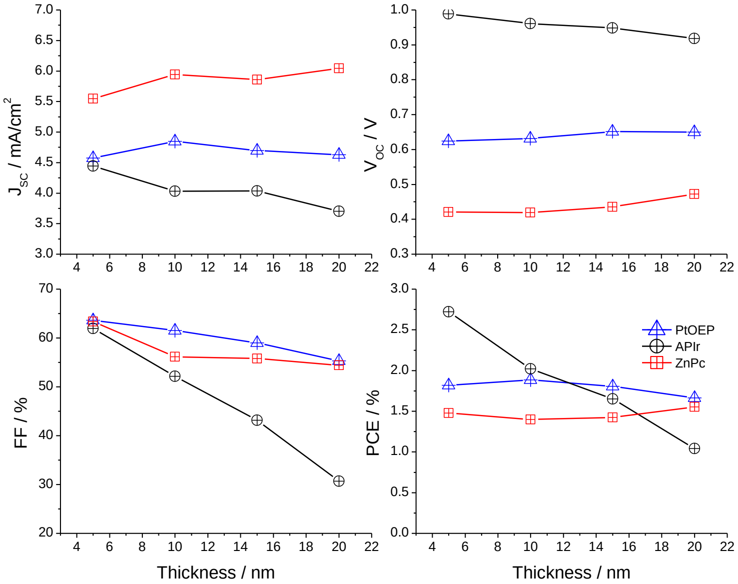

Figure 21. The dependence of device characteristics of APIr (circles), PtOEP (triangles), and ZnPc (squares) based bilayer solar cells on the thickness of donor layer with a general structure of ITO/donor(x nm)/C_{60}(30 nm)/PTCDI(10 nm)/BCP(14 nm)/Al. The data is reported under AM1.5G 1 sun conditions.

To determine the effect of donor layer thickness, devices were fabricated with donor thicknesses from 5-20 nm. The device performance parameters given in Figure 21 showed small changes in V_{OC} for all three donor materials. Also, the devices for both PtOEP and ZnPc showed minimal changes in J_{SC}, yet the devices for APIr decreased significantly from 5 nm to 20 nm. Additionally, the APIr device demonstrated a more pronounced drop in FF compared to those of ZnPc and PtOEP devices. These trends are likely due to the minimal stacking of the octahedral APIr molecules resulting in reduced intermolecular orbital overlap leading to a slower charge hopping process and a lower mobility. Thus, the benefits of long exciton diffusion length and large V_{OC} could not be fully utilized due to the restriction on APIr thickness.

The high η_p value of the APIr device compared with ZnPc and PtOEP can be mainly attributed to its large V_{OC} despite their similar oxidation values.[28,64] The HOMO and LUMO energy levels of APIr and AP, as well as ZnPc and PtOEP, are provided in the inset of Figure 22, based on estimation from the oxidation and reduction values.[65] The achievement of 0.99V V_{OC} is among the highest reported values for bilayer small molecule OPVs and this boost in V_{OC} is a significant step in the formation of future high efficiency OPVs. Moreover, it is encouraging that a large V_{OC} (1.0 V) can be generated despite an exciton energy of only about 1.55 eV (based on the emission spectrum of APIr, Figure 18). Uncovering factors resulting in this high V_{OC} is critical to the goal of maximizing the device efficiency of organic solar cells and minimizing unnecessary power loss due to low V_{OC}.

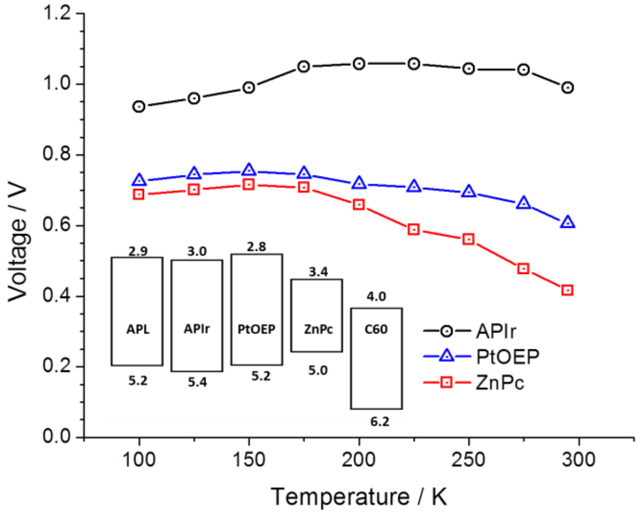

Figure 22. Temperature dependence of V_{OC} for APIr (circles), PtOEP (triangles), and ZnPc (squares) in the device architecture ITO/donor(5 nm)/ C_{60} (30 nm)/PTCDI(10 nm)/BCP(14 nm)/Al.

The difference in V_{OC} among ZnPc, PtOEP and APIr is attributed to a decrease in the dark (diode) current due in part to an increase in the donor-acceptor energy offset from the change in APIr HOMO level. However, a 0.2eV reduction in APIr HOMO level does not fully explain such a dramatic increase in V_{OC}. Previous reports suggest that the V_{OC} is strongly related to the molecular geometry of the donor materials.[66,67] Thus, the increase in V_{OC} may be influenced by adopting an octahedral geometry compared the planar structures of the porphyrin and phthalocyanine donors. To further explore the effect of the donor material on V_{OC} the devices were tested at various illumination intensities using neutral density filters and at various temperatures using a liquid nitrogen cooled cryostat (Janis VNF100) for a temperature range from 100K to room temperature. Previously reported experiments have shown that V_{OC} approaches a maximum attainable value at low temperatures and maximum light intensities.[45] Thus, under typical operating conditions of 1 sun and room temperature the V_{OC} could be significantly lower than the maximum attainable value. Consequently, in order to avoid the costly and complex operation at high light intensities and low temperatures, devices and materials should be designed to give as close to the maximum attainable value of V_{OC} as possible under typical operation conditions of 1 sun and room temperature. It is evident from the temperature dependencies given in Figure 22 that both ZnPc and PtOEP show this behavior of enhanced V_{OC} at low temperatures approaching a maximum value at 150 K and high light intensities. These two materials also show continual increases in V_{OC} for illumination intensities up to 3 suns shown in Figure 23. The V_{OC} of APIr, however, is almost independent of the temperature change and shows minimal improvement in V_{OC} at illumination intensities beyond 1 sun. As a result the V_{OC} at 1 sun and room temperature is well over 90% of its maximum attainable value. The reason for the different temperature dependencies of the V_{OC} for the different donor materials is under continued investigation.

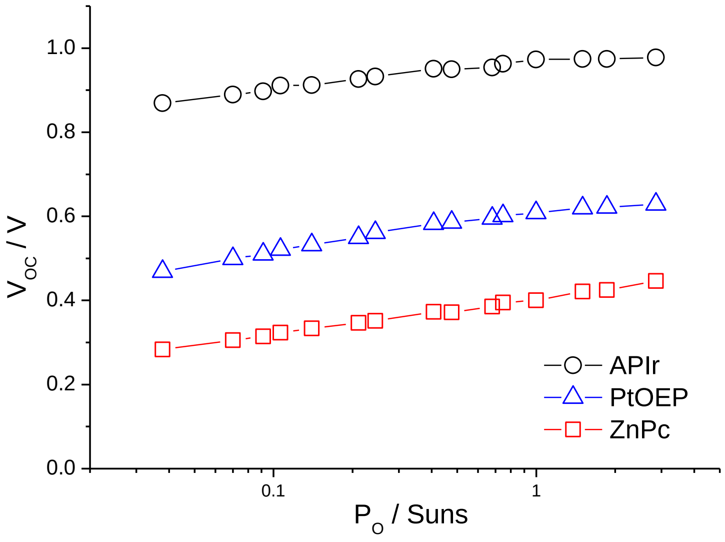

Figure 23. Plots of V_{oc} vs. illumination intensity for APIr (circles), PtOEP (triangles), and ZnPc (squares) devices, with a general structure of ITO/donor(5 nm)/C_{60}(30 nm)/PTCDI(10 nm)/BCP(14 nm)/Al.

In conclusion, cyclometalated Ir complexes have been demonstrated to work efficiently as absorbers for solar cell applications. An efficient bilayer organic PV cell with η_p of 2.8% was fabricated with APIr as a donor-type material. Compared with its organic counterpart, Ir complexes can have improved thermal stability, broader absorption spectrum and tunable HOMO and LUMO energy levels. In addition, compared to commonly used porphyrin complexes, APIr showed dramatically improved V_{OC} despite having similar oxidation and reduction potentials. Furthermore, the high V_{OC} of APIr devices showed minimal temperature and light intensity dependence. As a result, nearly 1V V_{OC} was achieved at typical operating conditions for an absorber material with an approximated exciton energy of only 1.55 eV. Future development of Ir complexes with improved mobility and wider absorption range will enable this class of materials to make an even more significant impact.

4. ENHANCEMENT OF SHORT CIRCUIT CURRENT EMPLOYING ANODE INTERFACIAL LAYERS

4.1 Anode Interfacial layers for PdPc planar heterojunctions

One recent major advancement in improving the efficiency of organic solar cells is the introduction of interfacial layers between the indium tin oxide (ITO) anode and the donor layer. Initial studies into the application of AILs were driven by the need for carrier selective ohmic contacts for solution processed bulk heterojunction devices. Much of the research focused on using conductive polymers or metal oxides aimed at modifying the electrode work functions.[34,68,69] However, research on these materials for small molecular solar cells, in particular thermally evaporated small molecules, has been limited. The desirable characteristics for such an anode interfacial layer for small molecular solar cells are:

(i) Planarization of the rough ITO anode surface

(ii) Carrier selective ohmic contacts which requires appropriate energy level alignment

(iii) High hole mobility to maintain low series resistance

(iv) High-lying lowest unoccupied molecular orbital (LUMO) level to block both electron leakage to the anode and to block excitons from the donor layer to prevent quenching or dissociation at the anode.

(v) High bandgap for optical transparency

(vi) Control over successive organic layer deposition morphology

The most common anode interfacial layer for both polymer and small molecule based OPVs remains poly(3,4-ethylenedioxythiophene) poly(styrenesulfonate) (PEDOT:PSS) which forms a planar surface, has appropriate energy level alignment with MPc's, excellent hole mobility, and relatively good optical transparency.[70] However, PEDOT:PSS has been reported to be an exciton quenching interface and its acidic nature leads to device degradation, making it imperative to find alternative AILs.[71] Among these reports, n-type inorganic materials such as the transition metal oxides[68-69] MoO_3,V_2O_3, or WO_3 or n-type organic materials such as 1,4,5,8,9,11-hexaazatriphenylene-hexacarbonitrile (HAT-CN)[72] or copper(II) hexadecafluoro-phthalocyanine (F_{16}CuPc)[73] have been widely studied as hole injection materials for both organic light emitting devices and organic photovoltaics. These materials, which function by transporting electrons from ITO through their LUMO orbitals and recombine with holes at the AIL/donor interfaces, have seen reasonable success as hole selective ohmic contacts for both polymer and small molecule based OPVs due to appropriate alignment between their LUMO or conduction band levels and the highest occupied molecular orbital (HOMO) level of donor materials. These classes of materials however, also lack the ability to effectively block electron leakage or exciton quenching and both HAT-CN and F_{16}CuPc have been reported to induce an unfavorable edge-on stacking formation of MPc's. The use of p-type NiO,[74] CuI,[75] and organic hole transport materials[76] as AILs have also been reported. Unlike, n-type materials, these p-type materials transport holes from the donor to the acceptor through their HOMO orbitals or valence band and thus, given sufficient band gap, are able to block excitons and electrons due higher lying LUMO or valence band levels. Furthermore, CuI and select organic materials such as perylene-3,4,9,10-

tetracarboxylic-3,4,9,10-dianhydride (PTCDA), biphenyl bithiophene (BP2T),[77]or pentacene[78] have been shown to yield improved crystallinity through the favorable face-on stacking formation of MPc's to yield stronger absorption and improved electrical properties. Nevertheless, many of these attempts have yielded only moderate improvement in power conversion efficiencies and few reports have exhibited efficiencies over 3% even when employing more advanced planar-mixed heterojunction structures.[75]

Due to the difficulty of selecting a material that satisfies all the requirements of an ideal AIL candidate, the application of dual anode interfacial layers can be a useful strategy to achieve the highest device performance.[79] PEDOT:PSS acts as an efficient hole injection material between the ITO anode and the organic layers and also planarizes the surface but has been known to quench excitons. Therefore, the high-lying LUMO energy level (2.4 eV below the vacuum level) for tetracene is sufficiently higher than the LUMO energy level for PdPc, while tetracene's HOMO level of 5.1 eV aligns well with PEDOT:PSS (5.0 eV) and PdPc (5.2 eV).[28] Thus, tetracene should make an effective exciton blocking layer due to its high and appropriately aligned band gap while maintaining a low resistance contact. This is in contrast to other reported anode interfacial layers such as PTCDA which has undesirable exciton dissociation at PTCDA/donor interfaces.

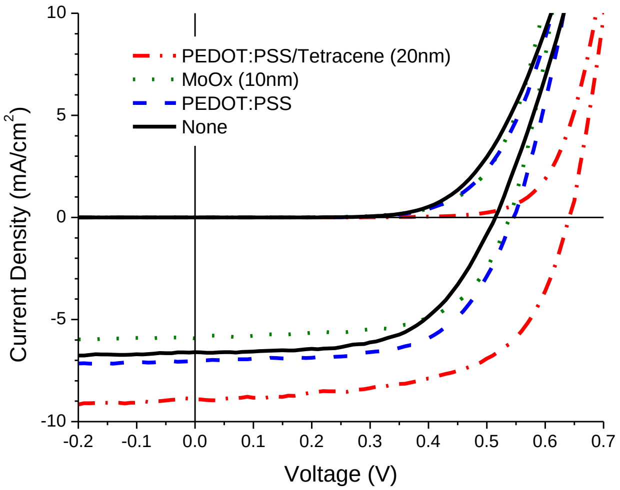

Figure 24. Plots of current density vs. voltage characteristics for devices with the general structure: ITO/ AIL/PdPc (10nm)/C_{60} (30nm)/PTCDI (10nm)/BCP (14nm)/Al where the AILs are: none (i.e., bare ITO, solid), PEDOT:PSS (dashed), 10 nm MoO_X (dotted), and PEDOT:PSS/20nm tetracene (dash-dot).

Planar heterojunction devices employing the donor material PdPc and a C_{60} acceptor were fabricated with a dual layer of PEDOT:PSS and 20 nm thick tetracene. Reference devices with bare ITO, single PEDOT:PSS layer, and 10 nm MoO_X were also fabricated. All devices were employed in the device structure: ITO/ AIL/ PdPc (10nm)/ C_{60} (30nm)/ PTCDI (10nm)/BCP (14nm)/Al where N,N'-dihexyl-perylene-3,4,9,10-bis(dicarboximide) (PTCDI) was added as an interfacial layer between the acceptor layer (C_{60}) and the bathocuproine (BCP) exciton blocking layer to improve the electron injection.[63] The pre-patterned ITO substrates were washed through subsequent sonication in DI-H_2O, acetone, and isopropanol followed by a 15 minute UV-ozone treatment. For the required devices, an approximately 40 nm thick PEDOT:PSS layer was spun coat on the substrates and was baked at 180°C in air for 40 minutes. The current density-voltage characteristics of these OPV devices in the dark and under 1 sun AM1.5G simulated solar illumination from a Xe-arc lamp determined using a Hamamatsu Si reference cell (Model C24 S1787-04) calibrated by NREL, are given in Figure 24.

As shown in Figure 24 the addition of anode interfacial layers had various effects on the device performance parameters. As summarized in Table 1, devices without any anode interfacial layer had a short-circuit current density of J_{SC} = 6.6mA/cm^2, an open-circuit voltage of V_{OC} = 0.51V, and a fill factor of FF = 0.59 yielding a power conversion efficiency (PCE) of η_P = 1.97%, similar to that of previous literature reports.[28] The addition of MoO_X reduces the series resistance of the devices from R_S = 7.2 Ωcm^2 to 1.8 Ωcm^2 leading to a higher fill factor of 0.62, likely due to the lower contact resistance created by the n-type material. This enhancement, however, was accompanied by a slight reduction in J_{SC} and only small increases in V_{OC}, hence the power conversion efficiency remains approximately 2.0%. The PEDOT:PSS based devices had slightly lower series resistance than bare ITO but higher than that of MoO_X yet had a slight enhancement in J_{SC} to just over 7 mA/cm^2 and also exhibited an increase in Voc. Furthermore, by adding an additional layer of tetracene, the series resistance is further reduced, maintaining a high fill factor; more importantly, both the V_{OC} and J_{SC} have 20% or higher increases, leading to a maximum η_P = 3.66%.

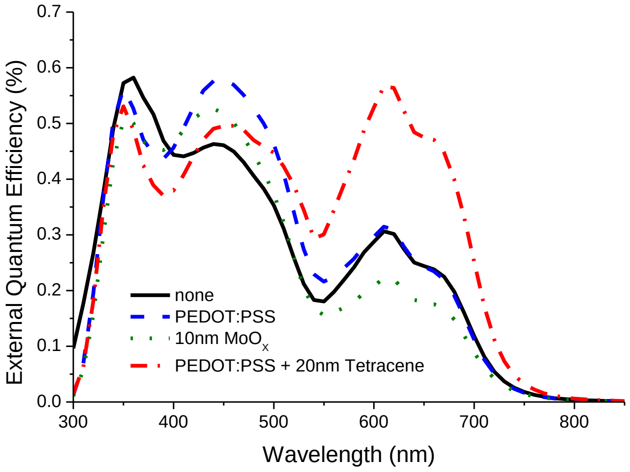

Figure 25. Plots of External Quantum Efficiency vs. wavelength for the devices with the general structure: ITO/ AIL/PdPc (10nm)/C_{60} (30nm)/PTCDI (10nm)/BCP (14nm)/Al where the AILs are: none (i.e., bare ITO, solid), PEDOT:PSS (dashed), 10 nm MoO_X (dotted), and PEDOT:PSS/20nm tetracene (dash-dot).

To further explore the differences in short circuit current, the device EQE, η_{EQE}, as a function of wavelength was determined from the photocurrent output generated in the device from an incident monochromatic light source using an Optronic Lab OL750 series spectroradiometer. The EQE was determined by comparing this photocurrent to the monochromatic beam intensity measured using a calibrated Si photodetector. The EQE spectra of these devices are shown in Figure 25. The integration of the EQE spectra with the standard AM1.5G solar spectrum was also used to determine short circuit current to account for the spectral mismatch from the solar simulator, which have been included in Table 1 (see the "J_{SC} (EQE)" column). The application of MoO_x led to decreases in the donor contribution to EQE (between 550 nm to 750 nm) resulting in the lower short circuit current given in Table 1. This is likely due to the inability of MoO_x to effectively block excitons at the anode interface which is supported by the reduction of current from the donor contribution only. PEDOT:PSS, on the other hand, maintained an EQE similar to that of bare ITO of η_{EQE} = 32% at 610nm (near the peak donor n_{EQE}) and also yielded an increase in the acceptor contribution to EQE below 500nm. Furthermore, devices employing a tetracene and PEDOT:PSS dual anode interfacial layer, show a peak EQE of 57% at 610 nm which represents an 85% enhancement. This is a much greater improvement than previous reports employing anode interfacial layers. The slight decrease in the EQE in the 400-500 nm is likely due to absorption of light by the tetracene which does not contribute much to the photocurrent generation, which reduces the amount of light reaching the C_{60} acceptor layer.

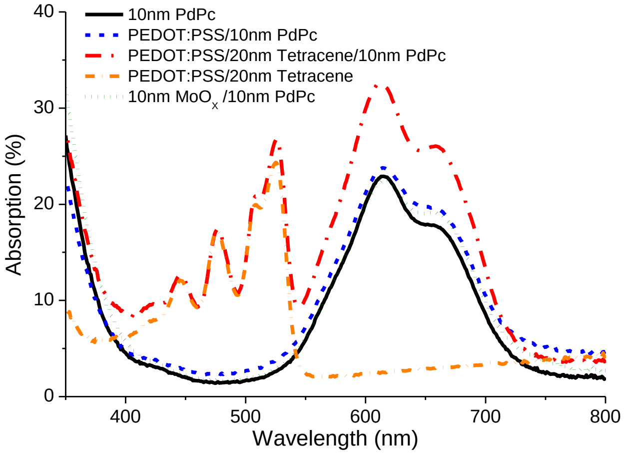

Figure 26. Plots of absorption efficiency vs. wavelength for thin films of PdPc in the general structure: Glass/ITO/AIL/PdPc (10nm). Where AILs are: AILs are: none (i.e., bare ITO, solid), PEDOT:PSS (dashed), 10 nm MoO_X (dotted), and PEDOT:PSS/20nm tetracene (dash-dot). The absorption of Glass/ITO/PEDOT:PSS/ 20nm Tetracene (short dot-dash) was given for comparison.

To explore the origin of these EQE differences, the absorption spectra were measured for the thin films of Glass/ITO/AIL/PdPc (10 nm) using reflectance corrected transmission data from a UV-CARY 5000 spectrometer. The spectra are shown in Figure 26. It is apparent that there is only minimal changes in the PdPc absorption by adding MoO_X or PEDOT:PSS layers, lying between 22.5-23.8%. However, when tetracene is added, the peak absorption rises to 32.5% at 610 nm. This absorption enhancement is similar to that observed in various other reports employing anode interfacial layers such as CuI or PTCDA which attributes this absorption enhancement to increased crystallinity and morphology change from an edge-on orientation of the phthalocyanine molecules on the substrate to a “flat-lying“ orientation when deposited on a templating layer.[74-76]

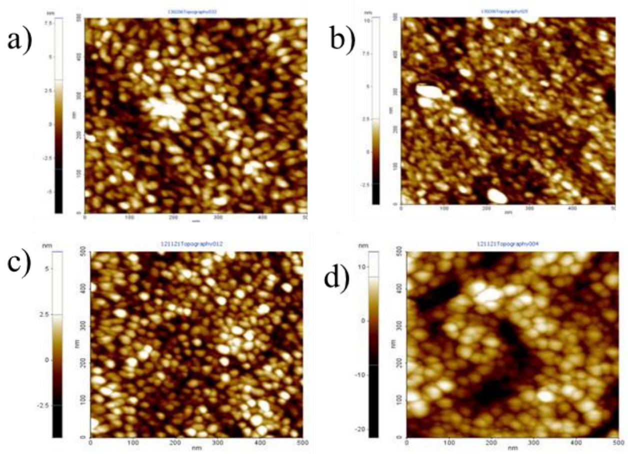

Figure 27. Atomic Force Micrographs for thin films of PdPc in the general structure: Glass/ITO/AIL/PdPc (10nm). Where AILs are: AILs are: (a) none (i.e., bare ITO, (b) PEDOT:PSS, (c) 10 nm MoO_X, and (d) PEDOT:PSS/20nm tetracene. The scale of the micrographs are 0.5 µm x 0.5 µm and were collected using a non-contact scan.

To confirm this morphology change, atomic force microscopy was carried out using a Park XE-150 AFM in non-contact mode for 0.5 µm scans for films with the PdPc on the various interfacial layers. As can be seen in the micrographs given in Figure 27, the morphology of PdPc on bare ITO, MoO_X, and PEDOT:PSS all show similar features of small dot-like domains and all maintain root mean square roughnesses between 1 and 2 nm (see in Table 1). The films on the PEDOT:PSS/tetracene dual layer, on the other hand, showed both an increase in the size of the PdPc crystalline domains and an increase in roughness. These results confirm the increase in the degree of crystallinity which been correlated with an increase in mobility and exciton diffusion length.[80] This increased crystallinity accounts for the increase in absorption as well as the decrease in series resistance from the device with just PEDOT:PSS. Furthermore, the increase in V_{OC} for the device can be associated with this change in molecular orientation or increased roughness. Since, the 85% enhancement in Donor EQE is only partially due to the enhancement in absorption, it is likely that the exciton diffusion efficiency is responsible for a large portion of the enhancement. An increase in exciton diffusion efficiency is possibly a combination of an exciton blocking effect from the wide bandgap tetracene material, a slightly increased region of intimate donor and acceptor contact from the increased roughness, and an increase in the exciton diffusion length resulting from the increased crystallinity. More experimental effort will be needed to clarify which effects lead to the high EQE. Thus, the overall increase in EQE can be attributed to a combination of the factors: (i) enhanced absorption through the increase in the degree of crystallinity, (ii) enhanced exciton diffusion efficiency through more efficient exciton diffusion in the crystalline domains accompanied by an increased donor acceptor interface area and an electron blocking effect from the higher bandgap tetracene layer, and (iii) enhanced charge collection efficiency due to the presence of the anode interfacial layer.

Table 1. Device performance characteristics for the devices with the general structure: ITO/ AIL/PdPc (10nm)/C_{60} (30nm)/PTCDI (10nm)/BCP (14nm)/Al. η_P is determined using the EQE.

AIL	J_{SC} (mA/cm^2)	V_{OC} (V)	FF	Rs (Ω cm^2)	η_P (%)	R_{RMS} (nm)	n_{EQE} (@610nm)
None	6.60	0.51	0.59	7.22	1.97	1.69	0.31
MoOx	5.92	0.54	0.62	1.80	1.96	1.26	0.22
PEDOT	7.02	0.55	0.62	2.75	2.42	1.26	0.32
PEDOT/Tetracene	8.92	0.64	0.61	1.92	3.66	4.14	0.57

In conclusion, dual layers of PEDOT:PSS and tetracene proved to be an excellent candidate for the anode interfacial interface with preferable energy levels for alignment between ITO and phthalocyanine-based donors and good exciton blocking properties. Furthermore, the tetracene behaved as a template to change the morphology of the subsequent donor layer. The morphology change led to an increase in absorption, an 85% increase in EQE and ultimately a 3.66% efficiency in a thin planar heterojunction device. Further optimization in device thicknesses, use of different architectures such as planar-mixed heteorojunction or tandem structures and employing tetracene anode interfacial layers with the state-of-the-art donor materials should yield even greater efficiencies going forward. Thus, the use of dual anode interfacial layers provides a viable route to enhance the efficiency of small molecular organic photovoltaic devices and may eventually contribute to their potential commercialization.

4.2 Anode Interfacial layers for ZnPc planar heterojunctions

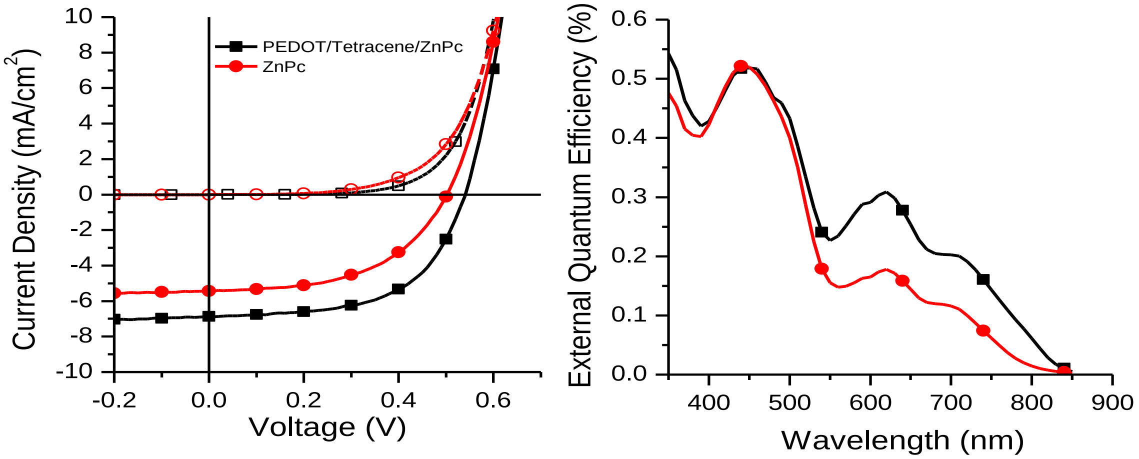

Figure 28. a) Current-voltage characteristics and b) EQE spectra for planar heterojunction devices of ZnPc with and without a tetracene interfacial layer

Devices of zinc phthalocyanine with and without a tetracene anode interfacial layer were fabricated in the general structure ITO/PEDOT:PSS/ Tetracene (0, 20nm)/ ZnPc

(10nm)/C_{60} (30nm)/PTCDI (10nm)/BCP (14nm)/Al. As shown in Figure 28,upon the addition of the tetracene layer the current-voltage curve shifts down leading to an increase in both open circuit voltage from 0.5V to 0.54V and short circuit current from 5.44 mA/cm^2 to 6.86 mA/cm^2. This leads to an overall power conversion efficiency of 2.13% for the devices with the tetracene anode interfacial layer versus only 1.42% for the devices without such a layer. Since the majority of the enhancement is from the increase in photocurrent, the external quantum efficiency was measured as a function of wavelength, shown in Figure 28b. From this plot it is apparent that the enhancement is mainly from the 550nm-800nm portion of the spectrum where ZnPc absorbs with the maximum EQE at 620nm increasing from 18% to 31%. This 80% enhancement is much greater than that observed in previous reports of anode interfacial layers.[73-78]

The external quantum efficiency, which is given by the equation: EQE= $\eta_A \cdot \eta_{ED} \cdot \eta_{CT} \cdot \eta_{CC}$, is simply the product of the efficiencies of four successive processes: light absorption (η_A), exciton diffusion to the donor acceptor interface (η_{ED}), charge transfer (η_{CT}), and charge collection at the electrodes (η_{CC}). Thus, the enhancement in the donor contribution to the EQE must stem from the enhancement of at least one of these processes. To determine the effect of the tetracene interfacial layer, the absorption was measured from thin films of Glass/ITO/ PEDOT:PSS/ Tetracene (0, 20nm)/ ZnPc (10nm). As is apparent from the plot shown in Figure 29, there is not a major overall enhancement in the absorption of the film in the region 550-800, beyond where the tetracene layer absorbs. However, the shape of the absorption curve changes with the peak at 620nm increasing relative to the peak at about 700nm for the films with the tetracene layer. It has been previously reported for phthalocyanine materials that the 620nm peak is correlated with dimer or higher order aggregates whereas the 700nm peak is associated with monomer absorption, indicating an increase in the degree of crystallinity of the ZnPc layer when deposited on the PEDOT:PSS/tetracene dual interfacial layer.[47] Ultimately, since the total absorption is only minimally changed the enhancement in external quantum efficiency must be related to either exciton diffusion to the donor acceptor interface (η_{ED}), charge transfer (η_{CT}), and charge collection at the electrodes (η_{CC}). A change in charge collection efficiency should manifest itself in a change in the slope of the current voltage characteristics, yet at short circuit current the current voltage curve is approximately parallel for devices with or without tetracene. Furthermore, minimal change is expected in the charge transfer efficiency since the ZnPc/C60 heterojunction is maintained and is expected to be near unity for the devices whether or not tetracene is used. Thus, it is suspected that the enhancement is mostly the result of an exciton diffusion efficiency enhancement from the combined effect of modified exciton diffusion length from increased crystallinity as well as the exciton blocking properties of the larger bandgap tetracene layer.

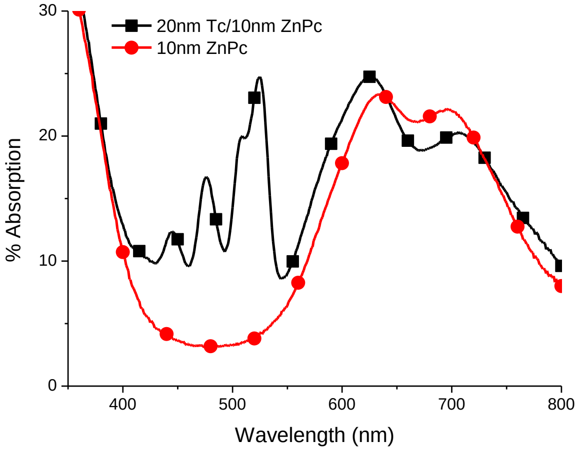

Figure 29. a) Percent absorption as a function of wavelength for devices with (squares) or without (circles) a tetracene anode interfacial layer in the structure: glass/ITO/PEDOT:PSS/Tetracene (0 or 20nm)/ ZnPc (10 nm) where percent absorption is determined from transmission and reflection measurements.

To further explore the effect of tetracene on the morphology of the ZnPc layer, AFM measurements were done on the thin film samples. ZnPc on PEDOT:PSS formed small dot-like features similar to what has been previously reported for phthalocyanine materials.[81] When the ZnPc was deposited on the tetracene layer elongated crystalline features were formed that had a much larger domain size indicating a morphology change on the nanometer scale within the film. Additionally, the root-mean-squared roughness increased from 1.1nm to 3.1nm when the tetracene layer was added. While it is apparent that there are major morphological differences between these two films, the relationship between this difference and the enhanced η_{ED} (and therefore EQE) will require a more comprehensive investigation but previous studies have shown improvements in exciton diffusion length as the degree of crystallinity in organic film increases.[80]

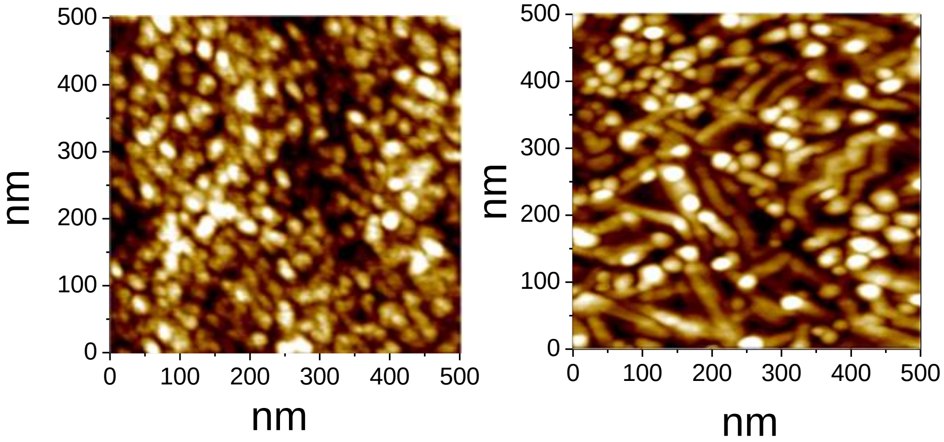

Figure 30. Atomic force micrographs for 10 nm ZnPc deposited on (a) PEDOT:PSS and (b) PEDOT:PSS/ 20 nm Tetracene.

To further study the performance of planar heterojunction devices, the donor layer thickness was increased to 20, 30, or 40nm and the external quantum efficiency was measured, shown in Figure 31. Rather than demonstrating further increases in photocurrent from the increased absorption, the donor contribution for EQE drops significantly for devices with the tetracene. Of particular note is that the drop in EQE is only observed for devices with the tetracene layer whereas the devices without such a layer remain at approximately the same value. Furthermore, since the drop occurs across the entire tested spectral range, it is likely that the losses are originating at the donor acceptor interface and it is speculated that the change in film morphology is responsible for such losses. As a result, the optimal performance for the ZnPc/C_{60} planar heterojunction device is achieved for donor layer thicknesses between 10 nm and 20 nm.

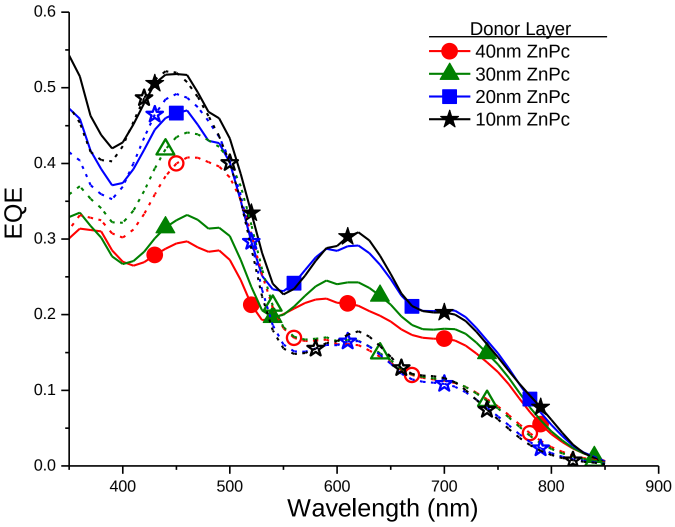

Figure 31. External quantum efficiency as a function of wavelength for devices with 20nm tetracene (solids) or without tetracene (open symbols) in the structure: ITO/PEDOT:PSS/Tetracene (0 or 20nm)/ ZnPc (x nm)/ C60 (30 nm)/PTCDI (10nm)/ BCP (14 nm)/Al.

In summary, the fabrication of planar heterojunction ZnPc/C_{60} devices with a dual anode interfacial layer of PEDOT:PSS and tetracene led to an over 80% enhancement in the EQE at the peak donor contribution leading to a maximum device efficiency of 2.1%. Through absorption and AFM measurement it was determined that the EQE enhancement was likely the result of enhanced exciton diffusion efficiency stemming from either exciton blocking effects from the properly selected anode interfacial material or from increased exciton diffusion length as a result of the modified donor layer morphology when deposited on top of tetracene. The application of tetracene as an interfacial layer with a variety of donor materials demonstrated increases in short circuit current for all materials tested but further optimization of these other material systems or the use of other state-of-the-art donor materials is necessary to reach higher efficiencies.

4.3 ZnPc/C60 Planar Mixed Heterojunctions

Typically ZnPc/C_{60} heterojunctions demonstrate low efficiencies of η_P = 1-2% due to their low open-circuit voltages of less than 0.5 V and limited exciton diffusion length of ~10 nm.[19] Previously, I showed a simple one-step, solvent-free reaction using inexpensive reagents 1,2-dicyanobenzne and zinc chloride to produce partially chlorinated ZnPc (denoted as $ZnPc^{HS}$) at a large scale in high yield. This material demonstrated a significant increase in both the open-circuit voltage and fill factor in ZnPc/C_{60} planar heterojunction photovoltaic cells as compared to a commercially obtained ZnPc (denoted as $ZnPc^{CS}$).[82] The current density-voltage (J–V) characteristics of planar heterojunction devices employing these two materials are shown in Figure 32, which have the structure of: indium-tin oxide (ITO)/$ZnPc^{CS}$ or $ZnPc^{HS}$ (15 nm)/C_{60} (30 nm)/PTCDI (10 nm)/BCP (14 nm)/Al. Here N,N’-dihexyl-perylene-3,4,9,10-bis(dicarboximide) (PTCDI) was employed as an interfacial layer between the C_{60} acceptor and the bathocuproine (BCP) exciton blocking layer.[63] From Figure 32a, it is apparent that the two devices have nearly identical short-circuit current densities of approximately 5.8 mA/cm^2 under 1 sun AM1.5G solar illumination, but the open-circuit voltage increases from 0.43 ± 0.01 V to 0.64 ± 0.01 V and the fill factor from 0.55 ± 0.01 to 0.70 ± 0.01 when the commercial ZnPc was replaced by ZnPc^{HS}, leading to an overall η_P enhancement from 1.4 ± 0.1% to 2.6 ± 0.1% (also see Table 1).

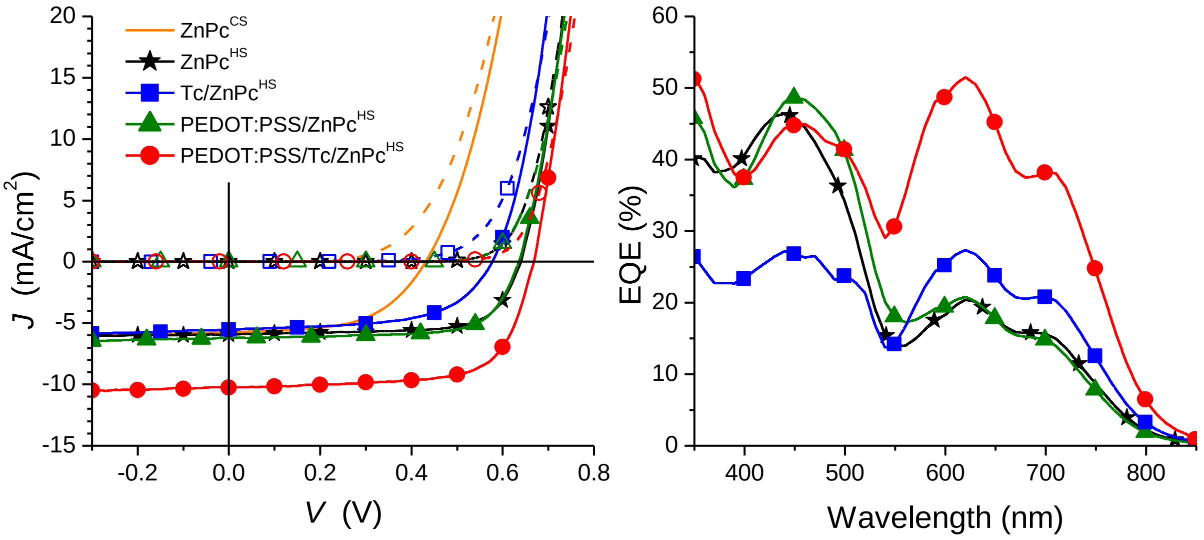

Figure 32. (a) Current density vs. voltage (*J*–*V*) characteristics in the dark (open symbols/dashed lines) and at 1 sun AM1.5G illumination (solid symbols/lines) and (b) external quantum efficiency (EQE) spectra for planar heterojunction devices of ZnPc^{CS} (no symbols), ZnPc^{HS} (stars), and ZnPc^{HS} with the anode interfacial layers: 10 nm Tetracene (Tc, circles), PEDOT:PSS (triangles), and PEDOT:PSS/10 nm Tc (squares) in the device structure: ITO/AIL/Donor 15 nm/C_{60} 30 nm/PTCDI 10nm/BCP 14 nm/Al.

To improve the efficiency of the ZnPc^{HS} devices, three different interfacial layers between the ITO anode and the ZnPc^{HS} donor layer are employed: a 10 nm thick tetracene (Tc) layer, a poly(3,4-ethylenedioxythiophene) poly(styrenesulfonate) (PEDOT:PSS) layer, or a PEDOT:PSS/tetracene (10nm) bilayer. The J−V characteristics of ZnPc (15 nm)/C_{60} (30 nm) planar heterojunction devices with the various interlayers are shown in Figure 32a, and the photovoltaic performance parameters of these devices are summarized in Table 1. When a single PEDOT:PSS layer is used, there is minimal change in the J−V characteristics with only a slight increase in J_{SC} to 6.2 ± 0.3 mA/cm^2. Conversely, a single 20 nm thick Tc interlayer actually leads to noticeable reductions in both J_{SC} and V_{OC}. However, when tetracene is deposited on top of PEDOT:PSS, there is a dramatic increase in J_{SC} by approximately 4 mA/cm^2 to 10.3 ± 0.5 mA/cm^2. Along with a minor increase in V_{OC} to 0.67 ± 0.01 V and nearly constant fill factor, the power conversion efficiency is increased from 2.8 ± 0.2% to 4.7 ± 0.3%. This is amongst the highest reported for small molecular planar heterojunction devices and is especially high considering the simplicity of the materials system.[22]

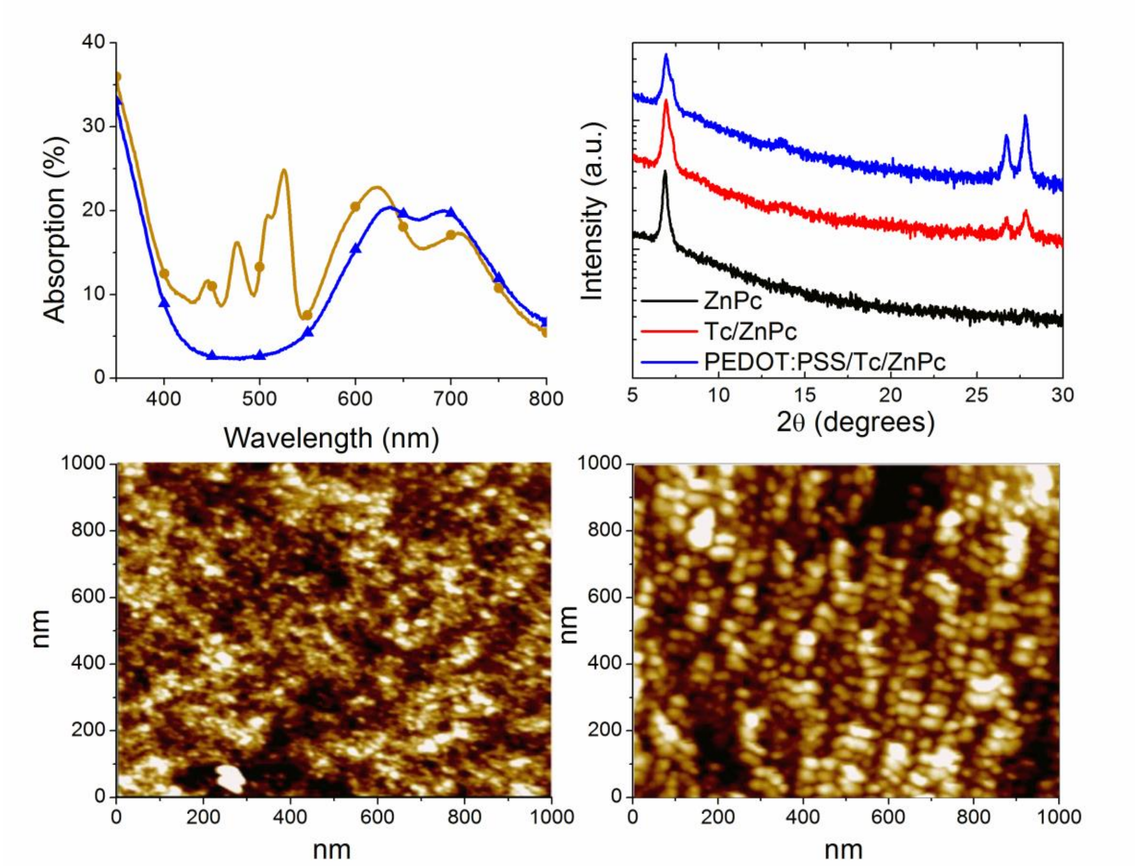

Figure 33. a) Thin film absorption spectra for Glass/ITO/PEDOT:PSS/ZnPc^{HS} (triangles) and for Glass/ITO/PEDOT:PSS/tetracene (10 nm)/ZnPc^{HS} (15 nm) (circles). b) X-ray diffraction patterns of 150 nm ZnPc films, with or without interlayers, grown on Si substrates coated with a thermal SiO_2 layer. c-d) Atomic force micrographs for thin films of ZnPc in the general structure: Glass/ITO/AIL/ ZnPc^{HS} (15nm) where AIL is either (c) PEDOT:PSS, (d) PEDOT:PSS/tetracene (10 nm).

The external quantum efficiency (EQE) spectra of these ZnPc/C_{60} planar heterojunction devices with various interfacial layers are shown in Figure 32b. The EQE spectra for devices without any anode interfacial layer or with a single PEDOT:PSS layer showed very similar shape and magnitude. When a single Tc layer is employed, the EQE spectrum shows an enhancement in the region where ZnPc absorption dominates (λ = 550 nm to 800 nm) from a maximum of 21% to 27%, although that is compensated by a significant reduction of EQE at $\lambda < 550$ nm where C_{60} absorption dominates. However, when the PEDOT:PSS/Tc dual layer is used, the high EQE below 550 nm is mostly restored, and a much stronger enhancement in EQE in the ZnPc absorption region is observed. The peak EQE at $\lambda = 620$ nm increases from 21% to 52%, a relative increase of approximately 150%. The minimal decrease in EQE at $\lambda < 500$ nm is most likely due to absorption in the Tc layer since, by comparing the absorption spectra (Figure 33a) to the EQE for the tetracene-containing devices, it is inferred that absorption in Tc ($\lambda = 400$ nm to 550 nm) does not contribute to the photocurrent.

The thin film absorption for the multilayer stack of Glass/ITO/PEDOT:PSS/Tc (0 or 10 nm)/ZnPc^{HS} (15 nm) determined from reflection and transmission measurements using a UV Cary 5000 spectrophotometer equipped with an integration sphere is shown in Figure 33a. Upon comparing the absorption spectra of the ZnPc^{HS} films with or without the Tc layer, it is apparent that the large increase in EQE in the ZnPc^{HS} spectrum is not a result of an increase in absorption. There is, however, a significant change in the shape of the ZnPc^{HS} absorption spectrum when the Tc layer is included as the intensity ratio of the peak centered at $\lambda = 610$ to 620 nm to the peak at $\lambda \approx 700$ nm becomes significantly higher, along with the appearance of a noticeable shoulder at $\lambda \approx 580$ nm. This has been previously attributed to an increase in the concentration of dimer and higher order aggregates,[83] suggesting an increase in crystallinity when the ZnPc^{HS} is deposited on Tc (on PEDOT:PSS).

To examine the morphology change, x-ray diffraction (XRD) patterns of ZnPc^{HS} on the various interfacial layers in the θ-2θ mode were collected and are shown in Figure 33b. Without either PEDOT:PSS or Tc, ZnPc^{HS} has a single diffraction peak centered at $2\theta = 6.9°$, corresponding to a 12.7 Å interplanar spacing which has been attributed to the

(200) molecular plane of the α phase of ZnPc with edge-on orientation on the substrate. For the ZnPc^{HS} films grown on tetracene and PEDOT:PSS/Tc, this feature evolves into a doublet with peaks at 6.9° and 7.3°, the latter peak corresponding to the (001) plane of the highly crystalline Tc layer.[84] In addition to the (200) α-ZnPc diffraction peak, the film grown on PEDOT:PSS/Tc interfacial layers shows a weak feature centered at 13.6°, which, while not very concluive, corresponds to the higher order (400) diffraction of α-ZnPc, again suggesting improved crystallinity in this ZnPc^{HS} film. A pair of peaks at 2θ = 26.7° and 27.8° are present in ZnPc films deposited on top of Tc and PEDOT:PSS/Tc, which agree with the $(0\bar{1}2)$ and $(\bar{1}\bar{1}2)$ diffractions of the triclinic α-ZnPc phase, respectively.[85] These high angle diffraction peaks correspond to interplanar spacings of 3.2 to 3.3 Å, which is close to the interplanar distance in ZnPc crystals along the molecular stacking direction. Given the geometry of the θ-2θ mode of XRD measurements, this suggests that the Tc interfacial layer, especially with an additional underlying PEDOT:PSS layer, promotes the growth of ZnPc molecules in the “face-on” orientation such that the molecular stacking direction is mostly normal to the substrate surface. The different growth mode of ZnPc^{HS} thin films as affected by the anode interfacial layer is also analyzed using non-contact atomic force microscopy (AFM). There is an apparent change from a random organization of small dot-like ZnPc domains with a root-mean squared roughness (r_{rms}) of 1.1 ± 0.1 nm for ZnPc^{HS} on a single layer of PEDOT:PSS (Figure 33c) to a well-structured arrangement of larger ZnPc^{HS} domains and r_{rms} of 5.1 ± 0.5 nm for PEDOT:PSS/Tc-templated ZnPc^{HS} (Figure 33d), further supporting both an increase in the crystallinity of the film and a change in the growth mode of the ZnPc^{HS} domains. It is also noted that from AFM measurements, that the Tc

film directly deposited on ITO shows only incomplete (~70%) coverage and very rough surface (r_{rms} = 13 nm for a Tc film with 20 nm nominal thickness), indicative of the three-dimensional, island growth mode. The PEDOT:PSS underlying layer appears to change the growth of the Tc overlayer to the layer-plus-island mode, leading to a significantly smoother surface (r_{rms} = 3.3 nm) with larger domains and near complete coverage (>95%).

From the device and thin film characterization, the EQE increase in the donor absorption region is attributed to an increase in exciton diffusion efficiency, likely through a combination of multiple factors. The tetracene layer, which has a wider optical gap than ZnPc (see Figure 33a), serves as an exciton blocking layer at the anode interface, thus preventing the quenching of photogenerated excitons in the ZnPc layer by the anode. The tetracene layer increases the crystallinity of the donor layer, which has been correlated to an increase in the exciton diffusion length.[80]**Error! Bookmark not defined.** Moreover, s revealed by the XRD results, the orientation of ZnPc molecules was changed from mostly edge-on without the tetracene layer to a mixture of edge-on and face-on with the tetracene layer. The face-on configuration suggests that the molecular $\pi-\pi$ stacking direction is in the film thickness direction, thus further promoting the exciton diffusion process towards the donor-acceptor interface. For the devices without the PEDOT:PSS layer, the incomplete coverage of Tc on ITO results in direct contact of ZnPc with ITO in certain areas, leading to incomplete exciton confinement and therefore lower photocurrent. Furthermore, the lower EQE in the C_{60} absorption region for the ITO/Tc/ZnPc device as compared to the ITO/ZnPc device may suggest a hole collection problem at the ITO/Tc interface due to the deeper HOMO level of Tc, which could be alleviated to some extent by the inclusion of the PEDOT:PSS layer due to the higher work function of PEDOT:PSS than ITO. More experimental effort will be needed to clarify which effects lead to the high exciton diffusion efficiency and consequently high external quantum efficiency in the devices with the anode interlayers.

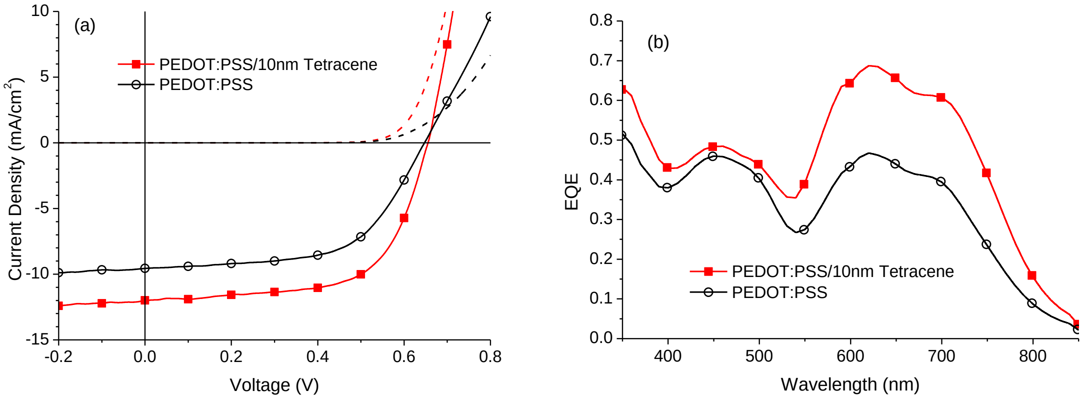

Figure 34. a) Current density vs. voltage (*J*–*V*) characteristics and b) external quantum efficiency vs. wavelength for planar-mixed heterojunction devices of ZnPc^{HS} with the anode interfacial layers PEDOT:PSS (black circles) and PEDOT:PSS/10 nm Tetracene (red squares) in the device structure: ITO/AIL/ZnPc^{HS} 15 nm/ ZnPc^{HS}:C_{60} 20 nm (2:1 by weight)/C_{60} 30 nm/PTCDI 10nm/BCP 14 nm/Al

In order to further increase the efficiency of these devices, planar-mixed heterojunction devices were fabricated by adding an additional 20 nm thick ZnPc:C_{60} mixed layer in between the neat donor and acceptor layers. Planar-mixed heterojunctions have been used previously to circumvent the tradeoff between the thin films needed for efficient exciton diffusion and the thick films needed for complete absorption, allowing simultaneous optimization of both absorption and internal quantum efficiency.[38] Devices were fabricated with the structure: ITO/PEDOT:PSS/Tc (0 or 10 nm)/ZnPc^{HS} (15 nm)/ZnPc^{HS} : C_{60} (20 nm, 2:1 by weight)/C_{60} (30 nm)/PTCDI (10 nm)/BCP (14 nm)/Al. As seen in Figure 34a as well as in Table 1, a significant increase in J_{SC} from 10.0 ±0.5 mA/cm^2 to 13.9 ±0.5 mA/cm^2 was obtained when the Tc anode interfacial layer was included, which was accompanied by a nearly identical V_{OC} and a slight increase in FF from 0.59 to 0.63. The external quantum efficiency in Figure 34b shows that the enhancement is again mainly attributed to enhanced contribution from absorption by the $ZnPc^{HS}$ layer. The maximum EQE of the Tc-containing device approaches 70% at λ = 620 nm, whereas it was below 50% for the device without the Tc layer. The net increase in J_{SC} of 3.9 mA/cm^2 is approximately the same as that for the planar heterojunction devices (4.1 mA/cm^2), which further supports our conclusion above that the photocurrent increase is mainly due to improved exciton diffusion efficiency in the neat ZnPc layer. Furthermore, the slightly higher fill factor for the planar-mixed heterojunction device with the Tc layer tends to indicate that the creation of larger, more crystalline ZnPc domains in the neat layer may aid the formation of a more structured interpenetrating network in the mixed layer which will enhance both the fill factor and the short circuit current. As a result, the inclusion of the Tc anode interfacial layer improves the power conversion efficiency of the ZnPc:C_{60} planar-mixed heterojunction devices from η_P = 3.8 ± 0.3% to 5.8 ± 0.3%, among the highest achieved to date for single donor-acceptor heterojunction (i.e., non-tandem) devices based on this material system and among the highest small molecule-based non-tandem OPV devices.

Table 2. Photovoltaic performance characteristics for ZnPc/C_{60} planar heterojunction (PHJ) and planar-mixed heterojunction (PMHJ) devices with or without anode interface layers. The PHJ devices have an active region of $ZnPc^{CS}$ or $ZnPc^{HS}$/C_{60} (15 nm/30 nm), whereas the PMHJ devices have an active region of $ZnPc^{HS}$(15 nm)/$ZnPc^{HS}$:C_{60} (2:1, 20 nm)/C_{60} (30 nm).

Device Structure	Jsc [mA/cm^2]	Voc [V]	FF	η_{PCE} [%]
$ZnPc^{CS}$ (PHJ)	5.8 ± 0.3	0.43 ± 0.01	0.55 ± 0.01	1.4 ± 0.1
$ZnPc^{HS}$ (PHJ)	5.9 ± 0.3	0.64 ± 0.01	0.70 ± 0.01	2.6 ± 0.1
PEDOT:PSS/ $ZnPc^{HS}$ (PHJ)	6.2 ± 0.3	0.64 ± 0.01	0.68 ± 0.02	2.8 ± 0.2
Tetracene/ $ZnPc^{HS}$ (PHJ)	5.5 ± 0.3	0.58 ± 0.01	0.58 ± 0.03	1.9 ± 0.3
PEDOT:PSS/ Tetracene/ $ZnPc^{HS}$ (PHJ)	10.3 ± 0.5	0.67 ± 0.01	0.69 ± 0.01	4.7 ± 0.3
PEDOT:PSS/ $ZnPc^{HS}$ (PMHJ)	10.0 ± 0.5	0.65 ± 0.01	0.59 ± 0.03	3.8 ± 0.3
PEDOT:PSS/ Tetracene/ $ZnPc^{HS}$ (PMHJ)	13.9 ± 0.5	0.66 ± 0.01	0.63 ± 0.03	5.8 ± 0.3

In summary, the effect of using a tetracene anode interfacial layer on the efficiency of organic photovoltaic cells based on a home-synthesized ZnPc was demonstrated. Planar heterojunction devices employing the tetracene anode interfacial layer achieved an EQE enhancement of 150% in the spectral region corresponding to ZnPc absorption. This was mainly attributed to the enhancement in exciton diffusion efficiency, with the tetracene layer providing exciton-blocking function at the anode/donor interface and increasing the exciton diffusion length in the ZnPc layer due to increased crystallinity and more preferred molecular orientation/stacking. Applying these principles to a planar-mixed heterojunction ultimately yielded a η_P of 5.8 ± 0.3% and a peak EQE of nearly 70%. Further application of state-of-the-art donor and acceptor materials as well as integration of light trapping structures, tandem devices, or other architectures will likely further increase the efficiencies of these devices and one day may contribute to the development of commercial production of OPV devices.

5. ORGANIC LIGHT EMITTING DIODES

Organic electroluminescent (EL) materials have always received a great deal of attention from academia and industry since the first report of EL spectra from crystals of anthracene in the 1960s.[86] The introduction of an organic heterojunction by Tang *et al.* in 1980s, led to the first practical devices.[87] This device employed a heterojunction of a diamine type hole transporting layer (HTL) which has a high HOMO level and good hole mobility and an Alq_3 electron transporting layer (ETL) which has a lower HOMO and LUMO levels and good electron mobility. Emission originated from the Alq material since electrons were blocked by the high LUMO levels of the HTL and some holes were eventually injected into the Alq layer where excitons would form on the Alq layer and emit via a fluorescence emission process. Due to the restriction of having the same material as an electron transport material as well as the emitter, color tuning in this structure proved quite challenging. These concerns were alleviated with the development of a guest-host system in which an emissive material, which is color tunable through molecular modification, is doped into a larger bandgap matrix material.[88] In this system electrons and holes are separately injected and transported through their respective transport layers and eventually injected to an emissive layer (EML) where excitons can either be formed directly on the dopant material or on the matrix followed by a rapid energy transfer to the lower energy dopant molecule and devices with efficiencies of over 2% were achieved.

One major complication in early electroluminescent devices is the uncorrelated nature of the injected electrons and holes. Once the electrons and holes meet to form an exciton, there are 4 possible spin conformations as shown:

$$S = 0\colon \frac{1}{\sqrt{2}}\{\uparrow(1)\downarrow(2) - \downarrow(1)\uparrow(2)\}$$

$$S = 1\colon \frac{1}{\sqrt{2}}\{\uparrow(1)\downarrow(2) + \downarrow(1)\uparrow(2)\}$$

$$\uparrow(1)\uparrow(2)$$

$$\downarrow(1)\downarrow(2)$$

One combination giving a total spin of S=0 is antisymmetric, denoted a singlet, while there are 3 possibilities for S=1 which are symmetric and is denoted a triplet due to the degeneracy S=1 state. As a consequence of the Pauli Exclusion Principle, the spin of the initial and final states must have similar symmetry in order for an optical transition to occur. Thus, optical transitions between two triplet states or two singlet states are allowed but transitions between the two are formally forbidden. Since the ground state of almost all organic molecules are of singlet character due to the Pauli exclusion principle, only transitions between singlet excited states and singlet ground states will produce a photon, in a process called fluorescence, while the other 75% of the excitons of triplet character will decay non-radiatively. Thus, to achieve efficient emission, these triplet states need to be harvested.[89]

Spin-orbit coupling, which involves the interaction of the electronic spin and the magnetic moment of an electron in a closed orbit, facilitates the possibility of mixing singlet and triplet character to allow conversion between singlet and triplet states. The strength of this spin orbit coupling interaction is proportional to the atomic number to the 4th power so it is much more significant for heavy metals.[90] Thus, through the incorporation of heavy metals with organic ligands, transitions between singlets and triplets are possible. In this system triplet excitons may recombine radiatively in a process called phosphorescence.[59] Additionally, the formation of singlet excitons on such a molecule can undergo rapid intersystem crossing to the lower energy triplet excited state where it will also emit via a phosphorescent process with a theoretical 100% electron to photon conversion efficiency emitting from the triplet excited state. Since the development of phosphorescent emitters, the OLED field has flourished with devices emitting at high efficiencies across the visible spectrum and even extending into the ultraviolet and infrared regions of the electromagnetic spectrum.[91]

5.1 OLED device operation

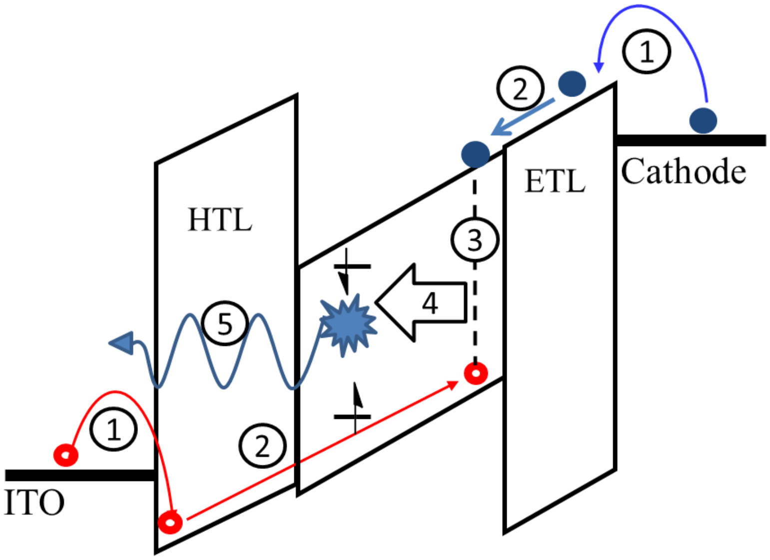

Figure 35. Operation of OLED

The typical operation of an OLED is given in Figure 35. Upon applying a forward bias, electrons and holes are injected over a small energetic barrier into hole transport and electron transporting layers respectively (1). The injected charges are then transported towards the emissive layer due to the applied electric field via a thermally activated hopping mechanism between neighboring molecules, show in Figure 36a-b.[8] Holes, or radical cations, drift toward the emissive layer via consecutive hops along the HOMO levels while electrons, or radical anions, drift by consecutive hops along the LUMO levels. Due to differences in charge mobility and the presence of energetic barriers, charges usually build up along the interface of the emissive layer and one of the transport materials. Once a charge of opposite polarity reach each other they will form a localized coulombically bound excited state called a Frenkel exciton. As mentioned previously, the statistical distribution of excitons will be 25% singlets and 75% triplets. In either case, the formed excitons can either recombine radiatively, recombine non radiatively, or can transfer its energy to another molecule. The transport of excitons can either occur as a coincident electron and hole exchange with a neighboring molecule or via a long range mechanism, called Förester resonant energy transfer.[92] The latter case, when the emission energy of a molecule has significant spectral overlap with the absorption spectrum of another molecule, a dipole coupling between the two molecules may occur and a long range radiationless energy transfer process may occur on length scales of the order 10-100Å.[93] Such is commonly the case for transfer of energy from a high bandgap host to a lower bandgap dopant molecules. Consequently, nearly exclusive emission can be achieved from a dopant molecule even at doping concentration of 1% or lower. Upon localization on the dopant molecule, the emitter can through either fluorescence or phosphorescence process, can transfer its energy to another dopant, or can be quenched by impurities. Thus, care has to be taken to make sure no impurities or lower energy species are present so that the primary recombination pathway will be through emission from the selected dopant molecule.

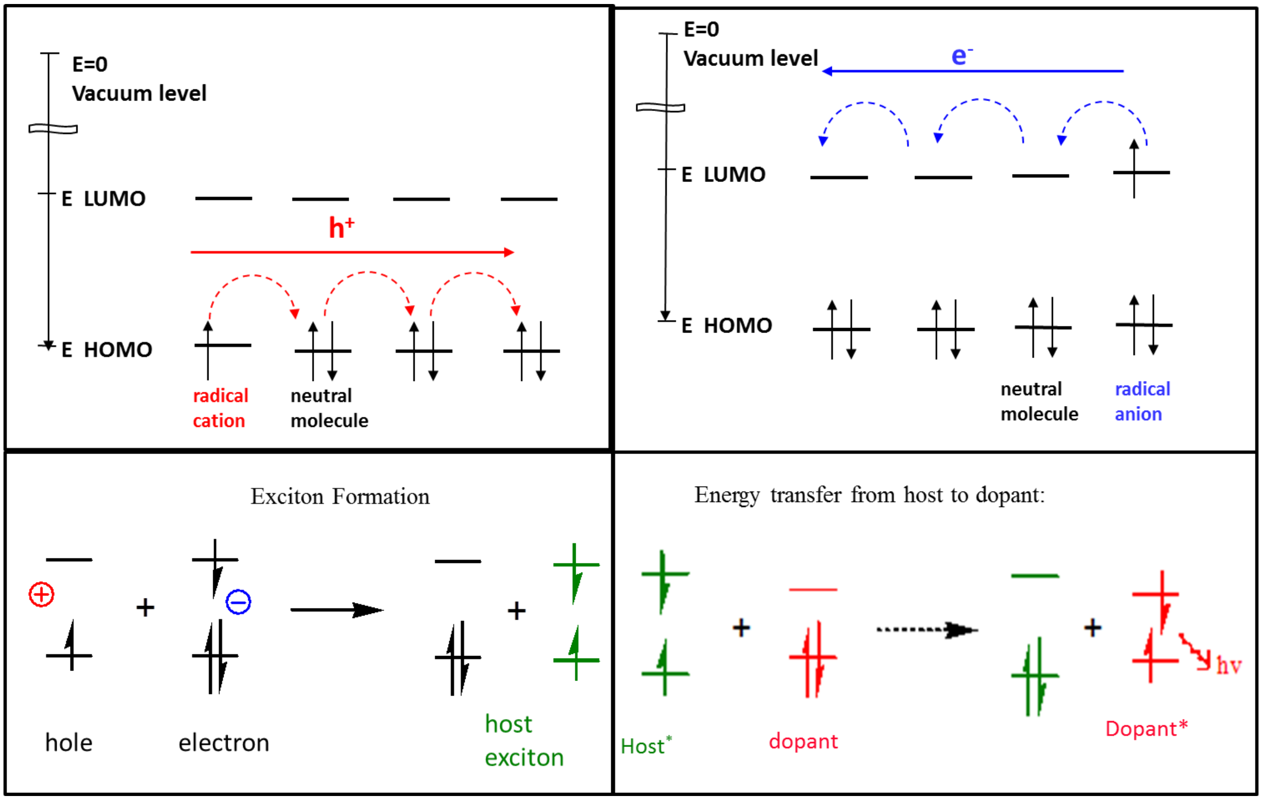

Figure 36. Energy transfer processes

5.2 Performance parameters

The efficiency of the electron to photon conversion process, also known as external quantum efficiency (EQE) can be described by the equation: $\eta_{\mathrm{ext}} = \chi \cdot \eta_{\mathrm{r}} \cdot \eta_{\mathrm{t}} \cdot \eta_{\mathrm{out}} \cdot \Phi_{\mathrm{PL}}$.[94] Steps 1-3 of Figure 35 can be lumped into a single term (η_r) for the efficiency of exciton formation from injected charges which depends on the charge balance and the presence of charge traps. Step 4 is described by, η_t, the efficiency of the energetic transfer of excitons to the dopant molecules and depends on the doping concentration, any nonradiative recombination pathways, and undesirable energy transfer to other species. Step 5 is described by the efficiency of the emission which is the product of $\chi \bullet \Phi_{PL}$, where χ is the fraction of excitons which can contribute to emission (0.25 for fluorescent emitters and 1 for phosphorescent emitters) and Φ_{PL} is the quantum yield of the emitter and depends on the radiative and non radiative decay rates of the emitter. Finally, Step 6 is the outcoupling of the emitted light to air, η_{out}, and is typically between 25-30% due to waveguiding effects, substrate losses, plasmon quenching, and other optical losses.[95] Thus, for optimized devices with an efficient phosphorescent emitter, EQE of 20-30% is possible without any advanced outcoupling techniques.[96] Another commonly used metric, power efficiency (PE), is the ratio of power of the emitted light to the electrical power input as perceived by the human eye measure in lumens per watt (Lm/W). Such a metric takes into account the driving voltage, as a component of the power input, as well as the color of the emitted light and the responsivity of the human eye.[94] Both of these in addition to other more specific values such as the maximum achieved luminance (measured in cd/m^2), turn on voltage (i.e. the voltage at 1cd/m^2), or EQE and PE at 1000cd/m^2 are important parameters for the evaluation of OLED devices.

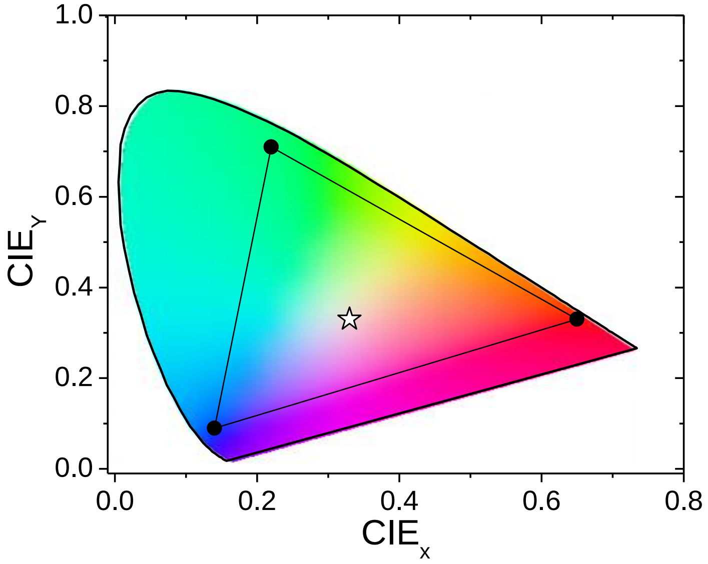

Figure 37. CIE color space

The measurement of the color emitted by OLEDs is also highly standardized. Rather than reporting peak emission wavelength of emitted light, which doesn't provide much information on the peak broadness or the intensity of secondary peaks, it is convenient to assign numerical values to the overall emission color as perceived by the human eye. Such a metric has been developed by the Commission Internationale de l'Eclairage which developed a coordinate system and a color space in which perceived color is measured, shown in Figure 37.[97] Furthermore the National Television System Committee (NTSC) set up standard coordinates in the CIE color space for red, green, and blue emission which are (0.67, 0.33), (0.21, 0.71), and (0.14, 0.08) respectively and is shown as the corners of the black triangle in Figure 37.[98]

5.3 Color Tuning:

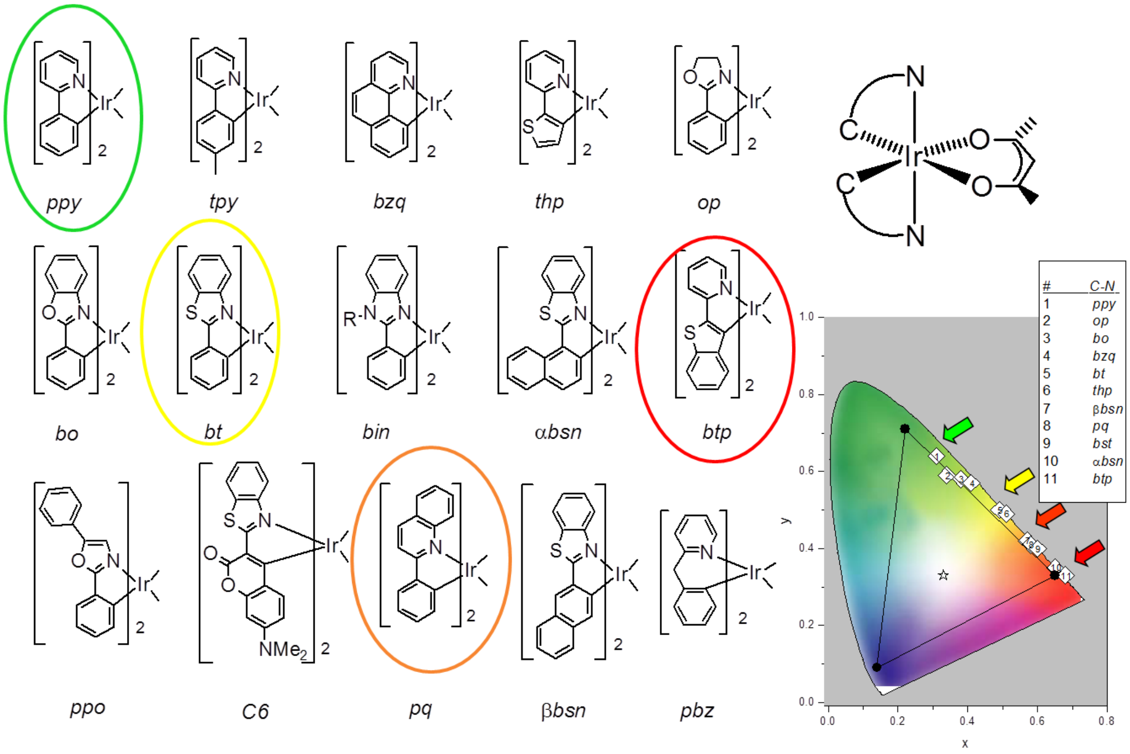

Figure 38. Color tuning of Ir complexes. From Lamansky et. al.[99]

In order to cover the full visible spectrum, efficient and stable blue, green and red phosphorescent emitters are needed. To this end, cyclometalated Ir and Pt complexes have been the focus of considerable research as emitters in organic light emitting diodes. These metal complexes are praised for their ability to harvest both electro-generated singlet and triplet excitons, resulting in a theoretical 100% electron to photon conversion efficiency.[96] The majority of the efforts for the development of stable and efficient emitters have employed Ir complexes.[100] In the seminal work by Lamansky and coworkers, the emission color of Ir complexes can be easily tuned through gradual modification of the main cyclometalating ligand.[99] In particular, the color can be tuned from green to red through the extension of the conjugation of the cyclometalating ligand or through the use of electron rich or electron deficient groups as shown in Figure 38. Phosphorescent cyclometalated Pt complexes have also been developed but are much less studied than those of Ir. One notable study however, by Brooks and coworkers show that employing similar bidentate cyclometallating ligands as those used by Lamansky et al. the emission color could be tuned from red to deep blue through extension of conjugation or addition of electron withdrawing groups, shown in Figure 39.[101] However, despite the significant progress in efficiencies and color tuning of phosphorescent emitters, a number of challenges remain. Namely, stable and efficient Ir and Pt complexes that emit in the range of 400-460 nm ("blue" region), appear much more challenging than their analogs emitting in the "green"[58,99] and "red"[102-105] region and is vital for both lighting and display applications.[106,107] Furthermore, the development of an efficient, stable, and balanced white OLED remains elusive and great challenges lie ahead to simplify the device architectures for reduced fabrication costs in order to compete with current low cost lighting sources.[108]

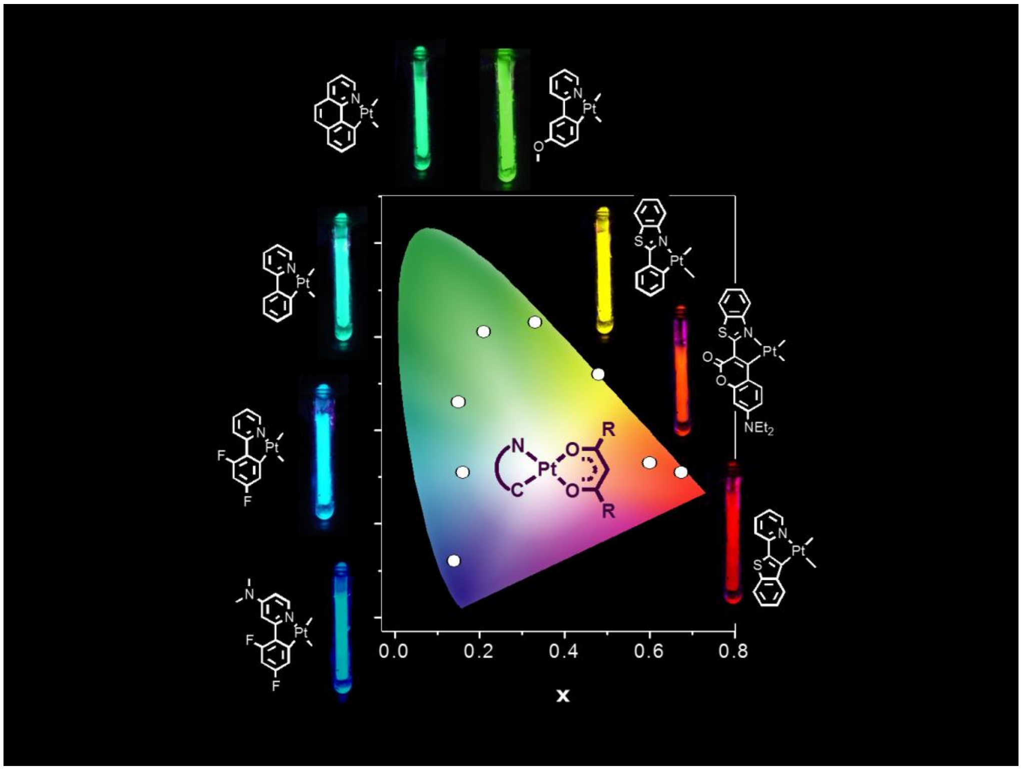

Figure 39. Color tuning of cyclometalated Pt complexes from Brooks et al.[101]

6. EFFICIENT DEEP BLUE DEVICES BASED ON PLATINUM(II) COMPLEXES

The development of efficient and stable deep blue OLEDs have been a particularly challenging goal in the pursuit of efficient next generation display and lighting technologies.[100,109] There are a number of unique disadvantages present for the development of deep blue OLEDs including the tradeoff between conjugation for charge transport and high bandgap, decomposition pathways present for high excited state energies, and the balance between appropriate energy level alignment and keeping energy barriers low. Thus, a number of obstacles remain, in particular, the development of stable host and charge transport materials with sufficient energy levels for deep blue emission and the development of deep blue emitters with high quantum yields that are stable and have a reduced of vibronic sideband for improved color coordinates.[109] The former requires the design and synthesis of charge transporting materials, charge and exciton blocking materials, and host materials and is studied thoroughly by a number of groups but only a few general comments and molecular designs will be discussed here. The latter challenge, the development of stable, narrow, and efficient emissive materials is the focus of a large portion of the OLED field and will be discussed thoroughly in the following sections.

6.1 Host and Charge Transporting Material Design

The hole transporting layers (HTL) for deep blue OLEDs have to meet a number of requirements in order to efficiently transport charge while simultaneously avoiding the creation of non-radiative recombination pathways. The former condition requires that a good hole transport material have good hole mobility while also having an a HOMO level that is appropriately balance between that of the host material (~5.8eV-6.1eV) and the work function of the anode, typically ~4.8- 5.0 eV for indium tin oxide (ITO). For example, a HTL with a HOMO level close to the host HOMO level but much deeper than that of the anode work function will have poor hole injection into the HTL material which will increase both the turn-on voltage (low power efficiency) and will decrease charge balance (low efficiencies at high brightness). The condition of preventing non-radiative recombination requires that the triplet energy of the hole transporting materials be higher than that of the emissive dopant to avoid energy transfer to the poorly emissive transport materials.[110] Care must also be taken to ensure that the LUMO level of the HTL is higher than that of the host (~2.4-2.8) in order to block the transport of electrons into the HTL where direct recombination with holes can take place.[111] The requirements can be summarized as below:

- High hole mobility
- E_T > 2.8-3.0 eV
- HOMO: 5.5-6.1 eV
- LUMO: <2.4 eV

In order to achieve such a criteria in a single material can be quite challenging but has been demonstrated with a number of material designs typically employing carbozole or triaryl amine moeities due to their hole transporting properties and high triplet energies examples of which are given in Figure 40.[112-117] However, no material has been developed which can satisfy all the conditions in addition to being thermal and electrochemically stable. Thus, it is often convenient to deconstruct the hole transporting process into separate funtions, that is, hole injection, hole transport, and electron and exciton blockers. This greatly relieves the constraints on each material. As such, a hole injection layer (HIL), need only have an energy level between the HOMO energy of the transporting material with the work function of the anode an have moderate hole mobility so as to not retard the flow of charges which has been achieved with conductive polymers like PEDOT:PSS,[70] or n-type organic materials such as HATCN.[112] A hole transport layer must have an energy level between that of the hole injection material and the host material and a strong hole mobility, but does not require a large band gap or high LUMO level; such conditions are typically satisfied with the use of materials such as NPD.[113] To fulfill the exciton and electron blocking effect, the layer adjacent to the emissive layer, called the electron blocking layer (EBL), must have a high LUMO level to block electrons, and high triplet energy to block excitons, but does not need a HOMO level close to the anode work function nor is it required to have a very high hole mobility as this layer can be kept thin. This layer can be satisfied by materials with either carbazole or triaryl amine moieties due to their hole transporting properties while also disruption conjugation for high bandgap, such as in TCTA,[117] TrisPCz,[116] mCP,[115] or TAPC.[114] TAPC, in particular is capable of giving high efficiencies for deep blue devices with its LUMO of 2.0eV and E_T of 2.98eV and will be employed as the EBL throughout all this work, while NPD will be used as the HTL, and either HATCN or PEDOT:PSS will be used as the HIL.

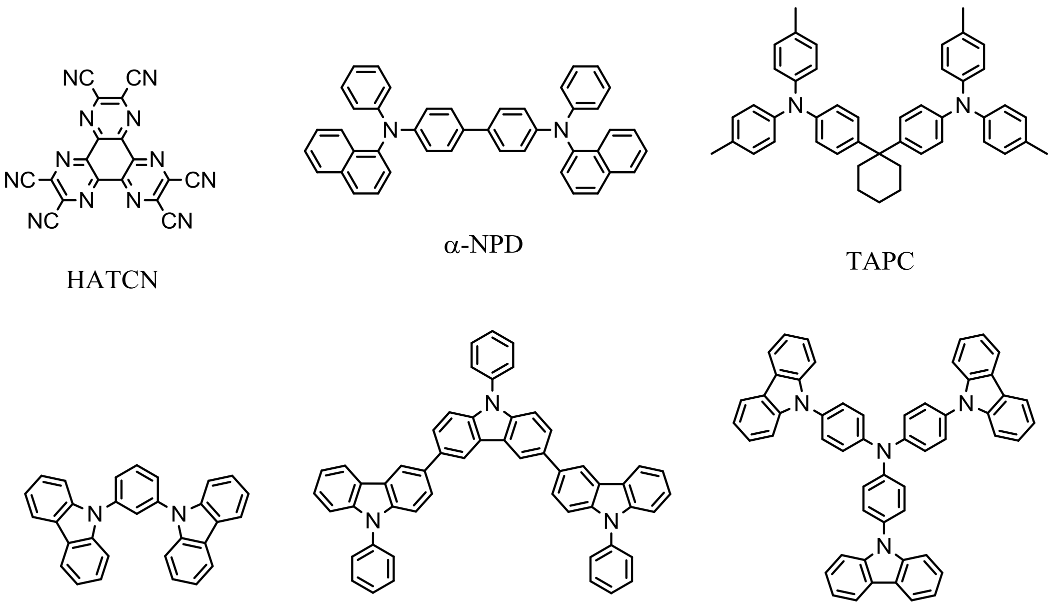
HATCN

α-NPD

TAPC

mCP

TrisPCz

TCTA

Figure 40. Examples of hole transport materials

The electron side of the device is similar and requires high electron mobility, high triplet energy, deep HOMO levels to block holes, and appropriate LUMO levels for efficient electron injection which are summarized below:

- High electron mobility
- $E_T > 2.8\text{-}3.0$ eV
- HOMO: >6.1 eV
- LUMO: 2.5-3.0 eV

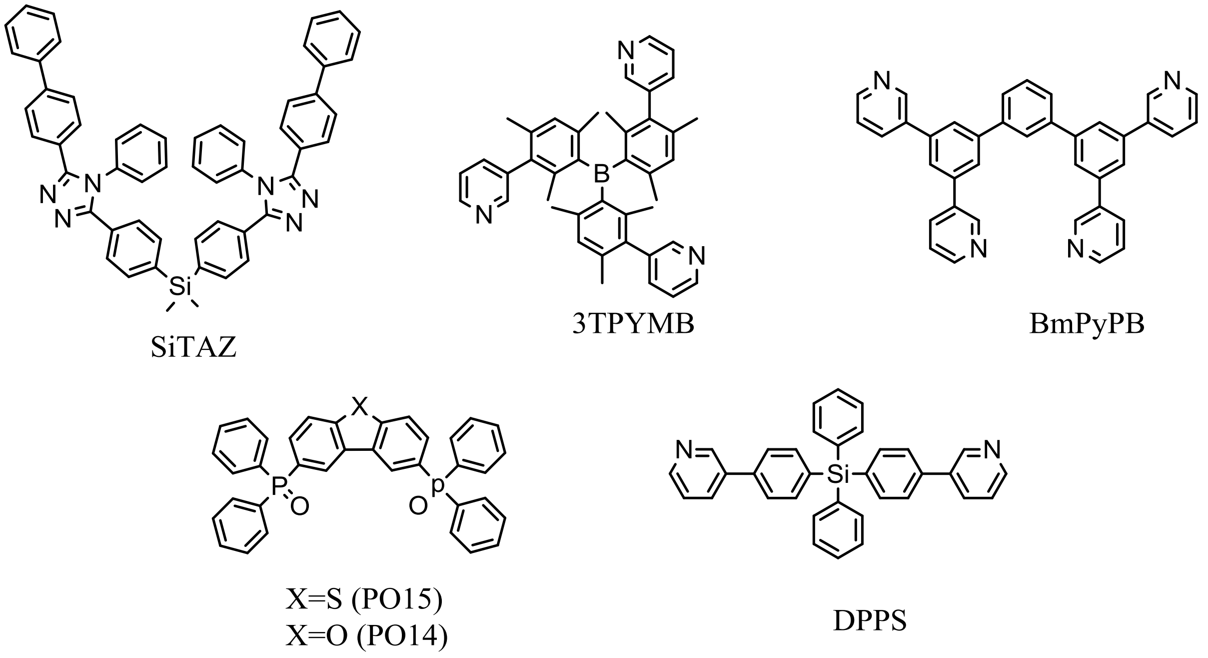

Figure 41. Examples of electron transport materials

Materials with strong electron transporting properties are quite challenging as the electron mobility is often 2 to 3 orders of magnitude lower than hole mobility of HTMs.[118] It is worth noting that it is possible to achieve high external quantum efficiencies employing materials with poor charge mobility as long as the charges and excitons are confined to the emissive layer, such is the case with DPPS.[119] The poor mobility does however lead to much lower power efficiencies as well as higher efficiency roll-off at high brightness so designing materials with both high electron mobility and exciton confining properties will be desired. High electron mobility can be achieved if electron-withdrawing groups such as pyridine are employed and high triplet energy can be achieved by disrupting π-conjugation through silanes (DDPS), boron (3TPYMB),[120] phosphine oxides (PO15),[121] or triazole groups (SiTAZ)[122] as shown in Figure 41. Again, due to the challenge of satisfying all the stringent constraints, the separation of the injection, transport, and blocking functions has proven very effective in the development of deep blue OLEDs. For electron injection, the most common strategy is to tune the workfuction of the Al cathode with the deposition of a thin layer of LiF dipoles tuning the work function to 3.0eV.[123] For electron transport materials, Alq has long been the favored materials due to its remarkable electron mobility but the large energy steps from the Alq to the emissive layer is likely to reduce efficiencies. Recently the planar starburst pyridine based material, such as BmPyPB have demonstrated dramatic improvement in electron mobility while maintaining a moderate E_T~2.7.[124] Hole blocking layers with very deep HOMO levels and high triplet energies can be achieved for phosphine oxide based materials such as PO15 (E_T= 3.07eV, HOMO= 6.6eV),[121] tetraphenylsilane materials such as DPPS (E_T= 2.7eV, HOMO= 6.5eV),[119] pyridine derivatives with a boron core such as 3TPYMB (E_T= 2.98eV, HOMO= 6.77eV),[120] or triazoles such as SiTAZ (E_T= 2.84eV, HOMO= 6.45eV).[122] Throughout this work devices employ either BmPyPB or PO15 as electron transporting layers due to their high electron mobility resulting from the electron deficient pyridine or thiophene units respectively. Furthermore, for blocking layers DPPS and PO15 were used due to their deep HOMO levels and high bandgaps.

Host materials are another crucial element to the fabrication of stable and efficient devices. Since both electrons and holes are present in the emissive layer, an ideal host material should have both good hole and electron mobility as well as appropriate HOMO and LUMO level alignment with the adjacent blocking layers. Perhaps most important is that the triplet energy of the host be significantly higher than that of the dopant, which for deep blue OLEDs should be greater than 2.9eV. An additional requirement toward eventual commercialization of OLEDs is that the host be stable which requires that the material be electrochemically stable under both oxidation and reduction as both electrons and holes are present in the emissive layer.[127]

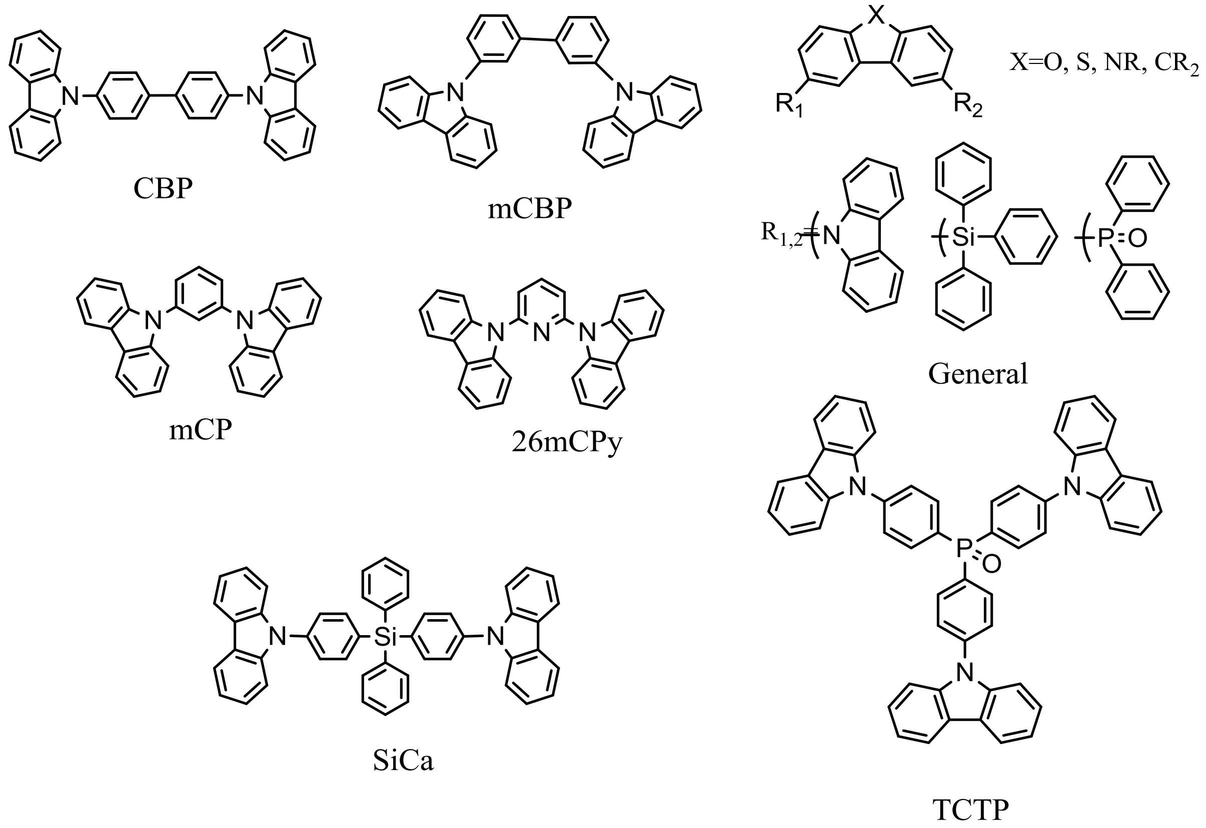

Figure 42. Examples of commonly used host materials

The most commonly used hosts are based on carbazole as shown in the various structures in Figure 42. The carbazole unit is highly desirable due to its high hole mobilities, moderately high triplet energy due to the disruption of conjugation by the nitrogen, and good electrochemical stability. CBP is the prototypical host material and is commonly used for green OLEDs for highly efficient devices with operational lifetimes estimated on the order of 100,000 hours.[96] For deep blue OLEDs, however, the triplet energy of CBP (E_T=2.6eV) is insufficient for deep blue OLEDs. By moving the carbazole groups to the meta positions the triplet energy can be significantly increased for mCBP

(E_T=2.9eV).[116] Similarly, removing the phenyl group also leads to high triplet energy of E_T=2.9eV for mCP or E_T=2.8eV 26mCPy.[125,126] A number of other structures exist based on carbazole, fluorene, debenzofuran, or dibenzothiophene cores with various hole or electron transporting units attached to the 3 and 6 positions of the core unit.[127] This general structural provides a wide variety of energy levels and different hole and electron mobilities due the electron rich or donating nature of the various moieties, but all retain high triplet energy due to the interrupted conjugation of the nitrogen, silicon, or phosphine oxide linkages. Furthermore, host materials with silicon or phosphine oxide cores also exist, for example, SiCa(E_T=3.0eV) or TCTP (E_T=3.0eV) which have both electron transport character due to their cores as well as hole transport character as a result of their peripheral carbazole units.[128,129] Such materials provide a great variety of options of electron and hole mobilities and energy levels in order to appropriately design an optimal structure for a selected dopant and/or transporting materials. Furthermore, it is also possible to codeposit two host materials, one with hole transporting character and one with electron transporting character in order to achieve a low turn on voltage and have ambipolar charge transport within the EML for improved charge balance.[130]

6.2 Deep Blue Emitter Design

Deep blue emissive dopants are the most important component of efficient blue OLEDs and is the focus of a large number of research groups. The requirements for such an emitter is a high emission energy in the range of 2.7eV to 2.8eV corresponding to roughly 44nm-460nm.[97] Such an emission can be achieved from either from the singlet excited state (fluorescence) or triplet excited state (phosphorescence). Despite the 4-fold improvement in exciton harvesting efficiency, many commercial displays still use fluorescent emitters for deep blue emission as they have already been developed and have demonstrated good operational stability.[131] Furthermore, until recently, much of the deep blue emitters were either very inefficient or suffered from poor color purity.[109] Thus, the design of efficient and potentially stable phosphorescent metal complexes is of the utmost importance.

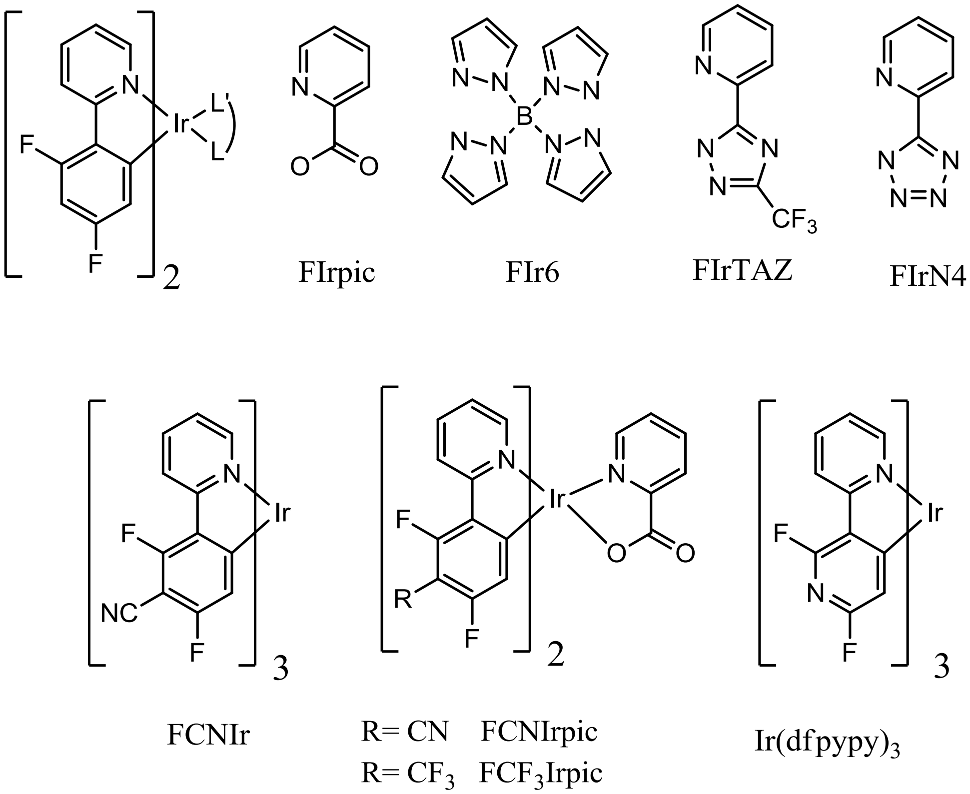

Figure 43. Phenylpyridine based deep blue Ir emitters

The vast majority of reports on the development of deep blue phosphorescence have employed cyclometalated Ir complexes.[109] An appropriate starting point for the discussion of color tuning is the prototypical Ir complex Ir(PPy)$_3$ which is a green emitter that exhibits nearly 100% internal quantum efficiency and has demonstrated an estimated half life of 160,000h.[132] In order to blue shift the emission of the Ir complexes the triplet energy of the emitter must be increased. As the HOMO is located on the phenyl group and the LUMO is located on the pyridyl group tuning the band gap can be achieved through either stabilizing the HOMO level through adding electron withdrawing groups or destabilizing the LUMO level through adding electron donating groups.[99] The former strategy has been widely successful through the addition of fluorine atoms to the 4 and 6 positions of the phenyl ring to form Ir(46dfppy)$_3$.[58] However, there can be large difference in emission energy depending on whether it is the facial or merino isomer, i.e *fac*-Ir(46dfppy)$_3$ and *mer*-Ir(46dfppy)$_3$ have PL emission peaks at 468nm and 482nm respectively.[58] This isomerism can be broken by replacing 1 or 2 two of the 4,6 difluorophenylpyridine cyclometalating ligands with an ancillary ligand as has been employed for a number of blue emitting complexes some of which are shown in Figure 43.[133-136] The emission can be tuned through ancillary ligands with electron withdrawing character such as with picolinate (FIrpic),[134] tetrakis(1-pyrazolyl)borate (FIr6),[135] triazolate (FIrtaz),[136] and tetrazolate (FIrN4),[136] which achieve peak PL emission in the range of 470nm for FIrpic to 459nm for FIrN4. Furthermore, such complexes can be extremely efficient and devices employing FIrpic have achieved peak EQE as high as 26.0% and power efficiencies as high as 55 Lm/W.[134] Nevertheless, the emission peaks at only 460-470nm are still far from achieving a saturated blue so more work needs to be done on the modification of the main ligand to achieve efficient deep blue emission with desirable CIE coordinates (0.15, 0.15) or lower. This can be achieved through the addition of CN at the 5 position of the phenyl ring for FCNIr or FCNIrpic which achieved deep blue emission ~450nm and CIE of (0.14,0.16) and (0.14,0.18) respectively.[115,137] FCNIrpic is among the most efficient Ir complexes for deep blue emission achieving a peak EQE of 25.1% and low roll off to 22.3% and 1000cd/m^2.[115] Further color tuning is also possible through the replacement of the difluorophenyl ring with and electron deficient difluoropyridine ring to shift the emission peak to 438nm.[138]

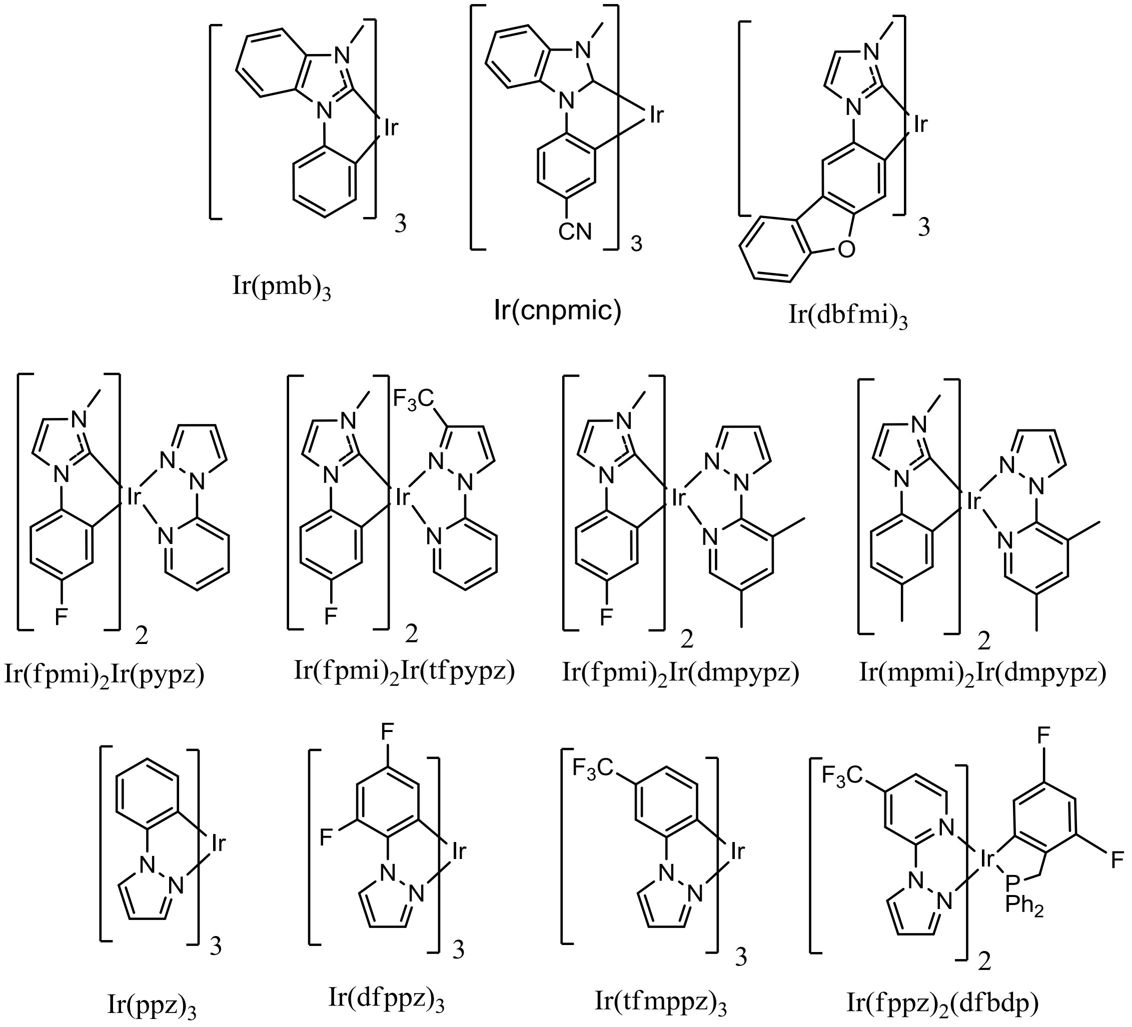

Ir(pmb)$_3$ Ir(cnpmic) Ir(dbfmi)$_3$

Ir(fpmi)$_2$Ir(pypz) Ir(fpmi)$_2$Ir(tfpypz) Ir(fpmi)$_2$Ir(dmpypz) Ir(mpmi)$_2$Ir(dmpypz)

Ir(ppz)$_3$ Ir(dfppz)$_3$ Ir(tfmppz)$_3$ Ir(fppz)$_2$(dfbdp)

Figure 44. Deep blue emitting Ir complexes containing 5 membered rings

Another strategy to achieve high triplet energy is to break the conjugation of the pyridine ring by replacing it with 5 membered rings such as imidazole, pyrazole, or triazole. Breaking the conjugation and constraining the ring size has the effect of raising the LUMO level to achieve a large bandgap. One such class is metal complexes cyclometalated with the 2-phenyl-methylimidazole(pmi) ligand and related analogues that are coordinated to the metal through a neutral carbene.[139-142] These include homoleptic complexes such as tris(1-cyanophenyl-3-methylimidazolin-2-ylidene-C,C2') iridium(III) [Ir(cnpmic)],[139] mer-tris(phenyl-methyl-benzimidazolyl) iridium(III), [m-Ir(pmb)$_3$],[140] and *mer*-tris(N-dibenzofuranyl-N′-methylimidazole) iridium(III) [Ir(dbfmi)].[141] m-Ir(pmb)$_3$ exhibits remarkable deep blue emission at 395nm resulting in one of the few OLEDs with a CIE$_y$ value below 0.1 with coordinates (0.17,0.06), yet such a complex was very inefficient and EQE of only 5.8% could be achieved.[140] For Ir(dbfmi), a maximum EQE of 18.6% was achieved with CIE coordinates of (0.15, 0.19).[141] In each of these two cases, the molecules have a fluorine-free cyclometalating ligand design, which has the potential for improved optoelectronic stability compared to fluorinated derivatives.[143] Further exploration of this class was done by modification of the ancillary ligand for a main ligand of fluorophenyl methylimidazole (fmpi). The emitter Ir(fpmi)$_2$(pypz) gave high peak quantum efficiencies of 14.1% and deep blue color coordinates of (0.14,0.18).[142] Upon adding a strong electron withdrawing group on the pyrazole of the ancillary ligand the color was significantly blue shifted achieving (0.14,0.10) for Ir(fpmi)$_2$(tfpypz) which is one of the deepest blue emitters developed so far yet again the poor energy confinement for such a large bandgap emitter led to only 7.6% efficiency.[142] On the other hand, two very efficient devices employing the emitters Ir(fpmi)$_2$(dmpypz) and Ir(mpmi)$_2$(dmpypz) achieved 17.1% and 15.4% efficiencies respectively for color of (0.13, 0.16) and (0.13, 0.18) which is among the best reported device performances for carbene based materials.[144]

Another typical ligand design is the application of phenylpyrazole cyclometalating ligands which have higher triplet energy than their phenylpyridine counterparts due to higher LUMO level from the reduced conjugation from pyridine to pyrazole. Ir(ppz), Ir(dfppz), and Ir(tfmppz) all have very high bandgaps and very high LUMO levels and peak emissions below 400nm are observed for this series of emitters.[58] Nevertheless, the poor emission properties of this class of emitters yeilded too inefficient of emission for device application. Pyridyl pyrazole ligands on the other hand, as in Ir(dfpypz)$_2$(dfbdp), showed high quantum yields of 0.73 in a doped thin film leading to efficiencies of 11.9% for color coordinates of (0.15,0.11).[145]

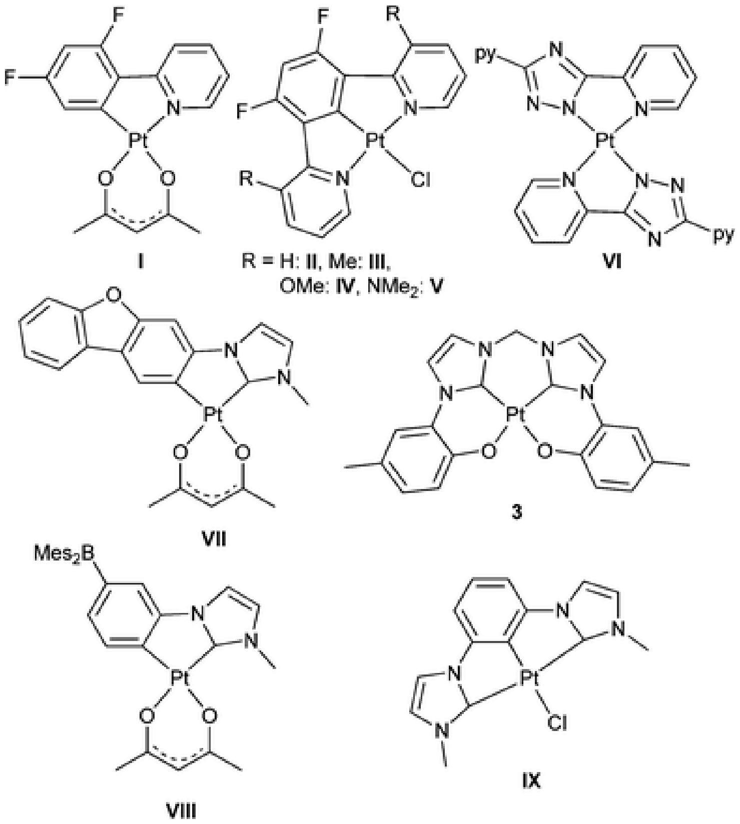

Figure 45. Reported deep blue Pt emitters. From Che et al.[146]

Recently, a number of platinum complexes with deep blue emission have also been developed. Unlike Ir complexes which typically require bidentate ligands to complex to the octahedral Ir metal, Pt complexes can take a number of different ligand designs due to its square planar coordination.[147] The most common of which are bidentate cyclometalating ligands due to the simplicity in the complexing reaction as well as their similarity to the well studied Ir analogs. FPt, complex I in Figure 45 is the direct Pt analog to the dfppy based Ir complexes and has been widely employed as a sky blue emitter with CIE of (0.11, 0.24) but had a low EQE of 4.3%.[148] Furthermore, a number of halogen free bidentate emitters have also been demonstrated employing triazole or carbene ligands to achieve deep blue emission. [149-151] Furthermore, tridentate cyclometalating ligands based on Py^Ph^Py type complexes have been well studied by Williams et al. where the addition of electron withdrawing groups to the central phenyl ring and electron donating groups to the outside pyridyl rings has a net effect of shifting the emission peak to 453nm for complex V in Figure 45.[152] Likewise, tetradentate pt complexes are also possible.[153] One such class of complexes based on dianionic cyclometalating ligands with 2 Pt-O bonds is shown in Figure 45.[154] This complex was capable of achieving blue emission of CIE (0.16, 0.16) but an efficiency of <1%. Furthermore, the electrochemical stability of such a complex and in particular the Pt-O bonds is unknown. In the following several sections, I will demonstrate my work done on the development and device fabrication of cyclometalated Pt complexes for deep blue emission as well as some new design principles for the next generation of emitter designs.

6.3 Deep blue devices based on Pt(II) N-Heterocyclic carbenes

In the design of cyclometalated Pt complexes for deep blue OLEDs much more work is needed to achieve efficiencies comparable to their Ir analogs. The photophysical properties of Pt complexes are very sensitive to the structural changes of the complexes or the selection of the metal complex system. For example, Pt(N^C^N)Cl complexes have demonstrated higher emission efficiencies and shorter luminescent lifetimes than their (C^N)Pt(acac) and Pt(N^N^C)Cl analogs, where N^C^N are tridentate coordinating ligands like di(2-pyridinyl)benzene, C^N are bidentate coordinating ligands like phenylpyridine, and N^N^C are tridentate coordinating ligands like 2-phenyl-bipyridine.[155] Thus, efficient blue phosphorescent OLEDs can be fabricated utilizing the analogs of platinum(II) 3,5-di(2-pyridinyl)benzene chloride (Pt-1).

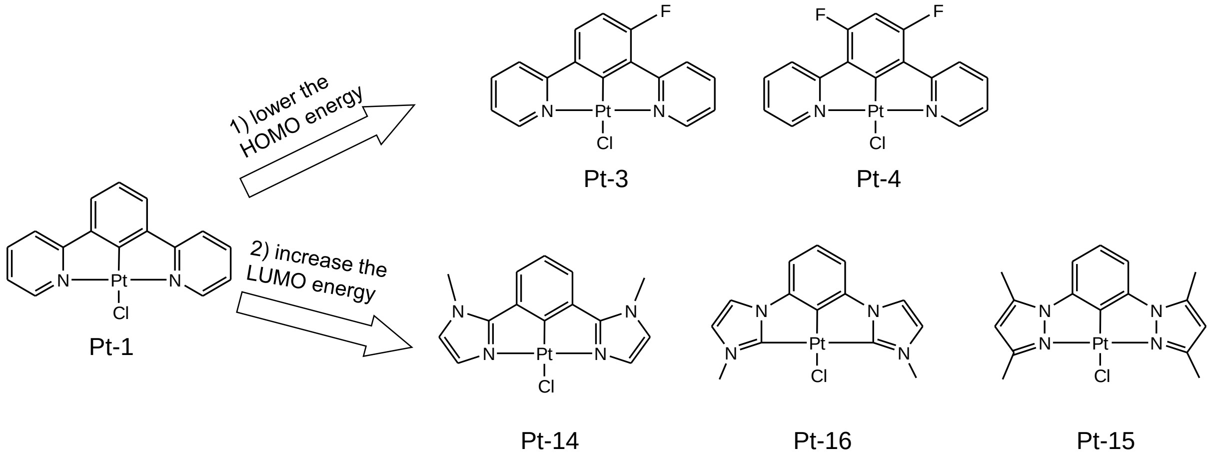

Figure 46. Materials design and chemical structures of tridentate platinum-based blue phosphorescent emitters

Similar to the reported color tuning strategy on the (C^N)Pt(acac) complexes,[101] the maximum emission wavelength (λ_{max}) of Pt-1 analogs can be shifted to the shorter wavelength range by ether stabilizing the highest occupied molecular orbital (HOMO) through the fluorination of the phenyl ring as in platinum(II) 1-fluoro- 2,4-di(2-pyridinyl)benzene chloride (Pt-3) and platinum(II) 1,3-difluoro-4,6-di(2-pyridinyl)benzene chloride (Pt-4) (Figure 46), or destabilizing the lowest unoccupied molecular orbital (LUMO) through the utilization of the electron accepting groups with higher reduction potential. Previously, an efficient blue phosphorescent OLED based on Pt-4 acheived a maximum EQE of 16%, yet the CIE coordinates (0.16, 0.26) are still unsatisfactory for a deep blue OLED.[156] Here, the pyridinyl groups of Pt-1 will be replaced with methyl-imidazolyl group or pyrazolyl group, which could potentially increase the LUMO energy level of Pt complexes, resulting in blue-shifted emission spectra. Although deep blue Ir-based emitters like Ir(dbfmi) utilize the ligands of phenyl-3-methylimidazolium and its analogs,[141] (C^N)Pt(acac) complexes incorporated with such ligands did not appear to have comparable device performance to their Ir analogs.[150] Moreover, the development of Pt(N^C^N)Cl analogs employing such cyclometalating ligands required much more synthetic efforts than that of their Ir analogs. Here, I report the synthesis, photophysics and device characterization of a series of blue-emitting Pt complexes employing such cyclometalating ligands.

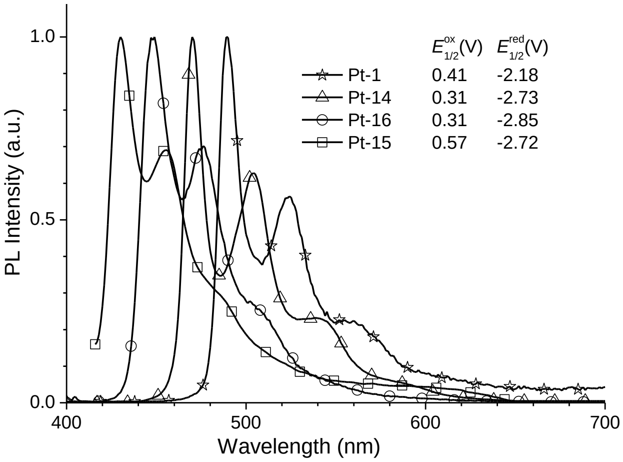

Figure 47. Room temperature emission spectra of Pt-1 (stars), Pt-14 (triangles) and Pt-16 (circles) in CH2Cl2 and Pt-15 (squares) in a 2%-doped PMMA film. Redox values (V) are shown in the inset, which are reported relative to Fc/Fc+

Devices employing Pt-4, Pt-14, Pt-15 and Pt-16 as emitters were fabricated on glass substrates pre-coated with a patterned transparent indium tin oxide (ITO) anode using a general structure of ITO/PEDOT:PSS/NPD(30 nm)/TAPC(10 nm)/2% emitter:26mCPy(25 nm)/PO15(40 nm)/LiF/Al. Prior to organic depositions, the ITO substrates were cleaned by sonication in water, acetone, and isopropanol followed by UV-ozone treatment for 15 minutes. PEDOT:PSS was filtered through a 0.2 μm filter and spin-coated on the precleaned substrates, giving a 40 nm thick film. Organic materials were thermally evaporated at deposition rates of 0.5 to 1.5 Å/s at a working pressure of less than 10^{-7} Torr. The deposition rates and thicknesses were monitored by quartz crystal microbalances. A thin 1 nm LiF layer was deposited at rates of <0.2 Å/s. Aluminum cathodes were deposited at rates of 1-2 Å/s through a shadow mask without breaking vacuum. Individual devices had areas of 0.04 cm^2. All device operation and measurement were carried out inside a nitrogen-filled glove-box. I-V-L characteristics were taken with a Keithley 2400 Source-Meter and a Newport 818 Si photodiode. EL spectra were taken using the Jobin Yvon Fluorolog spectrofluorometer. Agreement between luminance, optical power and EL spectra was verified with a calibrated Photo Research PR-670 Spectroradiometer with all devices assumed to be Lambertian emitters.

The electrochemical properties of Pt-14, Pt-15, and Pt-16 were examined using cyclic voltammetry. Compared with Pt-1, the changes of the electron-accepting groups modify the reduction potential of the Pt complexes and leave the oxidation potential largely unaffected. Thus, the reduction potentials of these three Pt complexes are in the range between -2.7 and -2.8 V vs. Fc/Fc^+, which are much higher than that of Pt-1 (Figure 47 inset). The comparison of room temperature emission spectra of Pt-1, Pt-14, Pt-15 and Pt-16 is presented in Figure 47, which were taken from the samples in a dilute solution of dicholoromethane for Pt-1, Pt-14 and Pt-16, and a doped thin film sample for Pt-15. Although all three synthesized Pt complexes have similar oxidation and reduction potentials, their emission energies are significantly different. The λ_{max} values of Pt-14, Pt-16 and Pt-15 are 470, 448 and 430 nm respectively. Both Pt-14 and Pt-16 emit strongly in a degassed solution at the room temperature, making them suitable as emitters for blue phosphorescent OLEDs. On the other hand, Pt-15 was weakly emissive in degassed solution and only provided a measurable photoluminescent spectrum in a 2%-doped PMMA film. For Pt-15, the poor quantum yield of emission can be attributed to a combined result of an accelerated high non-radiative decay rate and a low radiative decay rate, similar to its reported analogs like *fac*-Ir(ppz)$_3$ and Pt(dpzt)Cl [11].[106,157]

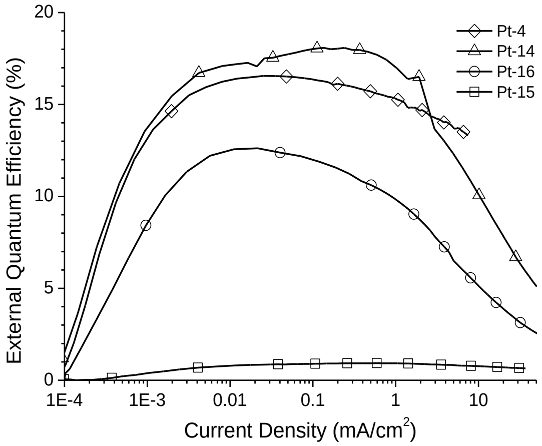

Figure 48. External quantum efficiency-current density characteristics for Pt-4 (diamonds), Pt-14 (triangles), Pt-16 (circles) and Pt-15 (squares) devices with the structure of ITO/PEDOT:PSS/NPD(30 nm)/TAPC(10 nm)/2% emitter:26mCPy(25 nm)/PO15(40 nm)/LiF/Al.

The EQE values are plotted vs. current density for devices employing Pt-4, Pt-14, Pt-15 and Pt-16, in Figure 48, with the corresponding EL spectra and CIE coordinates displayed in Figure 49. A summary of device performance is presented in

Table **3**. The dopant concentration is controlled to be around 2%(w/w) to minimize the formation of excimers which tend to broaden the EL spectrum of device and increase the values of CIE coordinates.[158]

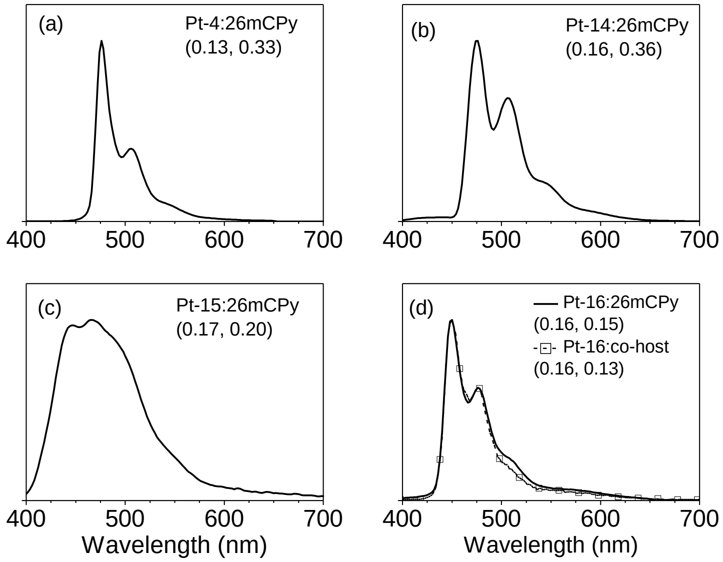

Figure 49. Normalized electroluminescent spectra, accompanied by CIE values of (a) Pt-4, (b) Pt-14, (c) Pt-15 and (d) Pt-16 devices at 1mA/cm^2. The general device structure is ITO/PEDOT:PSS/NPD(30 nm)/TAPC(10 nm)/2% emitter: host(25 nm)/PO15(40 nm)/LiF/Al. The host materials could be ether 26mCPy or co-host of TAPA:PO15 (1:1).

Due to the use of a better hole blocking layer (PO15) and electron blocking layer (TAPC) than those reported in a previous Pt-4 device, the Pt-4 device has demonstrated an improved device efficiency (close to 17%) with a similar EL spectrum. This improvement indicates a good confinement of dopant excitons inside of emissive layer, and affirms that the triplet energy of host material (26mCPy) is suitable for the emitters. Similarly, both Pt-14 and Pt-16 devices have demonstrated high EQE values of over 10% and obtained EL spectra resembling their emission spectra in solution, confirming the fact that the EL spectra are generated exclusively from the emitters themselves. Pt-14 can be used as an efficient phosphorescent emitter to fabricate a “blue-green” emitting OLED with a maximum EQE of over 18% and CIE coordinates of (0.16, 0.36). The CIE coordinates of Pt-16 device are (0.16, 0.15), making Pt-16 a perfect candidate as a deep blue phosphorescent emitter. Moreover, it is worth mentioning that 26mCPy,[126] a carbazole-based host material with an estimated triplet energy of 2.9 eV can be used for deep blue phosphorescent OLEDs if the emitter is judiciously designed. On the other hand, although Pt-15 has a higher emission energy than Pt-16 and can provide an EL spectrum with more desirable CIE coordinates, the Pt-15 device has a maximum EQE of less than 1%. The EL spectrum is broader than the PL spectrum of doped thin film, indicating that the EL spectrum is not generated exclusively from the emitter itself, resulting in a decrease in device efficiency. Thus, the extremely low efficiency of the Pt-15 device can possibly be attributed to the combined results of its low emission efficiency and the use of host materials without high enough triplet energy. Further studies suggest that the utilization of ultra-high bandgap host materials like UGH2 failed to significantly improve the efficiency of the Pt-15 devices.[159]

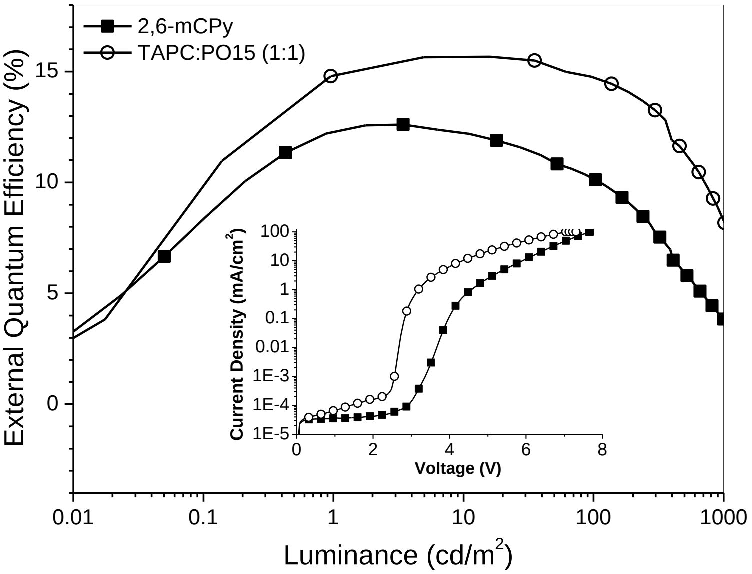

Figure 50. External quantum efficiency-lluminance and current density-voltage (inset) characteristics for the Pt-16 devices with different host materials: 26mCPy and co-host of TAPC:PO15 (1:1). The general device structure is ITO/PEDOT:PSS/NPD(30 nm)/TAPC(10 nm)/2% Pt-16:host(25 nm)/PO15(40 nm)/LiF/Al.

In order to improve the performance of the Pt-16 devices, a co-host system was utilized to further resolve any potential charge carrier imbalance in the emissive layer. A mixed layer of TAPC:PO15 is documented as one example,[130] which can replace 26mCPy as host materials in a similar device setting. Forward viewing external quantum efficiency vs. luminance and current density vs. voltage (inset) are plotted for the device of ITO/PEDOT:PSS/NPD(30 nm)/TAPC(10 nm)/2% Pt-16:TAPC:PO15(25 nm)/PO15(40 nm)/LiF/Al in Figure 50. A maximum forward viewing EQE of η_{ext}=15.7% was achieved at a current density of J=0.02 mA/cm^2, and only decreases to a half of its peak value at a current density of J=10.9 mA/cm^2. This device also gives a maximum forward power efficiency of η_p=22 lm/W and remains at a high η_p=19.3 lm/W at a practical luminance (100 cd/m^2). Moreover, the co-host system modified solubility, and thus the molecular packing, of Pt-16 in the emissive layer, resulting in a significant decrease in excimer and aggregate formation and attenuated vibronic features of Pt-16 emission bands (Figure 49). Such small changes in the EL spectrum yielded highly desirable CIE coordinates of (0.16, 0.13) for the Pt-16 devices, which also demonstrated an independence of current density. The color quality of the Pt-16 device is comparable or even superior to the best deep blue phosphorescent OLEDs which focus on the use of Ir-based complexes. Although the maximum EQE of the Pt-16 device is lower than that of the Ir(dbfmi) device, the Pt-16 device can maintain an EQE of 14.8% at 100 cd/m^2 and an EQE of 8.3% 1000 cd/m^2 due to a small roll-off at a high current density. On the other hand, the EQEs of the Ir(dbfmi) device are 13.3% at 100 cd/m^2 and 6.2% at 1000 cd/m^2.[141]

Table 3. A summary of device characteristics for the structure: ITO/NPD(30 nm)/TAPC(10 nm)/EML(25 nm)/PO15(40 nm)/LiF/Al. Each device is listed by its emissive layer at a luminance of 100 cd/m^2. Parameters listed are driving voltage (bias), current density, forward viewing external quantum efficiency (EQE), CIE coordinates and power efficiency (P.E.).

Emissive Layer	Bias [V]	Current Density [mA/cm^2]	EQE [%]	CIEx	CIEy	P.E. [Lm/W]
2% Pt-4:26mCPy	5.1	0.35	15.9	0.13	0.33	17.4
2% Pt-14:26mCPy	5.2	0.24	18.1	0.16	0.36	23.3
2% Pt-15:26mCPy	7.8	25.7	0.68	0.17	0.20	0.16
2% Pt-16:26mCPy	4.5	0.81	10.1	0.16	0.15	8.96
2% Pt-16:co-host	3.0	0.51	14.8	0.16	0.13	19.3

The OLED utilizing Pt-16 with a maximum EQE of 15.7% and CIE coordinates of (0.16, 0.13) represens a significant step in the development of efficient and deep blue OLEDS. Compared with their Ir-based analogs, Pt(N^C^N)Cl complexes can display a “deeper blue” color with similar emission energy due to their narrower emission bandwidth and attenuated vibronic features of their emission spectra. It is also very encouraging to demonstrate that carbazole-based host materials can be used as host materials for efficient deep blue phosphorescent OLEDs. Moreover, Pt-16 is a fluorine-free blue phosphorescent emitter indicating that its design is aligned with molecules that have demonstrated stability for long operational lifetime.[143] However, further work is needed to develop stable and efficient deep blue phosphorescent emitters for displays and lighting applications.

6.4 Tetradentate Deep Blue-Emitting Cyclometalated Platinum(II) Complexes

In order to develop a stable and efficient class of deep blue emitters it is desirable to replace fluorine containing cyclometalating ligands, with other classes of ligands for improved electrochemical stability.[143,160] An example of such a class of materials is metal complexes cyclometalated with the 2-phenyl-methylimidazole (pmi) ligand and related analogues that are coordinated to the metal through a neutral carbene. Several Ir complexes have been reported to have efficient deep blue phosphorescent emission at room temperature, including mer-tris(N-dibenzofuranyl-N-methylimidazole) iridium(III) [Ir(dbfmi)],[141] tris(1-cyanophenyl-3-methylimidazolin-2-ylidene-C,C2') iridium(III) [Ir(cnpmic)],[139] and mer-tris(phenyl-methyl-benzimidazolyl) iridium(III), [m-Ir(pmb)$_3$].[140] However, these complexes suffer from either long luminescent decay or relatively low quantum efficiency compared to Ir complexes based on the cyclometalated 2-phenylpyridine ligand that have quantum efficiency (Φ) of 0.8-1 and luminescent lifetime (τ) of 1-5μs.[125] This difference can be attributed to the combined effects of a high non-radiative decay rate (k_{nr}) and low radiative decay rate (k_r) which are dictated by the intrinsic properties of the selected metal complex system.[161] Thus, it will be highly desirable to identify rational design motifs that can improve the luminescent properties of deep blue phosphorescent emitters.

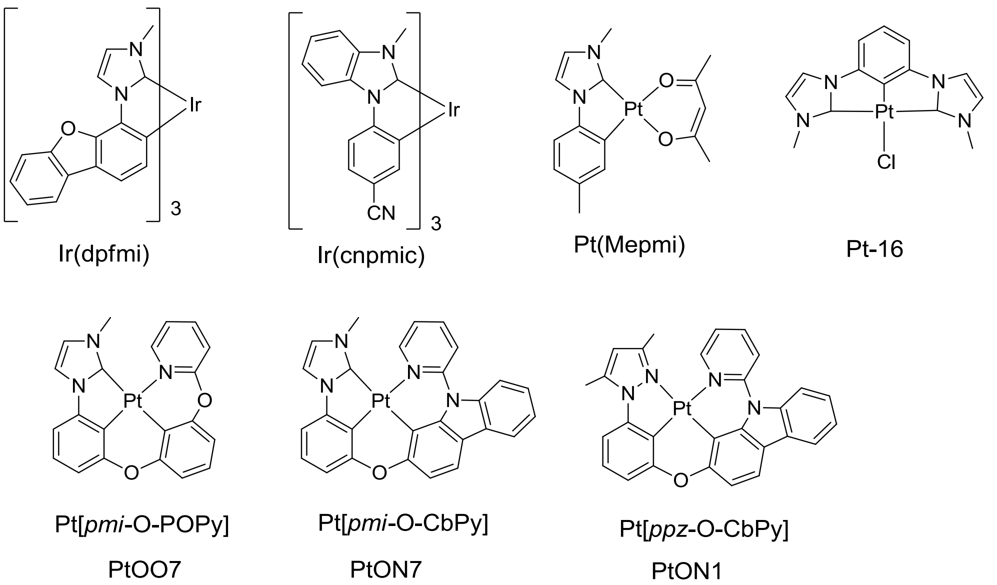

Ir(dpfmi)

Ir(cnpmic)

Pt(Mepmi)

Pt-16

Pt[*pmi*-O-POPy]
PtOO7

Pt[*pmi*-O-CbPy]
PtON7

Pt[*ppz*-O-CbPy]
PtON1

Figure 51. Chemical structures of cyclometalated Ir and Pt complexes

Compared to Ir analogues, there are relatively few reports on platinum complexes cyclometalated with phenylimidazole carbene ligands.[146] However, platinum(II) bis(methyl-imidazolyl)benzene chloride (Pt-16), has demonstrated impressive device performance with a maximum external quantum efficiency (EQE) of 15.7% and Commission Internationale de L'Éclairage (CIE) coordinates of (0.16, 0.13). Moreover, Pt(II) complexes can provide additional structural variation owing to the square planar configuration allowing ligands to be designed that are bidentate, tridentate and tetradentate.[147] These variations can significantly alter the ground and excited state properties of Pt complexes. Thus, a new class of Pt complexes with tetradentate ligands are synthesized and demonstrate higher luminescent quantum yield and faster radiative decay process than published Ir carbene analogues. The complexes have a conventional cyclometalated fragment bridged with oxygen to an LL' chelating group, where LL' is an ancillary chelate, such as, phenoxyl pyridine (POPy) or carbazolyl pyridine (CbPy). The structures of Pt[pmi-O-POPy], Pt[pmi-O-CbPy], and Pt[ppz-O-CbPy] are shown in Fig. 1, which are denoted as PtOO7, PtON7, and PtON1.

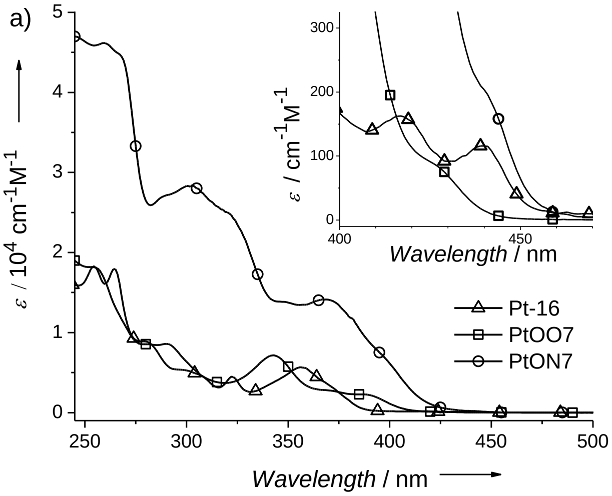

Figure 52. The comparison of room temperature absorption spectra of Pt-16, PtOO7 and PtON7 in CH_2Cl_2. The T_1 absorption transitions are shown in the inset of part

The absorption spectra for Pt-16, PtOO7 and PtON7 are shown in Figure 52. All complexes exhibit very strong absorption bands below 300 nm assigned to $^1\pi$-π^* transitions localized on the cyclometalating ligands (^{1}LC). The intense bands in the 300-420 nm region are attributed to metal to ligand charge transfer (^{1}MLCT) transitions. Weaker absorption bands between 420-450 nm can be identified as the triplet absorption on the basis of the small energy shift between absorption and emission at room temperature. Compared to the tridentate structure, Pt-16, both PtOO7 and PtON7 demonstrate stronger MLCT transitions at longer wavelengths (between 380-410 nm). Moreover, both PtOO7 and PtON7 possess a less resolved triplet absorption band (Figure 52 inset). Among the three Pt complexes, PtON7 demonstrates the most intense absorption for all of three types of transitions (^{1}LC, ^{1}MLCT and$S_0 \rightarrow T_1$).

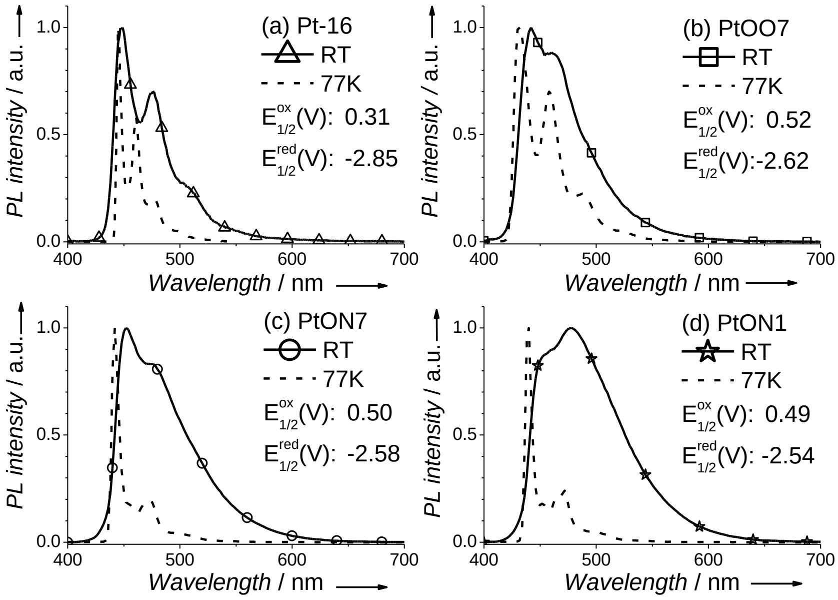

Figure 53. The emission spectra of (a) Pt-16, (b) PtOO7, (c) PtON7, and (d) PtON1 in solution at room temperature and 77K with the redox potentials for each compound are given in the legends.

The room temperature and low-temperature (77 K) solution emission spectra and solid state emission spectra at 5 wt% in an optically inert polymethylmethatcrylate (PMMA) matrix were recorded for both PtOO7 and PtON7 and their analogues (Table 1 and suplemental materials). The emission spectra for Pt-16, PtOO7, PtON7, and PtON1 at room temperature and 77 K are shown in Figure 53. Unlike literature reported bidentate Pt(Mepmi) and tridentate Pt-16 which have structured luminescent spectra displaying resolved vibronic progressions,[146,150] both PtOO7 and PtON7 have a less vibronically structured room temperature emission spectra, resembling their Ir analogs, e.g. tris-cyclometalated Ir(dpfmi) and Ir(cnpmic).[139,141] Moreover, both PtOO7 and PtON7 have much greater radiative decay rates ($> 20 \times 10^4$ s^{-1}) than Pt and Ir analogues with similar emitting ligands reported in the literature (Table 1). The less resloved T_1 absorption band, supressed vibronic structure in the room temperature solution emission spectra and faster radiative process indicate tetradentate Pt complexes like PtON7 may have more ^{1}MLCT/^{3}MLCT character in their lowest excited states.[62] This can be attibuted to the structural changes of metal complexes by adding the ancillary POPy and CbPy chelates. Between the two structures described here, PtON7 has much lower non-radiative decay rate than PtOO7, resulting in a higher quantum efficiency (0.89). Therefore PtON7 is considered a desireable candiate as a blue emissive material for OLED applications.

Table 4. Photophysical properties of PtON7 and their analogs in a doped PMMA film, except a) PO9 film.

Complex	λ_{max} (nm)	Φ(%)	τ (μs)	k_r ($\times 10^4$ s^{-1})	k_{nr} ($\times 10^4$ s^{-1})
PtON7	452	89	4.1	21	2.6
PtOO7	442	58	2.5	23	17
Pt-16	450	32	5.1	6.3	13.3
Pt(Mepmic)[150]	419	20	25	0.8	3.2
Ir(cnpmic)$_3$[139]	425(sh), 450	78	19.5	4	1.1
Ir(dbfmi)[141]	445	70[a]	19.6	3.6	1.5
PtON1	449	85	4.5	19	3.3

Devices employing Pt-16, PtOO7, and PtON7 as emitters were fabricated in the following device structure (Type I): ITO/PEDOT:PSS/NPD (30nm)/TAPC (10nm)/2%

emitter:26mCPy (25nm)/ PO15 (40nm)/ LiF/Al. NPD is N,N′-diphenyl-N,N′-bis(1-naphthyl)-1,1′-biphenyl-4,4″-diamine, TAPC is di-[4-(N,N-ditolyl-amino)-phenyl]cyclohexane, 26mCPy is 2,6-bis(N-carbazolyl)pyridine, and PO15 is 2,8-bis(diphenylphosphoryl) dibenzothiophene.[130] The corresponding EL spectra and CIE coordinates for each device are displayed in Figure 54a-b, and EQE vs. current density plots are shown in Figure 54d. A summary of device performance at the brightness of 100 cd/m^2 and 1000 cd/m^2 are presented in Table 5. Unlike tridentate Pt-16, PtON7 and PtOO7 do not show evidence of excimer formation. Both PtON7 and PtOO7 devices demonstrate EL spectra similar to their room temperature solution emission spectra, confirming that the EL spectra are generated exclusively from the emitters themselves. The CIE coordinates of the PtON7 device are (0.14, 0.19) and its peak device efficiency exceeds 16%.

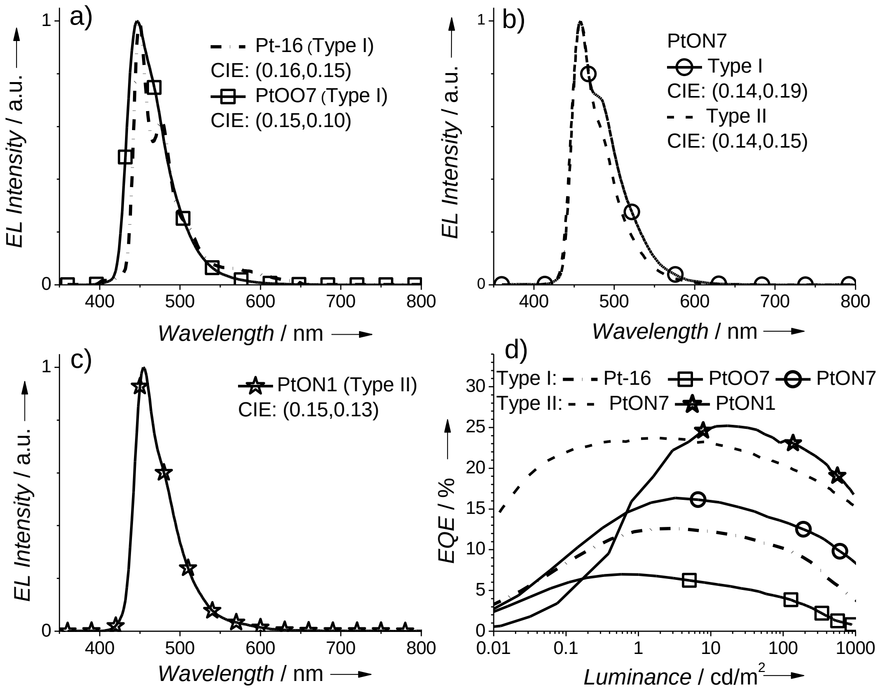

Figure 54. (a)-(c) Plots of electroluminescent spectra for Pt-16, PtOO7, PtON7, and PtON1 based devices with corresponding CIE coordinates. (d) Plots of external quantum efficiency (EQE) vs. current density for devices of the various emitters. Device Type I: PEDOT:PSS/NPD/TAPC/ 26mCPy:emitter(2%)/PO15/LiF/Al and Device Type II: ITO/HATCN/ NPD/TAPC/26mCPy:emitter(6%)/DPPS/LiF/Al. The EL spectra were measured at 100 cd/m^2.

PtON7 device performance was further improved by increasing the dopant concentration and using a different hole injection material, 1,4,5,8,9,11-hexaazatriphenylene-hexacarbonitrile (HATCN) and a different electron-transporting material, diphenyl-bis[4-(pyridin-3-yl)phenyl]silane (DPPS). Despite the weak electron transporting capabilities of DPPS, its high bandgap and deep HOMO level has allowed demonstrated performance of nearly 100% IQE for deep blue emitting devices.[119] Through the device structure (Type II), ITO/HATCN(10 nm)/NPD(40 nm)/TAPC(10 nm)/6% PtON7:26mCPy(25 nm)/DPPS(40 nm)/LiF/Al, a maximum forward viewing EQE of η_{ext}=23.7% was achieved at a luminance of 2 cd/m^2 and only decreases to 20.4% and 15.4% at 100 and 1000 cd/m^2 respectively. This device also gives a maximum forward power efficiency of η_p=26.9 lm/W but drops to η_p=16.8 lm/W at 100 cd/m^2 which is attributed to the weak electron transporting capabilities of DPPS. Moreover, a narrower EL spectrum was observed yielding highly desirable CIE coordinates of (0.14, 0.15) for the PtON7 devices. A similar improvement was observed for phenylpyraole-based Pt complexes such as PtON1 (Figure 51, Figure 53, Figure 54, Table 1 and Table 2) reaching a maximum forward viewing EQE of η_{ext}=25.2%. The color quality and device efficiency of the PtON7 and PtON1 devices are better than the best reported deep blue phosphorescent OLEDs with fluorine-free Ir-based complexes (a maximum EQE of 18.6% and CIE coordinates of (0.15, 0.19) for the Ir(dbfmi) device) in a similar device setting.[141] Furthermore, PtON7 and PtON1 device performances are also comparable or superior to the best reported deep blue phosphorescent OLEDs, which employed the fluorinated complex, iridium(III) bis(3´,5´-difluoro-4´-cyanophenyl-pyridinato-N,$C^{2´}$) picolinate (FCNIrpic) as an emissive material (a maximum EQE of 24.2% and CIE coordinates of (0.14, 0.20).[115] It is also notable that 26mCPy, a carbazole-based host materials with an estimated triplet energy of 2.9 eV, can be used for deep blue phosphorescent OLEDs.

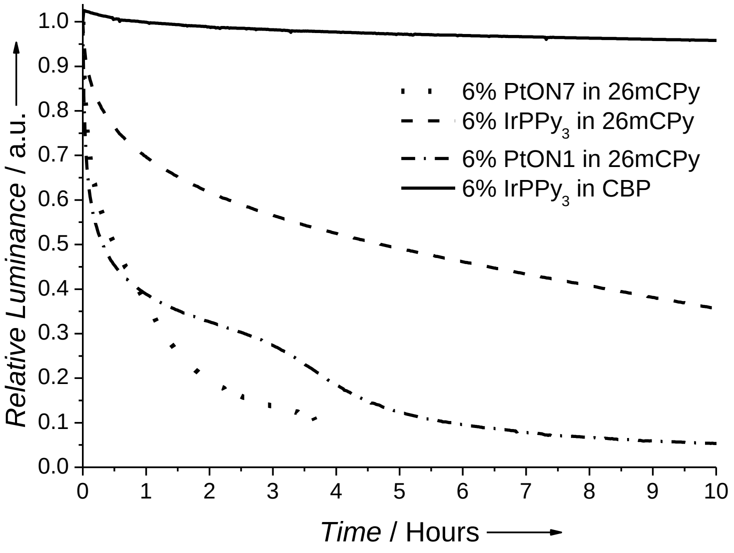

Figure 55. Plot of relative Luminance vs. Time (hours) for Ir(ppy)$_3$ (dashed), PtON7 (dotted), and PtON1 (dash-dot) based devices with the structure ITO/HATCN/NPD/TAPC/6% emitter:26mCPy/DPPS/LiF/Al. Also plotted are the lifetime data for the device: ITO/HATCN/NPD/6%Ir(ppy)$_3$:CBP/ BAlq/Alq/LiF/Al. (solid). The devices are run at a constant current of 2mA/cm^2.

The best devices of PtON7 and PtON1 (Type II) were also tested for device lifetime at 2 mA/cm^2 which corresponds to a normal operational brightness in the range of 400-500 cd/m^2. For comparison, devices were fabricated with the stable and efficient green emitter, fac-Ir(ppy)$_3$, in the same structure as well as the known stable structure: ITO/HATCN(10 nm)/NPD(40 nm)/6% Ir(ppy)$_3$:CBP(25 nm)/ BAlq(10 nm)/Alq(40 nm)/LiF/Al, where CBP is 4,4'-bis(N-carbazolyl) biphenyl, BAlq is bis(2-methyl-8-quinolinolato) (biphenyl-4-olato)aluminum, and Alq is tris-(8-hydroxyquinoline) aluminum.[132] In Figure 55, the relative luminance versus time is plotted for 10 hours of constant operation. It is encouraging that the devices of both PtON7 and PtON1 retained a significant percentage of their initial luminance for over an hour and in particular, that PtON1 emitted a non-negligible relative luminance up to 10 hours. Furthermore, it is evident from the comparison of Ir(ppy)$_3$ devices between the two structures that the reduced device lifetimes in the Type II devices can be greatly attributed to the degradation of either the electron or hole blockers, TAPC and DPPS respectively, or the 26mCPy host. Therefore, it is challenging to create any significant conclusions about the stability of these complexes until stable host and charge blocking materials are developed for deep blue phosphorescent devices. Thus, more efforts towards using these phosphorescent emitters with stable hosts and blockers are necessary and improvement of more than two orders of magnitude in device operational lifetime can be expected.

Table 5. A summary of device characteristics at 100 cd/m^2 and 1000 cd/m^2 for the devices with two different structures. Device type I: PEDOT:PSS/NPD/TAPC/ 26mCPy: emitter(2%)/PO15/LiF/Al. Device type II: ITO/HATCN /NPD/TAPC /26mCPy: emitter(6%)/DPPS/ LiF/Al.

Device	Emitter	@100 cd/m^2				@1000 cd/m^2	
		CIEx	CIEy	EQE [%]	P.E. [Lm/W]	EQE [%]	P.E. [Lm/W]
I	Pt-16	0.16	0.15	10.1	9.0	3.8	2.4
I	PtOO7	0.15	0.10	4.1	3.7	0.5	0.25
I	PtON7	0.14	0.19	13.5	14.3	8.35	6.6
II	PtON7	0.15	0.14	20.4	16.8	15.4	10.2
II	PtON1	0.15	0.13	23.3	20.6	16.8	11.7

6.5 Narow band OLEDs

Despite the progress in efficiencies and color spanning the visible spectrum for both Ir and Pt complexes, most organic emissive materials exhibit broad emission, with full-width at half-maximum (FWHM) of photoluminescence (PL) spectra typically between 40 and 70 nm. This results in unsatisfactory emissive properties for certain optical applications which could hinder the further growth of organic electronic devices by compromising the colour purities in displays,[162] decreasing the outcoupling efficiency in resonant microcavity devices[163] and lowering the luminance efficacy rating (LER) of white OLEDs since the broad emission of many red emitters extends partially into the deep red and near infra-red range (beyond 650 nm).

In order to develop organic thin film devices with narrow-band EL spectra, current research efforts focus on developing various LEDs using colloidal quantum dots (QDs) as the emissive layers. For example, CdSe(ZnS) nanocrystal QDs can be continuously tunable crossing the visible spectrum, with a high PL quantum efficiency and a FWHM value less than 30nm, yet, the synthetic condition of QDs needs to be strictly controlled in order to prevent a larger particle size distribution and maintain a narrow emission spectral bandwidth.[162] Nevertheless, QD-based LEDs have progressed rapidly in the past decade with reported device efficiency over 18% for red LEDs[164] and reasonable device operational stability.[165] However, blue QD LEDs remain a big challenge due to the stringent constraints on the small particle size and uniformity. Typically, blue QD LEDs exhibit very low external quantum efficiencies of much less than 1%, although a few recent reports have demonstrated greater external quantum efficiencies, with the highest reported to date of 7.1%[166] which is much lower than state-of-the-art deep blue OLEDs (~20%). Additionally, there is no clear solution to solve the problem of poor interfacial energy barriers between QD emissive layers and organic transporting layers, and furthermore, the energy transfer processes at these interfaces remains poorly understood.

To overcome these inherent problems with QDs, it is desirable to fabricate OLEDs using an organic emitter with a narrow emission spectral bandwidth (or a narrow-band emission). A narrow-band emission spectrum can be easily achieved if the radiative decay process originates from atomic excited states as in lanthanide complexes, in which the emission bands as well as absorption bands (f-f transitions) are extremely sharp, in the range of 10-15 nm.[167] However, these emitters have not demonstrated high electron-to-photon conversion efficiency in devices due to inefficient energy transfer from organic ligand to lanthanide metal ions as well as poor energy transfer process between host materials and lanthanide based emitters.[168] Similarly, rigid macrocyclic complexes like 2,3,7,8,12,13,17,18-octaethyl-21H,23H-porphine platinum(II) (PtOEP) have also demonstrated narrow-band emission with a FWHM of around 20 nm.[59] Although PtOEP demonstrated early promise as a phosphorescent emitter for OLEDs, further development has been hindered by its long-lived triplet lifetime (in the range of 100 μs) and large difficulty in structural modification for colour-tuning of porphine materials. On the other hand, cyclometalated Ir and Pt complexes have high luminescent quantum yields and comparatively short phosphorescent lifetimes due to strong spin-orbit coupling, making them ideal emissive dopants in OLEDs. By harvesting all the electro-generated triplet and singlet excitons, carefully designed devices have demonstrated emission with nearly 100% internal quantum efficiency (IQE).[96] One outstanding issue with this class of complexes, however, is that they typically exhibit broad emission spectra making them non-ideal for display applications. Thus, it will be extremely desirable to further develop cyclometalated Ir and Pt complexes having small FWHM values with a judicious molecular design in order to develop efficient organic EL devices with narrow-band emission tunable across the visible spectrum.

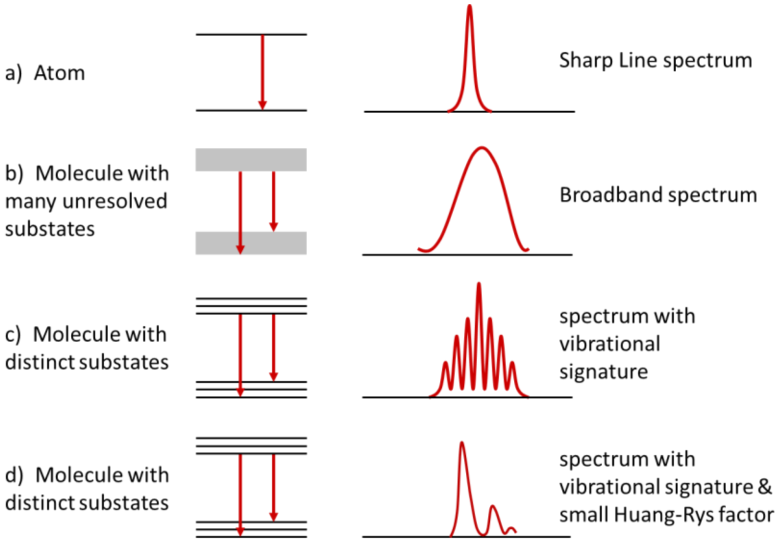

Figure 56. (a) Sharp-line emission spectrum for atoms at low pressure in the vapor phase; (b) Broadband emission spectrum for certain rigid molecules; (c) Structureless broadband emission spectrum for normal organic molecules in solvents; (d) Narrowband emission spectrum for certain rigid molecules with small Huang-Rys factors.

The shape and spectral bandwidth of the emission and absorption spectra of phosphorescent emitters are directly determined by the properties of the ground state and the lowest excited state. To achieve narrow bandwidth it is preferred to have a single dominant peak which has narrow atomic-like radiative transitions as exemplified in Figure 56a. It is well documented that the luminescence from cyclometalated Ir(III) and Pt(II) complexes originates from the lowest triplet excited (T_1) state that is a ligand centered charge transfer state (^{3}LC) with metal-to-ligand-charge-transfer characters (^{1}MLCT/^{3}MLCT) mixed in through spin–orbit coupling. At room temperature most of these complexes exhibit either broad Gaussian-shape emission, if the T_1 state has a majority of ^{3}MLCT character (Figure 56b),[99] or have an emission spectrum with vibronic features, when its T_1 state mainly consists of ^{3}LC characters (Figure 56c);[62] neither of which are conducive to narrow band emission. However, if an emitter has a rigid molecular structure with a single dominant vibrational stretch, it will show an emission spectrum with more defined vibronic features. Moreover, if the Huang-Rys factor (S_M),[62] which is approximated by the intensity ratio of the first major vibrational transition to the highest energy peak, is minimized, the emission spectrum of phosphorescent emitters will have much smaller FWHM values (Figure 56d), resembling to the emission spectrum of QDs.

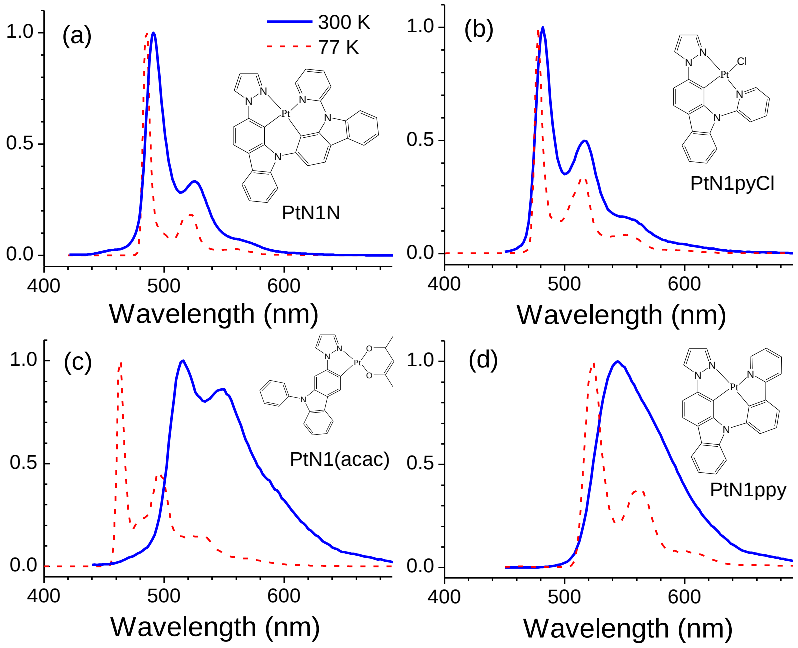

Figure 57. The emission spectra and chemical structures (inset) for (a) PtN1N, (b) PtN1pyCl, (c) PtN1(acac) and (d) PtN1ppy at room temperature (solid line) and 77 K (dot line).

Following this proposed molecular design principle, PtN1N is prepared as a green-emitting phosphorescent emitter with a FWHM of 18 nm and a S_M value of 0.3 at room temperature. The chemical structure of PtN1N is illustrated in the inset of Figure 57, where the tetradentate cyclometalating ligand is designed to include a rigid ligand of pyrazolyl-carbazole (functioning as a lumophore) bonded to pyridyl-carbazole (functioning as an ancillary ligand). The choice of ancillary ligands needs to be carefully selected in order to prevent the localization of the T_1 state on the ancillary ligand and minimize the S_M value by controlling the properties of the T_1 state. The room temperature and 77 K emission spectra of PtN1N and its analogs are shown in Figure 57. Due to the selection of similar lumophores, both PtN1pyCl and PtN1acac have similar emission spectra at 77K to PtN1N in terms of emission energies and vibronic spacing energies of the emission spectra. The room temperature and 77 K emission spectra of PtN1ppy, however, are drastically different, which indicates a different T_1 state for PtN1ppy due to its improper choice of ligands bonded to the designated lumophore. Despite their similar emission energies, PtN1acac has a much larger S_M value (0.4) than those of PtN1N (0.2) and PtN1pyCl (0.3) at low temperature. Such a difference can be attributed to the different properties of the T_1 states, which are affected by the degree of ^{1}MLCT characters mixed with ^{3}LC characters and can be related to the selection of cyclometalating ligand. Moreover, a larger variation in their emission spectra was observed at the room temperature for these three compounds. In addition to its narrow-band emission, the tetradentate Pt complex, PtN1N, also has a higher emission quantum yield ($\Phi = 0.81$) than its bidentate analog, i.e. PtN1acac ($\Phi = 0.03$) and its tridentate analog, i.e. PtN1pyCl ($\Phi = 0.03$). Furthermore, the PL quantum efficiency of PtN1N in a doped PMMA film is experimentally determined to be 0.90 ± 0.05, close to unity.

Table 6. Photophysical properties of PtN1N and its analogs in a solution of dicholoromethane at room temperature and in a solution of 2-methyl THF at 77 K.

Complex	Emission at RT				Emission at 77K	
	λ_{max} (nm)	FWHM (nm)	Φ (%)	τ (μs)	λ_{max} (nm)	τ (μs)
PtN1(acac)	516	75	3	9.9	464	74.5
PtN1pyCl	482	18	3	2.3	478	52.4
PtN1ppy	544	68	13	1.4	524	5.9
PtN1N	491	18	81	12.9	484	14.4
PtON7-t-Bu	446	20	83	6.6	439	8.2
PtN7N	510	18	61	10.9	503	12.3
PtN8ppy	573	26	40	3.4	564	7.7

To evaluate the electroluminescent properties of PtN1N, a series of OLEDs were fabricated in the device structure: PEDOT:PSS/NPD/TAPC/x% PtN1N:26mCy/PO15/BmPyPB/ LiF/Al, with the dopant concentration ranging from 2-14%. The EL spectra and forward viewing external quantum efficiency is plotted versus brightness for these devices in Figure 58a-d. Similar to the previously reported phosphorescent OLEDs, increasing the dopant concentration slightly lowers the driving voltage and exhibited a smaller efficiency roll-off as a result of improved charge carrier balance. Moreover, increasing high dopant concentration maintains high device efficiency and the 14% PtN1N device demonstrated an extremely high maximum forward viewing EQE of η_{ext}=25.6% at a brightness of 10 cd/cm^2, and only decreases slightly to η_{ext}=25.5% at a high forward viewing luminance of 100 cd/m^2. This device also gives a maximum forward power efficiency of η_p=66.5 lm/W and remains at a high η_p=48.5 lm/W at a practical luminance (100 cd/m^2) for displays. These efficiencies are among the highest reported for OLEDs without any outcoupling enhancement, representing an approximately 100% internal quantum efficiency. More importantly, the PtN1N retained the impressive narrow band emission in the device setting resulting in a FWHM value of only 18 nm for the 2% PtN1N device. Additionally, excimer emission was not observed at increased dopant concentrations and the EL spectra of PtN1N devices are not significantly broadening with FWHM values only increasing to 22 nm.

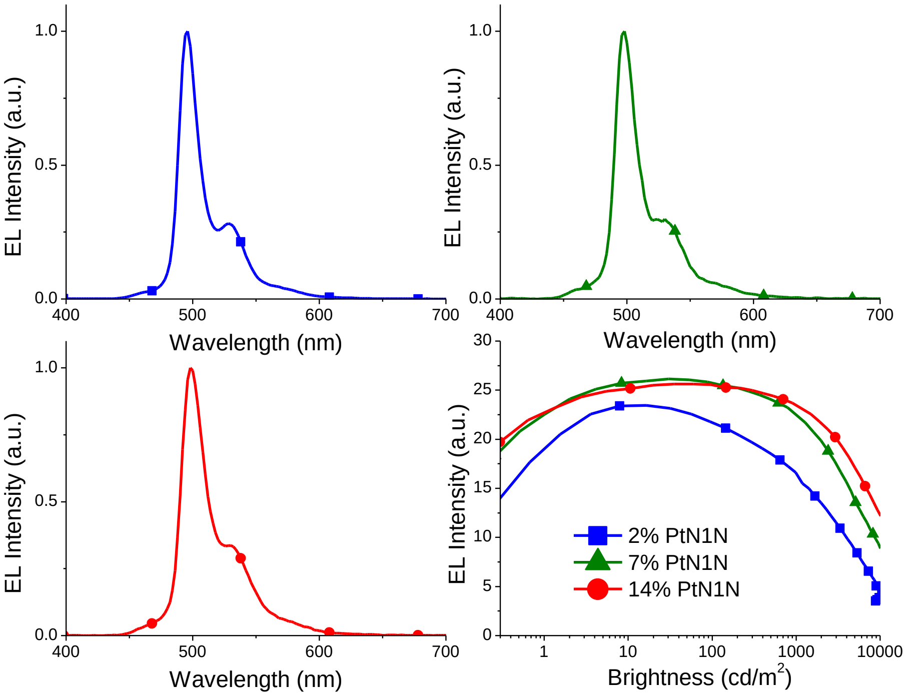

Figure 58. Plots of electroluminescent spectra (a-c) and (d) plots of external quantum efficiency vs. brightness for the devices of ITO/PEDOT:PSS/NPD/TAPC/x% PtN1N:26mCPy/PO15/BmPyPB/LiF/Al, where x = 2, 7, 14.

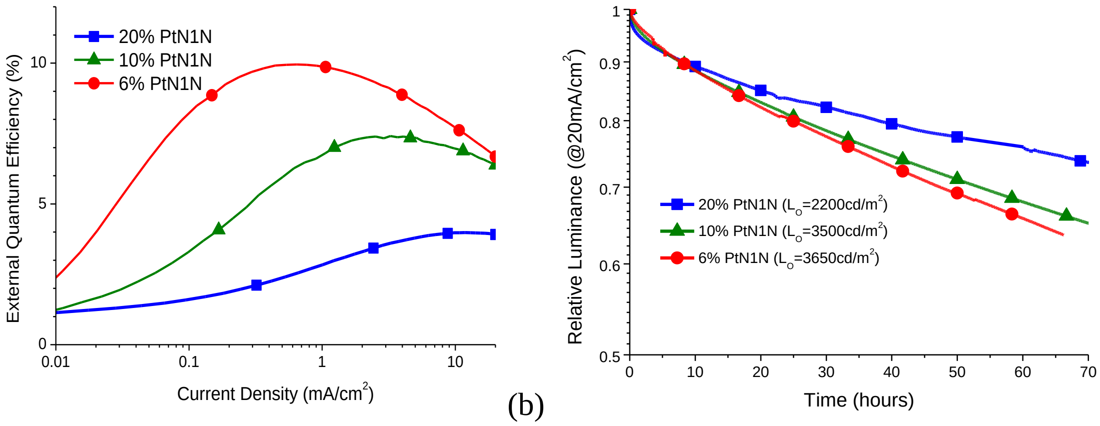

(a) (b)

Figure 59. Plots of (a) external quantum efficiency vs. current density and (b) luminance at constant current of 20 mA/cm^2 vs. operational time for the devices of ITO/HATCN/NPD/x% PtN1N:CBP/BAlq/Alq3/LiF/Al, where x = 6, 10, 20. The initial brightness of devices at 20 mA/cm^2 are presented in the inset of part (b).

The stability of PtN1N as a phosphorescent emitter was tested using a known stable device structure: ITO/HATCN(10 nm)/NPD(40 nm)/x% PtN1N:CBP(25 nm)/ BAlq(10 nm)/ Alq(40 nm)/ LiF/Al.[132] The device efficiency, shown in Figure 59, drops considerably compared to our previously optimized device due to the lack of state-of-the-art stable host and blocker materials. Thus, at any given current density the amount of light extracted from the device is significantly lower than in a more efficient structure but such devices will still provide valuable information on the electrochemical stability of PtN1N in a device setting which is a strong indication for the potential commercialization of such class of materials. Furthermore, due to poor charge balance in this stable structure and the lack of efficient charge and exciton confining materials, there is a large drop off in peak efficiency from 10.0% to 4% as the dopant concentration is increased from 6% to 20%, which ultimately yields lower lifetimes (when corrected for elevated initial luminance) for the devices with higher dopant concentrations. In Figure 59b, the relative luminance versus time is plotted for devices operated at a constant current of 20 mA/cm^2 which corresponds to an initial luminance (L_0) in the range of 2200-3550 cd/m^2. It is very encouraging to report that the lifetime at 70% initial luminance, LT_{70}, of 6%, 10%, and 20%-doped PtN1N devices are 46.5 hrs (L_0=3550 cd/m^2), 53.5 hours (L_0=3500 cd/m^2) and 70 hrs (L_0=2200 cd/m^2) respectively. This can be translated to a LT_{70} at 100 cd/m^2 of over 18,000 hrs for the 20% device and 32,000 hrs for the 10% device using the formula $LT(L_1)=LT(L_0)*(L_0/L_1)^{1.7}$,[169] which is approaching the requirement for potential commercialization at an early stage. Much improvement will be expected with the incorporation of more advanced host and blocking materials in optimized device architectures. This result is comparable to the best reported lifetimes for red emitting platinum complexes[170] and is a significant improvement from the previous report on blue or green platinum based emitters. Thus, this molecular design method should serve as a major step forward in the development of stable platinum based phosphorescent emitters for OLEDs applications.

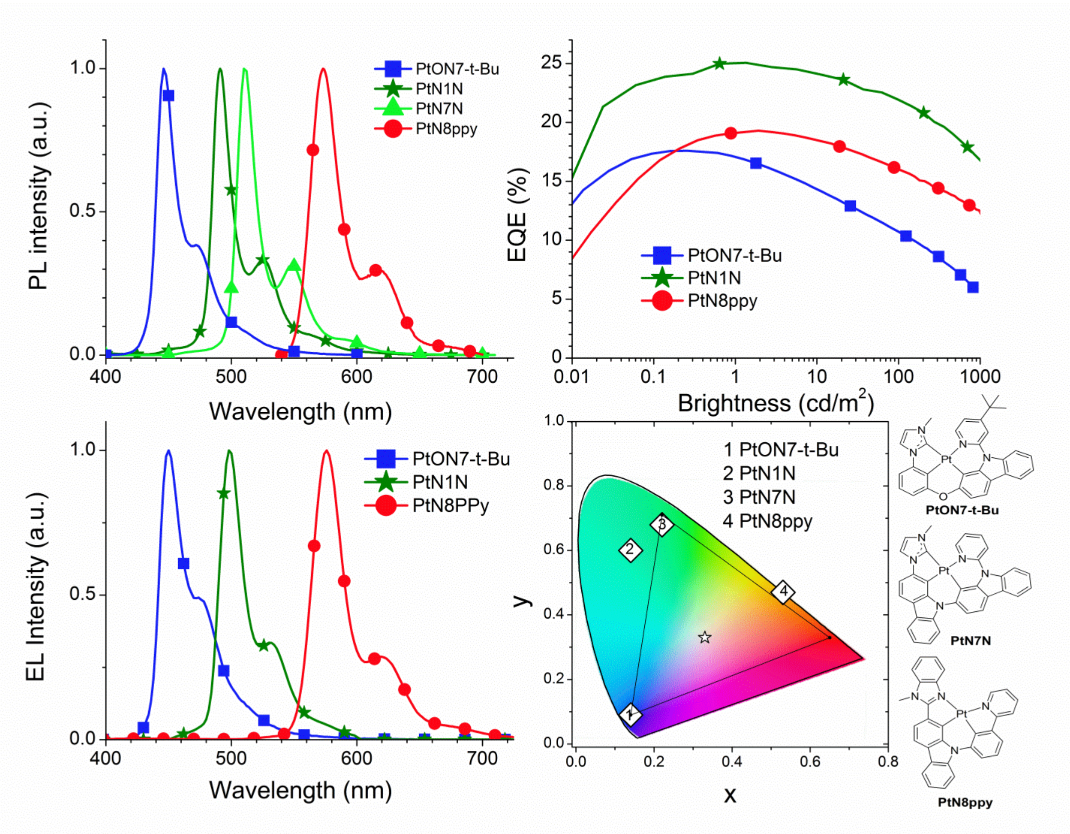

Figure 60. (a) Emission spectra of PtON7-t-Bu, PtN1N, PtN7N and PtN8ppy at room temperature. Plots of (b) external quantum efficiency vs. brightness, (c) electroluminescent spectra and (d) color coordinates of devices in CIE chromaticity diagram for PtON7-t-Bu, PtN1N and PtN8ppy in devices and CIE values of PtN7N calculated based on its room temperature emission spectrum in a solution of dichloromethane.

Following a similar materials design principle, a series of narrow-band phosphorescent emitters were developed with emission colours across the visible spectrum. Although the frame of the tetradentate cyclometalated complex structure is maintained, the lumophores were modified individually to phenyl methyl-imidizolyl group for blue-emitting PtON7-t-Bu, methyl-imidizolyl carbazolyl group for bright green-emitting PtN7N and benzo-methyl-imidizolyl carbazolyl group for orange-emitting PtN8ppy. Moreover, in order to ensure a narrow-band emission, the components of ancillary ligands were also modified accordingly to t-butyl-pyridyl carbazole for blue-emitting PtON7-t-Bu and phenyl-pyridine for orange-emitting PtN8ppy. The room temperature emission spectra and the chemical structures of PtON7-t-Bu, PtN7N and PtN8ppy are presented in the part (a) and (d) of Figure 60. The highly saturated colours from our developed narrowband phosphorescent emitters enable us to achieve the colour coordinates within proximity to the blue and green points in the CIE chromaticity diagram. Moreover, all of the Pt complexes have high quantum efficiency in solution (Table 1) and have also demonstrated high device efficiencies of close to 20% in the device settings for the deep-blue emitting and orange-emitting devices (Figure 60). The CIE coordinates of the PtON7-t-Bu device (0.14,0.09) is very close to the National Television Systems Committee (NTSC) standards for blue (0.14,0.08) which is noteworthy since few reports have ever demonstrated a CIE_y coordinate of less than 0.1.[22] Furthermore, the PtON7-t-Bu device has a much higher device efficiency than any previously reported deep blue OLED with a CIEy value of less than 0.1.[140,171] This achievement is attributed to the fact that most deep blue emitting OLEDs with such desirable CIE coordinates, such as $Ir(fppz)_2(dfbdp)$, which achieved 11.7% peak EQE and CIE of (0.155, 0.106),[145] or $Ir(pmb)_3$, which achieved 5.8% peak EQE and CIE of (0.17, 0.06),[140] require strong emission peaks between 380-450nm due to their broad tails or large sidebands extending into the blue-green or green portion of the visible spectrum. Due to the narrow emission spectrum of PtON7-t-Bu, devices can achieve highly desirable colour without having to dramatically shift the primary emission energy to the UV-Blue or deep-blue region. The comparably lower energy emission of PtON7-t-Bu can avoid potential quenching by either the host or blocker materials and does not require the use of ultra-high bandgap materials.[172] Such advantages are essential for potentially achieving both high efficiencies and long operational lifetimes for blue phosphorescent OLEDs. This result highlights the benefits and importance of narrow-band emitters to tune the emission to the precise colours desired in order to achieve the most efficient and high colour purity devices possible.

Table 7. A summary of device characteristics at peak value and 100 cd/m^2 for the devices with two different structures. Device type I: PEDOT:PSS/NPD/TAPC/x% PtN1N: 26mCPy/PO15/BmPyPB/LiF/Al. Device type II: ITO/HATCN/NPD/TAPC/x% emitter:26mCPy /DPPS/BmPyPB/LiF/Al.

EML	λ_{max} (nm)	FWHM (nm)	CIE	η_{EQE} (%)		η_P (Lm/W)	
				peak	@ 100 cd/m^2	peak	@ 100 cd/m^2
2% PtN1N^I	496	18	(0.13,0.55)	23.5	21.7	50.3	42.9
7% PtN1N^I	498	20	(0.15,0.56)	26.1	25.8	61.7	56.3
14% PtN1N^I	498	22	(0.15,0.58)	25.6	25.5	67.3	61.1
8% PtN1N^{II}	498	22	(0.14,0.60)	25.1	21.9	66.5	48.5
6% PtON7-tBu^{II}	450	28	(0.14,0.09)	17.6	10.7	14.4	5.3
2% PtN8ppy^{II}	576	28	(0.53,0.47)	19.3	16.0	48.3	29.1

6.6 Efficient “Pure” Blue OLEDs from Pt Complexes with Narrow Spectral Bandwidth

Despite the demonstrated success in achieving high efficiencies for both Ir and Pt complexes, the commonly reported CIE coordinates for claimed “deep blue” emission fall near (0.15,0.15) rather than the Nation Television System Committee (NTSC) coordinates for “pure” blue of (0.14,0.08).[98] This slight shortcoming actually poses a very substantial challenge since the achievement of a CIE_Y value below 0.1 requires that the *majority* of the emission must fall within the deep blue region. Consequently, only a few such reports exist all of which are relatively inefficient.[140] The difficulty in achieving such an emission relates to the broad emission or pronounced vibronic progressions characteristics of many phosphorescent metal complexes and consequently, substantial emission in the “green” region.[99] Thus, in order to utilize current phosphorescent emitters for “pure blue” emission, a substantial amount of the emission must be either filtered out or the triplet energy must be increased. The latter strategy renders the emitters incompatible with known stable and efficient host, charge blocking and transporting materials illustrating an undesirable trade-off between deep blue color and efficiency or stability.[172] Such is the case for the iridium complex, $Ir(pmb)_3$ which achieved CIE of (0.17, 0.06) and peak EQE of only 5.8%.[140]

One strategy to achieve CIE_Y value below 0.1 without significantly shifting the triplet energy is through the recent development of thermally activated delayed fluorescent materials in which thermal activation from the lower energy triplet excited state to the higher energy singlet state enables a higher energy emission through fluorescence with high quantum yields.[173,174] Consequently, significant emission between 380-450nm, with a peak external quantum efficiency of 9.9% has been achieved despite triplet energies below that of common carbazole based hosts.[173] Nevertheless, the efficiency is still much lower than that of many phosphorescent metal complexes and the resulting broad fluorescent emission contains a sizeable portion of light below 450nm in the region where the human eye has very low responsivity. An alternative approach to achieve efficient pure blue emission is through the development of a series of rigid tetradentate Pt complexes with narrow spectral bandwidth. These complexes emit with a single dominant emission peak in the deep blue region with greatly suppressed vibronic sidebands to achieve CIE_X ~0.15 and CIE_Y <0.1. The high spectral purity of these emitters demonstrate the ideal case with no wasted emission in the near UV, where responsivity of the human eye is low and triplet energy is high, and minimal color contamination from green region of the visible spectrum.

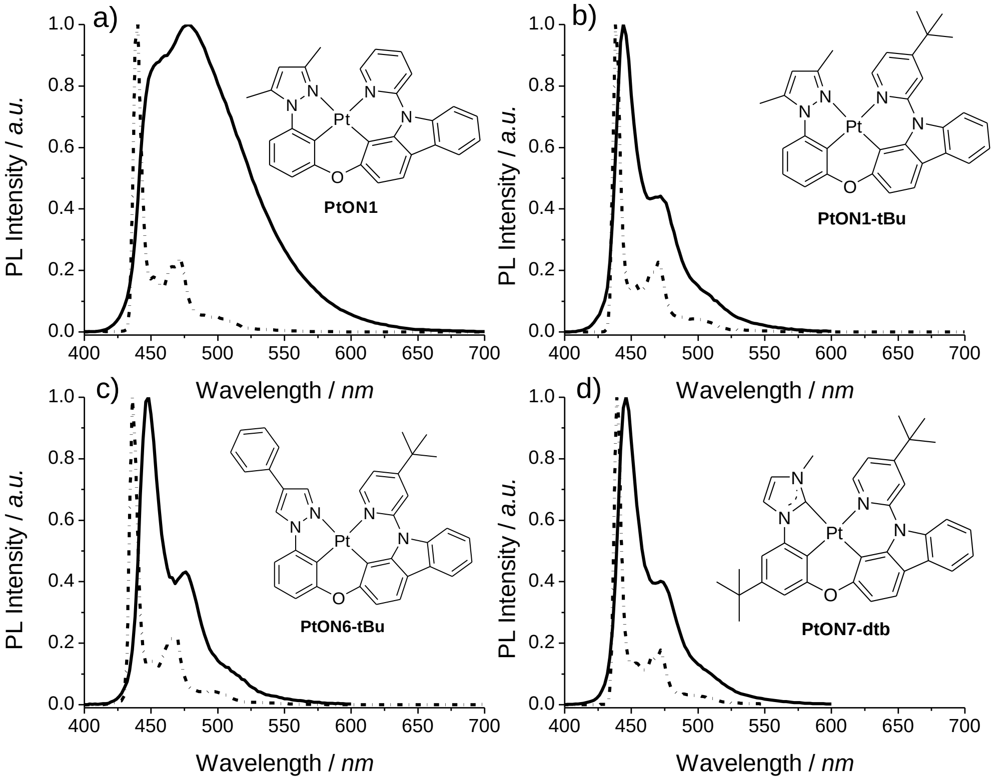

Figure 61. Photoluminescence spectra of a) PtON1, b) PtON1-tBu, c) PtON6-tBu, d) PtON7-dtb at room temperature in CH_2Cl_2 (Solid) and 77K in 2-Me-THF (dash-dot) with the molecular structure of each emitter inset.

It was previously demonstrated that deep blue emission could be achevied from tetradentate cyclometalated Pt complexes containing phenyl methylimidazole or phenyl pyrazole emissive ligands, such as PtON1. Such a molecular design proved extremely successful with EQE as high as 25.2% for deep blue emission and will thusly serve as an appropriate starting point for further molecular design. The photoluminescent (PL) spectra of PtON1 at low temperature (77K) in 2-methyl-THF and room temperature in CH_2Cl_2 are given in Figure 61a. The low temperature emission spectrum shows a dominant emission peak at λ_{max}=440nm and a small vibronic sideband at 472nm. At room temperature, however, the PtON1 emission spectrum is significantly broadened with a full-width at half-maximum (FWHM) of 85nm and a peak emission at 478nm, attributed to a high degree of ^{1}MLCT/^{3}MLCT mixing in its lowest excited state, similar to that of many Ir complexes.[139-141] Upon adding an electron donating group such as tert-butyl (tBu) to the 4-position of the pyridine ring significant spectral narrowing is observed in the room temperature emission spectrum for PtON1-tBu (Figure 61b). This may be attributed to increasing the energy of the ^{1}MLCT state of the carbazole pyridine moiety resulting in reduced influence of such a state in the lowest triplet state, yet more synthetic efforts and photophysical studies are needed to clarify this effect. The net effect of adding the tert-butyl functional group to form PtON1-tBu is a low temperature emission spectrum that is nearly identical to PtON1 (λ_{max}=438nm), but with a room temperature emission spectrum with a very narrow spectral bandwidth yielding an emission peak of 444nm and FWHM of only 20nm. Such emission is among the narrowest for any cyclometalated complex and has color purity comparable or even superior to many quantum dot LEDs that are widely praised for their high color purity.[162-166] Furthermore, films of PtON1-tBu doped in poly(methyl methacrylate) (PMMA) demonstrated very high photoluminescent quantum yields of Φ=0.88 which are similar to that of PtON1 (Φ=0.85).

To further illustrate the utility of this molecular design, two other Pt complexes with different emissive ligands, namely PtON6-tBu and PtON7-dtb, were synthesized and their photoluminescent emission spectra are given in Figure 61c-d. Both of these complexes also demonstrate room temperature emission spectra with reduced vibronic sidebands yielding deep blue emission at 448nm and 446nm with FWHM values of 20nm and 19nm for PtON6-tBu and PtON7-dtb respectively. Furthermore, the photoluminescent quantum yields for all the mentioned complexes are over 0.7 in doped PMMA films.

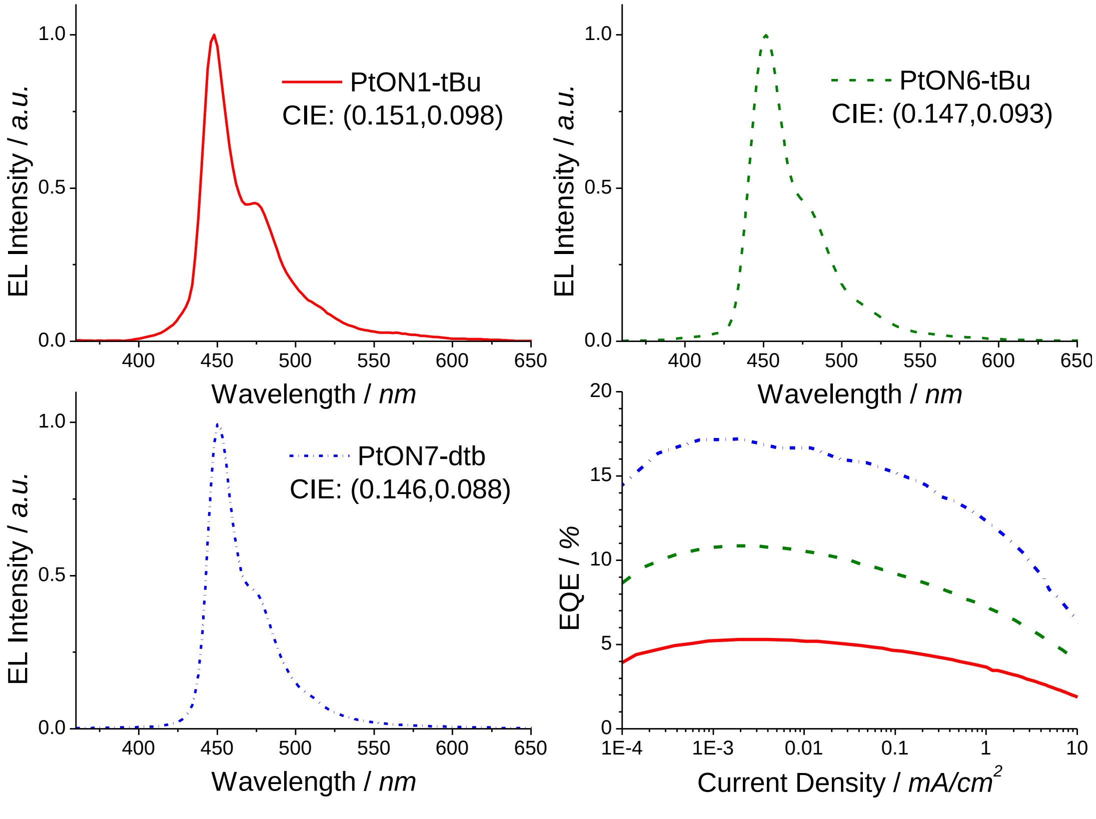

Figure 62. EL Spectra of a) PtON1-tBu (solid), b) PtON6-tBu (dash), and c) PtON7-dtb (dash-dot). d) EQE vs. current density for devices of each emitter in the structure: ITO/HATCN(10 nm)/NPD(40 nm)/TAPC(10 nm)/2% Dopant: 26mCPy(25 nm)/DPPS(10 nm)/BmPyPB(40 nm)/LiF/Al.

Deep blue OLEDs employing PtON1-tBu, PtON6-tBu, and PtON7-dtb were fabricated in the structure ITO/HATCN(10 nm)/NPD(40 nm)/TAPC(10 nm)/2% Dopant: 26mCPy(25 nm)/DPPS(10 nm)/BmPyPB(40 nm)/LiF/Al where HATCN is 1,4,5,8,9,11-hexaazatriphenylene-hexacarbonitrile, NPD is N,N'-diphyenyl-N,N'-bis(1-naphthyl)-1,1'-biphenyl-4,4"-diamine, TAPC is di-[4-(N,N-di-toylyl-amino)-phyenyl]cyclohexane, 26mCPy is 2,6-bis(N-carbazolyl) pyridine, DPPS is diphenyl-bis[4-(pyridin-3-yl)phenyl]silane, and BmPyPB is 1,3-bis[3,5-di(pyridin-3-yl)phenyl]benzene. Prior to deposition, the pre-patterned ITO coated glass substrates were cleaned by subsequent sonication in deionized water, acetone, and isopropanol. Organic layers were deposited at rates of 0.5 to 1.5 Å/s, monitored by quartz crystal microbalances, in a custom-made vacuum thermal evaporation chamber built by Travato Man. Inc. The Al cathode was deposited through a shadow mask without breaking vacuum, defining device areas of 0.04cm^2. The current-voltage-luminance characteristics were measured using a Keithley 2400 SourceMeter in conjunction with a Newport 818 Si Photodiode. Electroluminescent spectra were measured with a Horiba Jobin Yvon FluoroLog-3 spectrometer. The dopant concentration was initially kept low at 2% (w/w) in order to avoid any spectral broadening from aggregation of the Pt complexes.[158] The resulting electroluminescent (EL) spectra are given in Figure 62a-c, the plots of EQE are given in Figure 62d, and tabulated spectral and device performance data are given in Table 1. All of the complexes show narrow deep blue emission that are similar to that of the solution PL spectra with emission peaks at 448nm, 452nm, and 452nm, for PtON1-tBu, PtON6-tBu, and PtON7-dtb respectively. Consequently, CIE$_X$ ~0.15 and CIE$_Y$ <0.1 were achieved for all three complexes. The PtON1-tBu emission spectrum however, shows a possible nonexclusive emission between 400 and 425 which may be attributed to undesirable energy transfer within the device from the high triplet energy emitter. This is further supported by the low EQE of the 2% PtON1-tBu doped devices peaking at 5.3% and dropping to only 2.7% at a practical luminance of 100cd/m^2. Devices of PtON6-tBu and PtON7-dtb on the other hand show more exclusive emission in their EL spectra and correspondingly yield better peak EQEs of 10.9% and 17.2% respectively. These results suggest that the slightly higher emission energy of PtON1-tBu (λ_{max}= 448nm) compared to PtON6-tBu (λ_{max}= 452nm) and PtON7-dtb (λ_{max}= 451nm) leads to incompatibility with this efficient device structure, and the present emitters push the limits for triplet energies while remaining compatible with carbazole based hosts such as 26mCPy.[140]

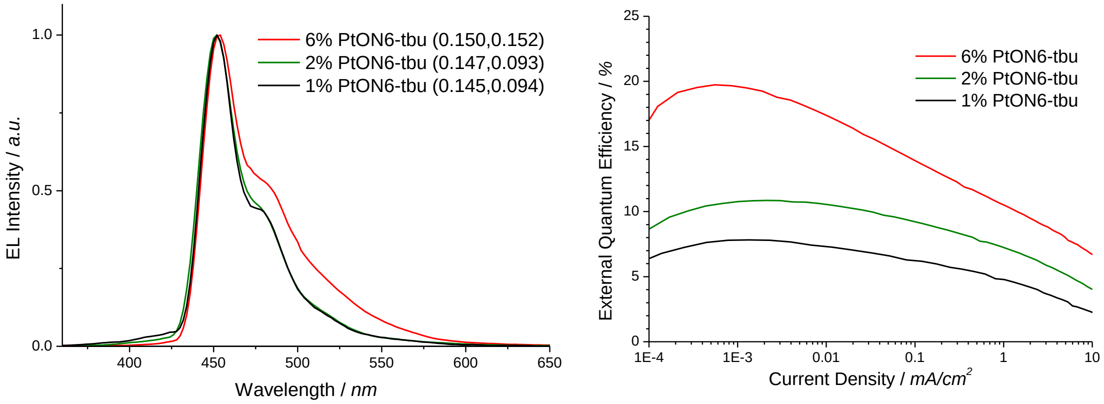

Figure 63. a) EL Spectra and b) EQE vs. current density for devices PtON6-tBu doped at concentrations of 1%, 2%, and 6%. CIE values are given in the inset to part a.

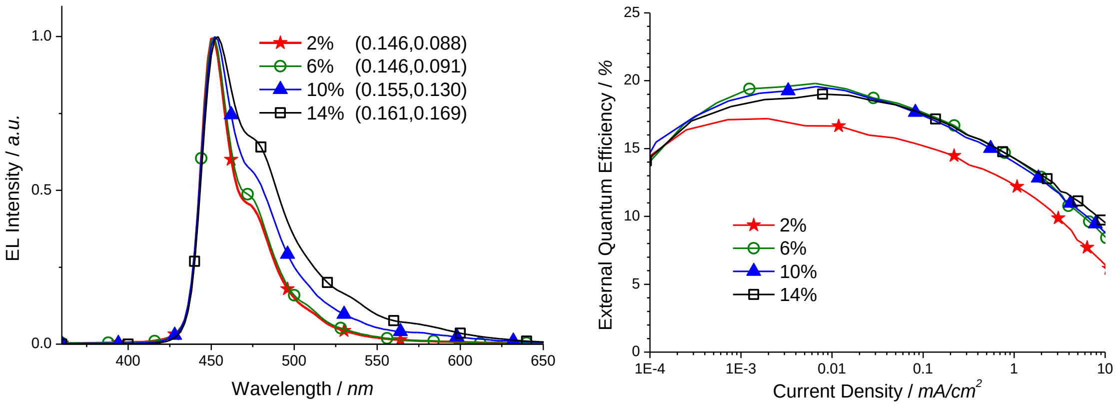

Figure 64. a) EL Spectra and b) EQE vs. current density for PtON7-dtb devices with dopant concentrations of 2% (stars), 6% (circles), 10% (triangles), and 14% (squares). CIE values are given in the inset to part a.

To further improve the efficiency of the devices, the effect of increasing dopant concentration of the efficient PtON7-dtb emitter was studied. Devices were fabricated in the structure: ITO/HATCN(10 nm)/NPD(40 nm)/TAPC(10 nm)/x% PtON7-dtb: 26mCPy(25 nm)/DPPS(10 nm)/BmPyPB(40 nm)/LiF/Al for additional dopant concentrations of 6%, 10%, and 14%. The electroluminescent spectra shown in Figure 64a shows a similar emission spectra for 2% and 6% doping concentrations with CIE coordinates of (0.146,0.088) and (0.146,0.091), but further increasing the dopant concentration resulted in significant spectral broadening and CIE coordinates of (0.155,0.13) and (0.161,0.169) for 10% and 14% doping concentrations respectively. Efficiency enhancements and reductions in efficiency roll off were achieved for all dopant concentrations between 6-14% (Figure 64b, Table1) with the highest peak EQE of 19.8% achieved for the 6% PtON7-dtb doped device. However, at practical luminances of 500 cd/m^2 the EQE increases with doping concentration reaching 12.2% at for the 14% doped device compared to 9.9% and 6.7% for 6% and 2% doped devices. Nevertheless, the superior color purity and high peak efficiencies of the 6% doped device achieves an appropriate balance between high color purity and high efficiency.

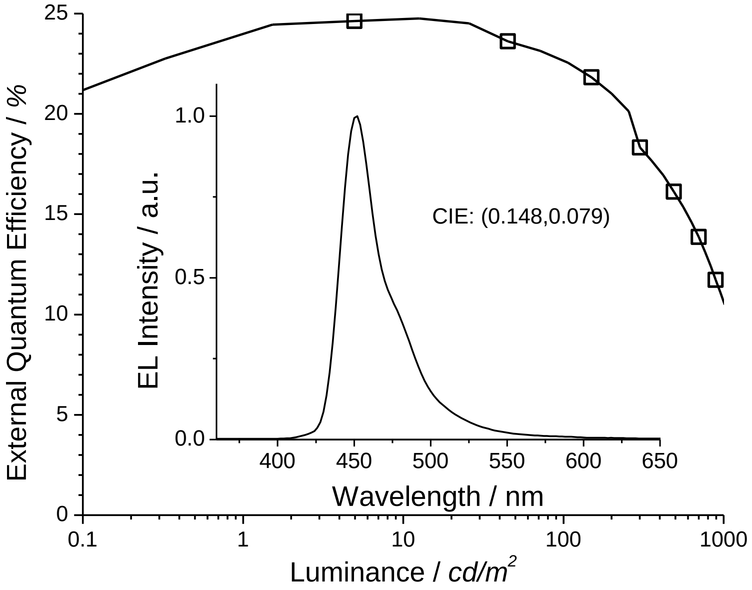

Figure 65. EQE vs. Luminance for PtON7-dtb device in the structure: ITO/HATCN(10 nm)/NPD(40 nm)/TAPC(10 nm)/6% PtON7-dtb: 42% TAPC: 42% PO15 (25 nm)/PO15(10 nm)/BmPyPB(30 nm)/LiF/Al. The EL Spectra and CIE coordinates are given in the inset.

In order to reduce any other potential quenching effects from poor triplet energy alignment with the host or blocking materials and potentially reduce the efficiency roll off at high current densities, the 26mCPy host was replaced with a cohost of TAPC and the high bandgap electron transporting material 2,8-bis(diphenylphosphoryl)-dibenzothiophene (PO15).[130] These devices were fabricated in the structure ITO/HATCN(10 nm)/NPD(40 nm)/TAPC(10 nm)/6% PtON7-dtb: 42% TAPC: 42% PO15 (25 nm)/PO15(10 nm)/BmPyPB(30 nm)/LiF/Al, where the DPPS hole blocking layer was also replaced by PO15 and the BmPyPB layer thickness was reduced to 30nm to improve charge balance. As a result of this optimization, the peak EQE improved to 24.8% and remained as high as 22.7% at a practical luminance for display applications of

100cd/m^2 which is among the highest efficiencies for deep blue OLEDs. Furthermore, the emission color of such a device was also improved in the cohost structure leading to CIE values of (0.148,0.079) which are remarkably close to the NSTC standards for blue of (0.14,0.08).[98] This result is the first report of an efficient blue OLED with a CIE$_Y$ value less than 0.1 and EQE over 20%.

Table 8. Summary of device performance data for narrow band blue devices

Dopant	Conc.	λmax (nm)	FWHM (nm)	CIE$_X$	CIE$_Y$	η_{EQE} (%) (peak)	η_{EQE} (%) (100 cd/m^2)
PtON1-tBu	2%	448	24	0.151	0.098	5.3	2.7
PtON6-tBu	2%	452	30	0.147	0.093	10.9	6.6
PtON7-dtb	2%	451	23	0.146	0.088	17.2	12.4
PtON7-dtb	6%	452	25	0.146	0.091	19.8	14.7
PtON7-dtb	10%	452	39	0.155	0.130	19.6	14.9
PtON7-dtb	14%	454	47	0.161	0.169	19.0	15.5
PtON7-dtb[a]	6%	451	29	0.148	0.079	24.8	22.7

a) Using a cohost of TAPC:PO15 (1:1)

These high efficiencies are more than double the efficiency of the recently reported pure blue OLEDs employing a donor-acceptor type fluorescent emitter which reached a peak EQE of 12% and 5.3% at 100cd/m^2 for CIE coordinates of (0.15,0.06).[175] Such efficient and pure deep blue emission should serve as a benchmark for all future blue OLEDs.

6.7 Efficient Pd(II) complexes exhibiting both phosphorescence and metal assisted delayed fluorescence emission

Despite the impressive efficiencies and color of deep blue OLEDs demonstrated for both Ir and Pt complexes, the stability of such devices remains a substantial deficit for the on-going efforts in the field of organic displays and lighting. [108,109] Moreover, it has been speculated that the formation of triplet excitons tends to directly facilitate the dissociation of σ-bonds, as has been demonstrated for Si-Si in polysilane materials and other material systems, indicating a greater challenge for developing stable deep blue triplet emitters.[176] Thus, from the energy standpoint, it will be ideal to develop efficient blue emitters with triplet energy in "green" or "red" region which can also harvest all of "blue" singlet and triplet excitons. Such requirements have exceeded the individual capability of existing blue fluorescent emitters, which cannot harvest the triplet excitons, or green phosphorescent emitters, which cannot emit in the blue region. Thus, a special and innovative molecular design will be needed to achieve such a goal.

The investigations on the detailed mechanisms of harvesting electro-generated excitons inside of organic electroluminescent devices have been well documented in the past two decades.[89,93,177] For most organic fluorescent emitters, fluorescence (Figure 66a) is the main pathway for their radiative decay process where phosphorescence is severely suppressed due to its symmetry forbidden character. On the other hand, cyclometalated Ir and Pt complexes have fast intersystem crossing and rapid phosphorescence process (Figure 66b) due to strong spin-orbit coupling, enabling themselves to harvest both electro-generated singlet and triplet excitons, resulting in a theoretical 100% electron to photon conversion efficiency.[59,96] Recent studies on carbazolyl-dicyanobenzene derivatives and copper(I) based metal complexes, characterized as thermal activated delayed fluorescent (TADF) emitters, have also demonstrated high emission quantum yield at the room temperature and can be utilized in the device settings to harvest both singlet and triplet excitons.[173,174,178,179] As illustrated in Figure 66c, when the energy levels of the lowest triplet excited state (T_1) and the lowest singlet excited state (S_1) are close, the triplet excitons can decay radiatively through the combination of intersystem crossing ($T_1 \rightarrow S_1$) and delayed fluorescence ($S_1 \rightarrow S_0$) processes. This approach has the benefit of being able to achieve a higher energy emission for a given triplet energy which enables the incorporation of these emitters into known stable host and transport materials unlike many deep blue Ir or Pt emitters.[159] Nevertheless, this process is necessarily endothermic and a portion of the triplet excitons will decay non-radiatively due to the absence of an efficient phosphorescent emission process, thus high efficiencies can only be achieved for very small S1-T1 energy splitting.[180]

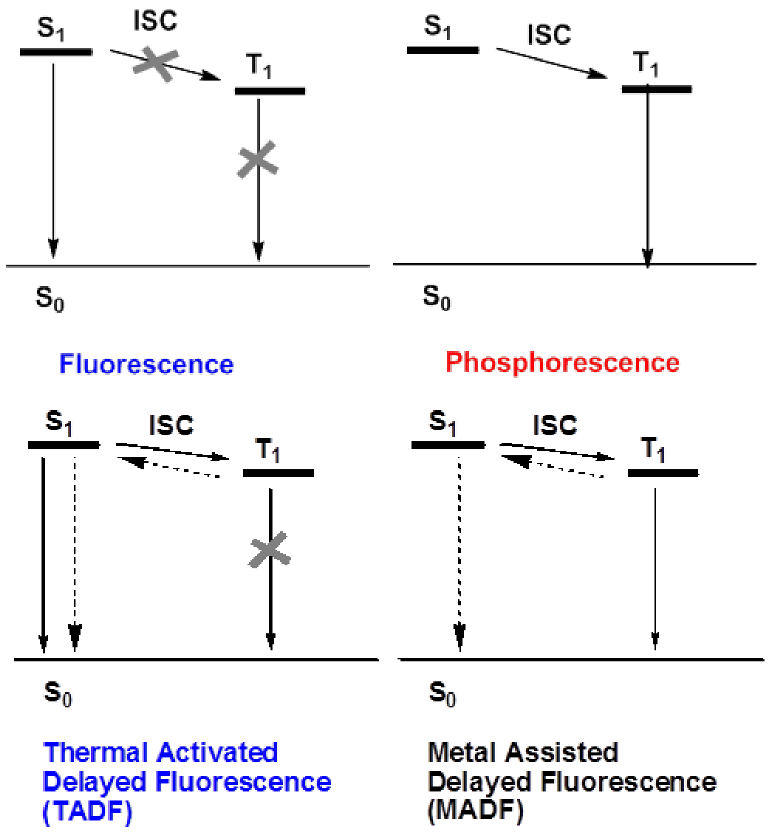

Figure 66. Illustration of the various emission mechanisms for organic emitters.

Here I demonstrate another mechanism of utilizing electro-generated excitons, denoted metal-assisted delayed fluorescence (MADF) process, where a heavy metal ion will be incorporated into the complex system to ensure both efficient phosphorescence and delayed fluorescent processes. As proposed in Figure 66d, when the energy levels of the T_1 state and the S_1 state are reasonably close, the two radiative decay process, i.e. phosphorescence ($T_1 \rightarrow S_0$) and thermally activated delayed fluorescence ($S_1 \rightarrow S_0$) can potentially occur simultaneously, enabling dual emission pathways. Due to its efficient triplet emission process, the MADF emitters can harvest all of singlet and triplet excitons regardless of comparably larger energy difference between the T_1 and S_1 states. Two green emitting palladium complexes, i.e. PdN3N and PdN3O, which exhibit both an efficient phosphorescent and delayed fluorescent processes are described. Devices of

PdN3N achieved nearly 21% peak external quantum efficiency (EQE) and also demonstrated remarkable device operational stability to 90% initial luminance (LT90) estimated at over 20,000hrs at 100 cd/m^2.

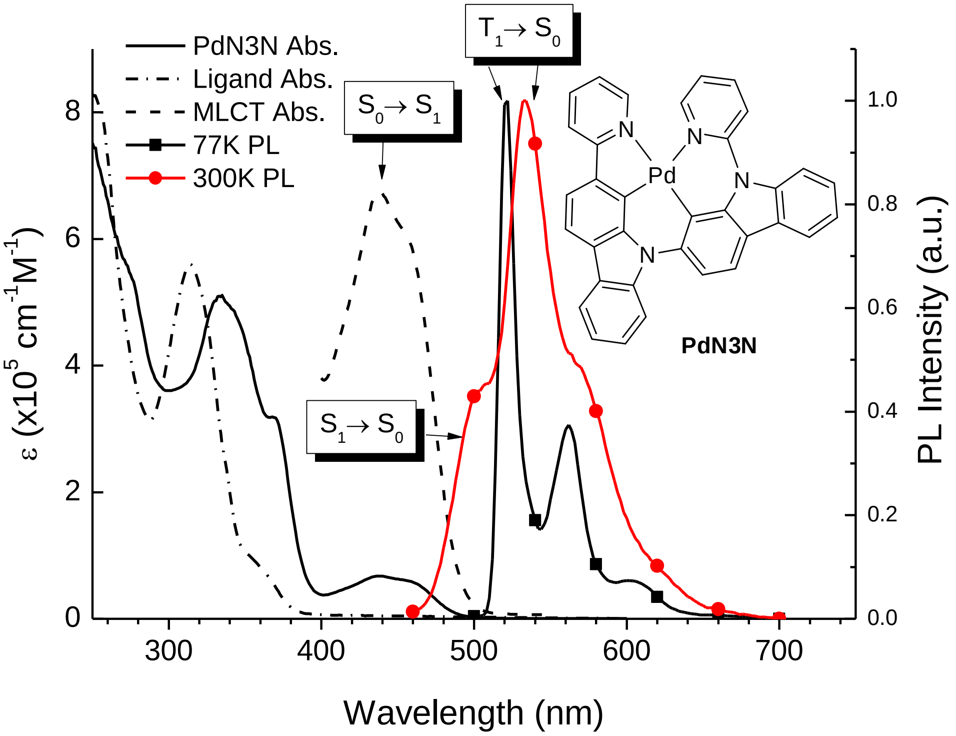

Figure 67. The extinction coefficient of Ligand N3N (dash-dot) and PdN3N (solid) and in a solution of dichloromethane, the PL spectrum at 77K in a solution of 2-Me-THF (squares), and 300K in a solution of CH2Cl2 (circles). The MLCT character of the absorption spectrum is enlarged for clarity (dashed line).

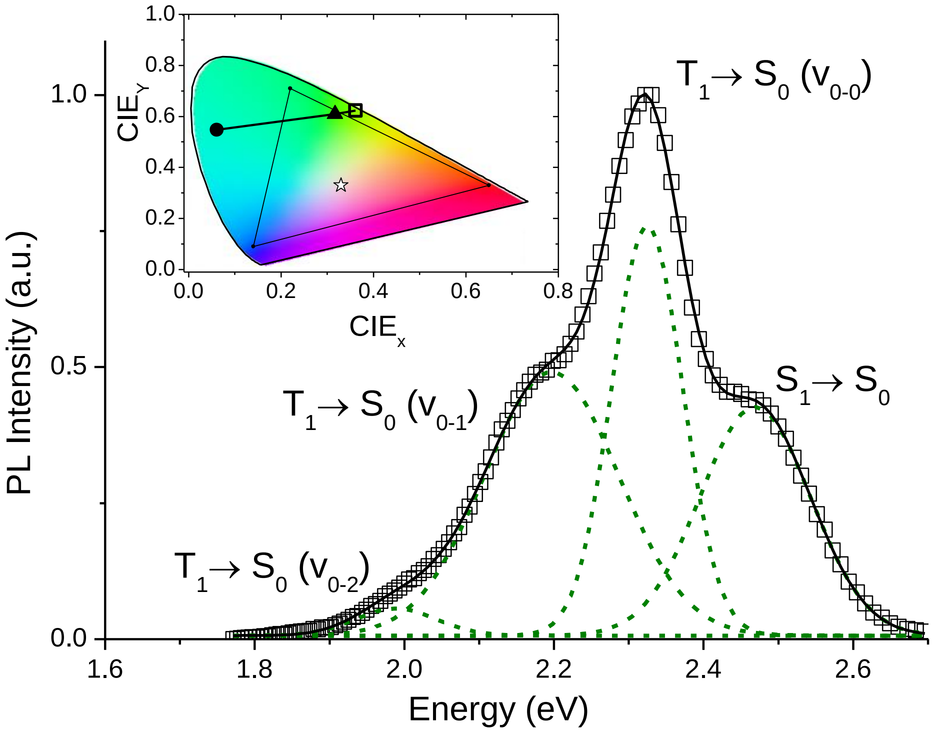

Figure 68. PL spectrum vs. energy (squares) with Gaussian oscillator fits (solid line). CIE coordinates of spectra for fluorescent only (solid circle), phosphorescent only (open square, and combined (triangle) are given in the inset.

The absorption spectra for PdN3N as well as the N3N ligand are shown in Figure 67. Both the complex and ligand exhibit very strong absorption bands below 400 nm assigned to $^1\pi$-π* transitions localized on the cyclometalating ligands. The small shift to lower energy of these transitions in the complex is attributed to the preferable planar molecular geometry of the ligand when complexed to Pt as well as the anionic nature of the ligand in the complex. The intense band in the 400-500 nm region that appears only in the complex is attributed to metal to ligand charge transfer (^{1}MLCT) transitions.

The 77K emission spectrum shows a narrow primary emission peak at 522 nm with small vibronic peaks characteristic of many phosphorescent emitters. The emission at 522 nm is attributed T1→S0 transition on the basis of the large Stokes shift from the absorption cut-off. This is a higher wavelength than many existing phenyl-pyridine complexes due to its extended conjugation through the carbazole units.[181] At room temperature (300K) the dominant emission peak is slightly red shifted to 534nm and significantly broadened as is typically seen at elevated temperatures. Unlike previously reported heavy metal phosphorescent complexes, a shorter wavelength peak appears (~505 nm) at the elevated temperatures indicating the presence of a thermally activated emission process. By comparing the absorption and emission spectra this higher energy emission process can be attributed to a S1→S0 transition (fluorescence) on the basis of the relatively small stokes shift. Thus, this demonstrates the existence of both phosphorescence and thermally activated delayed fluorescence within the single emitter.

In order to model the relative phosphorescent and fluorescent contributions to the emission, Gaussian oscillators were fit to the emission spectrum on a linear energy axis. The phosphorescence was fit with three transitions: v0-0 being the highest energy and the highest intensity and v0-1 and v0-2 being the first and second vibronic progressions as is characteristic for many aromatic cyclometalated Pt complexes.[62] The fluorescent shoulder was fit with a single oscillator. The integrated area of the three phosphorescent oscillators corresponds to approximately 73% of the emission while the fluorescent corresponds to 27 % of the emission. In the inset to Figure 68, a CIE plot showing the approximate emission color of either pure phosphorescence, fluorescence, or the combination of the two. The dramatic shift in the CIE_X values for the pure fluorescent emission highlights the value of the relatively large T1-S1 gap to achieve blue emission from an emitter with triplet energy in the “green” region. Further materials development of MADF emitters to further blue shift the emission or increase the fluorescence to phosphorescence ratio is of the utmost importance for this goal.

To explore the origins and characteristics of the MADF, PL spectra as a function of temperature was measured for both PdN3N and an analog, PdN3O, shown in Figure 69 and Figure 70 respectively. The designed molecules can be described as containing two parts: a C^N cyclometalating ligand containing the pyridyl-carbazole portion of the molecules and the D-A portion of either cabazole-phenoxyl-pyridine or carbazole-carbazolyl-pyridine. The triplet state consists mostly of the lower energy C^N portion of the molecules which is localized on the pyridyl-carbazole and as such the phosphorescent peak at 77K is approximately the same for PdN3O (518 nm) and PdN3N (522 nm). At higher temperatures a MADF peak appears in both complexes, however, there are distinct differences in both the energy and magnitude of this peak. When the carbazole pyridine ligand of PdN3N is replaced with a phenoxy-pyridine ligand the energy of the delayed fluorescent emission blue shifts. This can be attributed to the nature of singlet state which is of charge transfer character and thus related to the highest occupied molecular orbitals and lowest unoccupied molecular orbitals which are primarily located on this D-A region.[181] As a result the insertion of phenoxy-pyridine decreases the conjugation and raises the energy of this CT transition, thus blue shifting the S1→S0 emission. Furthermore, since the S1-T1 gap is larger for PdN3O the probability of the T1→S1 transition decreases and thus the ratio of MADF to phosphorescence decreases.

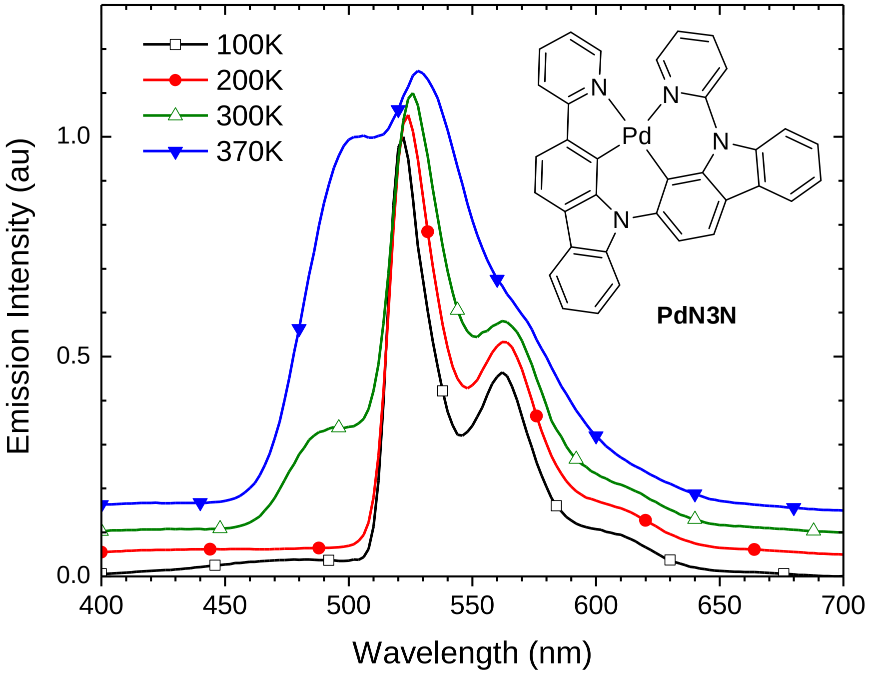

Figure 69. The PL spectrum as a function of temperature for PdN3N doped 6% (wt/wt) in PMMA film.

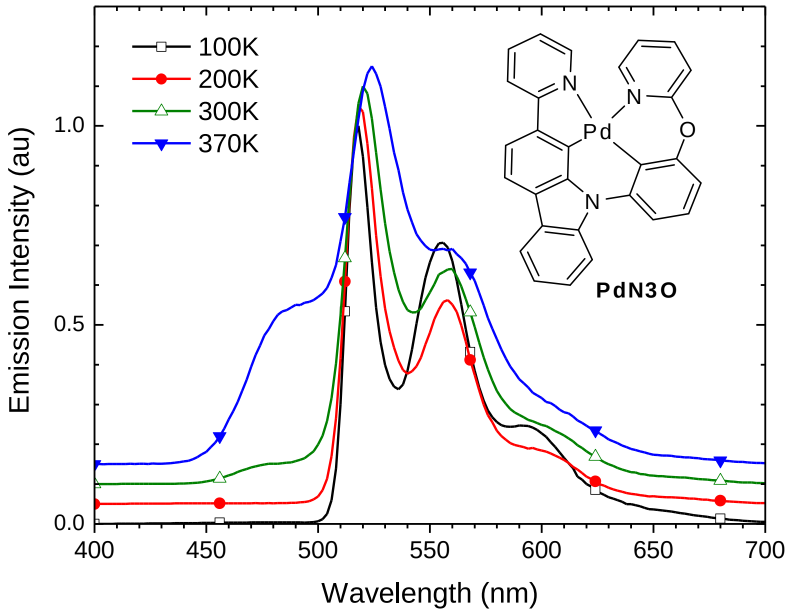

Figure 70. The PL spectrum as a function of temperature for PdN3O doped 6% (wt/wt) in PMMA film.

To explore the device performance of these emitters, OLEDs of both PdN3O and PdN3N were fabricated on a glass substrate pre-coated with a patterned transparent indium tin oxide (ITO) anode in the structure of ITO/HATCN(10 nm)/NPD(30 nm)/TAPC(10 nm)/6% dopant: 26mCPy (25 nm)/DPPS(10 nm)/BmPyPB(40 nm)/LiF/Al where HATCN is 1,4,5,8,9,11-hexaazatriphenylene-hexacarbonitrile, NPD is N,N'-diphyenyl-N,N'-bis(1-naphthyl)-1,1'-biphenyl-4,4"-diamine, TAPC is di-[4-(N,N-di-toylyl-amino)-phyenyl]cyclohexane, 26mCPy is 2,6-bis(N-carbazolyl) pyridine, DPPS is diphenyl-bis[4-(pyridin-3-yl)phenyl]silane, and BmPyPB is 1,3-bis[3, 5-di(pyridin-3-yl)phenyl]benzene. The EQE is shown in Figure 71 with the electroluminescent spectrum inset. The EQE of PdN3N and PdN3O peaked at 20.9% and 20.4% respectively, demonstrating that these dual emitting materials are capable of achieving electron to photon conversion efficiencies approaching unity. It is worth noting that these efficiencies are among the highest achieved for any Pd complex and are comparable to both their Ir and Pt analogs.[182] One apparent drawback to devices employing these complexes is the large efficiency roll off at higher luminance dropping to 14.3% and 13.9% for PdN3N and PdN3O at 100 cd/m^2. This is attributed to a combination of poor charge balance due to the poor electron transporting properties of DPPS and the long triplet lifetime of the two Pd complexes.[119] This issue can be addressed through improved charge balance or by improving the spontaneous radiative decay rate as has been demonstrated previously employing more advanced structures such as plasmonic nanostructures or microcavities.[183]

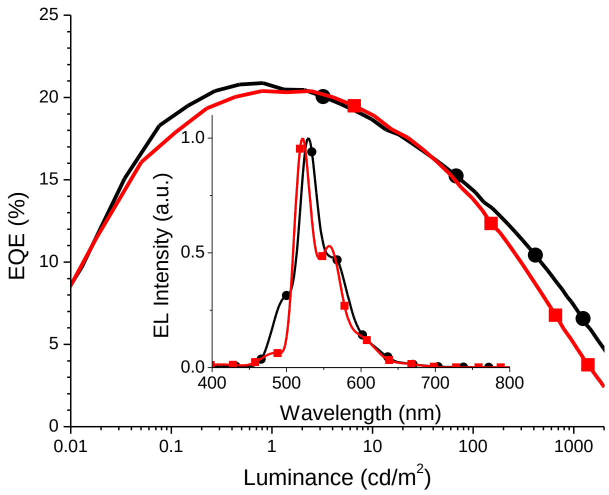

Figure 71. EQE versus Luminance with the corresponding EL spectra at 1 mA/cm2 inset for devices of PdN3N (circles) and PdN3O (squares) in the structure: ITO/ HATCN/ NPD/ TAPC/ 6% dopant: 26mCPy/ DPPS/ BmPyPB/ LiF/ Al.

The electroluminescent characteristics show both fluorescent and phosphorescent emission in the devices. PdN3N devices showed delayed fluorescent peak of approximately 30% of the phosphorescent peak height but the color was still dominantly from the green emission phosphorescent emission spectrum with CIE (0.30,0.61). In accordance with the PL spectra the MADF emission of PdN3O is low due to the larger T1-S1 resulting in green emission with CIE coordinates (0.30,0 .62). The very similar emission efficiencies despite the different T1-S1 splitting highlights the benefit of MADF emitters over their organic TADF counterparts since excitons unable to overcome the S1-T1 energy barrier can still emit through the efficient phosphorescent radiative pathway. Further tuning the molecular structure to modify the relative heights of the delayed fluorescent peak and shift the phosphorescent emission should yield even more ideal spectra.

In order to further explore the potential application of these Pd complexes as stable emitters, a PdN3N device was fabricated in the known stable structure

ITO/HATCN (10 nm)/NPD (40 nm)/10% PdN3N: CBP (25 nm)/ BAlq (10 nm)/Alq (30 nm)/LiF/Al where CBP is 4,4'-bis(N-carbazolyl) biphenyl, BAlq is bis(2-methyl-8-quinolinolato) (biphenyl-4-olato)aluminum and Alq is tris-(8-hydroxyquinoline) aluminum.[132] While these devices demonstrated a significant reduction in peak EQE to 6.0% due to poor charge transport and blocking materials, these devices will provide crucial information on the effectiveness of this class of materials for stable light emitting devices. Accelerated device operational lifetime of the PdN3N was carried out by driving the device at a constant current of 20 mA/cm^2 corresponding to an initial luminance of approximately 1700 cd/m^2. The lifetime to 90% of the initial luminance at these elevated conditions was 170 h which translates to over 20,000 h at 100 cd/m^2 using the conversion equation $LT(L_1)=LT(L_0)*(L_0/L_1)^{1.7}$.[169] These results are superior to most previous reports of Pt based emitters and comparable to its Ir analog Ir(ppy)$_3$. To the authors knowledge, this is the first report of long device operational lifetime for a Pd complex and should serve as a benchmark for future progress on such complexes.

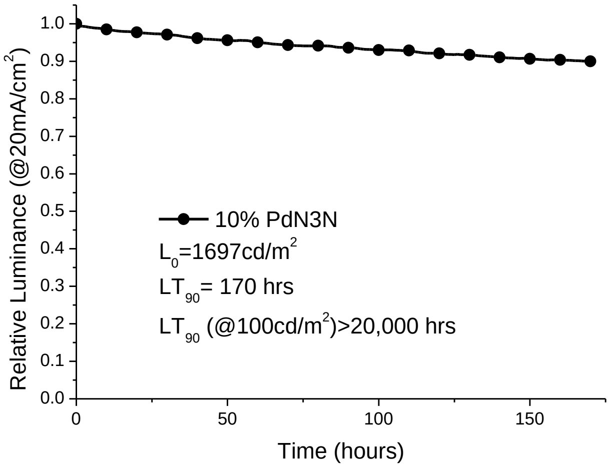

Figure 72. Device operational lifetime for the structure: ITO/HATCN/NPD/ 6% PdN3N: CBP/BAlq/Alq/LiF/Al at a constant driving current of 20 mA/cm^2

7. SINGLE DOPED WHITE OLEDS

One of the primary remaining frontiers in optoelectronic devices is the development of a cost effective and energy efficient replacement for existing white lighting technologies. White lighting is estimated to consume nearly 20% of electricity produced in the United States and two billion light bulbs are purchase annually in the United States.[184] This incredibly large market provides not only a large economic opportunity but also an opportunity to significantly reduce electricity consumption. The lighting market is currently dominated worldwide by inefficient incandescent bulbs which consumes a sizeable portion of electricity generated due to large heat losses, and generates a large amount of waste due to their short operational lifetime. A growing portion of world's lighting needs are being met by fluorescent bulbs which are more efficient but their disposal is significantly complicated by toxic materials in their composition such as Hg, and tend to have non-ideal emission color.[185] Solid state lighting through either organic or inorganic LEDs solve many of the issues of low efficiencies and lifetimes through their ability to directly convert electrical charges to light rather than secondary emission from a different primary excitation sources such as heat (incandescent lighting) or plasmas (fluorescent lighting). The development of highly efficient, environmentally benign solid state lighting with long operational lifetime could have an incredible impact, which by one US Department of Energy project could have the energy savings equivalent of removing 40 million cars from the roads.[186] The approach to achieve this target has been most successful in the development of white inorganic LEDs which have to date achieved laboratory efficiencies exceeding 250Lm/W and are already commercially available.[187] Nevertheless, the high fabrication cost of this technology could inhibit widespread worldwide adoption. Organic LEDs, on the other hand, are made from easily synthesized organic materials, on low cost substrate materials, are compatible with large scale roll to roll processing, and efficiencies exceeding 100Lm/W for white organic light emitting diodes (WOLEDs) have recently been reported.[188] Nevertheless, commercialization has not yet been realized due in part to the lower efficiencies than their inorganic counterparts, challenge in developing a stable and efficient blue emitter, and the dramatic limitation in the emission brightness. The drop off in efficiency at high brightness is especially challenging and will likely require large area panels in order to provide sufficient luminance in contrast inorganic LEDs which are point sources typically composed of 1 or several individual diodes.[184] The major consequence of this design constraint is that large area devices have to be fabrication easily and cheaply in order to compete with commercial lighting sources.

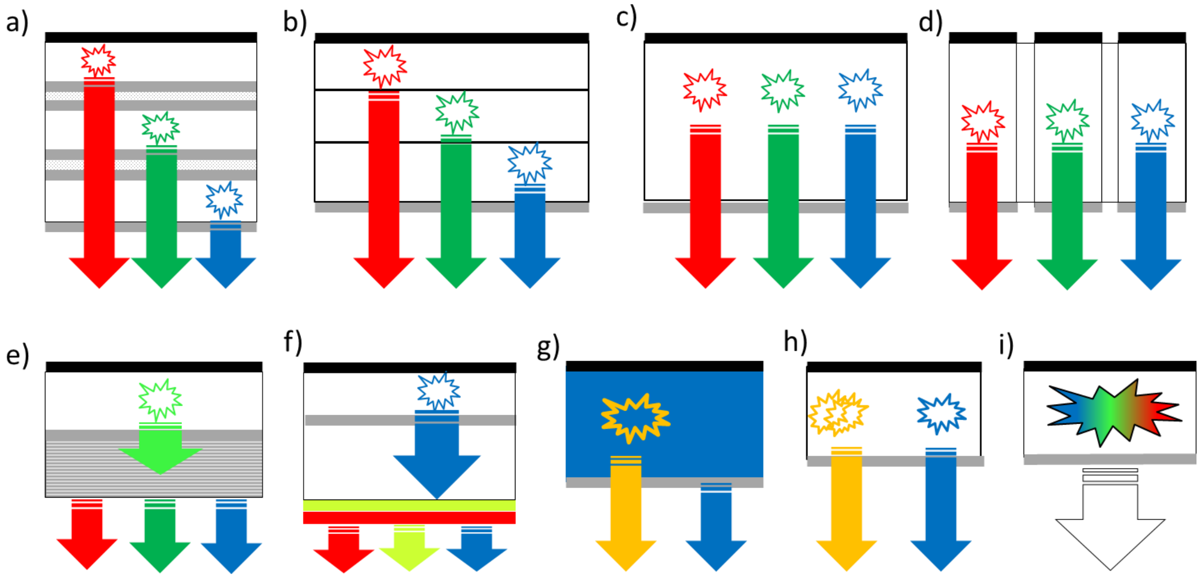

Figure 73. a)Tandem R, G, and B devices b)3 separate EMLs in single device c) 3 dopants in single EML d)Striped e)Microcavity based devices f)Down conversion to phosphors g)Emissive blue host plus phosphorescent dopant h)Excimer i)Single doped broadband white.

Since most organic emitters typically exhibit relatively narrow emission spectra, white light is typically produced from the combination of multiple emissive species spanning the visible spectrum. Device architectures for WOLEDs can be constructed in a number of unique way including: tandem or striped devices, blue devices with down-conversion phosphors, multiple emissive layers within a single device, multiple emissive dopants within a single layer, or even the combination of phosphorescent dopants in a fluorescent host.[108] The use of red, green, and blue emissive materials in separate layers has been widely reported and has been widely successful due to the ability to separately tune to the emissive layers to achieve an appropriate balance of colors and also achieve very high efficiencies.[189] Such a strategy necessarily increases the complexity of device to accommodate the additional layers as well as challenges maintaining the balance of color. With multiple emitters within a single emissive layer, while conceptually more simple to fabricate than multiple layer, rapid energy transfer from high energy blue emitters to lower energy red emitters significantly complicates the color balance and optimization of efficiency.[190] Furthermore, in all the aforementioned strategies, issues of color variation with increasing driving current or color aging due to different degradation rates of the various emissive materials have been observed and can pose a significant challenge to the development of a commercial product.[191] Thus, in order to reduce the complexity of the device structure for more economically feasible large area white lighting sources, a WOLED containing a single emitter would be greatly desired.

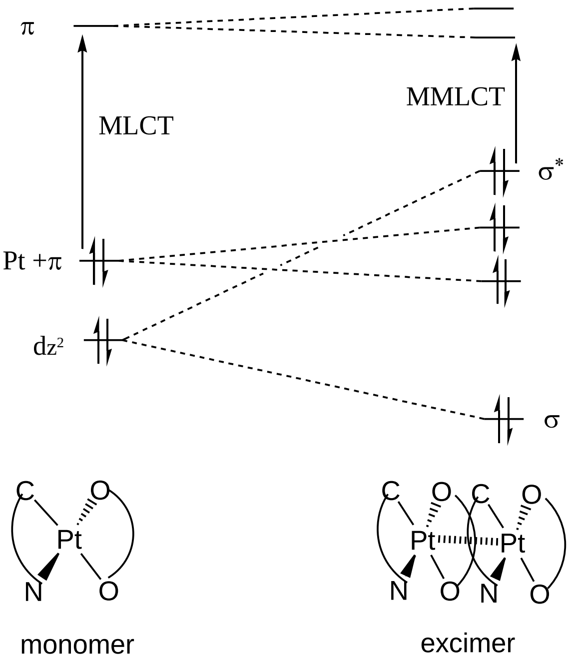

Figure 74. Example of excimer formation

One of the most significant progresses in the development of a single doped WOLED is the exploitation of the excimer emission properties of square planar metal complexes, typically cyclometalated Pt(II) complexes.[126,156,158] Excimers, or excited state dimers, are excited states shared between two emitter molecules which interact through either ligand centered π-π interactions and Pt-Pt bimetallic interactions, as shown in Figure 74.[192] Excimer emission, observed in both concentrated solutions and solid state, is a broad structure-less emission that is red shifted from that of the monomer. Through the combination of a blue monomer emission and a red excimer emission a broad white emission across the visible spectrum can be achieved. In contrast to ground state dimers, excimers have no bound ground state (i.e. no excimer absorption is observed) and hence the cascade of energy from blue monomer emitters to low energy excimer emitters can be avoided and a balanced white light can be achieved.[193] This is further supported by the photoluminescent excitation spectra which show that the excitation of the monomer and excimer are the same and that an excited monomer intermediate is formed prior to excimer formation.[194] Through careful theoretical work on phosphorescent excimers, design of new device structures, and the development of new emissive materials a greater understanding in the factors controlling the excimer emission has been achieved and white device exceeding 20% have now been demonstrated.[195]

To achieve an ideal white light, the emission source needs to both have an emission color close to that of natural sunlight and must exhibit significant emission spanning the entire visible spectrum. The CIE coordinates define the color of the emission source as perceived by the human eye and is controlled through the balance of red, green, and blue emission but provides no information on how well the emission spectrum matches that of natural light in rendering the colors of objects.[97] Thus, another parameter, the color rendering index (CRI) is needed to describe the ability of colors to reproduced with the illumination source in comparison with natural light sources. Excimers based WOLEDs, have a strong advantage in this case due to the typically broad emission of the excimer species that is complimentary to the high energy monomer emission. Nevertheless, the selection of materials with appropriate monomer and excimer energies and appropriate balance can be challenging.

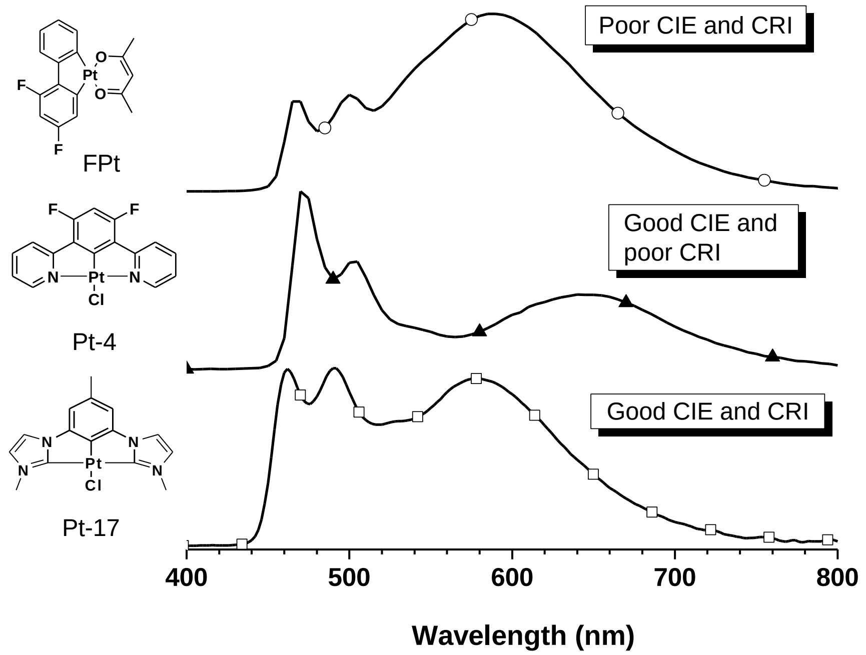

Figure 75. Dependence of emission spectrum shape on the molecular structure. From Bakken et al. [196]

To achieve an optimal white light a number of color tuning parameters must be precisely controlled: the monomer and excimer emission must be appropriately balanced to achieve a desirable CIE, the monomer emission must be sufficiently blue to span the visible spectrum for high CRI, and the excimer emission much be sufficiently red but not be too narrow or low in energy so as to leave a gap between the monomer and excimer emission.[196] The balance between monomers and excimers can typically be controlled by varying the dopant concentration since at higher concentration there is a higher probability of two dopants being nearest neighbors but this dependence can often depend on the molecular structure.[158] Tuning the monomer emission can be done through the appropriate design of cyclometalating ligand with high triplet energy or the application of electron-withdrawing ancillary ligands both of which have shown wide success in color tuning.[99,101,62] The tuning of the excimer emission is much more complicated and depends on a combination of a number of parameter including: monomer triplet energy, Pt-Pt separation, relative monomer orientations in the aggregate, and the distribution of the molecular orbitals. Consequently, concrete design rules for tuning the excimer emission have yet to be developed but can generally be described by the degree of π-π stacking and/or Pt-Pt separation but the relative contribution of these factors may vary amongst the different classes of cyclometalating ligand design.[197]

The importance of meeting the color tuning requirement can be illustrated with emission spectra of three different optimized excimer white devices given in Figure 75. For FPt, the monomer emission is insufficient to contain all the deep blue photons and the overwhelming dominance of the excimer emission yields both poor CIE and CRI.[126] If an optimized device can achieve color balance at moderate concentrations, as in Pt4 based white devices, good CIE coordinates can be achieved but large emission gaps and the lack of significant deep blue emission will still lower its CRI.[156] If the monomer emission is blue shifted and the excimer peak has appropriate energy and intensity both good CRI and CIE can be achieved, as is the case for Pt17.[196]

In addition to appropriately color tuning the emission of the excimer based white device, care must be taken to develop materials and device structures which optimize the device efficiency. In excimer emissive materials there are two emission processes, that is, monomer emission from an isolated molecule, and bimolecular excimer emission from a pair of molecules.[198] While the monomer emission can be made more efficient by designing the molecule with a rigid molecular structure and tuning the energy levels to favor radiative recombination pathways, bimolecular emission from the excimer species also requires consideration of the intermolecular interactions.[181] The exact nature of the emission process from excimer species is still under debate and the relationship between excimer properties (e.g. π orbital overlap, Pt-Pt separation, molecular rigidity, excimer energy) and the efficiency of excimer emission is unknown. In the following sections, some trends of molecular structure and emission efficiency will be demonstrated but more synthetic and theoretical work is necessary to fully understand these bimolecular emission processes.

7.1 Efficient single doped white devices employing carbene complexes

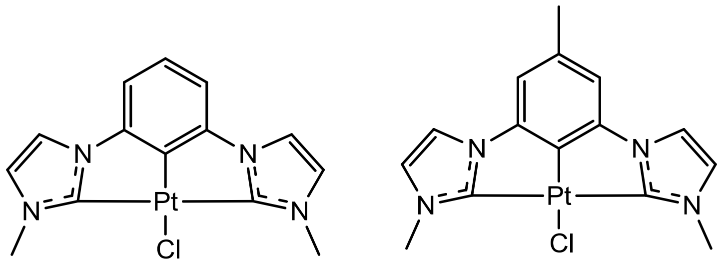

Pt-16 Pt-17

Figure 76: Molecular structures of Pt16 and Pt17

There is a lack of understanding of what determines the PL efficiency of excimers which can be affected by many factors such as: the excited properties of monomers, the variation in the intermolecular force between monomers due to different molecular packing, host materials, or processing conditions, and quenching processes for either excitons or excimers.[192,197] Here, the changes in emission spectra and efficiencies were studied for a series of devices employing two emissive materials which differ by only a small molecular structural modification, between platinum(II) bis(N-methyl-imidazolyl)-

benzene chloride (Pt-16) and platinum(II) bis(N-methyl-imidazolyl)-*toluene* chloride (Pt-17) shown in Figure **76**.

Compared with Pt-16, Pt-17 has a lower emission energy (10 nm red-shifted) for its monomer and a similar emission energy for its excimer, yet, the device characteristics of Pt-16 and Pt-17 based OLEDs are drastically different. A summary of Pt-16 and Pt-17 devices are presented in Table 9 and illustrated in Figure 77. With a similar device structure of ITO/PEDOT:PSS/NPD(30 nm)/TAPC(10 nm)/x%emitter:26mCPy(25 nm)/PO15(40 nm)/LiF/Al, Pt-16 and Pt-17 based OLEDs demonstrate different trends in the dependence of device efficiency on dopant concentration. The materials used have acronyms as follows. NPD: N,N′-diphenyl-N,N′-bis(1-naphthyl)-1,1′-biphenyl-4,4″-diamine. TAPC: di-(4-N,N-ditolyl-amino-phenyl) cyclohexane. PO15: 2,8-bis(diphenylphosphoryl)-dibenzothiophene. 26mCPy: 2,6-bis(N-carbazolyl) pyridine. BmPyPB: 1,3-bis(3,5-dipyrid-3-yl-phenyl)benzene. The layer sequence for WOLEDs on top of the ITO substrate is as below: 30nm NPD as a hole-transporting layer/10nm TAPC as an electron-blocking layer/25 nm emissive layer/40nm electron transporting layer and hole-blocking layer/1nm LiF/90nm Al cathode. The emissive layer consists of either 26mCPy as a host or TAPC:PO15(1:1) (Structures A and B) as co-host materials with Pt-16 and Pt-17 as a phosphorescent emitters. The exciton blocking layer and electron transporting layers are either a combined HBL/ETL of 40nm PO15 (structure A) or a separated HBL of 10nm PO15 and ETL of 30nm BmPyPB (structure B). EL sspectra were measured with an Ocean Optics HR-4000 spectrometer and I-V-L characteristics were taken with a Keithley 2400 Source Meter and a Newport 818 Si photodiode. All device operation and measurement were carried out inside a nitrogen-filled glove-box.

Individual devices had areas of 0.04 cm^2. Agreement between luminance, optical power and EL spectra was verified with a calibrated Photo Research PR-670 Spectroradiometer with all devices assumed to be Lambertian emitters.

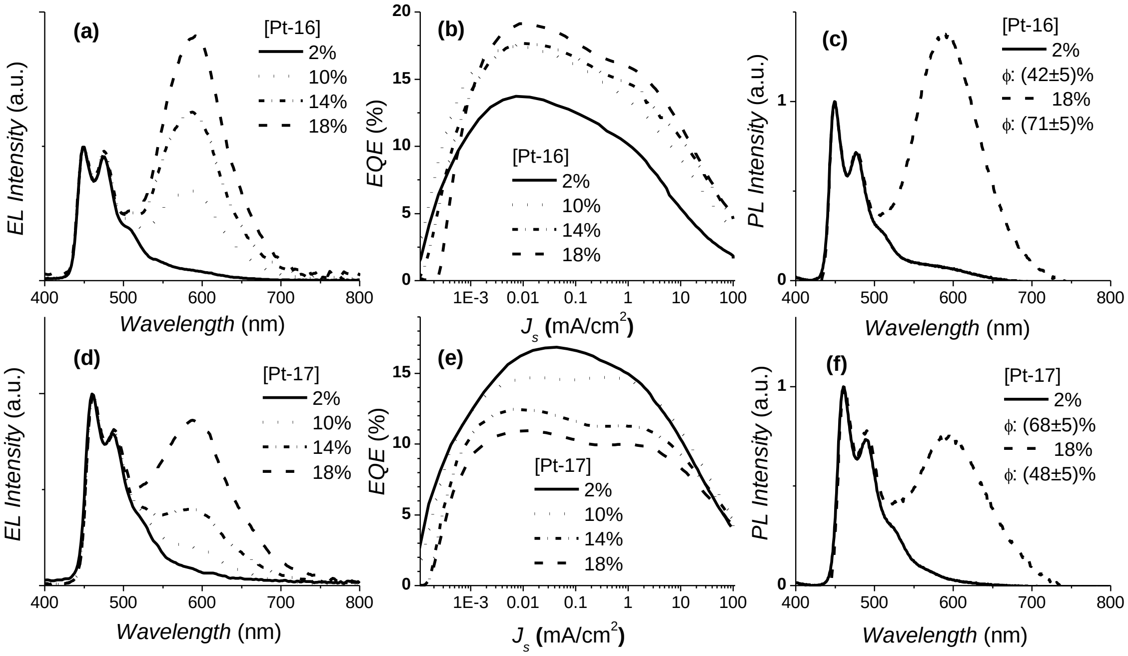

Figure 77. Electroluminescent emission spectra (a), Forward-viewing external quantum efficiency vs. current density (b) and doped 2,6mCPy thin film PL spectra and efficiencies(c) for Pt-17 and the electroluminescent emission spectra (d), Forward-viewing external quantum efficiency vs. current density (e) and doped 2,6mCPy thin film PL spectra and efficiencies(f) for Pt-16 for 2% (solid), 10% (dot), 14% (dash-dot), and 18% (dash) dopant concentrations.

With increasing dopant concentrations, both Pt-16 and Pt-17 based OLEDs observe the general trend of having a more pronounced red-shifted emission peak that is attributed to excimer emission rather than dimer emission on the basis of no observable red-shifted absorption band for Pt-16:26mCPy at high dopant concentrations [4] However, the device efficiencies of Pt-16 based OLEDs are much higher at high dopant concentrations and a slightly lower at low dopant concentration than those reported in Pt-17 based devices. As the dopant concentration for Pt-17 based OLEDs increases, the ratio of excimer emission vs. monomer emission increases and yields a white light emission with appropriate CIE coordinates and desirable CRI values only at concentrations as high as 18%. However, this increased excimer contribution at high concentrations is accompanied by a dramatic drop-off in maximum EQE from 16.9% for the 2%-doped Pt-17 device to 11.0% for the 18%-doped Pt-17 device. On the other hand, the peak EQE of Pt-16 devices increases with higher dopant concentration from 13.7% for the 2%-doped Pt-16 device to 19.2% for the 18%-doped Pt-16 device despite showing similar resistances in the current-voltage characteristics for devices with the same high dopant concentration. Moreover, for 10%-doped Pt-16 device (versus 18%-doped Pt-17 device), the excimer emission is strong enough to yield a white emission with CIE coordinates of (0.32, 0.32) and a CRI of 80. This high color quality emission spectrum showed minimal dependence on current density (and driving voltage) within the typical operating range as has been previously demonstrated for excimer based devices.[156]

The PL quantum efficiencies of doped films at various concentrations were measured in order to uncover the cause for the different device characteristics of Pt-16 and Pt-17 based OLEDs. The absolute PL quantum efficiency measurements of doped thin films were carried out on a Hamamatsu C9920 system equipped with a xenon lamp, integrating sphere and a model C10027 photonic multi-channel analyzer. Although both Pt-16 and Pt-17 have similar molecular structures, the quantum efficiency of 2% Pt-16:26mCPy film (42±5%) is much lower than that of 2% Pt-17:26mCPy film (68±5%). This can be attributed to a faster non-radiative decay process for Pt-16 due to its higher emission energy, resulting in a smaller energy difference between the lowest excited state and the metal-centered quenching state. A similar trend has also been observed for other blue-emitting Pt and Ir complexes.[157,161] However, it is surprising that the quantum efficiency of 18% Pt-16:26mCPy film (71±5%) is much higher than that of 18% Pt-17:26mCPy film (48±5%) with both excimers demonstrating similar emission spectra and emission energies. A few questions remain, including: why Pt-17 excimers are less emissive than Pt-17 monomers, which is the opposite of Pt-16, and why Pt-16 excimers are much more emissive than Pt-17 analogs with similar molecular structures. Nonetheless, the EQE decrease of the Pt-17 based OLEDs with higher dopant concentrations can be associated with the drop-off in PL quantum efficiency of the Pt-17 doped thin films, in addition to considering possible polaron-quenching and other exciton-quenching mechanisms.[160,199,200] Meanwhile, the significant increase in the PL quantum efficiency of Pt-16 doped thin films at high concentrations can explain the improvement in EQE for Pt-16 based OLEDs with larger dopant concentrations, which makes Pt-16 a perfect candidate for excimer based white OLEDs.

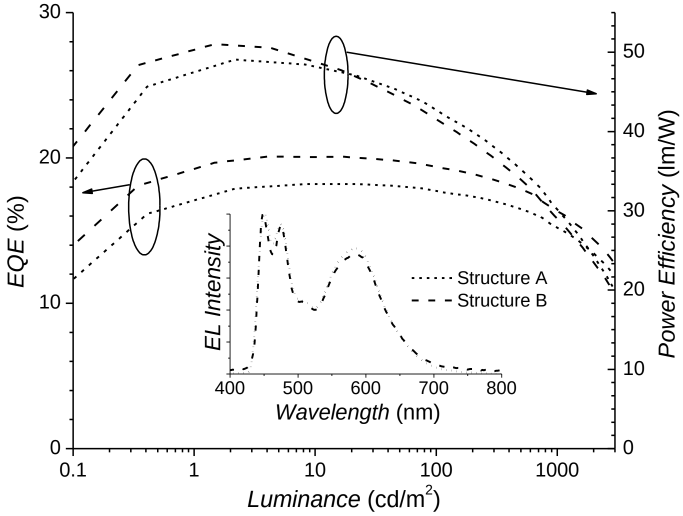

Figure 78. Forward-viewing external quantum efficiency (%) versus current density (mA/cm^2) of Pt-16 based WOLEDs of Structure A (dot) and Structure B (dash). Electroluminescent spectra (inset) of the devices at 1 mA cm^{-2}. Structure A is: ITO/PEDOT:PSS/30nm NPD/10nm TAPC/25nm 10:45:45 Pt-16: TAPC: PO15/40nm PO15/LiF/Al. Structure B is: ITO/PEDOT:PSS/20nm TAPC/25nm 10:45:45 Pt-16: TAPC: PO15/10nm PO15/30nm BmPyPB/LiF/Al

Utilizing the benefits of efficient Pt-16 excimer emission, devices were fabricated aimed at achieving high EQE at typical operating conditions of 100 to 1000cd/m^2. To reduce the high EQE "roll-off" at higher luminance, 26mCPy was replaced with a co-host of TAPC:PO15 (1:1) for 10%-doped Pt-16 device (labeled as Structure A) following the previous literature report.[130] Additionally, a 30nm BmPyPB layer was used to replace 30nm of the PO15 layer (label as Structure B) in order to further improve charge balance and resulting device efficiency. Although, BmPyPB has been reported to have a higher electron mobility than PO15, a 10nm PO15 layer is still necessary as a hole blocking layer as the LUMO level of BmPyPB is too low and will potentially quench Pt-16 excitons.[201] As a result, the Pt-16 device with the Structure B, exhibits the highest device efficiency (η_{EQE} = 20.1%) amongst all reported excimer-based WOLEDs. The EL spectrum of this device also yields highly desirable CIE coordinates of (0.33, 0.33) and a CRI of 80, with EL characteristics independent of current density. A maximum forward power efficiency of η_P=51 lm/W was recorded at the brightness of 1 cd/m^2, which remains at a high η_P=41 lm/W at 100 cd/m^2 and η_P=29 lm/W at 1000 cd/m^2. The performance of this device is comparable to the best reported WOLEDs in literature that have achieved maximum η_{EQE}=20.1% and peak η_P=41.3 lm/W for white light with CIE (0.38, 0.45) and CRI of 85 but used 3 different dopants embedded in multiple emissive layers. Another report demonstrated a maximum η_{EQE}=26.6% and peak η_P=67.2 lm/W for a WOLED employing a blue fluorescent host material and a yellow phosphorescent dopant but produced only a yellowish white light with CIE (0.46, 0.44), unsatisfactory CRI, and showed moderate voltage dependence in the emission color.[202,203]

Table 9. A summary of device characteristics at 1 mA cm^{-2}. The device structure is ITO(65nm)/PEDOT/NPD(30nm)/TAPC(10nm)/x%Emitter:26mCPy(25nm)/PO15(40nm)/LiF(1nm)/Al(90nm) unless otherwise noted (*†).

Emitter	Bias(V)	luminance (cd/m^2)	EQE (%)	CIEx	CIEy	CRI	P.E. (lm/W)
2%Pt-16	4.7	150	10.2	0.18	0.19	--	10.0
10%Pt-16	4.4	295	13.3	0.32	0.32	80	21.0
14%Pt-16	4.8	319	14.7	0.38	0.37	73	21.1
18%Pt-16	4.6	386	15.9	0.41	0.39	70	26.5
10%Pt-16*	3.3	371	16.8	0.32	0.33	80	35.2
10%Pt-16*†	3.5	396	18.2	0.33	0.33	80	35.2
2%Pt-17	4.8	249	15.0	0.18	0.25	--	16.3
10%Pt-17	5.2	285	14.5	0.23	0.30	64	17.2
14%Pt-17	4.6	236	11.3	0.29	0.33	76	16
18%Pt-17	4.5	226	10.0	0.37	0.38	80	15.9
18%Pt-17*	4.0	350	15.7	0.37	0.40	80	27.3

*A Cohost of TAPC:PO15 is used in the EML
†A 10nm PO15/30nm BmPyPB HBL/ETL is used

With the use of the developed Pt-16 complex, a peak EQE over 20%, CIE coordinates of (0.33, 0.33) and a CRI value of 80 was achieved for the first time with a single emissive dopant, which is comparable or superior to the state-of-the-art WOLED with multiple dopants. Moreover, excimer-based WOLED will have great potential to further improve the device efficiency if more efficient blue-emitting square planar Pt complexes can be developed. The record high power efficiency of Pt-16 based WOLEDs can be further improved by employing the state-of-the-art charge-injection materials and out-coupling techniques, which will set a clear path for the potential of a single-doped WOLED with

η_P of 100 lm/W. Overall, our demonstration of a single-doped WOLEDs with high efficiency and high illumination quality does present a unique opportunity to significantly simplify the device architecture and eliminate the problems of color aging and color instability for WOLEDs using multiple emitters. This will help to expedite the potential commercialization of WOLEDs for lighting applications.

7.2 Stable and efficient white OLEDs employing a single emitter

WOLEDs utilizing platinum(II) bis(methyl-imidazolyl)benzene chloride (Pt-16), demonstrated the achievement of CIE color coordinates of (0.33, 0.33), a CRI of 80 and improved the maximum EQE to 20.1%. Nevertheless, photoluminescent quantum yield (PLQY) measurements of doped thin films indicated that the Pt-16 monomer is inefficient, yielding a tradeoff between appropriate color and highest efficiencies. Thus, square planar platinum complexes which can achieve both efficient monomer and excimer emission are necessary to develop. Furthermore a new molecular design motif is needed since most common phosphorescent excimer emitting materials employ N^C^N cyclometalating ligands and their analogs, which typically still require potentially unstable functional groups including phenoxy or chloride as a fourth coordinating ligand bonded to the platinum metal ion.

Deep blue platinum emitters, PtOO7 and PtON7, which incorporated halogen-free tetradentate cyclometalating ligand based on a phenyl-carbene ligand and were capable of exhibiting deep blue emission. PtON7, in particular achieved a peak EQE of 23.7% and CIE coordinates (0.15, 0.14). The superior performance and color of this class of emitters, relative to both their iridium and platinum analogs, demonstrates that this design motif can be extremely useful for the development of efficient blue OLEDs. Unfortunately, none of these previously reported emissive materials exhibited excimer emission at elevated concentrations making them unsuitable for single-doped white devices. Nevertheless, the design motif of tetradentate platinum complexes related to PtOO7 and PtON7 may be utilized to develop planar, blue-emitting, Pt complexes for stable and efficient excimer based white OLEDs. Thus, a symmetric tetradentate cyclometalated platinum complex, Pt7O7, was synthesized and demonstrates for the first time, extremely high efficiency from both monomer and excimer emission.

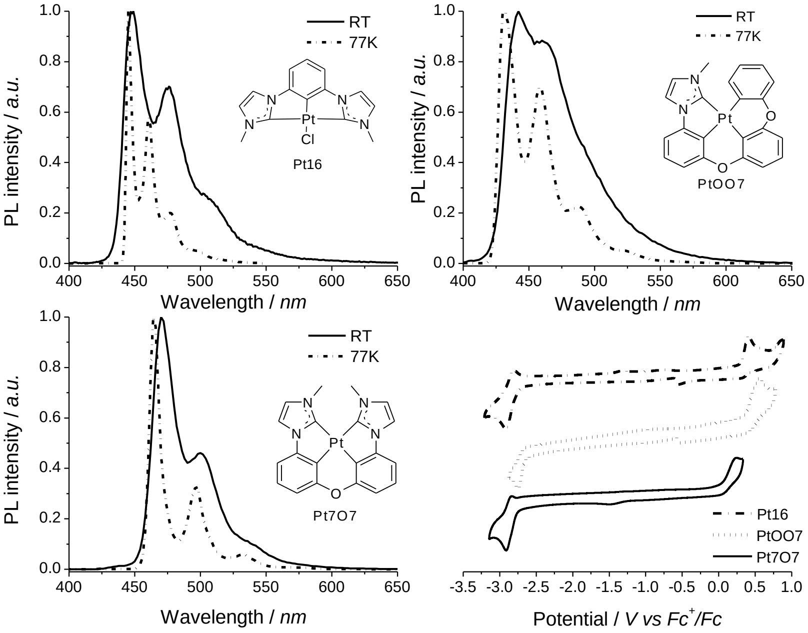

Figure 79. Room temperature photoluminescent emission spectra for (a) Pt-16, (b) PtO07, and (c) Pt7O7 with the molecular structure for each emitter inset in the plot and (d) the cyclic voltammograms for Pt-16 (dash-dot), PtOO7 (dot) and Pt7O7 (solid).

The electrochemical properties of Pt7O7 as well as the previously reported emitters Pt-16 and PtOO7 were examined using cyclic voltammetry (shown in Figure 79d) and differential pulse voltammetry using a CH Instrument 610B electrochemical analyzer.

Anhydrous DMF (Aldrich), stored under a nitrogen atmosphere, was used as the solvent and 0.1 M tetra(n butyl) ammonium hexafluorophosphate was used as the supporting electrolyte. A silver wire was used as the pseudo reference electrode, a Pt wire was used as the counter electrode, and glassy carbon was used as the working electrode. The oxidation potentials are based on the values measured from DPV and are reported relative to a ferrocenium/ferrocene (Fc^+/Fc) redox couple used as an internal reference (0.45 V vs SCE). The electrochemical bandgap is based on the difference between the first reduction and first oxidation peak measured from DPV. The reversibility of reduction or oxidation was determined using CV. The oxidation potential of Pt7O7 of 0.26V vs. Fc/Fc^+ is significantly lower than those of Pt-16 and PtOO7 which have oxidation potentials of 0.31V and 0.52V respectively. The lower oxidation potential and consequently destabilized highest occupied molecular orbital (HOMO) energy level can be attributed to weakened bond strength of Pt-C_{Ph} due to Pt-C_{Cb} at the trans position.[58] This ultimately results in a smaller electrochemical bandgap for Pt7O7 (3.08eV) compared to its phenyl-carbene based analogs like Pt16 or PtOO7 (~3.15eV). It is worth noting that these emitters employing phenyl-carbene ligands exhibit a qausi-reversible reduction process which is highly desirable for phosphorescent emitters with long device operational stability.[170]

Photoluminescent emission spectra were performed on a Horiba Jobin Yvon FluoroLog-3 at room temperature and 77K in a solution of dichloromethane for all three emitters and are shown in Figure 79a-c. The molecular structures of which are presented in the inset of each plot. Pt7O7 showed a primary emission peak at 472nm which is a 20nm shift to longer wavelengths compared to Pt-16 and PtOO7, which can be correlated to the lower oxidation potential and smaller electrochemical bandgap of Pt7O7. Nevertheless, the narrow emission spectrum (20nm FWHM) of Pt7O7 retains a moderate blue color by minimizing the green emission color originating mainly from either large sideband or broad tails that are exhibited for most phosphorescent cyclometalated Pt and Ir complexes. Furthermore, the triplet energy of 2.63eV could also be ideal to achieve maximum power efficiency by achieving the balance in maintaining high quality of white light (covering most of the visible spectrum) and minimizing the portion of deep blue photons with lower photopic responsivity.[166] Thus, Pt7O7 is well suited as a candidate for efficient blue and white OLED devices.

Device were fabricated on a glass substrate pre-coated with a patterned transparent indium tin oxide (ITO) anode in the structure of ITO/HATCN(10 nm)/NPD(30 nm)/TAPC(10 nm)/x% Pt7O7: mCBP(25 nm)/DPPS(10 nm)/BmPyPB(40 nm)/LiF/Al where HATCN is 1,4,5,8,9,11-hexaazatriphenylene-hexacarbonitrile, NPD is N,N'-diphyenyl-N,N'-bis(1-naphthyl)-1,1'-biphenyl-4,4"-diamine, TAPC is di-[4-(N,N-di-toylyl-amino)-phyenyl]cyclohexane, mCBP is 4, 4-bis(carbazol-9-yl)-2,2-biphenyl, DPPS is diphenyl-bis[4-(pyridin-3-yl)phenyl]silane, and BmPyPB is 1,3-bis[3, 5-di(pyridin-3-yl)phenyl]benzene. All small molecular materials were sublimed in a thermal gradient furnace prior to use. Prior to organic depositions, the ITO substrates were cleaned by sonication in water, acetone, and isopropanol followed by UV-ozone treatment for 15 minutes. Organic materials were thermally evaporated at deposition rates of .5 to 1.5 Å/s at a working pressure of less than 10^{-7} Torr. The deposition rates and thicknesses were monitored by quartz crystal microbalances. A thin 1 nm LiF layer was deposited at rates of <.2 Å/s and aluminum cathodes were deposited at a rate of 1 Å/s through a shadow mask without breaking vacuum. Individual devices had areas of 0.04 cm^2. All device operation and measurement were done inside a nitrogen-filled glove-box. I-V-L characteristics were taken with a Keithley 2400 Source-Meter and a Newport 818 Si photodiode. EL spectra were taken using the Jobin Yvon Fluorolog spectrofluorometer. Agreement between luminance, optical power and EL spectra was verified with a calibrated Photo Research PR-670 Spectroradiometer with all devices assumed to be Lambertian emitters.

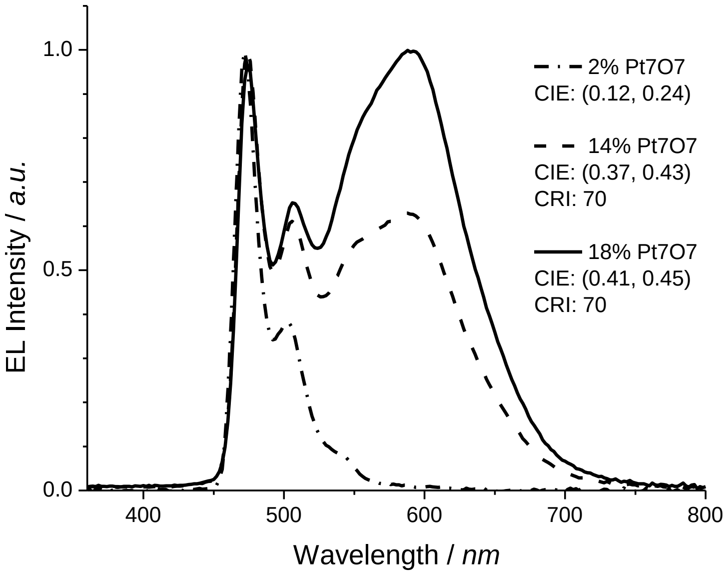

Figure 80. The EL spectrum for devices with Pt7O7 concentrations of 2% (dash-dot), 14% (dash), and 18% (solid) in the general structure: ITO/HATCN (10 nm)/NPD (40 nm)/TAPC (10 nm)/ x% Pt7O7:mCBP (25 nm)/DPPS (10 nm)/BmPyPB (40 nm)/LiF/Al.

The EL spectrum of the blue device (Figure 80) showed a sharp primary emission peak at 472 nm and exhibited CIE coordinates of (0.12, 0.24) which is within the blue emission region but falls short of (0.15,0.15) typically deemed deep blue. The device performance for 2% Pt707 (Figure 81) is remarkable with a peak EQE of 26.3% and a peak power efficiency of 32.4 Lm/W and remains at 20.5% and19.3Lm/W at a practical brightness of 100cd/m^2. These high peak efficiencies are much greater than that of most existing blue platinum complexes and is even superior to many of the state of the art Iridium complexes.[115,141]

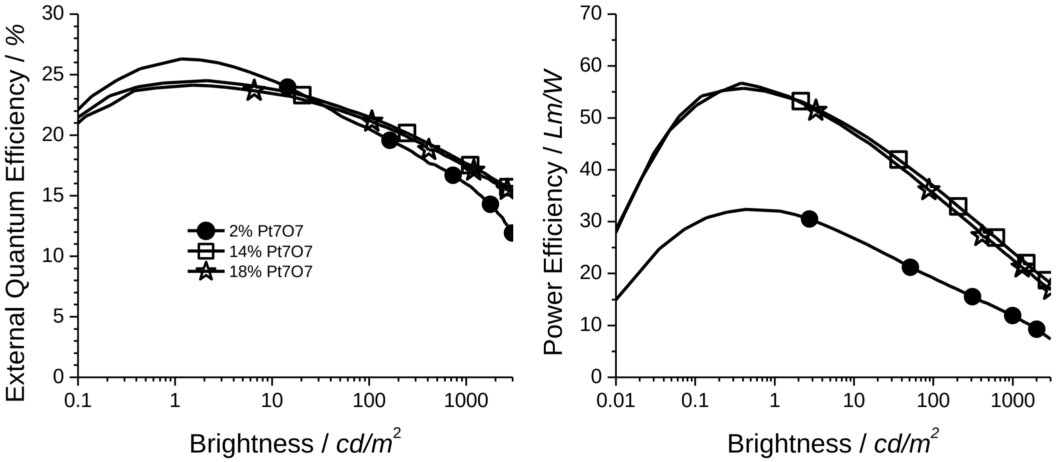

Figure 81. (a) The external quantum efficiency vs. brightness and (b) power efficiency vs. brightness for devices with Pt7O7 concentrations of 2% (circles), 14% (squares), and 18% (stars) in the general structure: ITO/HATCN (10 nm)/NPD (40 nm)/TAPC (10 nm)/ x% Pt7O7:mCBP (25 nm)/DPPS (10 nm)/BmPyPB (40 nm)/LiF/Al.

As the dopant concentration is increased to 14% and 18%, the EL spectrum shows the appearance of a broad peak centered at 600nm which is attributed to excimer formation, similar to the observed behavior for other square planar platinum complexes.[193] As a consequence the EL spectra exhibited the best color at a concentration of 14% Pt7O7 doped device with a CRI of 70 and CIE of (0.37, 0.42). This white emission spectrum showed minimal dependence on current density within the range of typical operating brightness (100 cd/m^2- 3500cd/m^2) as has been previously demonstrated for other excimer based devices.[156] Devices of Pt7O7 exhibited high efficiencies across all dopant concentrations yielding peak EQE of 24.5 and 24.1 for 14% and 18% dopant concentrations respectively. Furthermore, the improved conductivity and charge balance at higher concentrations led to lower roll off in EQE demonstrating 21.5% at 100cd/m^2 and 17.7% at 1000cd/m^2 for the 14% Pt7O7 doped device and 21.2% at 100cd/m^2 and 17.4% at 1000cd/m^2 for the 18% Pt7O7 doped device. The power efficiency of these devices were also very high, peaking at 55.7 Lm/W and 56.7 Lm/W but dropped to 24.0 Lm/W and 22.7 Lm/W at 1000cd/m^2 for both 14% and 18% Pt7O7 doped devices. The high roll-off in the power efficiency is most likely to the charge imbalance between the transport of the electrons and holes which leads to charge build up at one of the charge blocking interfaces.[119] This high roll-off can be avoided through the use of materials with improved charge transport or through more advanced structures such as mixed-host systems.[130]

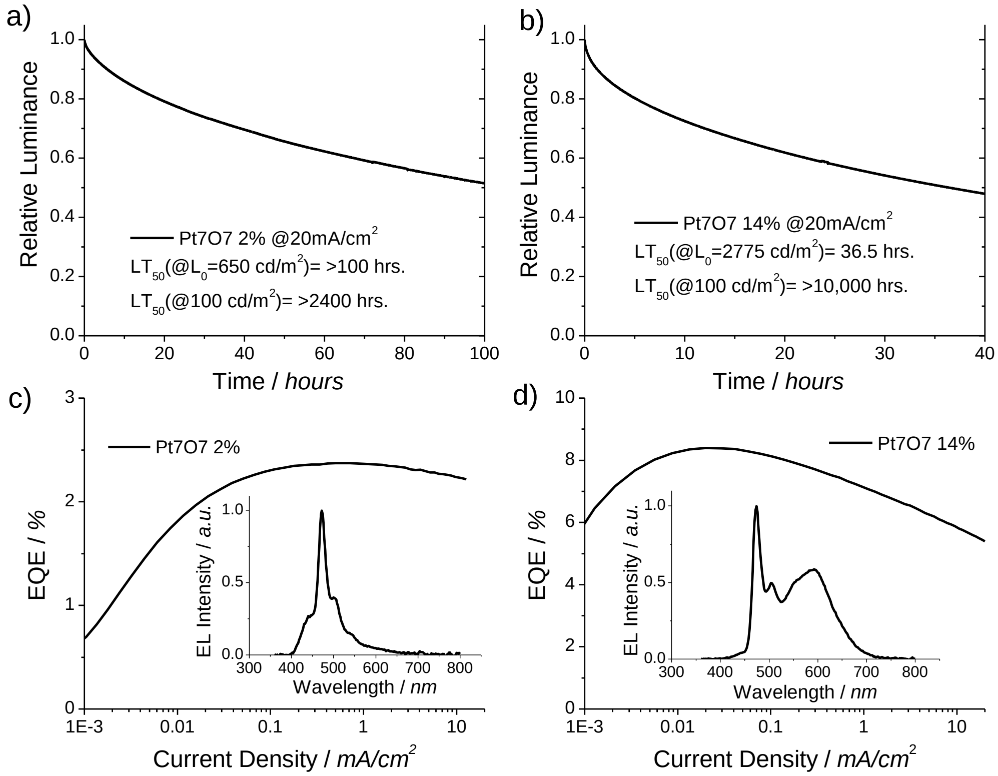

Figure 82. The operational lifetime for (a) 2% Pt7O7 and (b) 14% Pt7O7 devices run at a constant current of 20mA/cm^2 and the EQE versus current density for (c) 2% Pt7O7 and (d) 14% Pt7O7 devices with El spectra at a current of 1mA/cm^2 inset. Devices are in the general structure: ITO/HATCN (10 nm)/NPD (40 nm)/ x% Pt7O7:mCBP (25 nm)/BAlq (10 nm)/Alq (30 nm)/LiF/Al.

Long device operational stability is also a critical parameter for the development of OLEDs as next generation display and lighting technologies. As demonstrated previously, the efficient device structure employing TAPC and DPPS layers is unsuitable for device operational lifetime testing. Thus, in order to maintain high device efficiencies while the achieving long operational stability, it is necessary to develop electrochemically stable and appropriately energy tuned injection, transport, and blocking materials for both charge carriers as well as stable host and emissive materials. Such a task is typically challenging and exceeds the scope of most academic research labs. However, the application of Pt7O7 in a known stable, albeit inefficient, device structure is still valuable and informative for us to uncover the potential stability of Pt7O7 and its analogs in a device setting. Devices were fabricated in the structure: ITO/HATCN(10 nm)/NPD(40 nm)/x% Pt7O7:mCBP(25 nm)/ BAlq(10 nm)/ Alq(30 nm)/ LiF/Al where x is either 2% or 14% dopant concentration, BAlq is bis(2-methyl-8-quinolinolato) (biphenyl-4-olato)aluminum and Alq is tris-(8-hydroxyquinoline) aluminum.[132] The EL spectrum and EQE versus current density plot of the 2% Pt7O7 doped device, Figure 82c, shows that without the presence of an effective electron blocking material, there is significant recombination within the NPD layer resulting in moderate emission between 400-450nm and a very low device efficiency of less than 2.5%. However, at the higher dopant concentrations (14%), the EL emission, Figure 82d, mainly originates from the monomers and excimers of Pt7O7, leading to a much improved device efficiency of over 8% but still remains much lower than Pt7O7 devices with more advanced devices structures. In Figure 82a-b, the relative luminance versus time is plotted for devices operated at a constant current of 20 mA/cm^2 which corresponds to an initial luminance (L_0) of approximately 650 cd/m^2 for the 2% Pt7O7 doped device and 2775cd/m^2 for the 14% Pt7O7 doped device. It is very encouraging to report that the lifetime at 50% initial luminance, LT50, are 36.5 hrs. for the 14% Pt7O7 doped device and over 100hrs for the 2% Pt7O7 doped device. This can be translated to a LT_{50} at 100 cd/m^2 of over 10,000 hrs. for the white device and over 2,400 hrs. for the blue device using the formula $LT(L1)=LT(L0)*(L0/L1)^{1.7}$.[169] Further improvement in the device operational stability is expected with the incorporation of state-of-the-art host and blocking materials which can decrease the turn-on voltage, improve the electron to photon conversion efficiency, and eliminate other degradation mechanisms associated with the host and blocking materials.

Thus, this molecular design method should serve as a major step forward in the development of efficient and stable platinum based phosphorescent emitters for OLEDs applications. Thus, this molecular design motif demonstrates the ability to achieve stable and efficient single doped white OLEDs by maintaining high efficiency of both the monomer and excimer species. Further development of this class of stable and efficient materials, and further study into the molecular processes contributing to efficient emission, should contribute greatly to the eventual commercialization of these energy efficient technologies.

7.3 Tetradentate Platinum Complexes for Efficient and Stable Excimer Based White OLEDs

Much of the existing reports of excimer based white OLEDs employ either bidentate or tridentate cyclometalating ligands, both of which have typically demonstrated EQE less than 20% and often poor CRI or CIE coordinates.[126,156] Thus, a series of tetradentate Pt complexes were synthesized based on a phenyl methyl-imidazole emissive ligand (Figure 83). The previously reported blue emitter PtOO2 (Figure 83a) demonstrated a broad blue emission with emission onset just below 450nm and a primary emission peak at 470nm which should serve well for stable and efficient white lighting due to its blue color and compatibility with the triplet energy of many stable host materials.[204] However, no excimer formation is observed for this complex due to the out of plane distortion of this class of tetradentate emitters. Following the symmetric, planar backbone exhibited in Pt7O7, the complex Pt2O2 (Figure 83b) was synthesized. Despite retaining the same phenyl methyl-imidazole cyclometalating ligand as PtOO2, the primary emission peak of Pt2O2 was red shifted by 20nm to 490nm which reduces the blue component of the emission spectrum, but such a molecule may still prove useful as an excimer based white OLED.

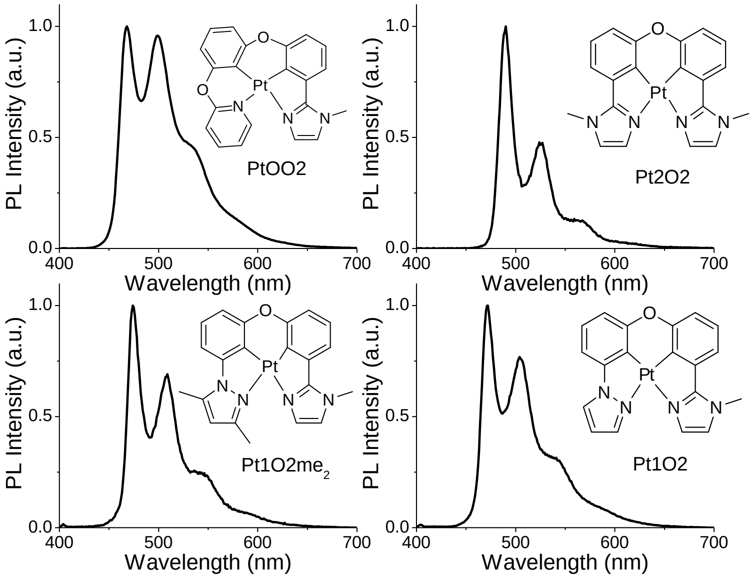

Figure 83. Photoluminescent emission spectra of PtOO2, Pt1O2, Pt2O2 and Pt1O2me$_2$ at room temperature in a solution of CH_2Cl_2

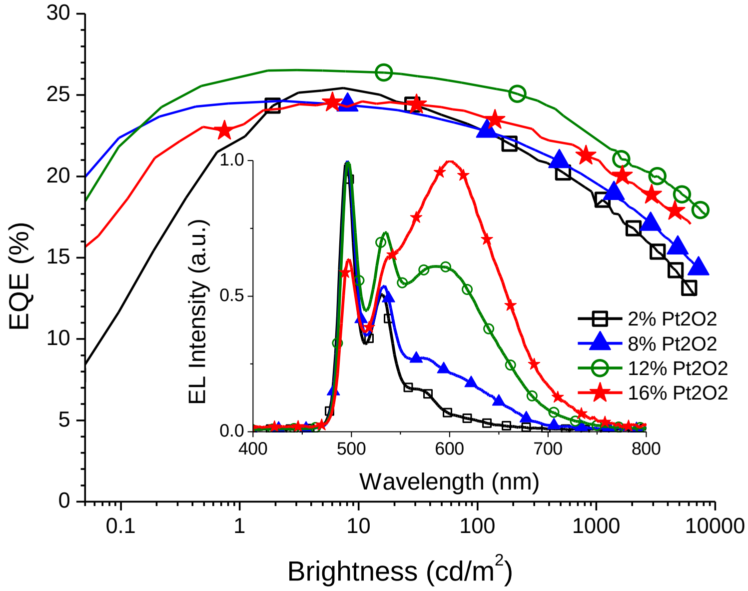

Figure 84. The EQE versus brightness plots for Pt2O2 devices in the structure: ITO/HATCN (10nm)/NPD (40nm)/TAPC (10nm)/x% Pt2O2: 26mCPy (25nm)/DPPS (10nm)/BmPyPB (40nm)/LiF (1nm)/ Al for 2% (squares), 8% (triangles), 12% (circles), and 16% (stars). The corresponding EL spectra are inset.

Devices of Pt2O2 were fabricated in the structure of ITO/HATCN(10 nm)/NPD(40 nm)/TAPC(10 nm)/x% Pt2O2: 26mCPy(25 nm)/DPPS(10 nm)/BmPyPB(40 nm)/LiF/Al where HATCN is 1,4,5,8,9,11-hexaazatriphenylene-hexacarbonitrile, NPD is N,N'-diphyenyl-N,N'-bis(1-naphthyl)-1,1'-biphenyl-4,4"-diamine, TAPC is di-[4-(N,N-di-toylyl-amino)-phyenyl]cyclohexane, 26mCPy is 2,6-bis(N-carbazolyl) pyridine, DPPS is diphenyl-bis[4-(pyridin-3-yl)phenyl]silane, and BmPyPB is 1,3-bis[3, 5-di(pyridin-3-yl)phenyl]benzene. For blue OLED devices with primarily monomeric emission character, the dopant concentration was controlled to be around 2% (w/w) to minimize the formation of excimers. The monochromatic devices demonstrated a very high peak EQE of 25.4% shown in Figure 84and Table 10 and a peak power efficiency of 57.0 Lm/W. These efficiencies represent electron to photon conversion efficiencies approaching unity and are amongst the highest of any OLEDs without light outcoupling techniques. The electroluminescent spectrum, shown in the inset to Figure 84, demonstrated green emission with a primary peak at 496nm and CIE coordinates of (0.231, 0.565).

As the Pt2O2 dopant concentration is increased to 8%, 12%, and 16% the formation of a broad, red-shifted emission peak appears in the EL spectra (Figure 84inset) which is attributed to the increased formation of excimers at the higher concentrations. This is in contrast to the observed concentration behavior of many other tetradentate platinum complexes such as PtOO2 and analogs.[204] This, can be explained by the planar nature of the Pt2O2 molecules compared to the twisted, non-planar geometry of PtOO2 shown in the previous report.[181] Ultimately, an orange-white emission with CIE coordinates of (0.48,0.48) and CRI of 72 is achieved at a concentration of 16% Pt2O2. These moderate CRI values are achieved in spite of the lack of a portion of the blue emission spectrum due to the broad and balanced emission color across the rest of the visible range. Furthermore, it is very encouraging that both the monomer and excimer species are very efficient as evidenced by the very high peak EQE values at all concentrations with the highest achieved peak EQE value of 26.5% for 12% Pt2O2 doped devices and remaining as high as 24.6% for 16% doped devices. These high efficiencies are comparable or superior to Pt7O7 indicating that this design motif is both extremely efficient and color tunable through small structural modifications.

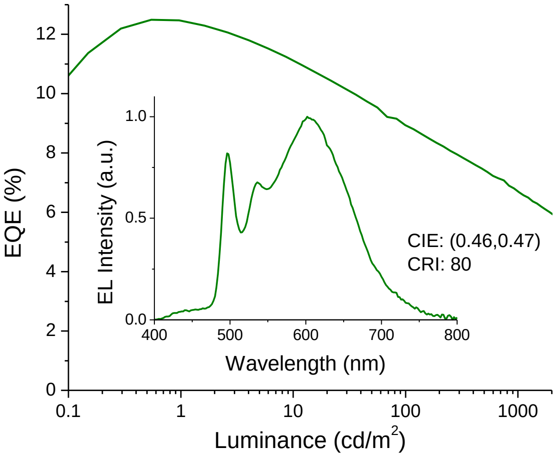

Figure 85. EQE vs. Luminance and EL spectra at 1mA/cm^2 (inset) 16% Pt2O2

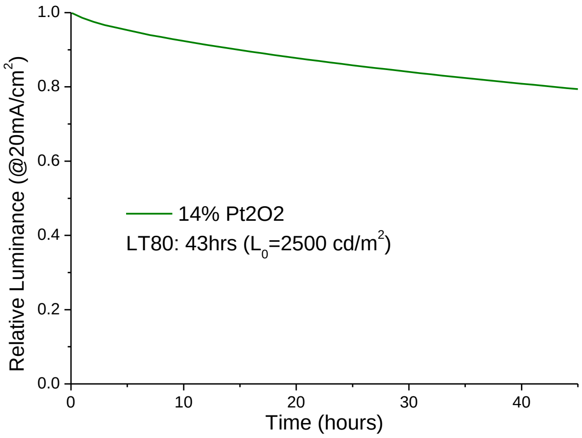

Figure 86. luminance versus time plots for 16% Pt2O2 devices operated at a constant driving current of 20mA/cm^2

To further explore the effectiveness of excimer emitting platinum emitters such Pt2O2 as a commercially viable white light source, the device operational lifetime must also be evaluated. Unfortunately, many of the organic materials including the electron and hole blockers are known to dramatically reduce device stability due to electrochemical degradation. Consequently, a known stable, albeit inefficient, structure of ITO/HATCN (10nm)/NPD (40nm)/ 16% Pt2O2: CBP (25nm)/BAlq (10nm)/Alq (30nm)/ LiF/Al can be used, where CBP is 4,4'-bis(N-carbazolyl) biphenyl, BAlq is bis(2-methyl-8-quinolinolato) (biphenyl-4-olato)aluminum and Alq is tris-(8-hydroxyquinoline) aluminum.[132] The resulting external quantum efficiency shown in Figure 85 is reduced to 12.5% due to the lack of state of the art blocking or transport materials resulting in charge imbalance or poor charge and exciton confinement. Nevertheless, such an efficiency is much higher that most previous reports employing a similar device structure.[132] The EL spectra (Figure 85 inset) shows similar emission to that observed in the efficient device structure except with the addition of a small peak between 400-500nm indicating poor exciton confinement. Remarkably, this small deep blue peak complimented the warm white Pt2O2 color to yield a CRI of 80 and CIE of (0.46,0.47). Accelerated lifetime testing was preformed on the device by driving it at a constant current of 20mA/cm^2 corresponding to an initial luminance of 2520 cd/m^2. The device demonstrated a lifetime to 80% of initial luminance (LT80) of 43 h at these elevated conditions. This corresponds to 207 h at 1000cd/m^2 or over 10,000 h at 100cd/m^2 using the conversion equation $LT(L_1)=LT(L_0)*(L_0/L_1)^{1.7}$ where L_0 is the measured luminance and L_1 is the desired luminance.[169] Further application of state of the art stable host, charge and exciton blocker, and charge transport materials may yeild even greater lifetimes. [116,170] The acheivement of stable and efficient Pt2O2 doped white devices with peak EQE of 12.5%, CRI of 80 and LT80 of over 200 h at 1000cd/m^2 is greater than that previously acheived for Pt7O7 and represents a significant step towards the possible commercializaiton of single doped OLED for solid state lighting.

In order to achieve better CRI and CIE in a single doped white device it is necessary to blue shift the monomer emission of Pt2O2. By replacing one of the phenyl-methylimidazole ligands of Pt2O2 with a higher energy ligand such as phenyl pyrazole (Pt1O2) or phenyl dimethyl-pyrazole (Pt1O2me$_2$), the PL emission (Figure 83) shifts to 474nm and 472nm respectively. These values are in accordance with most reported Pt emitters containing phenyl methyl-imidazole emissive ligands and should serve well for achieving white light while remaining compatible with known stable carbazole-based host materials.[159] The origin for the red shift in Pt2O2 relative to its analogs is under continued investigation but is similar to the shift reported for other symmetric Pt complexes.[153]

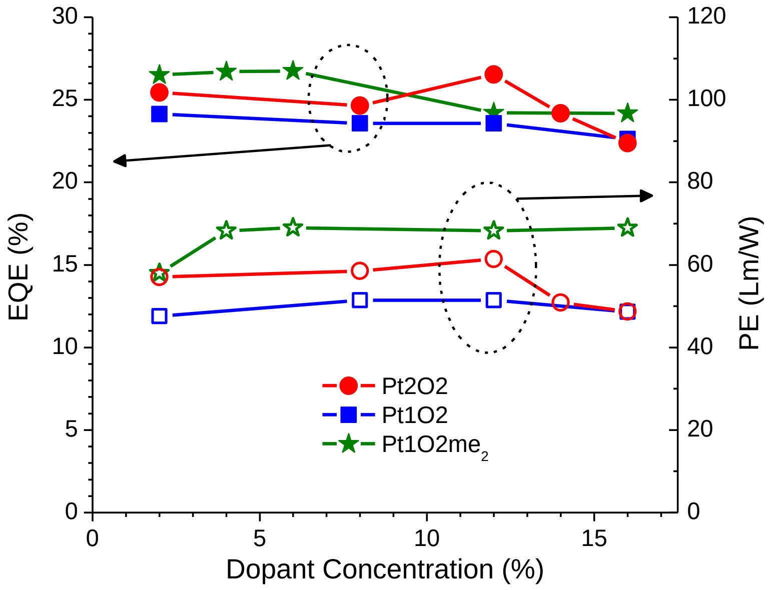

Figure 87. Peak EQE (solid symbols) and peak power efficiency (open symbols) for devices of Pt1O2, Pt2O2, and Pt1O2me$_2$ in the device structure: ITO/HATCN (10nm)/NPD (40nm)/TAPC (10nm)/x% Dopant: 26mCPy (25nm)/DPPS (10nm)/BmPyPB (40nm)/LiF (1nm)/ Al

Devices with various concentrations of Pt1O2 and Pt1O2me$_2$ where fabricated in the structure: ITO/HATCN(10 nm)/NPD(40 nm)/TAPC(10 nm)/x% emitter: 26mCPy(25 nm)/DPPS(10 nm)/BmPyPB(40 nm)/LiF/Al. As shown in Figure 87 and Table 10, both Pt1O2 and Pt1O2me$_2$ are also very efficient across all tested concentrations. The peak external quantum efficiency ranged from 22.6% to 24.1% for Pt1O2 and 24.2% to 26.7% for Pt1O2me$_2$ while the power efficiency ranged from 47.6 to 51.4 Lm/W and 58.0 to 69.0 Lm/W respectively. These results further demonstrate the high efficiencies of both the monomer and excimer species characteristic for this class of emitters.

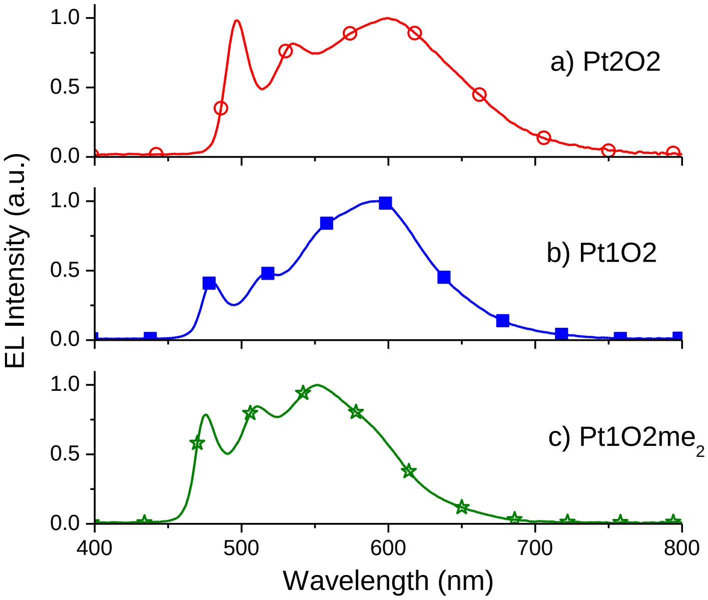

Figure 88. The EL spectra for white devices of a) 14% Pt2O2, b) 12% Pt1O2, and c) 6% Pt1O2me$_2$ in the structure: ITO/HATCN (10nm)/NPD (40nm)/TAPC (10nm)/x% Dopant: 26mCPy (25nm)/DPPS (10nm)/BmPyPB (40nm)/LiF (1nm)/ Al.

The emission spectra for white devise of Pt2O2, Pt1O2, and Pt1O2me$_2$ are shown in Figure 88 for concentrations of 14%, 12%, and 6% respectively. In accordance with the difference in the PL spectra, the monomer emission peak of both Pt1O2 (480nm) and Pt1O2me$_2$ (476nm) is blue shifted relative to Pt2O2 (496nm). The excimer emission peak on the other hand, is only slightly blue shifted for Pt1O2 (592 nm) compared to Pt2O2 (600 nm) although it is more narrow. This similarity in excimer emission is as expected due to the similarity in shape and planarity of the two molecules. The excimer emission of Pt1O2me$_2$, on the other hand, was significantly blue shifted to 556 nm. This shift is attributed to the likely distortion of the molecule due to the steric hindrance of methyl group on the 5 position of the pyrazole as has been reported previously with symmetric phenyl pyrazole Pt complexes.[197] Such distortion ultimately leads to a larger intermolecular spacing when two dopant molecules stack which leads to a higher energy for the excimer species. It is interesting however, that Pt1O2me$_2$ is capable of exhibiting such strong excimer character despite this increased intermolecular separation. As a result of the lessened constraints on intermolecular separation for excimer formation, there is a higher probability of excimer formation at a given concentration. At a Pt1O2me$_2$ concentration of only 8%, the emission spectrum is nearly dominated by excimer emission. Thus, in the design of white emitting square planar complexes, the choice of cyclometalating ligand needs to be carefully selected to achieve appropriate emission energy of both the monomer and excimer by controlling both the influence of both cyclometalating ligands on the energy of the monomer species and the effect of steric groups on the geometry of the complex.

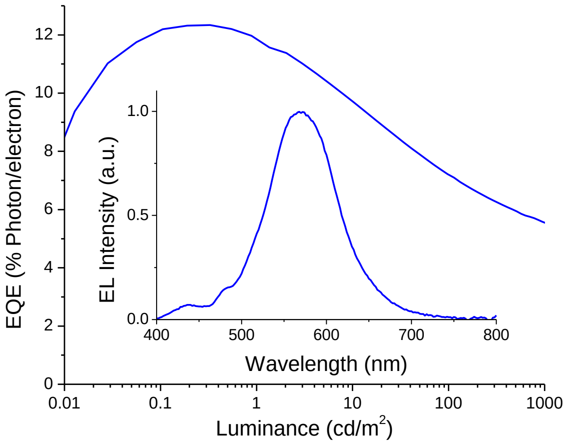

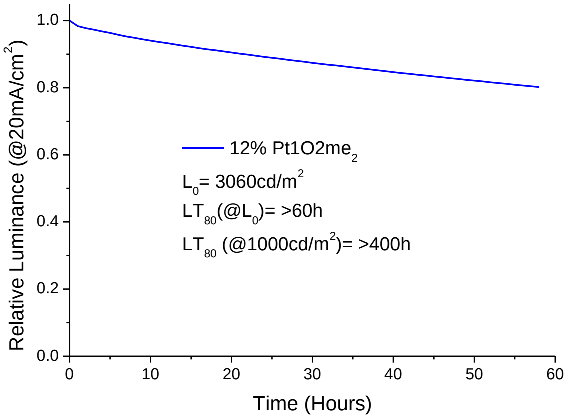

Figure 89. a) EQE vs. Luminance and EL spectra at 1mA/cm^2 (inset) and b) Luminance versus time plots for Pt1O2me$_2$ operated at a constant driving current of 20mA/cm^2 with the initial luminance and T_{80} values are given in the inset to the plot for devices with the structure: ITO/HATCN (10nm)/NPD (40nm)/ 12% Pt1O2me$_2$: CBP (25nm)/BAlq (10nm)/Alq (30nm)/LiF (1nm)/ Al.

An additional consequence of the efficient excimer emission at low concentrations for Pt1O2me$_2$ is the opportunity to explore the stability of the isolated excimer emissive species in a device setting. Device operational lifetime measurements were carried out for devices of the structure: ITO/HATCN (10nm)/NPD (40nm)/ 12% Pt1O2me$_2$: CBP (25nm)/BAlq (10nm)/Alq (30nm)/ LiF/Al. These devices exhibited nearly exclusive excimer emission which peaked at 567nm yielding an orange color with CIE coordinates of (0.43, 0.50) as shown in Figure 89a. The devices were also moderately efficient with a peak EQE of 12.3%, which is similar to that achieved with Pt2O2 in the stable device structure. For operational lifetime testing, devices were driven at a constant current of 20mA/cm^2 which corresponds to an initial luminance of 3060 cd/m^2. The device demonstrated an LT80 over 60h. which corresponds to over 400h. at 1000cd/m^2, which is amongst the highest for any Pt emitters. This long lifetime demonstrates that the excimer species can be very stable and should serve as a benchmark for future excimer based devices.

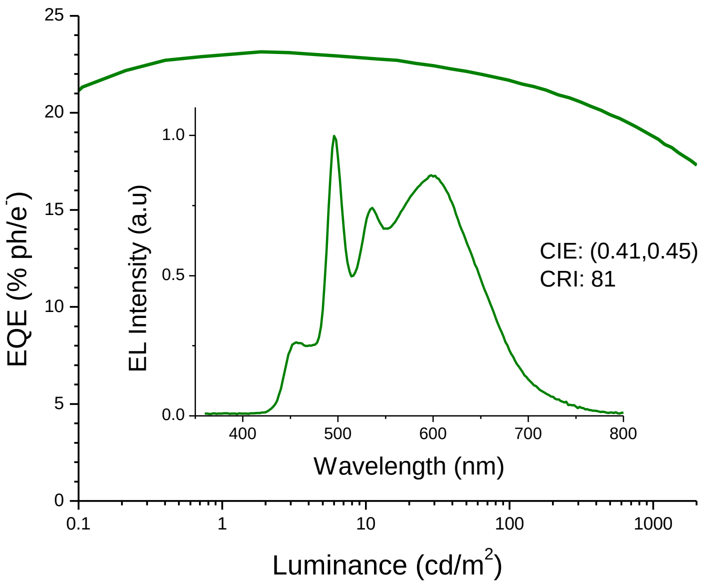

Figure 90. EQE vs. Luminance and EL spectra at 1mA/cm^2 (inset) for the multiple emissive layer white device in the structure: ITO/HATCN (10nm)/NPD (40nm)/TAPC (10nm)/16% Pt2O2:26mCPy (10nm)/6% PtON1:26mCPy (15nm)/DPPS (10nm)/BmPyPB(40)/LiF/Al

Due to the poor spectral coverage in the blue region with these select emitters, these Pt complexes can used as emitters in white devices employing multiple emissive layers to achieve a high efficiency and a high quality of white light. Due to the broad spectral coverage of the monomer and excimer emission, efficient OLEDs with emission covering most of the visible spectrum can be acheived using only 2 emissive materials. This is greatly desired compared to white OLEDs containing 3 or more emissive layers since the optimiztion of charge transport and energy transfer processes in white OLEDs becomes increasingly complex with additional layers.[205] Multilayer white OLEDs containing Pt2O2 and the previously reported deep blue emitter, PtON1, are fabricated in the structure ITO/HATCN(10 nm)/NPD(40 nm)/TAPC(10 nm)/ 16% Pt2O2: 26mCPy (10nm)/6% PtON1: 26mCPy/DPPS(10 nm)/BmPyPB(40 nm)/LiF/Al (15nm). The external quantum efficiency, shown in Figure 90, peaked at 23.1% and the power efficiency peaked at 49.7 Lm/W. The device had low roll-off at high current densities remaining at 18.8% EQE and 24.2 Lm/W at 1000cd/m^2. The emission spectrum showed a moderate deep blue contribution from PtON1 which dramatically improved the CRI to 81 and the CIE coordinates to (0.41,0.45). Further optimization and color balance of such devices is likely to yeild much greater performance but this demonstration underlines the importance of incoproroting the deep blue portion of the emission spectrum.

Table 10. Performance parameters of devices in the structure: ITO/HATCN (10nm)/NPD (40nm)/TAPC (10nm)/x% emitter:26mCPy (25nm)/DPPS (10nm)/BmPyPB(40)/LiF/Al

				Peak		1000 cd/m^2	
Dopant	Conc. (% w/w)	CIE†	CRI†	η_{EQE} (%)	η_{PE} (Lm/W)	η_{EQE} (%)	η_{PE} (Lm/W)
Pt2O2	2	(0.231,0.565)	--	25.4	57.1	18.2	27.2
Pt2O2	8	(0.327,0.536)	42	24.6	58.5	19.6	28.2
Pt2O2	12	(0.411,0.512)	58	26.5	61.4	20.1	29.8
Pt2O2	14	(0.450,0.489)	68	24.1	50.9	21.4	29.9
Pt2O2	16	(0.475,0.478)	72	22.4	48.7	19.2	25.0
Pt1O2	2	(0.215,0.438)	--	24.1	47.6	16.9	20.0
Pt1O2	8	(0.359,0.455)	61	23.6	51.4	17.7	24.7
Pt1O2	12	(0.454,0.480)	61	23.1	53.5	18.5	27.5

Pt1O2	16	(0.485,0.479)	57	22.6	48.7	19.3	28.8
Pt1O2me$_2$	2	(0.229,0.440)	--	26.5	58.0	17.6	24.2
Pt1O2me$_2$	4	(0.318,0.496)	44	26.7	68.3	17.6	28.5
Pt1O2me$_2$	6	(0.354,0.513)	45	24.7	69.0	17.7	31.0
Pt1O2me$_2$	12	(0.416,0.528)	44	24.2	68.2	20.4	35.7
Pt1O2me$_2$	16	(0.422,0.531)	42	24.2	69.0	20.6	35.4

† Color coordinates and CRI determined from spectrum collected at 1mA/cm^2

8. CONCLUSIONS AND FUTURE OUTLOOK

Through this work I have presented a number of materials and device structures for efficient organic optoelectronic devices, and laid out a number of structure-property relationships for further enhancements going forward. For OPVs, enhancement in the open circuit voltage was demonstrated through molecular modification to bring the V_{OC} closer to the effecting bandgap, ΔE_{DA}. This allowed the achievement of 1V V_{OC} for a heterojunction of a select Ir complex with estimated exciton energy of only 1.55eV. While a number of other material systems have also achieved high V_{OC}, this has typically been achieved through large ΔE_{DA} or large optical bandgaps which reduces the options for further increasing open circuit voltage or extending absorption. Furthermore, the development of anode interfacial layer for exciton blocking and molecular templating provide a general approach for enhancing the short circuit current and was demonstrated to be compatible with a large number of material systems. The ultimate achievement of 5.8% PCE in a single heterojunction of a phthalocyanine based material and C_{60} was remarkable considering the simplicity of the materials system and device structure. It is worth noting that the ZnPc material is prepared in a simple, one step, solvent free, synthesis and belongs to the family of dyes which are already produced in quantities on the order of millions of Kg.

Nevertheless, the OPV device performances presented here are less efficient that those using state-of-the-art donor and acceptor materials or advanced devices structures such as tandem devices, or light trapping techniques. It is fully expected that the two major OPV development principles demonstrated here (i.e. pushing Voc closer to EDA and applying exciton blocking anode interfacial layers) can be generally applied and incorporation of these principles with the state-of-the-art materials or device structures may lead to devices which are simplified and efficient enough to be an economic alternative to expensive crystalline Si cells.

For OLEDs, a number of efficient and stable Pt emitters emitting across the visible spectrum were demonstrated. In particular the development of deep blue emitters employing phenyl methylimidazole carbene or phenyl pyrazole cyclometalating ligands was extremely fruitful. Ultimately, a peak EQE of 24.8% and nearly perfect blue emission of (0.148,0.079) from the narrow band emitting, halogen free, tetradentate Pt complex, PtON7dtb, was achieved. Such an achievement approaches the maximum attainable performance from a blue OLED, with its near ideal color and IQE approaching unity, all while employing a halogen free ligand design that is aligned with electrochemically stable molecular designs. Furthermore, a new generation of emitter was introduced which exhibits both phosphorescence and delayed fluorescence emission in order to achieve a high energy emission while maintaining low triplet energy. This provides a potential route for highly efficient and stable deep blue emission which is compatible with known stable host and transport materials. Such a class of emitters is likely to make a big impact in the OLED field and continued development on these complexes will continue and likely have a role in next generation display and lighting technologies.

In addition to the development of deep blue emitters for display and lighting technologies, white OLEDs were also developed. Utilizing the excimer formation properties of square-planar Pt complexes, highly efficient and stable white devices employing a single emissive material were developed. A peak EQE of over 20% for pure white color (0.33,0.33) and 80 CRI was achieved with the tridentate Pt complex, Pt-16. Furthermore, the development of a series of tetradentate Pt complexes yielded highly efficient and stable single doped white devices due to their halogen free tetradentate design. Nevertheless, more emissive materials with excimer emission are needed to more fully understand the principles of the formation of excimers and the relationship of molecular structure with emission color and efficiency. Furthermore, the development of a stable and efficient single doped white OLED with ideal white color is still needed which will require deeper blue monomer emission, as well as stable and efficient transport and host materials to support such a high energy emission. The principles of color tuning, and efficiency achievements shown here mark an important step towards such a goal.

REFERENCES

1. N.S. Lewis, D. G. Nocera, Powering the planet: Chemical challenges in solar energy utilization. *Proceedings of the National Academy of Sciences USA*, **103**, 15729-15735 (2006); DOI: 10.1073/pnas.0603395103

2. U.S. Department of Energy. "Basic Research Needs for Solar Energy Utilization". www.er.doe.gov/bes/reports/abstracts.html#SEU

3. N.S. Lewis, Toward Cost-Effective Solar Energy Use. *Science*, **315**, 798-801 (2006**)**; DOI: 10.1126/science.1137014

4. Nobel Media AB, "Press Release: The 2000 Nobel Prize in Chemistry." http://www.nobelprize.org/nobel_prizes/chemistry/laureates/2000/press.html

5. S. R. Forrest, M. E. Thompson, Introduction: Organic Electronics and Optoelectronics. *Chemical Reviews*, **107**, 923-925 (2007); DOI: 10.1021/cr0501590

6. M. D. Halls, D. J. Giesen, T. F. Hughes, A. Goldberg, Y. Cao, High-throughput quantum chemistry and virtual screening for OLED material components. *Proceedings of SPIE*, **8829**, 882926 (2013). DOI: 10.1117/12.2025092

7. S. R. Forrest, The path to ubiquitous and low-cost organic electronic appliances on plastic. *Nature*, **428**, 911-918 (2004); DOI: 10.1038/nature02498.

8. V. Coropceanu, J. Cornil, D. A. S. Filho, Y. Olivier, R. Silbey, J.-L. Brédas, Charge Transport in Organic Semiconductors. *Chemical Reviews*, **107**, 926−952 (2007); DOI: 10.1021/cr050140x.

9. Turro, N. J. *Modern Molecular Photochemistry*. Mill Valley, CA: University Science Books 1991.

10. D. M. Chapin, C. S. Fuller, G. L. Pearson, A New Silicon p-n Junction Photocell for Converting Solar Radiation into Electrical Power. *Journal of Applied Physics*, **25**, 676-677 (1954); DOI: 10.1063/1.1721711.

11. Nelson, J. *The Physics of Solar Cells*. London: Imperial College Press 2003.

12. W. Shockley, H. J. Queisser, Detailed Balance Limit of Efficiency of p-n Junction Solar Cells. *Journal of Applied Physics*, **32**, 510–519 (1991); DOI: 10.1063/1.1736034.

13. M.A. Green. K. Emery, Y. Hishikawa, W. Warta, E.D. Dunlop, Solar cell efficiency tables (Version 41) *Progress in Photovoltaics: Research and Applications*, **21**, 1-11(2013); DOI: 10.1002/pip.2352

14. P. Gregory, Industrial applications of phthalocyanines. *Journal of Porphyrins and Phthalocyanines*, **4**, 432-437, (2000).

15. F. Padinger, R. S. Rittberger, N. S. Sariciftci, Effects of Postproduction Treatment on Plastic Solar Cells. *Advanced Functional Materials,* **13**, 85, (2003); DOI: 10.1002/adfm.200390011

16. G. Li, V. Shrotriya, J. S. Huang, Y. Yao, T. Moriarty, K. Emery, Y. Yang, High-efficiency solution processable polymer photovoltaic cells by self-organization of polymer blends. *Nature Materials,* **4**, 864 - 868 (2005); DOI: 10.1038/nmat1500.

17. Y. Matsuo, Y. Sato, T. Niinomi, I. Soga, H. Tanaka, E. Nakamura, Columnar Structure in Bulk Heterojunction in Solution-Processable Three-Layered p-i-n Organic Photovoltaic Devices Using Tetrabenzoporphyrin Precursor and Silylmethyl[60]fullerene. *Journal of the American Chemical Societry,* **131**, 16048-16050 (2009); DOI: 10.1021/ja9048702.

18. J. Peet, J.Y. Kim, N.E. Coates, W.L. Ma, D. Moses, A.J. Heeger, G.C. Bazan, Efficiency enhancement in low-bandgap polymer solar cells by processing with alkane dithiols. *Nature Materials,* **6**, 497-500 (2007); DOI: 10.1038/nmat1928

19. P. Peumans, A. Yakimov, S. R. Forrest, Small molecular weight organic thin-film photodetectors and solar cells. *Journal of Applied Physics,* **93**, 3693 (2003); DOI: 10.1063/1.1534621

20. B. P. Rand, J. Genoe, P. Heremans, J. Poortmans, Solar cells utilizing small molecular weight organic semiconductors, *Progress in Photovoltaics: Research and Applications*, **15**, 659 (2007);DOI: 10.1002/pip.788

21. M. J. Currie, J. K. Mapel, T. D. Heidel, S. Goffri, M. A. Baldo, High-Efficiency Organic Solar Concentrators for Photovoltaics. *Science,* **321**, 226-228 (2008); DOI: 10.1126/science.1158342.

22. J. Xue, Perspectives on Organic Photovoltaics. *Polymer Reviews,* **50**, 411-419 (2010); DOI: 10.1080/15583724.2010.515766.

23. S.E. Shaheen, D.S. Ginley, G.E. Jabbour, Organic-Based Photovoltaics: Toward Low-Cost Power Generation. *MRS Bulletin,* **30**, 10-19 (2005); DOI: 10.1557/mrs2005.2

24. F.C. Krebs, *Polymeric Solar Cells: Materials, Design, Manufacture.* Lancaster, PA, USA: DEStech Publications Inc. 2010.

25. A. K. Ghosh, D. L. Morel, T. Feng, R. F. Shaw, C. A. Rowe Jr., Photovoltaic and rectification properties of Al/Mg phthalocyanine/Ag Schottky-barrier cells. *Journal of Applied Physics,* **45**, 230 (1974); DOI: 10.1063/1.1662965

26. Tang C.W. Two-layer organic photovoltaic cell. *Applied Physics Letters* **48**, 183 (1986); DOI: 10.1063/1.96937

27. J. Xue, S. Uchida, B. P. Rand, S. R. Forrest, 4.2% efficient organic photovoltaic cells with low series resistances. *Applied Physics Letters,* **84**, 3013 (2004); DOI: 10.1063/1.1713036

28. I. Kim, H.M. Haverinen, Z. Wang, S. Madakuni, Y. Kim, J. Li, G.E. Jabbour, Efficient Organic Solar Cells Based on Planar Metallophthalocyanines. *Chemistry of Materials,* **21**, 4256-4260 (2009); DOI: 10.1021/cm901320p

29. S. Uchida, J. Xue, B.P. Rand, S.R. Forrest, Organic small molecule solar cells with a homogeneously mixed copper phthalocyanine: C60 active layer. *Applied Physics Letters*, **84**, 4218 (2004); DOI: 10.1063/1.1755833

30. J. J. M. Halls, C. A. Walsh, N. C. Greenham, E. A. Marseglia, R. H. Friend, S. C. Moratti, A. B. Holmes, Efficient photodiodes from interpenetrating polymer networks. *Nature*, **376**, 498- 500 (2002); DOI:10.1038/376498a0

31. G. Yu, J. Gao, J. C. Hummelen, F. Wudl and A. J. Heeger, Polymer Photovoltaic Cells: Enhanced Efficiencies via a Network of Internal Donor-Acceptor Heterojunctions. *Science*, **270**, 1789-1791 (1995); DOI:10.1126/science.270.5243.1789.

32. M. T. Dang, L. Hirsch, G. Wantz, J. D. Wuest, Controlling the Morphology and Performance of Bulk Heterojunctions in Solar Cells. Lessons Learned from the Benchmark Poly(3-hexylthiophene):[6,6]-Phenyl-C61-butyric Acid Methyl Ester System. *Chemical Reviews,* **113**, 3734–3765 (2013); DOI: 10.1021/cr300005u.

33. J. Xue, B. P. Rand, S. Uchida, S. R. Forrest, A Hybrid Planar–Mixed Molecular Heterojunction Photovoltaic Cell. *Advanced Materials*, **17**, 66–70 (2005); DOI: 10.1002/adma.200400617.

34. R. Smith, F. R. Kogler, C. J. Brabec, Interface materials for organic solar cells. *Journal of Materials Chemistry,* **20**, 2499-2512 (2010); DOI: 10.1039/B921624C.

35. H. Gommans, B. Verreet, B. P. Rand, R. Muller, J. Poortmans, P. Heremans, J. Genoe, On the Role of Bathocuproine in Organic Photovoltaic Cells. *Advanced Functional Materials,* **18**, 3686–3691 (2008); DOI: 10.1002/adfm.200800815.

36. Y. Zheng, R. Bekele, J. Ouyang, J. Xue, Organic photovoltaic cells with vertically aligned crystalline molecular nanorods. *Organic Electronics,* **10**, 1621-1625 (2005); DOI: 10.1016/j.orgel.2009.08.009.

37. J.Y. Kim, K. Lee, N.E. Coates, D. Moses, T.Q. Nguyen, M. Dante, A.J. Heeger, Efficient Tandem Polymer Solar Cells Fabricated by All-Solution Processing. *Science,* **317**, 222-225 (2007); DOI: 10.1126/science.1141711.

38. J. Xue, S. Uchida, B. P. Rand, S. R. Forrest, Asymmetric tandem organic photovoltaic cells with hybrid planar-mixed molecular heterojunctions. *Applied Physics Letters,* **85**, 5757 (2004); DOI: 10.1063/1.1829776

39. W.A. Luhman, R. J. Holmes, Investigation of Energy Transfer in Organic Photovoltaic Cells and Impact on Exciton Diffusion Length Measurements. *Advanced Functional Materials,* **21**, 764–771, (2011); DOI: 10.1002/adfm.201001928.

40. T. M. Clarke, J. R. Durrant, Charge Photogeneration in Organic Solar Cells. *Chemical Reviews,* **110**, 110, 6736–6767 (2010); DOI: 10.1021/cr900271s.

41. C.J. Brabec, A. Cravino, D. Meissner, N.S. Sariciftci, T. Fromherz, M.T. Rispens, L. Sanchez, J.C. Hummelen, Origin of the Open Circuit Voltage of Plastic Solar Cells. *Advanced Functional Materials,* **11**, 374-380 (2011); DOI: 10.1002/1616-3028(200110)11:5<374::AID-ADFM374>3.0.CO;2-W.

42. K.L. Mutolo, E.I. Mayo, B.P. Rand, S.R. Forrest, M.E. Thompson, Enhanced Open-Circuit Voltage in Subphthalocyanine/C60 Organic Photovoltaic Cells. *Journal of the American Chemical Society,* **128**, 8108-8109 (2006); DOI: 10.1021/ja061655o.

43. F.B. Kooistra, J. Knol, F. Kastenberg, L.M. Popescu, W.J.H. Verhees, J.M. Kroon, J.C. Hummelen, Increasing the Open Circuit Voltage of Bulk-Heterojunction Solar Cells by Raising the LUMO Level of the Acceptor. *Organic Letters,* **9**, 551 (2007); DOI: 10.1021/ol062666p.

44. C. Uhrich, D. Wynands, S. Olthof, M.K. Riede, K. Leo, S. Sonntag, B. Maennig, M. Pfeiffer, Origin of open circuit voltage in planar and bulk heterojunction organic thin-film photovoltaics depending on doped transport layers. *Journal of Applied Physics,* **104**, 043107 (2008); DOI: 10.1063/1.2973199.

45. B.P. Rand, D.P. Burk, S.R. Forrest, Offset energies at organic semiconductor heterojunctions and their influence on the open-circuit voltage of thin-film solar cells. *Physical Review B*, **75**, 115327 (2007); DOI: 10.1103/PhysRevB.75.115327.

46. Ying Zheng and Jiangeng Xue, Organic Photovoltaic Cells Based on Molecular Donor-Acceptor Heterojunctions. *Polymer Reviews,* **50**, 420-453 (2010); DOI:10.1080/15583724.2010.516051.

47. J. Xue, B.P. Rand, S. Uchida, S.R. Forrest, Mixed donor-acceptor molecular heterojunctions for photovoltaic applications. II. Device performance *Journal of Applied Physics,* **98**, 124903 (2005); DOI: 10.1063/1.2142073

48. R.F. Salzman, J. Xue, B.P. Rand, A. Alexander, M.E. Thompson, S.R. Forrest, The effects of copper phthalocyanine purity on organic solar cell performance. *Organic Electronics*, **6**, 242 (2005); DOI: 10.1016/j.orgel.2005.09.001.

49. Sze, S.M., Ng, K.K., *Physics of Semiconductor Devices, 3rd ed.,* Hoboken, New Jersey: Wiley 2007.

50. J. Drechsel, B. Mannig, D. Gebeyehu, M. Pfeiffer, K. Leo, H. Hoppe, MIP-type organic solar cells incorporating phthalocyanine/fullerene mixed layers and doped

wide-gap transport layers *Organic Electronics*, **5**, 175 (2004); DOI: 10.1016/j.orgel.2003.11.005.

51. S.R. Forrest, Ultrathin Organic Films Grown by Organic Molecular Beam Deposition and Related Techniques, *Chemical Reviews*, **97**, 1793 (1997); DOI: 10.1021/cr941014o.

52. R.J.C. Brown, A.R. Kucernak, N.J. Long, C. Mongay-Batalla, Spectroscopic and electrochemical studies on platinum and palladium phthalocyanines. *New Journal of Chemistry,* **28**, 676-680 (2004); DOI: 10.1039/B401880J.

53. R.M. Christie, D.D. Deans, An investigation into the mechanism of the phthalonitrile route to copper phthalocyanines using differential scanning calorimetry. *Journal of the Chemical Society*, *Perkin Transactions 2,* **2**, 193-198 (1989); DOI: 10.1039/P29890000193.

54. W.J. Potscavage, S. Yoo, B. Kippelen, Origin of the open-circuit voltage in multilayer heterojunction organic solar cells. *Applied Physics Letters,* **93**, 193308 (2008); DOI: 10.1063/1.3027061.

55. J.D. Myers, T.-K. Tseng, J. Xue, Photocarrier behavior in organic heterojunction photovoltaic cells. *Organic Electronics,* **10**, 1182-1186 (2009); DOI: 10.1016/j.orgel.2009.05.023.

56. W. Y. Wong, C. L. Ho, Organometallic Photovoltaics: A New and Versatile Approach for Harvesting Solar Energy Using Conjugated Polymetallaynes. *Accounts of Chemical Research*, **43**, 1246-1256 (2010); DOI: 10.1021/ar1000378.

57. W. Lee, T-H. Kwon, J. Kwon, J-K. Kim, C. Lee, J-I. Hong, Effect of main ligands on organic photovoltaic performance of Ir(III) complexes. *New Journal of Chemistry*, **35**, 2557-2563 (2011); DOI: 10.1039/C1NJ20446G.

58. A. B. Tamayo, B. D. Alleyne, P. I. Djurovich, S. Lamansky, I. Tsyba, N. N. Ho, R. Bau, M. E. Thompson, Synthesis and Characterization of Facial and Meridional Tris-cyclometalated Iridium(III) Complexes. *Journal of the American Chemical Society*, **125**, 7337-7387 (2003); DOI: 10.1021/ja034537z.

59. M. A. Baldo, D. F. O'Brien, Y. You, A. Shoustikov, S. Sibley, M. E. Thompson, S. R. Forrest, Highly efficient phosphorescent emission from organic electroluminescent devices. *Nature*, **395**, 151 (1998); DOI:10.1038/25954.

60. D. D. T. Gryko, J. Piechowska, M. Gałęzowski, Strongly Emitting Fluorophores Based on 1-Azaperylene Scaffold. *Journal of Organic Chemistry*, **75**, 1297-1300 (2010); DOI: 10.1021/jo902443s.

61. I. Kim, H. M. Haverinen, Z. Wang, S. Madakuni, J. Li, G. E. Jabbour, Effect of molecular packing on interfacial recombination of organic solar cells based on

palladium phthalocyanine and perylene derivatives. *Applied Physics Letters*, **95**, 023305 (2009); DOI: 10.1063/1.3177349.

62. J. Li, P. I. Djurovich, B. D. Alleyne, M. Yousufuddin, N. N. Ho, J. C. Thomas, J. C. Peters, R. Bau, M. E. Thompson, Synthetic Control of Excited-State Properties in Cyclometalated Ir(III) Complexes Using Ancillary Ligands. *Inorganic Chemistry*, **44**, 1713-1727 (2005); DOI: 10.1021/ic048599h.

63. I. Kim, H. M. Haverinen, J. Li, G. E. Jabbour, Enhancement of device performance of organic solar cells by an interfacial perylene derivative layer. ACS *Applied Materials and Interfaces*, **2**, 1390-1394 (2010); DOI: 10.1021/am100039m.

64. Y. Shao, Y. Yang, Efficient Organic Heterojunction Photovoltaic Cells Based on Triplet Materials. *Advanced Materials*, **17**, 2841-2844 (2005); DOI: 10.1002/adma.200501297.

65. B. W. D’andrade, S. Datta, S. R. Forrest, P. Djurovich, E. Polikarpov, M. E. Thompson, Relationship between the ionization and oxidation potentials of molecular organic semiconductors. *Organic Electronics*, **6**, 11-20 (2005); DOI: 10.1016/j.orgel.2005.01.002.

66. M. D. Perez, C. Borek, S. R. Forrest, M. E. Thompson, Molecular and Morphological Influences on the Open Circuit Voltages of Organic Photovoltaic Devices. *Journal of the American Chemical Society*, **131**, 9281-9286 (2009); DOI: 10.1021/ja9007722.

67. C.W. Schlenker, M.E. Thompson, The molecular nature of photovoltage losses in organic solar cells. *Chemical Communications*, **47**, 3702-3716 (2011); DOI: 10.1039/C0CC04020G.

68. S. Chen, J.R. Manders, S-W. Tsang, F. so, Metal oxides for interface engineering in polymer solar cells. *Journal of Materials Chemistry*, **22**, 24202 (2012); DOI: 10.1039/C2JM33838F.

69. H. Ma, H-L. Yap, F. Huang, A. K-Y. Jen, Interface Engineering for Organic Electronics. *Advanced Functional Materials*, **20**, 1371 (2010); DOI: 10.1002/adfm.200902236.

70. Y. Cao, G. Yu, C. Zhang, R. Menon, A.J. Heeger, Polymer light-emitting diodes with polyethylene dioxythiophene–polystyrene sulfonate as the transparent anode. *Synthetic Metals*, **87**, 171 (1997); DOI: 10.1016/S0379-6779(97)03823-X.

71. F. So, D. Kondakov, Degradation Mechanisms in Small-Molecule and Polymer Organic Light-Emitting Diodes. *Advanced Materials*, **22**, 3762 (2010); DOI: 10.1002/adma.200902624.

72. K. S. Yook, B. D. Chin, J. Y. Lee, B. E. Lassiter, S. R. Forrest, Vertical orientation of copper phthalocyanine in organic solar cells using a small molecular weight organic

templating layer. *Applied Physics Letters*, **99**, 043308 (2011); DOI: 10.1063/1.3621837.

73. Y-D. Liu, B. Chu, Z-S. Su, W-L. Li, T-J. Zhuang, F-M. Jin, X-W. Yan, B. Zhao, F. Zhang, D. Fan, J-B. Wang, Y. Gao, Mechanisms of the improved organic photovoltaic performance by using electron-transporting CuPc derivative as anode modifying layer. *Organic Electronics*, **13**, 2865 (2012); DOI: 10.1016/j.orgel.2012.08.027 .

74. M.D. Irwin, D. B. Buchholz, A.W. Hains, R.P.H. Chang, T. J. Marks, p-Type semiconducting nickel oxide as an efficiency-enhancing anode interfacial layer in polymer bulk-heterojunction solar cells. *Proceedings of the National Academy of Sciences U.S.A.*, **105**, 2783 (2008); DOI: 10.1073/pnas.0711990105.

75. C. H. Cheng, J. Wang, G. T. Du, S. H. Shi, Z. J. Du, Z. Q. Fan, J. M. Bian, M. S. Wang, Organic solar cells with remarkable enhanced efficiency by using a CuI buffer to control the molecular orientation and modify the anode. *Applied Physics Letters*, **97**, 083305 (2010); DOI: 10.1063/1.3483159.

76. P. Sullivan, T. S. Jones, A. J. Ferguson, S. Huetz, Structural templating as a route to improved photovoltaic performance in copper phthalocyanine/fullerene (C60) heterojunctions. *Applied Physics Letters*, **91**, 233114 (2007); DOI: 10.1063/1.2821229.

77. B. Yu, L. Huang, H. Wang, D. Yan, Efficient Organic Solar Cells Using a High-Quality Crystalline Thin Film as a Donor Layer. *Advanced Materials*, **22**, 1017 (2010); DOI: 10.1002/adma.200903023.

78. W. Zhao, J. P. Mudrick, Y. Zheng, W. T. Hammond, Y. Yang, J. Xue, Enhancing photovoltaic response of organic solar cells using a crystalline molecular template. *Organic Electronics*, **13**, 129 (2012); DOI: 10.1016/j.orgel.2011.10.016.

79. T-M. Kim, J. W. Kim, H-S. Shim, J-J. Kim, High efficiency and high photo-stability zinc-phthalocyanine based planar heterojunction solar cells with a double interfacial layer. *Applied Physics Letters*, **101**, 113301 (2012); DOI: 10.1063/1.4748123.

80. R. R. Lunt, J. B. Benziger, S.R. Forrest, Relationship between Crystalline Order and Exciton Diffusion Length in Molecular Organic Semiconductors. *Advanced Materials*, **22**, 1233 (2010); DOI: 10.1002/adma.200902827.

81. C. Schünemann, C. Elschner, A.A. Levin, M. Levichkova, K. Leo, M. Riede, Zinc phthalocyanine-Influence of substrate temperature, film thickness, and kind of substrate on the morphology. *Thin Solid Films*, **519**, 3939 (2011); DOI: 10.1016/j.tsf.2011.01.356.

82. T. B. Fleetham, N. Bakkan, J. P. Mudrick, J. D. Myers, V. D. Cassidy, J. Cui, J. Xue, J. Li, Enhanced open-circuit voltage in organic photovoltaic cells with partially

chlorinated zinc phthalocyanine. *Journal of Material Science*, **48**, 7104 (2013); DOI: 10.1007/s10853-013-7525-0.

83. B. P. Rand, J. Xue, S. Uchida, S. R. Forrest, Mixed donor-acceptor molecular heterojunctions for photovoltaic applications. I. Material properties. *Journal of Applied Physics,* **98,** 124902 (2005); DOI: 10.1063/1.2142072

84. S. Abthagir, Y.-G. Ha, E.-A. You, S.-H. Jeong, H.-S. Seo, J.-H. Choi, Studies of Tetracene- and Pentacene-Based Organic Thin-Film Transistors Fabricated by the Neutral Cluster Beam Deposition Method. *Journal of Physical Chemistry,***109**, 23918 (2005); DOI: 10.1021/jp054894r.

85. C. Schünemann, D. Wynands, K.-J. Eichhorn, M. Stamm, K. Leo, M. Riede, Evaluation and Control of the Orientation of Small Molecules for Strongly Absorbing Organic Thin Films. *Journal of Physical Chemistry C*, **117**, 11600 (2013); DOI: 10.1021/jp400604j.

86. W. Helfrich, W. G. Schneider, Recombination Radiation in Anthracene Crystals. *Physical Review Letters*, ***14***, 229 (1965); DOI: 10.1103/PhysRevLett.14.229.

87. C W. Tang, S. A. VanSlyke, Organic electroluminescent diodes. *Applied Physics Letters*, ***51***, 913 (1987); DOI: 10.1063/1.98799.

88. C. W. Tang, S. A. VanSlyke, C. H. Chen, Electroluminescence of doped organic thin films. *Journal of Applied Physics*, **65**, 3610-3616 (1989); DOI: 10.1063/1.343409.

89. M. A. Baldo, D. F. O'Brien, M. E. Thompson, S. R. Forrest, The excitonic singlet-triplet ratio in a semiconducting organic thin film. *Phys. Rev. B*, **60**, 14422– 14428 (1999); DOI: 10.1103/PhysRevB.60.14422.

90. H. Yersin, Triplet Emitters for OLED Applications. Mechanisms of Exciton Trapping and Control of Emission Properties. *Topics in Current Chemistry*, **241**, 1-26, (2004); DOI 10.1007/b96858.

91. P.-T. Chou, Y. Chi, Phosphorescent Dyes for Organic Light-Emitting Diodes. *Chemistry-A European Journal*, **13**, 380-395 (2007); DOI: 10.1002/chem.200601272.

92. T. Forster, Transfer mechanisms of electronic excitation. *Discussions of the Faraday Society*, **27**, 7-17 (1959).

93. M. A. Baldo, S. R. Forrest, Transient analysis of organic electrophosphorescence: I. Transient analysis of triplet energy transfer. *Physical Review B*, **62**, 10958 (2000); DOI: 10.1103/PhysRevB.62.10958

94. S.R. Forrest, D.D.C. Bradley, M.E. Thompson, Measuring the Efficiency of Organic Light-Emitting Devices. *Advanced Materials*, **15**, 1043-1048 (2003), DOI: 10.1002/adma.200302151.

95. K. Saxenaa, V.K. Jain, D. S.Mehta, A review on the light extraction techniques in organic electroluminescent devices. *Optical Materials*, **32**, 221-233 (2009); DOI: 10.1016/j.optmat.2009.07.014.

96. C. Adachi, R. C. Kwong, P. Djurovich, V. Adamovich, M. A. Baldo, M. E. Thompson, S. R. Forrest, Nearly 100% internal phosphorescence efficiency in an organic light-emitting device. *Applied Physics Letters*, **79**, 2082 (2001); DOI: 10.1063/1.1409582 .

97. Commission Internationale de l'Eclairage, *Proceedings of the 8th Session, Cambridge, 1931*. London: Cambridge University Press 1932

98. T.-C. Tsai, W.-Y. Hung, L.-C. Chi, K.-T. Wong, C.-C. Hsieh, P.-T. Chou, A new ambipolar blue emitter for NTSC standard blue organic light-emitting device. *Organic Electronics*, **10**, 158–162 (2009); DOI: 10.1016/j.orgel.2008.10.017.

99. S. Lamansky, P. Djurovich, D. Murphy, F. Abdel-Razzaq, H-E. Lee, C. Adachi, P. E. Burrows, S. R. Forrest, M. E. Thompson, Highly Phosphorescent Bis-Cyclometalated Iridium Complexes: Synthesis, Photophysical Characterization, and Use in Organic Light Emitting Diodes. *Journal of the American Chemical Society*, **123**, 4304-4312 (2001); DOI: 10.1021/ja003693s.

100. L.Xiao, Z. Chen, B. Qu, J. Luo, S. Kong, Q. Gong, J. Kido, Recent Progresses on Materials for Electrophosphorescent Organic Light-Emitting Devices. *Advanced Materials*, **23**, 926–952 (2011); DOI: 10.1002/adma.201003128 .

101. J. Brooks, Y. Babayan, S. Lamansky, P. I. Djurovich, I. Tsybe, R. Bau, M. E. Thompson, Synthesis and Characterization of Phosphorescent Cyclometalated Platinum Complexes. *Inorganic Chemistry*, **41**, 3055-3066 (2002); DOI: 10.1021/ic0255508.

102. F. I. Wu, H. J. Su, C. F. Shu, L. Y. Luo, W. G. Diau, C. H. Cheng, J. P. Duan, G. H. Lee, Tuning the emission and morphology of cyclometalated iridium complexes and their applications to organic light-emitting diodes. *Journal of Materials Chemistry*, **15**, 1035-1042 (2005); DOI: 10.1039/B415754K.

103. Y. J. Su, H. L. Huang, C. L. Li, C. H. Chien, Y. T. Tao, P. T. Chou, S. Datta, R. S. Liu, Highly Efficient Red Electrophosphorescent Devices Based on Iridium Isoquinoline Complexes: Remarkable External Quantum Efficiency Over a Wide Range of Current. *Advanced Materials*, **15**, 884-888 (2003); DOI: 10.1002/adma.200304630.

104. F. I. Wu, P. I. Shih, Y. H. Tseng, G. Y. Chen, C. H. Chien, C. F. Shu, Y. L. Tung, Y. Chi, A. K. Y. Jen, Highly Efficient Red-Electrophosphorescent Devices Based on Polyfluorene Copolymers Containing Charge-Transporting Pendant Units. *Journal of Physical Chemistry B*, **109**, 14000-14005 (2005); DOI: 10.1021/jp051747k.

105. A. Tsuboyama, H. Iwawaki, M. Furugori, T. Mukaide, J. Kamatani, S. gawa, T. Moriyama, S. Miura, T. Takiguchi, S. Okada, M. Hoshino, K. Ueno, Homoleptic Cyclometalated Iridium Complexes with Highly Efficient Red Phosphorescence and Application to Organic Light-Emitting Diode. *Journal of the American Chemical Society*, **125**, 12971-12979 (2003); DOI: 10.1021/ja034732d.

106. T. Sajoto, P. I. Djurovich, A. Tamayo, M. Yousufuddin, R. Bau, M. E. Thompson, R. J. Holmes, S. R. Forrest, Blue and Near-UV Phosphorescence from Iridium Complexes with Cyclometalated Pyrazolyl or N-Heterocyclic Carbene Ligands. *Inorganic Chemistry*, **44**, 7992-8003 (2005); DOI: 10.1021/ic051296i.

107. C.-H. Lin, Y.-Y. Chang, J.-Y. Hung, C.-Y. Lin, Y. Chi, M.-W. Chung, C.-L. Lin, P.-T. Chou, G.-H. Lee, C.-H. Chang, W.-C. Lin, Iridium(III) Complexes of a Dicyclometalated Phosphite Tripod Ligand: Strategy to Achieve Blue Phosphorescence Without Fluorine Substituents and Fabrication of OLEDs. *Angewandte Chemie*, **123**, 3240-3244 (2011); DOI: 10.1002/ange.201005624.

108. M. C. Gather, A. Kohnen, K. Meerholz, White Organic Light-Emitting Diodes. *Advanced Materials*, **23**, 233–248 (2011); DOI: 10.1002/adma.201002636.

109. K. S. Yook, J. Y. Lee, Organic Materials for Deep Blue Phosphorescent Organic Light-Emitting Diodes. *Advanced Materials*, **24**, 3169–3190 (2012); DOI: 10.1002/adma.201200627.

110. R. J. Holmes, S. R. Forrest, Y.-J. Tung, R. C. Kwong, J. J. Brown, S. Garon, M. E. Thompson, Blue organic electrophosphorescence using exothermic host–guest energy transfer. *Applied Physics Letters*, **82**, 2422 (2003); DOI: 10.1063/1.1568146.

111. V. I. Adamovich, S. R. Cordero, P. I. Djurovich, A. Tamayo, M. E. Thompson, B. W. D’Andrade, S. R. Forrest, New charge-carrier blocking materials for high efficiency OLEDs. *Organic Electronics*, **4**, 77-87 (2003); DOI: /10.1016/j.orgel.2003.08.003.

112. H. Sasabe, H. Nakanishi, Y. Watanabe, S. Yano, M. Hirasawa, Y.-J. Pu, J. Kido, Extremely Low Operating Voltage Green Phosphorescent Organic Light-Emitting Devices. *Advanced Functional Materials*, **23**, 5550-5555 (2013); DOI: 10.1002/adfm.201301069.

113. J. Lee, J.-I. Lee, K.-I. Song, S. J. Lee, H. Y. Chu, Influence of doping profile on the efficiency of blue phosphorescent organic light-emitting diodes. *Applied Physics Letters*, **92**, 133304 (2008); DOI: 10.1063/1.2904632.

114. P. M. Borsenberger, L. Pautmeier, R. Richert, H. Bässler, Hole transport in 1,1 -bis(di-4-tolylaminophenyl)cyclohexane. *The Journal of Chemical Physics*, **94**, 8276 (1991); DOI: 10.1063/1.460112.

115. S. O. Jeon, S. E. Jang, H. S. Son, J. Y. Lee, External Quantum Efficiency Above 20% in Deep Blue Phosphorescent Organic Light-Emitting Diodes. *Advanced Materials*, **23**, 1436-1441 (2011); DOI: 10.1002/adma.201004372.

116. H. Nakanotani, K. Masui, J. Nishide, T. Shibata, C. Adachi, Promising operational stability of high-efficiency organic light-emitting diodes based on thermally activated delayed fluorescence. *Scientific Reports*, **3**, 2127 (2013); DOI:10.1038/srep02127.

117. Y. Sun, S. R. Forrest, High-efficiency white organic light emitting devices with three separate phosphorescent emission layers. *Applied Physics Letters*, **91**, 263503 (2007); DOI: 10.1063/1.2827178.

118. H. Antoniadis, M. A. Abkowitz, B. R. Hsieh,Carrier deep-trapping mobility-lifetime products in poly(p-phenylene vinylene). *Applied Physics Letters*, **65**, 2030 (1994); DOI: 10.1063/1.112784

119. L. Xiao, S.-J. Su, Y. Agata, H. Lan, J. Kido, Nearly 100% Internal Quantum Efficiency in an Organic Blue-Light Electrophosphorescent Device Using a Weak Electron Transporting Material with a Wide Energy Gap. *Advanced Materials*, **21**, 1271-1274 (2009); DOI: 10.1002/adma.200802034.

120. D. Tanaka, T. Takeda, T. Chiba, S. Watanabe, J. Kido, Novel Electron-transport Material Containing Boron Atom with a High Triplet Excited Energy Level. *Chemistry Letters*, **36**, 262-263 (2007); DOI: 10.1246/cl.2007.262.

121. N. Chopra, J. Lee, Y. Zheng, S.-H. Eom, J. Xue, F. So, Effect of the Charge Balance on High-Efficiency Blue-Phosphorescent Organic Light-Emitting Diodes. ACS *Applied Materials and Interfaces*, **1**, 1169-1172 (2009); DOI: 10.1021/am900228b.

122. S. Kwon, K.-R. Wee, A.-L. Kim, S. O. Kang, Bis(4-(4,5-diphenyl-4H-1,2,4-triazol-3-yl)phenyl)dimethylsilane as Electron-Transport Material for Deep Blue Phosphorescent OLEDs. *Journal of Physical Chemistry Letters*, **1**, 295-299 (2010); DOI: 10.1021/jz900238h.

123. L. S. Hung, C. W. Tang, M. G. Mason, Enhanced electron injection in organic electroluminescence devices using an Al/LiF electrode. *Applied Physics Letters*, **70**, 152 (1997); DOI: 10.1063/1.118344.

124. H. Sasabe, E. Gonmori, T. Chiba, Y.-J. Li, D. Tanaka, S.-J. Su, T. Takeda, Y.-J. Pu, K. I Nakayama, J. Kido, Wide-Energy-Gap Electron-Transport Materials Containing 3,5-Dipyridylphenyl Moieties for an Ultra High Efficiency Blue Organic Light-Emitting Device. *Chemistry of Materials*, **20**, 5951-5953 (2008); DOI**:** 10.1021/cm801727d.

125. Y. Kawamura, K. Goushi, J. Brooks, J. J. Brown, H. Sasabe, C. Adachi, 100% phosphorescence quantum efficiency of Ir(III) complexes in organic semiconductor films. *Applied Physics Letters,* **86**, 071104 (2005); DOI: 10.1063/1.1862777.

126. E.L. Williams, K. Haavisto, J. Li, G.E. Jabbour, Excimer-Based White Phosphorescent Organic Light-Emitting Diodes with Nearly 100 % Internal Quantum Efficiency. *Advanced Materials,* **19**, 197-202 (2007); DOI: 10.1002/adma.200602174

127. Y. Tao , C. Yang, J. Qin, Organic host materials for phosphorescent organic light-emitting diodes. *Chemical Society Reviews,* **40**, 2943-2970 (2011) ; DOI: 10.1039/C0CS00160K

128. S. H. Kima, J. Janga, S. J. Leeb, J. Y. Lee, Deep blue phosphorescent organic light-emitting diodes using a Si based wide bandgap host and an Ir dopant with electron withdrawing substituents. *Thin Solid Films,* **517**, 722-726 (2008); DOI: 10.1016/j.tsf.2008.08.156.

129. H.-H. Chou, C.-H. Cheng, A Highly Efficient Universal Bipolar Host for Blue, Green, and Red Phosphorescent OLEDs. *Advanced Materials,* **22**, 2468-2471 (2010); DOI: 10.1002/adma.201000061.

130. N. Chopra, J. S. Swensen, E. Polikarpov, L. Cosimbescu, F. So, A. B. Padmaperuma, High efficiency and low roll-off blue phosphorescent organic light-emitting devices using mixed host architecture. *Applied Physics Letters,* **97**, 033304 (2010); DOI: 10.1063/1.3464969.

131. S.-W. Wen, M.-T. Lee, C. H. Chen, Recent Development of Blue Fluorescent OLED Materials and Devices. *Journal of Display Technology*, **1**, 90-99 (2005) ; DOI: 10.1109/JDT.2005.852802

132. R. C. Kwong, M. R. Nugent, L. Michalski, T. Ngo, K. Rajan, Y.-J. Tung, M. S. Weaver, T. X. Zhou, M. Hack, M. E. Thompson, S. R. Forrest, J. J. Brown, High operational stability of electrophosphorescent devices. *Applied Physics Letters*, **81**, 162 (2002); DOI: 10.1063/1.1489503.

133. S. Tokito, T. Iijima, Y. Suzuri, H. Kita, T. Tsuzuki, F. Sato, Confinement of triplet energy on phosphorescent molecules for highly-efficient organic blue-light-emitting devices. *Applied Physics Letters,* **83**, 569 (2003); DOI: 10.1063/1.1594834

134. J. S. Swensen, E. Polikarpov, A. V. Ruden, L. Wang, L. S. Sapochak, A. B. Padmaperuma, Improved Efficiency in Blue Phosphorescent Organic Light-Emitting Devices Using Host Materials of Lower Triplet Energy than the Phosphorescent Blue Emitter. *Advanced Functional Materials,* **21**, 3250 (2011); DOI: 10.1002/adfm.201100586.

135. Y. Zheng, S.-H. Eom, N. Chopra, J. Lee, F. So, J. Xue, Efficient deep-blue phosphorescent organic light-emitting device with improved electron and exciton confinement. *Applied Physics Letters,* **92**, 223301 (2008); DOI: 10.1063/1.2937403

136. S.-J. Ye, M.-F. Wu, C.-T. Chen, Y.-H. Song, Y. Chi, M.-H. Ho, S.-F. Chen, C. H. Chen, New Dopant and Host Materials for Blue-Light-Emitting Phosphorescent Organic Electroluminescent Devices. *Advanced Materials*, **17**, 285-289 (2005); DOI: 10.1002/adma.200401373.

137. K. S. Yook, S. E. Jang, S. O. Jeon, J. Y. Lee, Fabrication and Efficiency Improvement of Soluble Blue Phosphorescent Organic Light-Emitting Diodes Using a Multilayer Structure Based on an Alcohol-Soluble Blue Phosphorescent Emitting Layer. *Advanced Materials*, **22**, 4479-4483 (2010); DOI: 10.1002/adma.201002034.

138. K. S. Yook, S. O. Jeon, C. W. Joo, J. Y. Lee, High efficiency deep blue phosphorescent organic light-emitting diodes. *Organic Electronics*, **10**, 170-173 (2009); DOI: 10.1016/j.orgel.2008.10.018.

139. S. Haneder, E. DaComo, J. Feldmann, J. M. Lupton, C. Lennartz, P. Erk, E. Fuchs, O. Molt, I. Munster, C. Schildknecht, G. Wagenblast, Controlling the Radiative Rate of Deep-Blue Electrophosphorescent Organometallic Complexes by Singlet-Triplet Gap Engineering. *Advanced Materials*, **20**, 3325-3330 (2008); DOI: 10.1002/adma.200800630.

140. R. J. Holmes, S. R. Forrest, T. Sajoto, A. Tamayo, P. I. Djurocich, M. E. Thompson, J. Brooks, Y.-J. Tung, B. W. D'Andrade, M. S. Weaver, R. C. Kwong, J. J. Brown Saturated deep blue organic electrophosphorescence using a fluorine-free emitter. *Applied Physics Letters*, **87**, 243507 (2005); DOI: 10.1063/1.2143128.

141. H. Sasabe, J. Takamatsu, T. Matoyama, S. Watanabe, G. Wagenblast, N. Langer, O. Molt, E. Fuchs, C. Lennartz, J. Kido, High-Efficiency Blue and White Organic Light-Emitting Devices Incorporating a Blue Iridium Carbene Complex. *Advanced Materials*, **22**, 5003-5007 (2010); DOI: 10.1002/adma.201002254.

142. C.-H. Hsieh, F.-I. Wu, C.-H. Fan, M.-J. Huang, K.-Y. Lu, P.-Y. Chou, Y.-H. O. Yang, S.-H. Wu, I.-C. Chen, S.-H. Chou, K.-T. Wong, C.-H. Cheng, Design and Synthesis of Iridium Bis(carbene) Complexes for Efficient Blue Electrophosphorescence. *Chemistry-A European Journal*, **17**, 9180-9187 (2011); DOI: 10.1002/chem.201100317.

143. V. Sivasubramaniam, F. Brodkorb, S. Hanning, H. P. Loebl, V. Elsbergen, H. Boerner, U. Scherf, M. Kreyenschmidt, Fluorine cleavage of the light blue heteroleptic triplet emitter FIrpic. *Journal of Fluorine Chemistry*, **130**, 640–649 (2009); DOI: 10.1016/j.jfluchem.2009.04.009

144. K.-Y. Lu, H.-H. Chou, C.-H. Hsieh, Y.-H. O. Yang, H.-R. Tsai, H.-Y. Tsai, L.-C. Hsu, C.-Y. Chen, I.-C. Chen, C.-H. Cheng, Wide-Range Color Tuning of Iridium Biscarbene Complexes from Blue to Red by Different N^N Ligands: an Alternative Route for Adjusting the Emission Colors. *Advanced Materials*, **23**, 4933-4937 (2011); DOI: 10.1002/adma.201102886.

145. Y.-C. Chiu, J.-Y. Hung, T. Chi, C.-C. Chen, C.-H. Chang, C.-C. Wu, Y.-M. Cheng, Y.-C. Yu, G.-H. Lee, P.-T. Chou, En Route to High External Quantum Efficiency (~12%), Organic True-Blue-Light-Emitting Diodes Employing Novel Design of Iridium (III) Phosphors. *Advanced Materials*, **21**, 2221-2225 (2009); DOI: 10.1002/adma.200802546.

146. K. Li, G. Cheng, C. Ma, X. Guan, W.-M. Kwok, Y. Chen, W. Lu, C.-M. Che, Light-emitting platinum(II) complexes supported by tetradentate dianionic bis(N-heterocyclic carbene) ligands: towards robust blue electrophosphors. Chemical *Science*, **4**, 2630-2644 (2013); DOI: 10.1039/C3SC21822H.

147. J.Kalinowski, V. Fattori, M. Cocchi, J.A.G.Williams, Light-emitting devices based on organometallic platinum complexes as emitters. *Coordination Chemistry Reviews*, **255**, 2401-2425 (2011); DOI: 10.1016/j.ccr.2011.01.049.

148. B. Ma, P. I. Djurovich, S. Garon, B. Alleyne, M. E. Thompson, Platinum Binuclear Complexes as Phosphorescent Dopants for Monochromatic and White Organic Light-Emitting Diodes. *Advanced Functional Materials*, **16**, 2438-2446 (2006); DOI: 10.1002/adfm.200600614

149. U. S. Bhansali, E. Polikarpov, J. S. Swensen, W.-H. Chen, H. Jia, D. J. Gaspar, B. E. Gnade, A. B. Padmaperuma, M. A. Omary, High-efficiency turquoise-blue electrophosphorescence from a Pt(II)-pyridyltriazolate complex in a phosphine oxide host. *Applied Physics Letters*, **95**, 233304 (2009); DOI: 10.1063/1.3268434

150. Y. Unger, D. Meyer, O. Molt, C. Schildknecht, I. Münster, G. Wagenblast and T. Strassner, Green–Blue Emitters: NHC-Based Cyclometalated [Pt(C^C*)(acac)] Complexes. *Angewandte Chemie International Edition*, **49**, 10214-10216 (2010); DOI: 10.1002/anie.201001316

151. Z. M. Hudson, C. Sun, M. G. Helander, Y.-L. Chang, Z.-H. Lu, S. Wang, Highly Efficient Blue Phosphorescence from Triarylboron-Functionalized Platinum(II) Complexes of N-Heterocyclic Carbenes. *Journal of the American Chemical Society*, **134**, 13930-13933 (2012); DOI: 10.1021/ja3048656

152. L. Murphy, P. Brulatti, V. Fattori, M. Cocchi, J. A. G. Williams, Blue-shifting the monomer and excimer phosphorescence of tridentate cyclometallated platinum(II) complexes for optimal white-light OLEDs. *Chemical Communications*, **48**, 5817-5819 (2012); DOI: 10.1039/C2CC31330H.

153. D. A. K. Vezzu, J. C. Deaton, J. S. Jones, L. Bartolotti, C. F. Harris, A. P. Marchetti, M. Kondakova, R. D. Pike, S. Huo, Highly Luminescent Tetradentate Bis-Cyclometalated Platinum Complexes: Design, Synthesis, Structure, Photophysics, and Electroluminescence Application. *Inorganic Chemistry*, 49, 5107-5119 (2010); DOI: 10.1021/ic1002226.

154. K. Li, X. Guan, C.-W. Ma, W. Lu, Y. Chen, C.-M. Che, Blue electrophosphorescent organoplatinum(II) complexes with dianionic tetradentate

bis(carbene) ligands. *Chemical Communications*, **47**, 9075-9077 (2011); DOI: 10.1039/C1CC12943K.

155. A. F. Rausch, L. Murphy, J. A. G. Williams, H. Yersin, Improving the Performance of Pt(II) Complexes for Blue Light Emission by Enhancing the Molecular Rigidity. *Inorganic Chemistry*, **51**, 312-319 (2012); DOI: 10.1021/ic201664v.

156. X. Yang, Z. Xing, S. Madakuni, J. Li, G. E. Jabbour, Efficient Blue- and White-Emitting Electrophosphorescent Devices Based on Platinum(II) [1,3-Difluoro-4,6-di(2-pyridinyl)benzene] Chloride. *Advanced Materials*, **20**, 2405-2409 (2008); DOI: 10.1002/adma.200702940.

157. S. Develay, O. Blackburn, A. L. Thompson, J. A. G. Williams, Cyclometalated Platinum(II) Complexes of Pyrazole-Based, NCN-Coordinating, Terdentate Ligands: the Contrasting Influence of Pyrazolyl and Pyridyl Rings on Luminescence. *Inorganic Chemistry*, **47**, 11129-11142 (2008); DOI: 10.1021/ic8014157 .

158. V. Adamovich, J. Brooks, A. Tamayo, A. M. Alexander, P. I. Djurovich, B. W. D’Andrade, C. Adachi, S. R. Forrest, M. E. Thompson, High efficiency single dopant white electrophosphorescent light emitting diodes. *New Journal of Chemistry,* **26**, 1171-1178 (2002); DOI: 10.1039/B204301G.

159. X. Ren, J. Li, R. J. Holmes, P. I. Djurovich, S. R. Forrest, M. E. Thompson, Ultrahigh Energy Gap Hosts in Deep Blue Organic Electrophosphorescent Devices. *Chemistry of Materials*, **16**, 4743-4747 (2004); DOI: 10.1021/cm049402m.

160. N. C. Giebink, B. W. D’Andrade, M. S. Weaver, P. B. Mackenzie, J. J. Brown, M. E. Thompson, S. R. Forrest, Intrinsic luminance loss in phosphorescent small-molecule organic light emitting devices due to bimolecular annihilation reactions. *Journal of Applied Physics*, **103**, 044509 (2008); DOI: 10.1063/1.2884530

161. T. Sajoto, P. I. Djurovich, A. B. Tamayo, J. Oxgaard, W. A. Goddard III, M. E. Thompson, Temperature Dependence of Blue Phosphorescent Cyclometalated Ir(III) Complexes. *Journal of the American Chemical Society*, 131, 9813–9822 (2009); DOI: 10.1021/ja903317w.

162. Y. Shirasaki, G. J. Supran, M. G. Bawendi, V. Bulović, Emergence of colloidal quantum-dot light-emitting technologies. *Nature Photonics*, **7**, 13–23 (2013); DOI:10.1038/nphoton.2012.328.

163. K.-J. Chen, H.-C. Chen, K.-A. Tsai, C.-C. Lin, H.-H. Tsai, S.-H. Chien, B.-S. Cheng, Y.-J. Hsu, M.-H. Shih, C.-H. Tsai, H.-H. Shih, H.-C. Kuo, Resonant-Enhanced Full-Color Emission of Quantum-Dot-Based Display Technology Using a Pulsed Spray Method. *Advanced Functional Materials*, **22**, 5138-5143 (2012); DOI: 10.1002/adfm.201200765.

164. B.S. Mashford, M. Stevenson, Z. Popovic, C. Hamilton, Z. Zhou, C. Breen, J. Steckel, V. Bulovic, M. Bawendi, S. Coe-Sullivan, P. T. Kazlas, High-efficiency quantum-dot light-emitting devices with enhanced charge injection. *Nature Photonics*, *7*, 407-412 (2013); DOI:10.1038/nphoton.2013.70.

165. L. Qian, Y. Zheng, J. Xue, P. H. Holloway, Stable and efficient quantum-dot light-emitting diodes based on solution-processed multilayer structures. *Nature Photonics,* **5**, 543-548 (2011); DOI:10.1038/nphoton.2011.171.

166. K-H. Lee, J-H. Lee, W-S. Song, H. Ko, C. Lee, J-H. Lee, H. Yang, Highly Efficient, Color-Pure, Color-Stable Blue Quantum Dot Light-Emitting Devices. *ACS Nano*, **7**, 7295-7302 (2013); DOI: 10.1021/nn402870e.

167. J. Kido, Y. Okamoto, Organo Lanthanide Metal Complexes for Electroluminescent Materials. *Chemical Reviews*, **102**, 2357-2368 (2002); DOI: 10.1021/cr010448y.

168. G. Ponterini, N. Serpone, M. A. Bergkamp, T. L. Netzel, Comparison of Radiationless Decay Processes in Osmium and Platinum Porphyrins. *Journal of the American Chemical Society*, **105**, 4639-4645 (1983); DOI: 10.1021/ja00352a020.

169. C. Féry, B. Racine, D. Vaufrey, H. Doyeux, S. Cinà, Physical mechanism responsible for the stretched exponential decay behavior of aging organic light-emitting diodes. *Applied Physics Letters,* **87**, 213502 (2005); DOI: 10.1063/1.2133922

170. H. Fukagawa, T. Shimizu, H. Hanashima, Y. Osada, M. Suzuki, H. Fujikake, Highly Efficient and Stable Red Phosphorescent Organic Light-Emitting Diodes Using Platinum Complexes. *Advanced Materials,* **24**, 5099-5103 (2012); DOI: 10.1002/adma.201202167.

171. Q. Zhang, J. Li, K. Shizu, S. Huang, S. Hirata, H. Miyazaki, C. Adachi, Design of Efficient Thermally Activated Delayed Fluorescence Materials for Pure Blue Organic Light Emitting Diodes. *Journal of the American Chemical Society,* **134**, 14706-14709 (2012); DOI: 10.1021/ja306538w.

172. X. Ren, J. Li , R. J. Holmes , P. I. Djurovich , S. R. Forrest, M. E. Thompson, Ultrahigh Energy Gap Hosts in Deep Blue Organic Electrophosphorescent Devices. *Chemistry of Materials*, **16**, 4743-4747 (2004); DOI: 10.1021/cm049402m.

173. Q. Zhang, J. Li, K. Shizu, S. Huang, S. Hirata, H. Miyazaki, C. Adachi, Design of Efficient Thermally Activated Delayed Fluorescence Materials for Pure Blue Organic Light Emitting Diodes. *Journal of the American Chemical Society*, **134**, 14706 – 14709 (2012); DOI: 10.1021/ja306538w.

174. H. Uoyama, K. Goushi, K. Shizu, H. Nomura, C. Adachi, Highly efficient organic light-emitting diodes from delayed fluorescence. *Nature,* **492**, 234–238 (2012); DOI:10.1038/nature11687.

175. J.-Y. Hu, Y.-J. Pu, F. Satoh, S. Kawata, H. Katagiri, H. Sasabe, J. Kido, Bisanthracene-Based Donor–Acceptor-type Light-Emitting Dopants: Highly Efficient Deep-Blue Emission in Organic Light-Emitting Devices. *Advanced Functional Materials* (2013); DOI: 10.1002/adfm.201302907.

176. J. Michl, Relationship of bonding to electronic spectra. Comments. *Accounts of Chemical Research*, **23**, 127-128 (1990); DOI: 10.1021/ar00173a001

177. M. A. Baldo, M. E. Thompson, S. R. Forrest, High-efficiency fluorescent organic light-emitting devices using a phosphorescent sensitizer. *Nature,* **403**, 750-753 (2000); DOI:10.1038/35001541

178. M. Osawa, Highly efficient blue-green delayed fluorescence from copper(I) thiolate complexes: luminescence color alteration by orientation change of the aryl ring. *Chemical Communications*, **50**, 1801-1803 (2014); DOI: 10.1039/C3CC47871H

179. F. B. Dias, K. N. Bourdakos, V. Jankus, K. C. Moss, K. T. Kamtekar, V. Bhalla, J. Santos, M. R. Bryce, A. P. Monkman, Triplet Harvesting with 100% Efficiency by Way of Thermally Activated Delayed Fluorescence in Charge Transfer OLED Emitters. *Advanced Materials,* **25**, 3707-3714 (2013); DOI: 10.1002/adma.201300753

180. Q. Zhang, B. Li, S. Huang, H. Nomura, H. Tanaka, C. Adachi, Efficient blue organic light-emitting diodes employing thermally activated delayed fluorescence. *Nature Photonics,* **8**, 326–332 (2014) DOI:10.1038/nphoton.2014.12.

181. E. Turner, N. Bakken, J. Li, Cyclometalated Platinum Complexes with Luminescent Quantum Yields Approaching 100%. *Inorganic Chemistry,* **52**, 7344–7351 (2013); DOI: 10.1021/ic302490c.

182. P. K. Chow, C. Ma, W.-P. To, G. S. M. Tong, S.-L. Lai, S. C. F. Kui, W.-M. Kwok, C.-M. Che, Strongly Phosphorescent Palladium(II) Complexes of Tetradentate Ligands with Mixed Oxygen, Carbon, and Nitrogen Donor Atoms: Photophysics, Photochemistry, and Applications. *Angewandte Chemie International Edition,* **52**, 11775 –11779 (2013); DOI: 10.1002/anie.201305590.

183. C. Murawski, K. Leo, M. C. Gather, Efficiency Roll-Off in Organic Light-Emitting Diodes. *Advanced Materials,* **25**, 6801–6827 (2013); DOI: 10.1002/adma.201301603

184. F. So, J. Kido, P. Burrows, Organic Light-Emitting Devices for Solid-State Lighting. *MRS Bulletin*, **33**, 663-669 (2008); DOI:10.1557/mrs2008.137

185. S. Pimputkar, J.S. Speck, S.P. DenBaars, S. Nakamura, Prospects for LED lighting. *Nature Photonics*, **3**, 180-182 (2009); DOI:10.1038/nphoton.2009.32.

186. U.S. Department of Energy. "Solid State Lighting: Brilliant Solutions for America's Energy Future."

http://apps1.eere.energy.gov/buildings/publications/pdfs/ssl/ssl-overview_brochure_feb2013.pdf

187. Y. Narukawa, M. Ichikawa, D. Sanga, M. Sano, T. Mukai, White light emitting diodes with super-high luminous efficacy. *Journal of Physics D: Applied Physics*, **43**, 354002 (2010); DOI: 10.1088/0022-3727/43/35/354002

188. S. Reineke, F. Lindner, G. Schwartz, N. Seidler, K. Walzer, B. L¨ussem, K. Leo, White organic light-emitting diodes with fluorescent tube efficiency. *Nature*, **459**, 234-239 (2009); DOI:10.1038/nature08003.

189. Y. Sun, S. R. Forrest, High-efficiency white organic light emitting devices with three separate phosphorescent emission layers. *Applied Physics Letters*, **91**, 263503 (2007); DOI: 10.1063/1.2827178.

190. B.W. D'Andrade, M.E. Thompson, S.R. Forrest, Controlling Exciton Diffusion in Multilayer White Phosphorescent Organic Light Emitting Devices. *Advanced Materials*, **14**, 147-151 (2002); DOI: 10.1002/1521-4095(20020116)14:2<147::AID-ADMA147>3.0.CO;2-3

191. Y. Sun, N. C. Giebink, H. Kanno, B. Ma, M. E. Thompson, S. R. Forrest, Management of singlet and triplet excitons for efficient white organic light-emitting devices, *Nature*, **440**, 908-912 (2006); DOI:10.1038/nature04645.

192. B. Ma , J. Li , P. I. Djurovich , M. Yousufuddin , R. Bau , M. E. Thompson, Synthetic Control of Pt⋯Pt Separation and Photophysics of Binuclear Platinum Complexes. *Journal of the American Chemical Society*, **127**, 28-29 (2005); DOI: 10.1021/ja044313w

193. B.W. D'Andrade, J. Brooks, V. Adamovich, M.E. Thompson, S.R. Forrest, White Light Emission Using Triplet Excimers in Electrophosphorescent Organic Light-Emitting Devices. *Advanced Materials*, **14**, 1032-1036 (2002); DOI: 10.1002/1521-4095(20020805)14:15<1032::AID-ADMA1032>3.0.CO;2-6

194. B. D'Andrade, S. R. Forrest, Formation of triplet excimers and dimers in amorphous organic thin films and light emitting devices. *Chemical Physics*, **286**, 321-335 (2003); DOI: 10.1016/S0301-0104(02)00921-7

195. T. Fleetham, J. Ecton, Z. Wang, N. Bakken, J. Li, Single-Doped White Organic Light-Emitting Device with an External Quantum Efficiency Over 20%. *Advanced Materials*, **25**, 2573–2576 (2013); DOI: 10.1002/adma.201204602.

196. N. Bakken, Z. Wang, J. Li, Highly efficient white organic light-emitting device using a single emitter. *Journal of Photonics for Energy*, **2**, 021203 (2012); DOI:10.1117/1.JPE.2.021203

197. D. Kim, J.L. Brédas, Triplet Excimer Formation in Platinum-Based Phosphors: A Theoretical Study of the Roles of Pt−Pt Bimetallic Interactions and Interligand π−π

Interactions. *Journal of the American Chemical Society*, **131**, 11371-11380 (2009); DOI: 10.1021/ja809924t

198. B. Ma, P.I. Djurovich, M.E. Thompson, Excimer and electron transfer quenching studies of a cyclometalated platinum complex. *Coordination Chemistry Reviews*, **249**, 1501-1510 (2005); DOI: 10.1016/j.ccr.2005.02.004.

199. Y. Divayana, X.W. Sun, Observation of Excitonic Quenching by Long-Range Dipole-Dipole Interaction in Sequentially Doped Organic Phosphorescent Host-Guest System. *Physical Review Letters,* **99**,143003 (2007); DOI: 10.1103/PhysRevLett.99.143003

200. Y. Kawamura, J Brooks, J. J. Brown, H. Sasabe, C. Adachi, Intermolecular Interaction and a Concentration-Quenching Mechanism of Phosphorescent Ir(III) Complexes in a Solid Film, *Physical Review Letters,* **96**, 017404 (2006); DOI: 10.1103/PhysRevLett.96.017404.

201. S.-J. Su, E. Gonmori, H. Sasabe, J. Kido, Highly Efficient Organic Blue-and White-Light-Emitting Devices Having a Carrier- and Exciton-Confining Structure for Reduced Efficiency Roll-Off. *Advanced Materials,* **20**, 4189-4194 (2008); DOI: 10.1002/adma.200801375.

202. J. Ye, C.J. Zheng, X.M Ou, X.H. Zhang, M.K. Fung, C.S. Lee, Management of Singlet and Triplet Excitons in a Single Emission Layer: A Simple Approach for a High-Efficiency Fluorescence/Phosphorescence Hybrid White Organic Light-Emitting Device. *Advanced Materials,* **24**, 3410-3414 (2012); DOI: 10.1002/adma.201201124.

203. Q. Wang, J. Ding, D. Ma, Y. Cheng, L. Wang, F. Wang, Manipulating Charges and Excitons within a Single-Host System to Accomplish Efficiency/CRI/Color-Stability Trade-off for High-Performance OWLEDs. *Advanced Materials*, **21**, 2397-2401 (2009); DOI: 10.1002/adma.200803312.

204. J. Ecton, T. Fleetham, X. Hang, J. Li, Paper No 5.1: Highly Efficient Blue-Green OLEDs From Tetradentate Cyclometalated Platinum Complexes. *SID Int. Symp. Dig. Tec,* **44**, 152-155 (2013); DOI: 10.1002/sdtp.52.

205. R. Wang, D. Liu, H. Ren, T. Zhang, H. Yin, G. Liu, J. Li, Highly Efficient Orange and White Organic Light-Emitting Diodes Based on New Orange Iridium Complexes. *Advanced Materials*, **23**, 2823–2827 (2011); DOI: 10.100